Development of Optical Ratiometric Nanosensor Systems

Dissertation

zur Erlangung des akademischen Grades

doctor rerum naturlium
(Dr. rer. nat.)

im Fach Chemie: Spezialisierung:
Anorganische und Allgemeine Chemie

eingereicht an der

Mathematisch-Naturwissenschaftlichen Fakultät
der Humboldt-Universität zu Berlin

von

M. Sc. Sebastian Radunz

Präsidentin der Humboldt-Universität zu Berlin
Prof. Dr.-Ing Dr. Sabine Kunst

Dekan der Mathematisch-Naturwissenschaftlichen Fakultät
Prof. Dr. Elmar Kulke

Gutachter/innen:
1. Prof. Dr. Erhard Kemnitz
2. Prof. Dr. Kannan Balasubramanian
3. Prof. Dr. Ilko Bald

Tag der mündlichen Prüfung: 28.05.2020

2020

Die vorliegende Arbeit wurde in der Zeit von April 2016 bis Februar 2020 in der Arbeitsgruppe um Dr. Ute Resch-Genger (Abteilung 1 - Fachbereich 1.2, Biophotonik) an der Bundesanstalt für Materialforschung und -prüfung (BAM) angefertigt.

Danksagung

Hiermit danke ich allen, die mich während dieses Abschnitts meines Lebens begleitet und unterstützt haben.

Abstract

Optical probes for monitoring, imaging, and sensing of pH are of great interest for the scientific community as pH is a crucial marker for many processes in biotechnology, biology, medical diagnostics, biomedical research, and material corrosion. Thereby, optical pH sensors based on fluorescence have attracted interest in particular as fluorescence offers a high sensitivity down to the single molecule level, can be read out with relatively simple and readily miniaturized instrumentation, and allows online *in situ* measurements. Also the versatility ranging from molecular and nanosensor formats to planar optodes and fiber-optic sensors, and the non-invasive, non-destructive, and contactless nature of the measurement are application-friendly features. The information content, which is offered by a fluorescence intensity-based sensor, is usually unspecific and limited on the presence or the absence of the chromophore or analyte and can additionally be hampered by fluctuation of the excitation light intensity and changes in fluorophore concentration, e.g., due to photobleaching. Therefore, many fluorescence sensors are utilized in referenced systems, which enable two-wavelength ratiometric measurements of the fluorescence intensity by the introduction of an analyte-inert reference with a spectrally distinguishable emission.

This work presents the rational design of a versatile, modular, multi-component-based platform for ratiometric optical analyte sensing that can be simply adapted to different formats and measurement geometries. Therefore, readily available analyte-responsive fluorescent boron-dipyrromethene (BODIPY) dyes and near infrared (NIR)-excitable multicolour-emissive upconversion nanoparticles (UCNPs) were combined utilizing an inner filter-based strategy with spectrally matched moieties. BODIPY dyes were chosen because this outstandingly versatile dye class provides customized designs for specific and sophisticated applications by synthetically adjustable chemical and photophysical properties.

In this work, a set pH-sensitive BODIPY dyes with tunable pK_a values in dependence on the substitution pattern was synthesized. The pH-sensitivity is thereby induced by the phenolic *meso*-subunit exploiting a photoinduced electron transfer (PET). Subsequently, the optical properties of these dyes were extensively studied with respect to their structural parameters revealing a correlation of sterical hindrance and outstandingly good fluorescence quantum yield (Φ_Fl). A further modification of these dyes by substitution of heavy halogen atoms such as iodine at the chromophore core enables the generation of molecular oxygen in its singlet state ($^1\mathrm{O}_2$) by effectively shifting the deactivation pathway from fluorescence to intersystem crossing (ISC). This was used to rationally design BODIPY-based pH-activatable $^1\mathrm{O}_2$ generators with different pK_a values. Markedly different cytotoxicities of the pH-activatable

compounds upon illumination versus dark conditions were demonstrated, which underline their potential as photosensitizer (PS). A pH-dependent cytotoxicity, thus an on-switched $^1O_2$ generation at lower pH values, was demonstrated *in vitro* for one dye with a pK_a value of 6.4.

As second component of the dual-component platform, NIR-excitable UCNPs were used as they offer background free, sharp and defined luminescence signals in the ultraviolet-visible (UV-vis), and NIR upon excitation with 980 nm light. These unique properties were exploited twice in the work. First, the upconversion luminescence (UCL) of the UCNPs was used for *in situ* monitoring of the UCNP growth during their high-temperature synthesis in combination with *ex situ* monitoring of their UCL decay kinetics as well as their size in dependence of the reaction time. Therefore, the particle sizes were determined by transmission electron microscopy (TEM) and small-angle X-rays scattering (SAXS) with TEM also providing informations of the crystal phases of the nanoparticles. Second, the UCL of the UCNPs upon excitation with 980 nm was simultaneously utilized as nanolamp and reference for the ratiometric sensing platform. Thereby, the blue upconversion (UC) emission of the $NaYF_4$:Yb^{3+}/Tm^{3+} UCNPs was used for the excitation of the pH-sensitive BODIPY dyes, while the red UC emission was used as inert reference. By calculating the ratio of the emission intensities of the dye's green fluorescence and the particle's red UC emission in dependence of pH, monitoring of pH is possible. The potential of this strategy for sensing pH was demonstrated for the monitoring of time-dependent changes in pH induced by metabolizing Escherichia coli (*E. coli*).

Zusammenfassung

Optische Sonden für die Bildgebung auf Grundlage des pH-Wertes und zum Erfassen und Messen eben jenes sind für die Wissenschaft von großem Interesse, da es sich beim pH-Wert um eine entscheidende Kenngröße für viele Prozesse in der Biotechnologie, Biologie, medizinische Diagnostik, biomedizinische Forschung und Materialkorrosion handelt. Optische pH-Sensoren, deren Funktionsprinzip auf dem photophysikalischen Prozess Fluoreszenz basieren, sind dabei von besonderem Interesse, da die Fluoreszenz eine sehr hohe Empfindlichkeit, welche sogar die Auflösung einzelner Moleküle ermöglicht, bietet. Sie ermöglicht weiterhin ein relativ einfaches und miniaturisierbares instrumentelles Auslesen. Diese Vielseitkeit ermöglicht den Einsatz von molekularen über nanoskaligen Sensorformaten bis hin zur Anwendung in planaren Optoden oder faseroptischen Sensoren, und gilt, neben der nicht-invasiven, zerstörungsfreien und kontaktlosen Natur optischer Fluoreszenzmessungen, als anwendungsfreundliche Eigenschaft dieser optischen Sensoren. Der Informationsgehalt, welcher üblicherweise von einem auf Fluoreszenzintensität basierenden Sensor erhalten wird, ist normalerweise unspezifisch auf die An- oder Abwesenheit des Fluorophors und des Analyten beschränkt. Weiterhin kann er zusätzlich durch Schwankungen der Intensität des Anregungslichts und Änderungen der Fluorophorkonzentration, z.B. durch Photodegradation, beeinflusst werden. Aus diesem Grund werden viele Fluoreszenzsensoren oftmals in referenzierten Systemen verwendet. Diese Systeme ermöglichen, durch die Einführung einer analyt-inerten Referenz, ein duales, ratiometrisches Auslesen der Fluoreszenzintensitäten von zwei spektral unterscheidbaren Komponenten.

In dieser Arbeit wird das konzeptionelle Design einer modular variierbaren, auf mehreren Komponenten basierenden Plattform für die ratiometrische optische Analytmessung, welches an verschiedene Designformate und Messgeometrien angepasst werden kann, vorgestellt. Dazu wurden fluoreszente, leicht zugängliche und analyt-sensitive Boron-Dipyrromethene (BODIPYs) mit durch nahes Infrarot (NIR) anregbare, mehrfarbig emittierende Aufkonvertierungs-Nanopartikel (UCNPs) kombiniert. Das Sensorprizip beruht dabei auf einem inneren Filter-Effekt der spektral abgestimmten Komponenten. BODIPYs wurden als Fluorphore gewählt, weil sie eine außerordentlich vielseitige Farbstoffklasse sind, bei der durch synthetisch einstellbare chemische und photophysikalische Eigenschaften verschiedenste Molekülldesigns für spezifische und anspruchsvolle Anwendungen zugänglich sind.

In dieser Arbeit wurde ein Satz an pH-sensitiven BODIPY-Farbstoffen mit verschiedenen pK_{a}-Werten dargestellt. Der pK_{a} wurde dabei mit Hilfe des Substitutionsmuster des *meso*-Substituenten variiert. Die pH-Empfindlichkeit wird dabei durch einen photoinduzierten

Elektronentransfer (PET) der phenolischen *meso*-Untereinheit hervorgerufen. Von allen dargestellten Farbstoffen wurden die optischen Eigenschaften in Abhängigkeit ihrer Strukturparameter untersucht und es konnte eine Korrelation zwischen sterischer Hinderung, hervorgerufen durch die *meso*-Untereinheit, und außergewöhnlich guter Fluoreszenzquantenausbeuten (Φ_{Fl}) festgestellt werden. Eine zusätzliche Modifikation der Farbstoffe durch Substitution eines schweren Iodatoms am Chromophorkern ermöglicht die Erzeugung von molekularem Sauerstoff in seinem Singulettzustand ($^1O_2$). Dabei wird ein effektiver Wechsel des Deaktivierungsweges von der Fluoreszenz zum intersystem crossing (ISC) durch den Schweratom-Effekt des Iods ausgenutzt. Dies Erkenntnisse wurden verwendet, um BODIPY-basierte pH-aktivierbare $^1O_2$-Generatoren mit unterschiedlichen pK_{a}-Werten darzustellen. Dabei konnten deutliche Unterschiede der Zytotoxizitäten der pH-aktivierbaren Verbindungen bei Bestrahlung im Vergleich zu ohne Bestrahlung festgestellt werden. Eine pH-abhängige Zytotoxizität, d.h. $^1O_2$-Erzeugung bei niedrigeren pH-Werten, wurde *in vitro* für einen Farbstoff mit einem pK_{a}-Wert von 6.4 gezeigt.
Als zweite Komponente der Zweikomponentenplattform wurden NIR-anregbare UCNPs verwendet, da sie bei Anregung mit 980 nm Licht hintergrundfreie, scharfe und definierte Lumineszenzsignale im ultra-violetten (UV-vis), sichtbaren und nahen Infrarot (NIR) Spektrum emittieren. Diese einzigartigen optischen Eigenschaften wurden zunächst zur *in situ*-Erfassung des Partikelwachstums während der Hochtemperatursynthese der UCNPs ausgenutzt. Parallel dazu wurde *ex situ* die Abklingkinetik der Aufkonvertierungslumineszenz (UCL) der Partikel und deren Größe in Abhängigkeit von der Reaktionszeit ermittelt. Die Partikelgrößen wurden dafür via Transmissionselektronenmikroskopie (TEM) und Kleinwinkel-Röntgenstreuung (SAXS) bestimmt. Neben der Partikelgröße konnten durch die TEM-Messungen auch Informationen über die Kristallphasen der Nanopartikel erhalten werden. Neben der Erfassung des Partikelwachstums wurde die UCL der UCNPs für die ratiometrische Sensorplattform als Nanolampe und gleichzeitig als Referenzsignal verwendet. Die blaue Upconversion(UC)-Emission der $NaYF_4$:Yb^{3+}/Tm^{3+} UCNPs wurde dabei zur Anregung der pH-sensitiven BODIPY-Farbstoffe verwendet, während die rote UC-Emission als inertes Referenzsignal verwendet wurde. Die Berechnung des Verhältnisses der Emissionsintensitäten der grünen Fluoreszenz des Farbstoffs und der roten UC-Emission des Partikels ermöglicht eine Bestimmung des pH-Werts. Das Potenzial dieser Strategie zur Erfassung des pH-Werts wurde beispielhaft für die Bestimmung der zeitabhängigen Änderungen des pH-Werts einer metabolisierenden Escherichia coli (E. coli)-Suspension gezeigt.

Contents

Abbreviations and Glossary

Φ_{Δ} singlet oxygen quantum yield
$\Phi_{\mathbf{Fl}}$ fluorescence quantum yield
$\Phi_{\mathbf{UC}}$ upconversion luminescence quantum yield
$\tau_{\mathbf{Fl}}$ fluorescence lifetime
ε molar attenuation coefficient
E. coli Escherichia coli
$^{\mathbf{1}}\mathbf{O_2}$ molecular oxygen in its singlet state
$^{\mathbf{3}}\mathbf{O_2}$ molecular oxygen in its ground triplet state

$\mathbf{BF_3 \cdot OEt_2}$ boron trifluoride diethyl etherate
BODIPY boron-dipyrromethene

CET cooperative energy transfer
$\mathbf{CH_2Cl_2}$ dichloromethane
CI conical intersection
$\mathbf{CO_2}$ carbon dioxide

DDQ 2,3-dichloro-5,6-dicyano-1,4-benzoquinone
DFT density functional theory
DIPEA *N*,*N*-diisopropylethylamine
DNA deoxyribonucleic acid

EMU energy migration-mediated upconversion
ESA excited-state absorption
EtOH ethanol
ETU energy transfer upconversion

ICT intramolecular charge transfer
ISC intersystem crossing

LRET luminescence resonance energy transfer

MeOH methanol
ms millisecond

NaF sodium fluoride
NaOH sodium hydroxide

NH_4F ammonium fluoride
NIR near infrared
NO nitrogen monoxide

OA oleic acid
ODE *1*-octadecene
OM oleylamine

PA photon avalanche
PDT photodynamic therapy
PES potential energy surface
PET photoinduced electron transfer
PL photoluminescence
PS photosensitizer

QD quantum dots

RE rare-earth element
$RECl_3$ rare-earth trichloride
RET resonance energy transfer
ROS reactive oxygen species

S_1 first excited state
SAXS small-angle X-rays scattering

T_1 triplet state
TEM transmission electron microscopy
TFA trifluoroacetic acid

UC upconversion
UCL upconversion luminescence
UCNP upconversion nanoparticle
UV-vis ultraviolet-visible

List of Figures

1 Introduction & Motivation

1.1 Preliminary Remarks

Chemistry has always been a creative and constructive science with analytical and theoretical elements. While the synthetic chemist uses readily available compounds to craft more complex products through defined chemical reactions, the analytical chemist studies and reveals structural relations within molecules and materials, and the physical chemist investigates mechanisms of physicochemical processes. Although simplified, these descriptions represent the complexity and finesse of the chemical tasks of design, construction, analysis and investigation of new materials for the application in various fields from material to life sciences. Due to the ever-increasing demand of these materials with better quality and applicability by technological and social advancement of our society, chemists constantly strive to improve these material-based features by developing new methods, systems and procedures.

1.2 Boron-dipyrromethene (BODIPY) - A Versatile Chromophore

In the entire history of human mankind, chromophores have always been a tacit fellow in the development of the human society with increasing importance throughout the ages. While chromophores were mainly used for cultural purposes beginning from the stone age, e.g., for mural or body paintings, they later became important for various aspects of the sociocultural development of humanity, e.g., religion and art. Already ancient civilizations in the Andes and in Egypt synthesized organic dyes and inorganic pigments such as indigotin and Mayan and Egyptian blue, respectively, and used them for dyeing of clothes and decorative purposes.[1,2] At that time, however, these chromophores were rare and expensive as there was neither a chemical nor a physical fundamental understanding of these materials. Later, when scientists unfolded a basic understanding of chemical and physical properties of chromophores such as chemical structures and underlying photophysical processes, the availability of chromophores increased drastically and their importance for the human society became immeasurable on many levels.

Although there has always been a scientific interest in dye chemistry, a renewed research interest has evolved in the last years due to an impressive growth of modern approaches in chemistry. Especially for organic chromophores, the development of new molecular structures, e.g., by modifying available chromophores with desired substitution patterns that meet

specific requirements for targeted applications, is promoted by new synthetic approaches.[3] Particularly, organic molecules with the ability to emit fluorescence are of great interest as the recent technological advances in fluorescence based spectroscopic techniques together with the growing interest in real-time monitoring of biochemical processes on the nanoscale offer a huge scientific and technological potential. Although there are already numerous fluorophores commercially available that cover the ultraviolet-visible (UV-vis) as well as partially the NIR region, customized fluorescent probes, sensors and markers are mandatory for this purpose. Subsequently, the search for new organic fluorophores is an active research field with the task of finding molecular structures with improved photophysical properties such as application optimized spectral properties, fluorescence quantum yield (Φ_{Fl}), singlet oxygen quantum yield (Φ_{Δ}) and photostability, and additionally with functional moieties, e.g., for introducing analyte-responsiveness for sensing or for target-specific binding for optical imaging. Especially chromophores with ideally activatable dual functionality, which can be used simultaneously for diagnosis and therapy, termed theranostic, offer a unique application potential, e.g., for photodynamic therapy (PDT).[4,5]

4,4'-difluoro-4-bora-3a,4a-diaza-*s*-indacene dyes, abbreviated Boron-dipyrromethenes (BODIPY), are a class of boron-chelated organic heterocycles. They have evolved as one of the most promising dye classes for key applications in material and life sciences in recent years as these dyes outperform most other chromophore classes with respect to versatility, accessibility and key photophysical and chemical properties. Although they were already reported back in 1968 by Treibs and Kreuzer,[6] their full potential was not recognized until the early 1990s after first commercially available BODIPY-based fluorescent dyes were used for fluorescence microscopy.[7] The cycle of steadily increasing research interest and successive development and application progress has lead to an drastic increase of available BODIPY dyes for various applications. This ongoing progress is mainly attributed to the chemical versatility of the BODIPYs which was already expressed by Ziessel *et al.* in 2007, when they claimed that the chemistry of BODIPYs is "*a new El Dorado for fluorescence tools*".[8,9] Almost at the same time, Loudet and Burgess published a comprehensive review about the synthesis and spectroscopic properties of so far accessible BODIPY dyes which substantiated Ziessels statement.[10] This statement was later also supported by Bañuelos when he reviewed the question whether the BODIPY dyes are "*the most versatile fluorophore(s) ever?*" in 2016.[11] He stated, that although the increased interest and research effort put into BODIPY dyes already suggests a full exploration of the potential of this dye class, the real situation is the opposite with a promising future for this dye class due to its chemical versatility. The versatility of BODIPY is mainly based on their chemical accessibility and subsequent capability of functionalization which allows fine-tuning of photophyiscal properties.

1.2.1 Synthesis and Post-Functionalization

The most common synthesis routes of BODIPY dyes usually involve the condensation reaction of pyrrole derivatives with electrophilic carbonyl group, such as acyl chlorides, aldehydes or 2-ketopyrroles, followed by the boron chelation of the bridged pyrrole building blocks, which is the key for the planar, rigid and highly conjugated chromophore core of the BODIPY dyes. These and other routes and a whole variety of accessible BODIPY-based structures (see examples provided in chapter 1.2.2) have been summarized and discussed extensively in several reviews in the past.[8–10] Hence, this work will only provide a small excerpt of the synthesis of of BODIPYs for a contextual background.

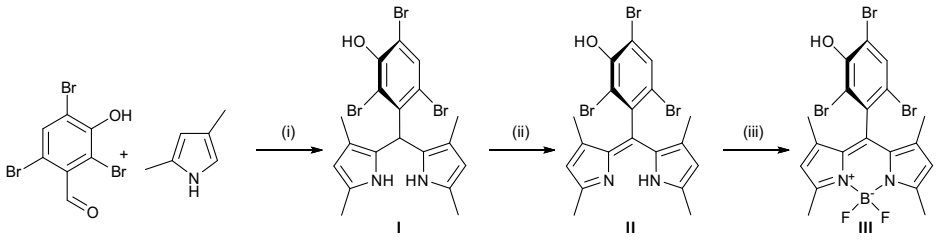

Figure 1: Synthesis route of BODIPY dyes using an aldehyde precursor. Reagents and conditions: (i) a) CH_2Cl_2, TFA, r.t., 18h b) CH_2Cl_2/EtOH (14/1 v/v), TFA, r.t., 18h (ii) *p*-chloranil, CH_2Cl_2, r.t., 1h (iii) DIPEA, $BF_3 \cdot OEt_2$ a) 13 %[12] b) 60 %.[13]

As exemplarily shown in Figure 1 for the synthesis route using a benzaldehyde precursor, the syntheses of BODIPY dyes involve multiple steps, which can be either performed stepwise with synthetic accessibility of the intermediate structures or carried out in a one-pot reaction. The first step is an acid-catalyzed condensation of the aldehyde precursor and two equivalents of the pyrrole precursor under formation of a dipyrromethane. This synthetic approach was initially developed by Lindsey and coworkers to employ access to *meso*-substituted dyprromethanes used as precursors for the synthesis of *meso*-porphyrins.[14,15] However, dipyrromethanes also proved to be excellent precursors for the synthesis of BODIPY-based dyes. Thus, the renewed research interest in dye chemistry has not only lead to developments in the synthesis of BODIPY dyes[16] but also to recent improvements in the accessibility of dipyrromethanes.[17,18] The second and third reaction steps of the BODIPY synthesis are the oxidation of the dipyrromethane to the corresponding dipyrromethene by an oxidizing agent such as *p*-chloranil or 2,3-dichloro-5,6-dicyano-1,4-benzoquinone (DDQ) followed by the amine-mediated boron chelation (see Figure 1). For the boron chelation, typically *N*,*N*-diisopropylethylamine (DIPEA) is used as amine base while boron trifluoride diethyl etherate ($BF_3 \cdot OEt_2$) is used as boron source. The overall reaction yields following the standard one-pot protocol commonly carried out in dichloromethane (CH_2Cl_2) are often reported in the range of 20 - 30 % and even lower reaction yields are obtained for dyes with sterically hindered *meso*-substituents.[19] While investigating the prepa-

ration of sterically demanding *meso*-mesityl porphyrins Lindsey reported in one of his first works in 1989 drastically increased yields for dipyrromethane formation in CH_2Cl_2 upon addition of ethanol (EtOH) as co-solvent.[20] Although this was already reported in 1989, Bartelmess *et al.* were the first who take advantage of this finding. By adjusting the synthetic procedure for their needs, they reported increased reaction yields for both, sterically hindered and sterically non-hindered BODIPY derivatives.[19] Surprisingly, this synthetic approach has not yet been established in the BODIPY community although drastically increased reaction yields of >50 % can be achieved by default without significant additional effort, e.g., upon addition of EtOH as co-solvent a remarkable reaction yield increase from 13 % to 60 % was achieved for the sterically hindered BODIPY exemplarily shown in Figure 1 (see route a) and b), respectively).[12,21]

The outstanding chemical versatility of BODIPY dyes is not only expressed by the synthesis of the chromophore core but by the variety of post-functionalization reactions, since their chromophoric core is selectively accessible to a large number of chemical reactions. Possible reactions, accessible structures and resulting photophysical properties of the dyes have been studied extensively and have already been summarized in various reviews.[22–24] While syntheses employing aldehyde precursors are common for the introduction of *meso*-substituents with defined functionalities, post-functionalization reactions can be utilized to introduce distinct functionalities at other positions of the chromophore. Both methods are utilized, e.g., for the development of BODIPY dyes for conjugation with biomolecules[25] and for the synthesis of analyte-responsive BODIPY dyes for sensing,[26] imaging[27] and photodynamic therapy (PDT).[28] As shown in Figure 2 a) this variability is achieved as each individual position at the chromophore core can be addressed by at least one post-functionalization reaction, which overall allows an exhaustive and rich substitution pattern.[22–24] Consequently, a large amount of studies focus exclusively on the correlation between structural and photophysical properties of BODIPYs.[29–33] Eventually, this helps to understand the fundamental processes governing the photophysics of BODIPY dyes, which subsequently can be exploited for different applications. The substitution at the chromophore core, e.g., enables specific modulation of the photophysical properties as exemplarily shown in Figure 2 b). The introduction of one or two styryl groups in 3/5-position of the BODIPY core by a Knoevenagel type reaction leads to a pronounced spectral redshift in dependence of the degree of substitution due to the extension of the π-electron system. The 1/7-position of the core are also accessible by Knoevenagel condensation enabling the synthesis of unique tetrastyryl substituted BODIPYs with an even more redshifted absorption and fluorescence emission.[34] Upon rational design, e.g., by the introduction of defined functionalities, tailor-made dyes with specific properties and with absorption and fluorescence emission covering the whole visible spectrum can be obtained.[35] These new BODIPY dyes often outmatch other dyes from other dye classes with

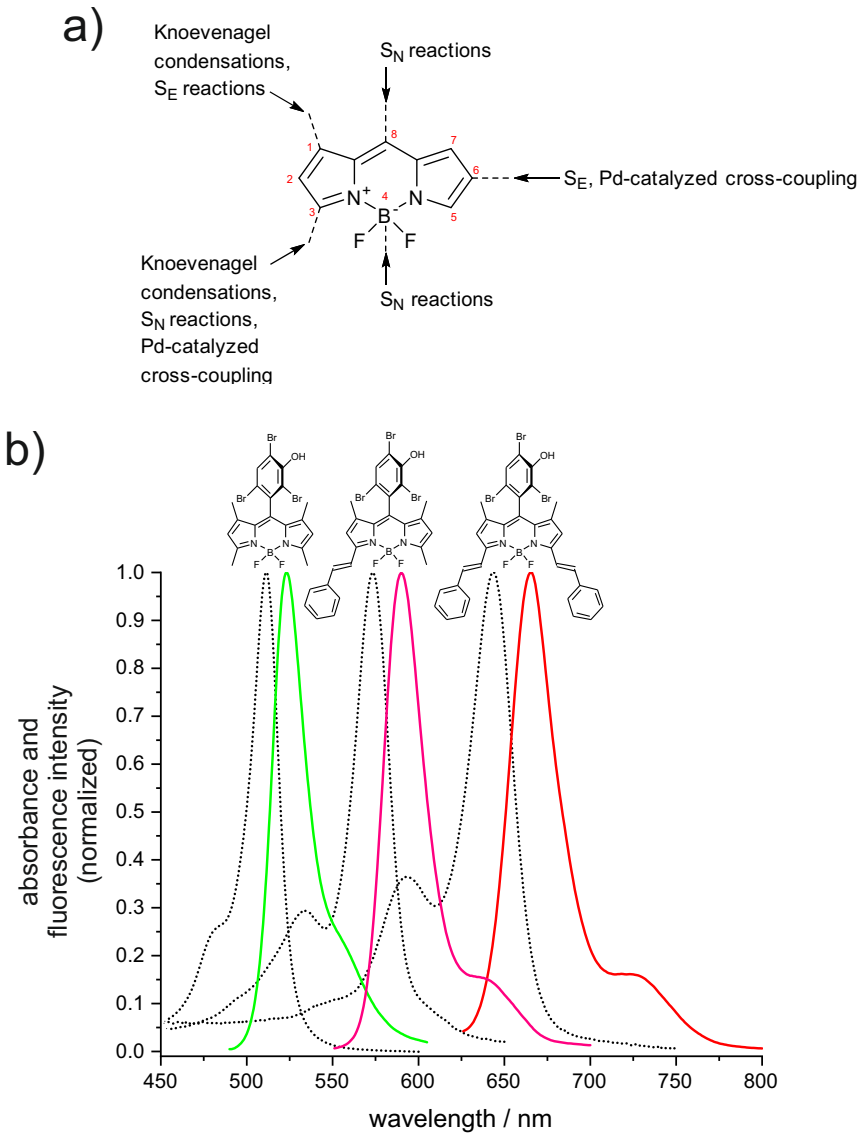

Figure 2: a) Molecular structure of the BODIPY core and possible organic reactions for post-functionalization.[22–24] b) Changes of the absorption and fluorescence emission in dependence of substitution degree in 3/5-position of the BODIPY core.

respect to photophysical and chemical performance as well as applicability, which explains the increased attention this dye class has received in the last decades.[24]

1.2.2 Application Fields of BODIPY dyes

So far, BODIPYs have been widely applied in material and life sciences.[8,9,11,24,27] Thereby, the increasing applicability of these dyes can be mainly attributed to their outstanding photophysical and chemical properties such as high Φ_{Fl}, high molar attenuation coefficient (ε), relatively narrow absorption and emission bandwidth, good photostability, chemical robustness and good solubility. This is additionally highlighted by the fact, that most of these

properties are synthetically adjustable for specific needs, which is exploited, e.g., for the design of BODIPY-based laser dyes,[36–39] building blocks for artificial photosynthetic models,[22] fluorescence probes for sensing and imaging,[26,27,40,41] or probes for medical diagnostics[42–44] and treatment.[45]

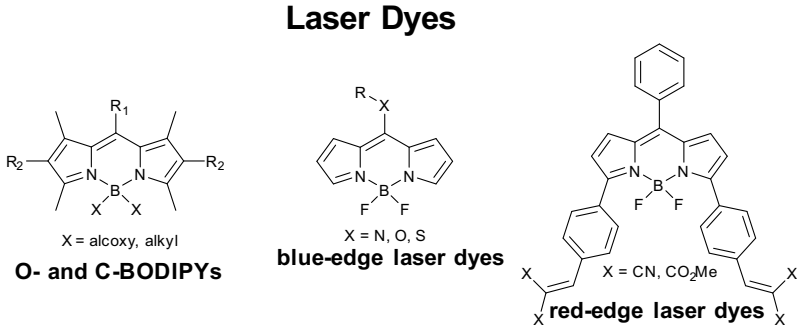

Figure 3: Representative molecular structures of BODIPYs used as laser dyes.[36–39]

BODIPY dyes naturally offer a high photostability and a remarkable fluorescence due to their rigid chromophore core. These are favourable properties for the use as photoactive compound in dye lasers. Thus, they "*bursted into* (this field of) *organic and physical chemistry and gained recognition by the scientific audience.*"[11] Despite their good basic performance in laser applications, several attempts were made to further improve their laser related properties by increasing their a) photostability and b) Φ_{Fl}. While BODIPY dyes with excellent photostability and improved Φ_{Fl} are accessible by substitution of the fluorine with alkoxy or alkyl substituents (see Figure 3), the applicability of these compounds is limited due to their limited spectral variability.[36,37] An increase of the spectral coverage while maintaining outstanding laser dye properties can be achieved by selective substitution at the chromophore core which consequently allows the design of highly efficient BODIPY-based laser dyes covering the whole visible spectral region. The amplitude and direction of the spectral shift upon substitution depends not only on the position but also on the nature of the substitutents. As illustrated in Figure 2 b), a bathochromic shift is straightforwardly accessible by substitution in 3/5-position with substitutents which extend the π-electron system. This, among other things, is exploited for the design of red-edge laser dyes (see Figure 3).[39] A hypsochromic shift of the spectral bands for blue-edge laser dyes while maintaining good laser properties was found for the presence of heteroatoms in *meso*-position (see Figure 3).[38]

The versatility of the BODIPYs with respect to the adjustable spectral properties can also be exploited for the design of BODIPY-based building blocks for artificial photosynthetic models.[22] Artificial photosynthetic models are bioinspired systems which mimic steps of the photosynthetic process in plants. A main goal to improve the efficiency of the photosynthetic process is to expand the spectral range that is used for excitation. This can be achieved, e.g., by the use of multiple chromophore which feature a resonance energy transfer (RET)-

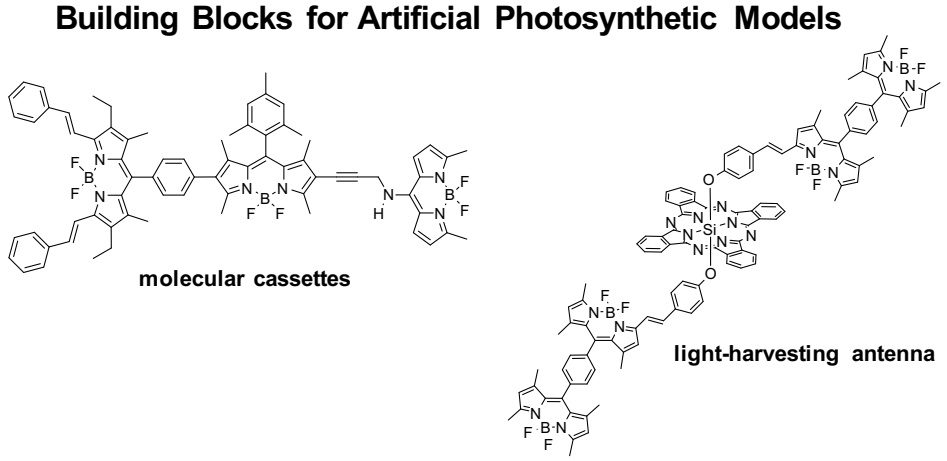

Figure 4: Representative molecular structures of BODIPYs used as building blocks for artificial photosynthetic models.[46,47]

mediated transfer of the excitation energy.[48] Mandatory prerequisites for RET are matching spectral properties of the dyes involved, namely overlapping emission and absorption spectra of donor and acceptor chromophores, respectively. Successive spectral overlaps of more than two chromophores with every component acting as donor and acceptor simultaneously eventually enable a cascade-like radiationless transfer of the excitation energy. For such systems different but complementary spectral properties of the components involved are mandatory. Overall, this expands the spectral range used for the excitation of photosynthetic model. By exploiting the aforementioned synthetic versatility, BODIPY-based building blocks for artificial photosynthetic models are readily accessible. Consequently, BODIPYs have already been successfully applied as components in optoelectronic conducting polymers,[49] molecular energy transfer cassettes,[47,50] and light-harvesting antennas (see Figure 4).[46,51] All of these BODIPY-based molecular antennas outstand with respect to the efficiency of the RET, the broadband absorption and the selective emission of the last acceptor, which is always redshifted due to the nature of the energy transfer cassette.

1.2.2.1 BODIPYs for Sensing Applications

BODIPY dyes and their photophysical properties are well-known for their insensitivity with respect to environmental conditions, which is expressed by their high chemical robustness and outstanding photostability. However, this can be reversed by the introduction of selected environmental-sensitive substituents, which promote usually undesirable fluorescence quenching phenomena such as intramolecular charge transfer (ICT) or PET.[11] This opens up completely new applications for BODIPYs in the field of optical chemical sensors. Optical chemical sensors are defined as "*miniaturised devices that can deliver real time and on-line information on the presence of specific compounds or ions in even complex samples.*", which offer many advantages such as non-destructive, contactless and highly sensitive

measurements.[40,52] So far, several reviews on fluorescent indicators based on the BODIPY framework have been published, which also focused on the basic mechanisms used for optical sensing.[26,27,41] A small excerpt of the great variety of BODIPY-based optical sensors

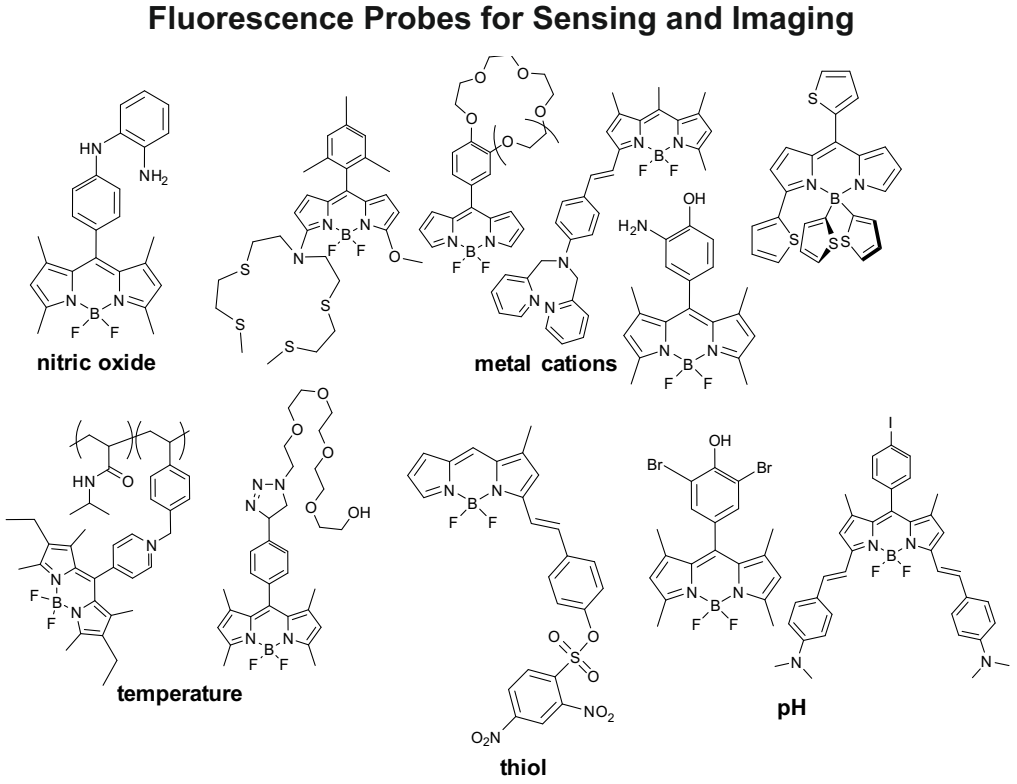

Figure 5: Representative molecular structures of BODIPYs used for sensing and imaging applications.[12,53–62]

is given in Figure 5. Environmental parameters such as temperature or viscosity can be, e.g., monitored with molecular rotors. However, the sensing principle of these sensors is not based on introduced fluorescence quenching processes such as ICT or PET, they simply exploit basic photophysical processes in BODIPY dyes.[59,60,63–65] These kind of sensor dyes often consists of two components, the basic chromophore core and a chain-like substituents which is typically attached to the *meso*-substituent. Upon changes of the microenvironment by temperature or viscosity, the rotation of the chromophore core and *meso*-substituent is drastically affected due to the interaction of the chain-like substituent with the surrounding molecules (solvent, biomolecules). While higher rotation rates are typically observed for high temperatures and low viscosities, lower rotation rates up to a freezing of the rotational motion can be observed for low temperatures and high viscosities. Thereby, the fluorescence quenching effect is based on an increased non-radiative deactivation of the first excited state (S_1) upon increased rotation exploiting the structural similarity of the transition state of the rotational motion and the relaxed state of the S_1.[66–68] A much broader application potential presents the detection and quantifying of certain molecular or ionic analytes upon

introduction of a fluorescence quenching process by defined substituents. This allows monitoring of analytes such as glucagon,[69] thiol,[61] nitric oxide,[53] hypochlorous acid,[70] nitroxyl,[71] fluoride,[72] and various metal cations such as Cd^{2+},[54] K^+, Rb^+, Cs^+ and Ba^{2+},[55] Cu^{2+} and Hg^{2+}.[56–58] From all reported sensor systems, the introduction of a PET-based fluorescence quenching process often showed the best performances with respect to sensitivity and signal enhancement. Since PET is highly efficient, analyte-induced on/off-switchable fluorescence readouts can be readily achieved, which in general is highly favourable for optical imaging. PET-based optical chemical sensors are particularly well suited for sensing of pH.[73] The determination of pH value is amongst the most commonly performed analytical measurements in the material and the life sciences as it presents a crucial parameter, e.g., for corrosion processes and as biomarker for medical diagnostics, molecular imaging, and cell biology indicating inflammatory and/or cancerous tissue. Consequently, the first BODIPY-based pH sensors were already reported by Werner *et al.* in 1997.[74] Additional fluorescent BODIPY-based pH sensors were developed since then, however, the amount of available sensors with pK_a values in the physiological range is still limited,[62,75–89] although they are particularly of high interest for *in vitro* and *in vivo* measurements, e.g., for determination of intracellular pH.[90–92]

1.2.2.2 BODIPYs for Photodynamic Therapy (PDT)

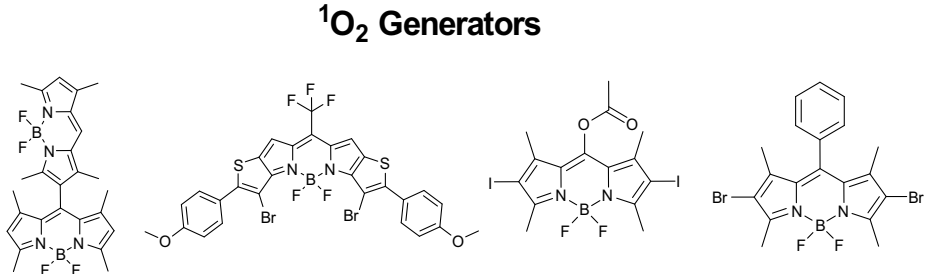

Figure 6: Representative molecular structures of BODIPYs capable of singlet oxygen generation upon illumination.[93–96]

PDT has emerged as a an easily applicable, low invasive, and very promising therapy for the treatment of a variety of cancers.[97] It is based on the presence of three individually non-toxic components, namely the PS, molecular oxygen in its ground triplet state ($^3O_2$), and light.[98] Generally, PDT provides better tissue selectivity than conventional chemotherapy as the presence of the PS is mandatory and only its light-activation results in the formation of $^1O_2$ and reactive oxygen species (ROS).[99] Due to their high reactivity, generated $^1O_2$ and ROS typically induce fatal cellular damage, which eventually leads to cell death by apoptotic and/or necrotic processes.[100] The $^1O_2$ generation utilizing a PS circumvents the usually spin and symmetry forbidden transition from $^3O_2$ to $^1O_2$ by the selective generation of the PS in its excited triplet state (T_1). As fluorescence and ISC are competing deactivation

pathways after light excitation of a chromophore from its ground state to its S_1 state, the ISC rate has to be increased in order to increase the population of the excited T_1 state to favour $^1O_2$ generation. For BODIPY dyes, this is commonly achieved by the introduction of heavy halogen atoms such as bromine or iodine as substituents at the chromophore core (see Figure 6).[94–96,101–107] However, an increase of the ISC rate can be also achieved by other strategies, e.g., in dimeric BODIPYs[93] (see Figure 6) or in BODIPY-fullerene dyads.[108] Due to aforementioned outstanding photophysical properties in combination with their unsurpassed versatility, BODIPY dyes are particularly suitable for PDT purposes, e.g., for theranostic applications. This was shown in a multitude of reviews in recent years.[28,109–112]

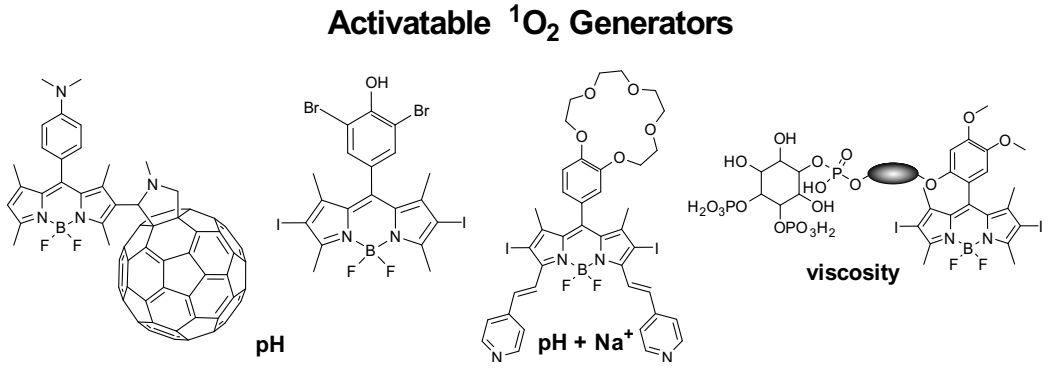

Figure 7: Representative molecular structures of BODIPYs with activatable singlet oxygen generation.[13,108,113,114]

Activatable PSs have become of great interest in recent years especially for theranostic applications[115] as they offer an additional layer of selectivity for PDT as well as they can also provide a real-time feedback of the state of the PS, e.g., by fluorescence intensity.[116,117] Most of the accessible activatable BODIPY-based PSs are thereby based on the combination of the conceptual designs for BODIPY-based sensors and BODIPY-based PSs as exemplarily shown in Figure 7 for pH- or viscosity-activatable PSs.[113,114,118–122]

1.3 Energy Upconverting Nanoparticles

The first development of upconverting phospors in the 60s has led to an increasing interest in the development of new materials for various applications utilizing this novel optical features.[123–125] Subsequently, new synthetic approaches enabled the access to small particles with the capability of photon upconversion (UC). In the last decades, a lot of research has been done on upconversion nanoparticles (UCNPs), which led to improvements of their synthetically accessibility as well as their optical properties. Nowadays, high-quality UCNPs with controllable size, shape and crystallographic phase as well as defined optical properties are readily accessible for a wide range of applications. Since nanocrystalline UC phosphors are promising candidates for applications ranging from material to life sciences, several re-

views have been published so far, which focus in detail on the development, investigation and application of UCNPs.[126–141]

1.3.1 Energy Upconversion - A Brief Description

Absorption and luminescence refer to photophysical processes in which atoms/ molecules can undergo changes in their energy states.[142] While the absorption of light increases the energy within the system leading to a higher population of the first excited state (S_1) and/or even higher energy states, luminescence in its many forms like fluorescence and photoluminescence (PL) is the radiative relaxation into lower energy states. Obeying the Stokes' law, the energy of the absorbed photon is generally higher than the energy of the emitted photon due to non-radiative relaxation processes prior emission.[143] However, in case of multiphoton excitation, in which one atom or molecules absorbs the energy of multiple photons sequentially, the emitted photons can have a shorter wavelength, thus a higher energy, than the incident photons. While the luminescence following Stokes' law is termed downconversion luminescence, the process involving an anti-Stokes shifted photoluminescence is called photon upconversion (UC). This luminescence is referred to upconversion luminescence (UCL).
Photon UC was already proposed in 1959 by Bloembergen[123] and experimentally discovered for systems containing rare-earth (RE) ions in 1966 by Auzel.[124,125] UC proceeds by different mechanisms, all referring to a non-linear optical process based on the sequential absorption of low-energy photons by metastable, long-lived energy states leading to the population of excited states of higher energy from which UCL eventually occurs. Certain ions of the d- and f-block elements were proposed to be most suitable for UC as their ladderlike arranged energy levels show lifetimes in the time range of milliseconds (ms), which favour sequential energy transfer to higher energy states. Subsequently, UC is observed for the d-block metal ions Ti^{2+},[144,145] Ni^{2+},[146–148] Mo^{3+},[149,150] Re^{4+},[149,151] and Os^{4+},[152,153] as well as for f-block ions when doped into suitable solid host materials.[154–156] The UC efficiencies observed for d- and f-block containing systems differ drastically with generally brighter UCL for f-block ions, especially for lanthanides. RE elements additionally feature more advantages such as multiple narrow and long lifetime emissions due to the presence of abundant, metastable energy levels with distinct energies.[135] Most of these properties can be attributed to the electronic configuration of the lanthanides with their 4f electrons being effectively shielded by the 5s and 5p electrons and to different mechanisms of the UC process. The mechanisms for UC are divided into several classes: energy-transfer upconversion (ETU), excited-state absorption (ESA), photon avalanche (PA), cooperative energy transfer (CET), and energy migration-mediated upconversion (EMU). These mechanisms have already been addressed, summarized and discussed extensively in review articles stating ETU as most efficient for UCL.[135,138,157,158] The efficiency of the UC process, however, does not only depend on the mechanism but also on the composition of the material, which includes the host material

and the activator and sensitizer components. In ETU, the component acting as sensitizer absorbs photons and transfers the energy to the activator, that emits UCL after multiple energy transfers. So far, the highest UC efficiencies were observed for RE ion-doped solids with Er^{3+}, Tm^{3+}, or Ho^{3+} acting as activator and Yb^{3+} or Nd^{3+} acting as sensitizer.[126–141] Yb^{3+} is predestined as sensitizer as it has only a single excited state which can be excited at 980 nm and possesses a relatively high absorption cross-section for a lanthanide although its 4f-4f transition is Laporte-forbidden. Additionally, the energy difference between the ground state $^2F_{7/2}$ and the excited state $^2F_{5/2}$ of Yb^{3+} matches very well with the energy differences in several other lanthanides, e.g., Er^{3+}, Tm^{3+}, and Ho^{3+}, as can been seen exemplarily for Yb^{3+}/Er^{3+}- and Yb^{3+}/Tm^{3+}-systems in Figure 8a and b, respectively.[135]

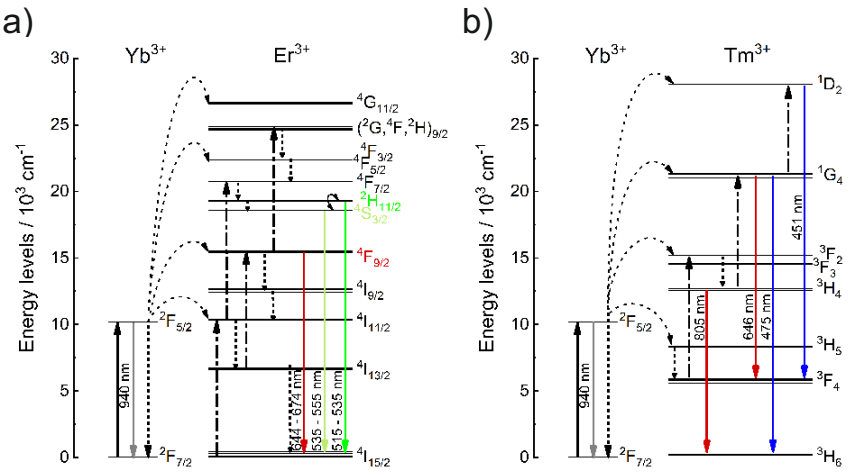

Figure 8: a) Energy scheme of Yb^{3+} and Er^{3+} in $NaYF_4$ host lattice showing possible ETU pathways. Reprinted with permission from S. Radunz *et al.*.[159] Copyright 2018 American Chemical Society. b) Energy scheme of Yb^{3+} and Tm^{3+} in $NaYF_4$ host lattice showing possible ETU pathways. Reprinted with permission from S. Radunz *et al.*.[21] Copyright 2019 American Chemical Society.

The efficiency of the UC process is particularly high for the Yb^{3+}/Er^{3+} system as the energy difference between the $^2F_{7/2}\rightarrow{}^2F_{5/2}$ transition of Yb^{3+} is well resonant with the subsequent $^4I_{15/2}\rightarrow{}^4I_{11/2}$ and $^4I_{11/2}\rightarrow{}^4F_{7/2}$ transitions of Er^{3+}. It is energetically also the in the same range of the $^4I_{13/2}\rightarrow{}^4F_{9/2}$ transition of Er^{3+}, with the latter transition being accessible after previous non-radiative relaxation from $^4I_{11/2}$ to $^4F_{13/2}$. Similar mechanisms apply for the resonant transitions for Yb^{3+}/Tm^{3+} systems (see Figure 8b).[135] The properties of lanthanides make them to the most versatile candidates for UC materials as defined systems of combined lanthanides enable UC by RET from one component acting as sensitizer to another component acting as activator, eventually resulting in UCL. However, more variables of the systems such as the composition, e.g., host material, lanthanide concentration, and design have to be considered as they have a significant impact on the UC efficiency.

1.3.2 Composition and Design of Upconversion Materials

UCL is only shown by lanthanides in their optically active ionic form RE^{3+}. This prerequisite is fulfilled best upon embedding the RE ions into a crystal lattice of a solid host material. Consequently, this renders the host material an essential part for the efficiency of an UC system with the host lattice having ideally the following properties: a) high tolerance for luminescent centers which minimizies defects of the crystal lattice which usually favour deleterious non-radiative deactivation, b) low phonon energy to minimize non-radiative relaxations, c) high transparency of the host material for free migration of the photons used for excitation of the lanthanides, and d) chemical inertness and high thermal stability.[135]
Trivalent optically inert RE^{3+}-containing hosts, with RE^{3+} = Ln^{3+}, Sc^{3+}, and Y^{3+}, were found to be the best suited matrices for UC materials as they have similar valence states and similar chemical and physical properties like the doped optically active RE^{3+} ions. So far, numerous reports of UC phosphors with crystalline host matrices based one RE^{3+}-doped oxides,[160,161] oxysulfides,[162] oxysalts,[163] and fluorides[164] have been published.[135] The surrounding crystal lattice of the RE^{3+} differs for each host material, which consequently affects the UC efficiency and therefore the emission properties such as luminescence intensity and color output.[165] However, the UC efficiency does not only depend on the crystallographic environment but also on the macroscopic surrounding. For nano-sized UC materials (UCNPs), RE fluorides have been proven to be the best host matrices in terms of the requirements mentioned above, since they have comparatively high chemical stabilities like oxides, while they have lower phonon energies than oxides.[126] Nonetheless, fluorides with cations other than RE^{3+} but of similar ionic size such as the alkaline earth ions Ca^{2+}, Sr^{2+}, and Ba^{2+} have also shown to be suitable as host lattices for UCNPs.[166] However, the optimum lattice with respect to UC efficiency was found within the $NaREF_4$ series, namely $NaYF_4$.[156,167] While there are two crystal phases present for $NaYF_4$, a cubic α-$NaYF_4$ and a hexagonal β-$NaYF_4$, respectively, the β-phase is commonly chosen for UC phosphors as it presents a much higher UC efficiency relative to the α-phase.[164,167]
It was found, that beside the host lattices, the dopant concentration as well as their relative ratios also have a tremendous impact on the UC efficiency, thus color output and brightness. For the by far most studied UC phosphors, β-$NaYF_4$ doped with Yb^{3+}/Er^{3+} or Yb^{3+}/Tm^{3+}, the optimum doping for β-$NaYF_4$:Yb^{3+}/Er^{3+} UCNPs was found to be 20% and 2% for Yb^{3+} and Er^{3+}, respectively, while the optimum doping of 20% and 0.5% for Yb^{3+} and Tm^{3+}, respectively, was found for β-$NaYF_4$:Yb^{3+}/Tm^{3+} UCNPs.[168–170] Since the doping ions as well as their concentrations and ratios are adjustable, the optical properties of UC materials can be adapted properly by needs for the intended use.[135,171] Although the embedding of additional RE ions into the host lattice is in general referred as doping, it is more of a replacement/substitution as the used quantities of the incorporated ions as well as the strong impact on the crystal lattice exceed the amount and effects of usually performed doping, e.g., for semi-conductors.[172] However, the strong impact on the crystal

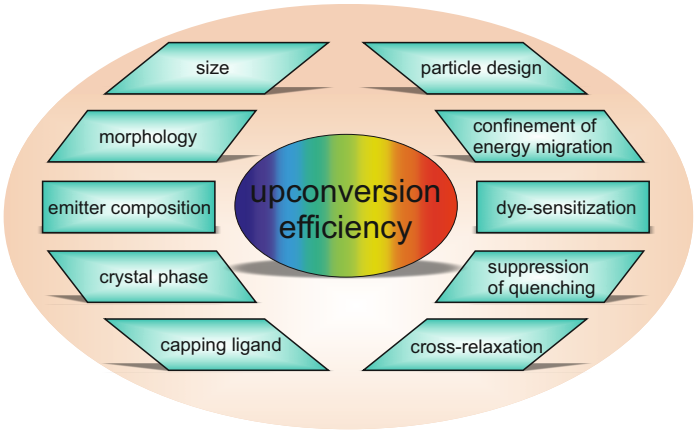

Figure 9: Schematic illustration of synthetically variable factors that affect the UC efficiency and strategies to improve the UC efficiency of UCNPs.

lattice, e.g. by distortion, is mandatory for UC of RE^{3+}-containing phosphors as it lowers the symmetry within the crystal lattice which favours the probability of usually parity forbidden f-f transitions within RE^{3+} ions.[141,171] Further improvements of the brightness and efficiency of UCNPs can be achieved by selected strategies for optimization of the UC performance, e.g., by dye-sensitization,[173–176] by suppression of surface-related quenching,[177–179] by elimination of deleterious cross-relaxation,[180,181] by confinement of energy migration,[182] or by the combination of active/inactive parts within the particles.[183,184] These strategies, however, require defined designs of the nanocrystals ranging from core to core-(multi)shell particles as size and morphology, crystal host material and crystal phase, surface-capping ligands and coatings, as well as dopant distributions within the particles are key parameters which all affect the UC efficiency of UCNPs (see Figure 9).[185]

1.3.3 Synthesis of Upconversion Nanoparticles

The synthetic accessibility of UC materials has always been of tremendous interest for the scientific community. The development of the synthesis of nanocrystalline UC phosphors therby released new options for the design of nano-materials with tunable optical properties as it also paved the road for new applications of these materials in life and material sciences. In early works, the synthesis of nanocrystalline UC phosphors was often accompanied with problems such as high polydispersities and uncontrollable and limited morphologies. However, new synthesis routes experienced an enormous development, which not only led to nowadays readily accessible UCNPs with controllable size, size distribution, morphology and shape, dopant ratio and distribution, and surface-capping ligands,[128,129,132,133] but also to further, steadily ongoing research on synthesis routes which enable access to even more complex nanocrystalline UC structures with remarkable features.[139] So far, several synthetic approaches for the synthesis of nanocrystalline UC phosphors such as thermal decomposition, hydrothermal/solvothermal synthesis, coprecipitation, and sol-gel synthesis (see Figure 10)

have been established. The thermal decomposition and the hydrothermal/solvothermal synthesis are the by far most popular methods for the synthesis of morphologically well-defined $NaREF_4$-based UCNPs. All methods presented in Figure 10) are referred as soft chemical routes as they naturally offer the possibility of the introduction of surface ligands, which prevent aggregation of the particles during and after the synthesis. Furthermore, they allow huge variations of synthesis factors such as precursor materials, solvents, additives, temperatures, and reaction times to conveniently manipulate size, shape and morphology of the particles. They additionally offer multiple potential advantages regarding economic aspects such as low energy need, simple apparatus, low cost and potential for large-scale production.[133]

The synthesis of nanocrystalline UC materials by thermal decomposition is an organic-phase reaction in a mixture of coordinating and non-coordinating high-boiling organic solvents such as oleic acid (OA), oleylamine (OM) and *1*-octadecene (ODE). The solvents do not only enable access to high reaction temperatures, the coordinating solvents oleic acid (OA) and oleylamine (OM) also prevent aggregation of the nanocrystals due to capping of the surface with their polar groups. They also affect the crystal growth during synthesis.[186] While this method usually provides UCNPs with nonpolar surface-capping ligands, the hydrothermal/solvothermal synthesis is performed in water-based systems yielding UCNPs with polar surface-capping ligands. The thermal decomposition is usually performed oxygen-free at elevated temperatures to prevent oxidation and assist the dissolving and decomposition of the precursor materials, respectively. This method can be further classified into three categories based on the precursors material used for synthesis: 1. trifluoroacetate precursor, 2. oleate, acetylacetonate, acetate, and other precursors, 3. methanol assisted organic-phase synthetic methods (see Figure 10).[133] Using trifluoracetates as precursors is advantageous as they act as both RE^{3+} and fluorine source at the same time. This makes the crystallization process of the nanocrystals easily controllable which in consequence allows the preparation of high-quality RE fluorides. This was first shown by Zhang *et al.* for OA-capped LaF_3 nanoplates.[187] Further research by the group of Yan lead to a general synthesis of optically active, transparent and colloidal stable OA-capped $AREF_4$ nanoparticles (A = Na, Li, K; RE = Pr- Lu, Y) via cothermolysis of the respective trifluoroacetates.[188–190] At this point, Mai *et al.* were already able to distinguish between cubic α-$NaYF_4$ and hexagonal β-$NaYF_4$ phase as well as they had access to both crystal phases by varying the synthese parameters. Subsequently, this leads to first assumptions of the mechanism of the formation of these nanoparticles and first attempts of monitoring the growth process by optical and analytical methods such as UCL measurments and transmissions electron microscopy (TEM).[188] Mai *et al.* proposed, that the formation of β-phase $NaYF_4$:Yb^{3+}/Er^{3+} UCNPs occurs via a delayed nucleation pathway with the α-phase acting as intermediate. Taking advantage of these findings, even more complex morphologies such as core-(multi)shell structures utilizing an epitaxal layer-by-layer growth technique are accessible. This is achieved either by injection of a solution containing reactive trifluoroacetate precursors into a hot solvent[191–193] or by

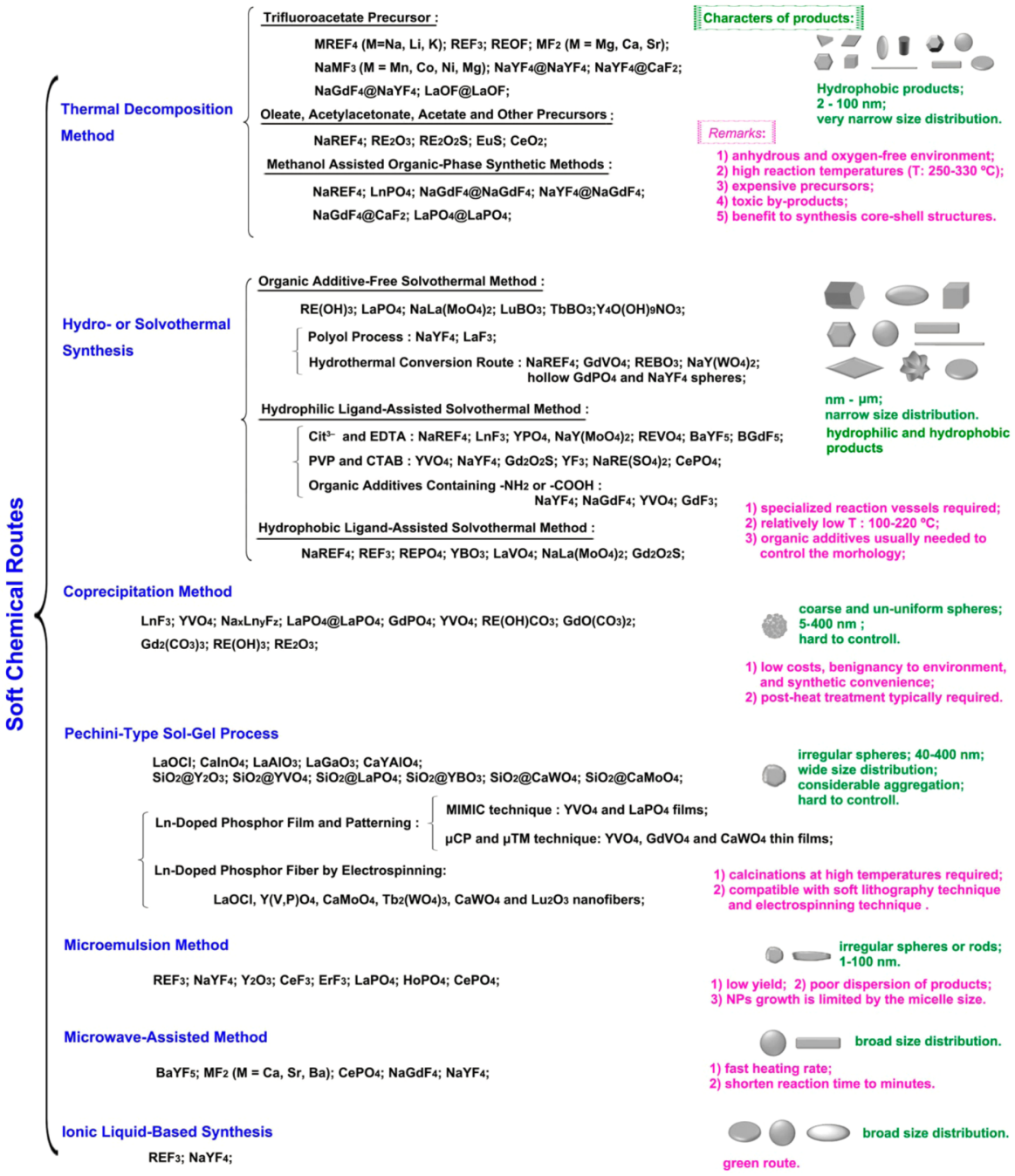

Figure 10: Chemical methods for the synthesis of UCNPs. Reprinted with permission from S. Gai *et al.*.[133] Copyright 2014 American Chemical Society.

injection of small sacrificial α-phase precursors particles into a core β-phase reaction solution prior heating.[175,180,183,194–196] The first technique is termed hot-injection method and is also used for the synthesis of nanoparticles of different kind such as quantum dots.[197] While the injected precursors in the precursor solution decomposes upon addition to the hot reaction solution and then grow onto the thermodynamically more stable β-phase, injected α-phase

particles are dissolved upon heating in favour of the growth of larger β-phase particles following the Ostwald ripening mechanism as reported by Johnson *et al.*.[198] The biggest drawbacks and limitations of the thermal decomposition of trifluoracetate precursors are the formation of very toxic fluorinated and oxyfluorinated carbon species and that non-fluorinated host lattices are not accessible. In order to overcome these issues, other rare-earth element (RE) precursors such as RE-oleates or -acetates were employed. Since a fluoride source was missing using other precursors than trifluoroacetates, NaF was introduced as inexpensive alternative. It is also possible to synthesize high-quality UCNPs following this procedure.[199–201] Furthermore, the newly introduced capability of adjusting the molar ratio of fluorine to RE prior the synthesis enables further adjustment of the morphology of the particles as reported by Lui *et al.*.[200] They showed, that shape and size of the obtained particles drastically depend on the sodium fluoride (NaF)-RE ratio. They yield nanoplates with sizes of 400 x 200 nm and sperical particles with diamters of less than 20 nm for NaF-RE ratios of 4 and bigger than 20, respectively. A even more handy, in terms of toxicity and versatility, thermal decomposition based method was introduced by Li and Zhang.[202] They reported a methanol-assisted organic-phase method, which is in general quite similar to the aforementioned methods. It differs in that fluorine precursors are used in stoichiometric amounts during synthesis for the first time, which drastically reduces the amount of toxic side-products. Additionally, this method facilitates the formation of high-quality nanocrystals as it separates the nucleation and particles growth process, which is reported to be key for achieving monodisperse nanocrystals.[133,197,203] This is accomplished by adding a methanolic solution of sodium hydroxide (NaOH) and ammonium fluoride (NH_4F) to a solution of the RE precursors in OA and *1*-octadecene (ODE) at room temperature. Eventually, a first nucleation results. Another advantage of this method is the usage of readily available rare earth chlorides ($RECl_3$) are used as precursor material. Similar as for the thermal decomposition methods mentioned above, the particle synthesis occurs at elevated temperature. Furthermore, dependencies of the size and morphology of the nanoparticles were found with respect to the reaction temperature and reaction time and the ratio of ODE/OA. Variations of these parameters enable access, e.g., to particles ranging from 15 nm α-phase nanospheres to 400 nm β-phase nanoplates.[202,204] Different morphologies of synthesized UCNPs were also observed for varying amounts of sodium hydroxide (NaOH) by exploiting differences in binding preferences of protonated and deprotonated OA to different crystal facets.[205] Overall, the methanol-assisted organic-phase synthetic method is exceptional suitable for the synthesis of uniform UCNPs and also for the synthesis of heterogeneous core-(multi)shell structures.[162,205–211] The mentioned synthetic procedures are all based on the proposed reaction mechanism of the particle synthesis which includes an initial formation of small α-phase particles which are then converted by a dissolution/recrystallization step to larger, thermodynamically more stable β-phase particles following the Ostwald ripening mechanism. This mechanism was proposed by several groups when they studied the formation of UCNPs. In early studies, these findings

were mainly achieved by prematurely termination the reaction and/or collecting samples during the course of reaction, followed by their analytical and optical characterization.[188,212–215] Later, Suter *et al.* were the first who exploited the intrinsic UCL properties of UCNPs which enables real-time monitoring of the particle growth.[216] Their findings support a thermodynamically driven dissolution/recrystallization process. They even proposed a four stage process for the growth of β-phase UCNPs, which is supported by our results..[159,217] As the most efficient UCNPs are mainly synthesized in organic solvents, the applicability is limited as the particles are stabilized by hydrophobic ligands. However, much effort was made to overcome solubility issues. Nowadays, a huge variety of strategies for surface modification by either ligand exchange or coating is available.[140,218] The huge versatility of the properties of UCNPs is based on the large variety of morphologies and compositions of the particles due to synthetic accessibility and post-synthetic modifiability. These features allow a functional design for targeted applications.

1.3.4 Applications of Upconversion Nanoparticles - Sensing

So far, the application potential of UCNPs for various areas from material to life sciences has been shown by the scientific community. However, there are only a few translations of UCNP technology based applications from the academic stage to the real-world.[185] The most promising UCNP applications in terms of this transition are security applications which exploit the advantages of spectral and lifetime multiplexing offered by core-(multi)shell UC nanoplatforms,[196,219] display technologies[172,220–222] and photovoltaic devices.[223–225] These examples are taken from material sciences whereas bioimaging[134,192,193,208,209,226–228] and theranostics[180,229] are examples for applications in life sciences. The term theranostic is thereby used for the description of diagnosis in combination with therapy within the same platform, e.g., for cancer treatment utilizing PDT.[230–236] UCNPs are ideal candidates for the development of such platforms on the nanoscale level as they have some unique advantages especially for biological applications compared to organic fluorophores such as dyes or fluorescent proteins or other inorganic fluorophores such as semicondocting nanoparticles, e.g., quantum dots (QD). In summary, these advantages include resistance to photobleaching of the particles due to the ultrastable photocycle, excitation with an inexpensive excitation source at 980 nm, which is in the biological window resulting in reduced scattering and deeper tissue penetration, and very low cytotoxicity of the particles.[209] Furthermore, UCNPs feature sharp and defined emission peaks originating from intra 4f orbital transitions of the RE ions which are barely affected by solvents or ligands bound to the surface. These favourable optical properties can be exploited for the design of ratiometric UCNP based optical probes. In general, optical probes are utilized to monitor specific environmental parameters in neutral or ionic form, such as temperature, oxygen, pH or ions of various kind. By combining UCNPs with environmental-sensitive compounds such as metallorganic complexes or organic chromophores, which selectively change their optical properties upon, e.g., temperature changes

or interaction with their target analytes, ratiometric optical probes are accessible. The basic prerequisites for the design of a ratiometric system are, beside the responsiveness to various micro-environmental changes, matching optical properties of UCNP and analyte-responsive compound. Thereby, the analyte-responsive compound typically acts as acceptor and its absorption matches one of the several UCL bands which enables a sensitized excitation of the analyte-responsive compound by the UCNPs. This sensitized excitation is either achieved by distance-dependent nonradiative processes such as luminescence resonance energy transfer (LRET) or by inner-filter-effect-based reabsorption.[131,140,237–239] So far, the ratiometric approach featuring UCNPs was used for several sensing applications, such as temperature sensing,[240,241] oxygen sensing utilizing iridium- or ruthenium-based metallorganic complexes,[242,243] and sensing of various neutral or ionic analytes, e.g., nitrogen monoxide (NO),[244] carbon dioxide (CO_2),[245] DNA,[246] NH_3,[247] Zn^{2+},[248] Fe^{3+},[226] Cu^{2+},[227,229] Ca^{2+},[249] CN^-,[250,251] Hg^{2+},[252,253] and pH.[228,245,247,254,255]

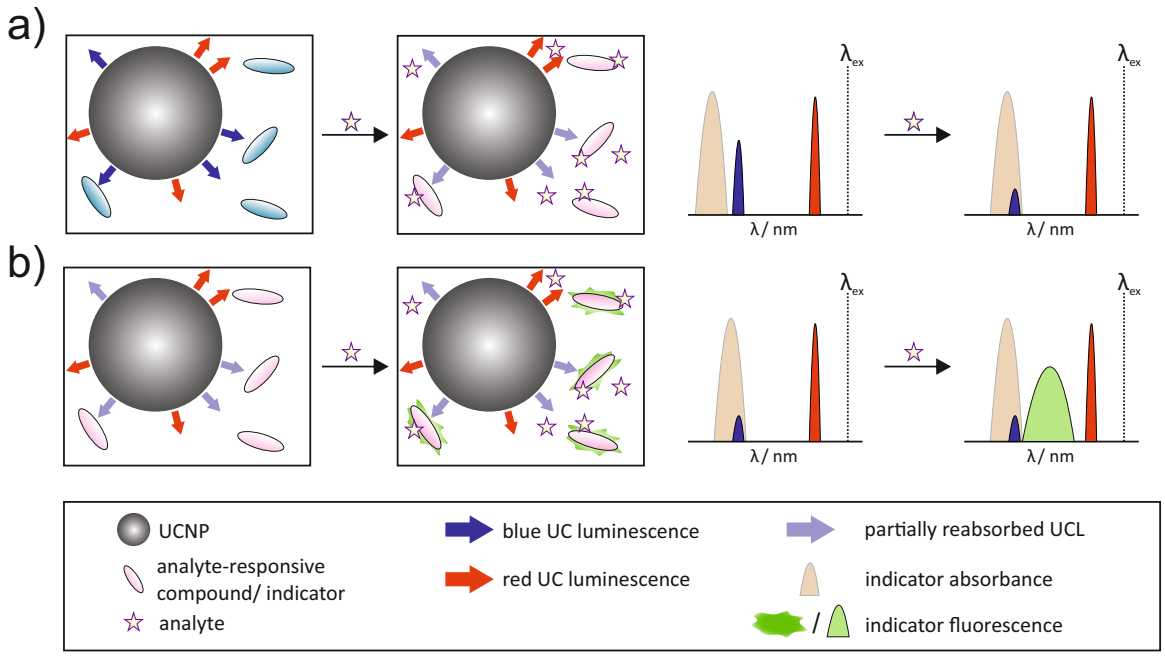

Figure 11: Main approaches for the readout of ratiometric responses utilizing UCNPs and analyte-responsive compounds, schematically illustrated for $NaYF_4$:Yb^{3+}/Tm^{3+}-doped UCNP featuring a) a colorimetric indicator showing an analyte-responsive shift in absorption and b) a fluorogenic indicator with analyte-responsive fluorescence. Adapted with permission from Andresen *et al.*.[140] Copyright 2019 American Chemical Society.

Depending on the optical properties of the analyte-responsive compound to be either colorimetrically or fluorogenically detected, there are two main principles for the readout of the ratiometric response, namely the readout of the quotient of the luminescence intensities of an analyte-responsive and a target-inert emission band. While one approach features a colorimetric analyte-responsive compound, the other approach presents a fluorogenic analyte-responsive compound with the UCNPs acting as intrinsic nanolamp (see Figure 11). The first

approach is based on analyte-responsive changes of the absorbance of the indicator upon interaction with the analyte. As schematically illustrated for $NaYF_4$:Yb^{3+}/Tm^{3+}-doped UCNP and a colorimetric indicator in Figure 11a), an increase of the spectral overlap of the indicators absorption with the blue UC emission band of the UCNPs upon presence of the analyte leads to a decrease of the blue UC emission band relatively to the inert red UC emission band used as reference. The modulation of the UCL is thereby cause by an inner-filter-effect-based reabsorption. In dependence of the indicator's optical properties, this can also take place vice versa with a decreasing spectral overlap of indicator and UC emission upon presence of analyte. This approach was used by Sun *et al.* for pH sensing as they exploited the spectral overlap of the absorbance of pH-responsive bromothymol blue with the green emission of $NaYF_4$:Yb,Er UCNPs.[254] For the fluorogenic approach, illustrated in Figure 11b), a spectral overlap of the indicators absorption and the blue UC emission band of the UCNPs is also mandatory as the UC emission is used as excitation source by either luminescence resonance energy transfer (LRET) or inner-filter-effect-based reabsorption. However, the fluorescence of the analyte-responsive compound should be in general spectrally distinguishable from the UC emission used as inert reference, so that the fluorescence response of the analyte relative to inert reference signal can be used to determine the analytes concentration.[21,228,255]

1.4 Motivation

The aim of this work is to present the design of a multi-component-based optical platform for analyte sensing which offers a ratiometric optical readout (see subsection 1.3.4) by combining the advantages of readily available analyte-responsive fluorescent BODIPY dyes together with NIR-excitable UCNPs. BODIPY dyes are an outstandingly versatile dye class that provides customized designs for specific and sophisticated applications by synthetically adjustable chemical and photophysical properties. Thereby, their properties can be often modified with relative ease with respect to the synthetic effort, which makes BODIPYs an attractive alternative to other dyes. The potential application range of these dyes is not limited and extends to material and life sciences. The applicability, however, is slightly limited for biological purposes as derivatives with far-red and NIR shifted spectral properties ($>$ 650 nm), which are mandatory with regard to the biological window, are barely available. Additionally, the available BODIPY derivatives with far-red and NIR shifted absorption and emission do often not possess desired water solubility.[256] Let alone, they rarely bear any other functionality, e.g., for sensing of analytes such as pH or other parameters, which are generally valuable especially in biological systems. Even if analyte-responsive dyes fulfill these demanding requirements, the extracted information of the dye's optical signal intensity is limited as long as there is no reference. However, the introduction of a reference, e.g., for a more valuable ratiometric readout, requires usually much effort. The nanomaterial based platform presented in this work is capable of overcoming the aforementioned issues. By utilizing BOD-

IPY dyes as versatile sensor molecules in combination with UCNPs acting as nanolamps and internal reference a ratiometric system is established. As the in detail presented BODIPYs show an efficient PET-based quenching of their fluorescence in dependence of pH, they can be utilized for pH sensing. Both components used for this work, the pH-sensitive dyes and the UCNPs, are synthetically readily accessible and their spectral properties match perfectly with respect to the requirements of a ratiometric system. Generally, this platform is highly variable regarding the analyte-responsiveness of the compound as well as its features such as a colorimetric or fluorescent response or the generation of $^1O_2$ as long as this chromophores have matching spectral properties with respect to the used UCNPs. In this work, the used components for such a platform have been studied intensively and initial conceptual evidence has been provided by:

(A) The synthesis and optical characterization of a set of fluorescent on/off switchable pH sensors with tunable pK_a values.

(B) The detailed photophysical investigation of the temperature dependency of Φ_{Fl} and fluorescence lifetime (τ_{Fl}) of these dyes, which result from their different structural parameters, was supported by single crystal X-ray structure analysis and quantum chemical density functional theory (DFT) calculations.

(C) The synthesis, optical characterization and *in vitro* application of pH-activatable $^1O_2$ generators based on fluorescent on/off switchable BODIPY-based pH sensors.

(D) The detailed study of UCNP growth during their high-temperature synthesis. This was performed *in situ* by monitoring their UCL and *ex situ* by monitoring their UCL decay kinetics as well as their size in dependence of the reaction time. The particle sizes were determined by TEM and SAXS with TEM also providing informations of the crystal phases of the nanoparticles.

(E) The proof of concept study for a simple self-referenced luminescent pH sensor based on pH-sensitive BODIPY dyes and UCNP, which was used for monitoring the pH value of metabolizing *E. coli*.

2 Results and Discussion

In the following chapter results of this work are presented. All parts of this work have already been published in scientific journals.

2.1 Broad range ON/OFF pH sensors based on pK_a tunable fluorescent BODIPYs

Sebastian Radunz, Harald Rune Tschiche, Daniel Moldenhauer, Ute Resch-Genger*

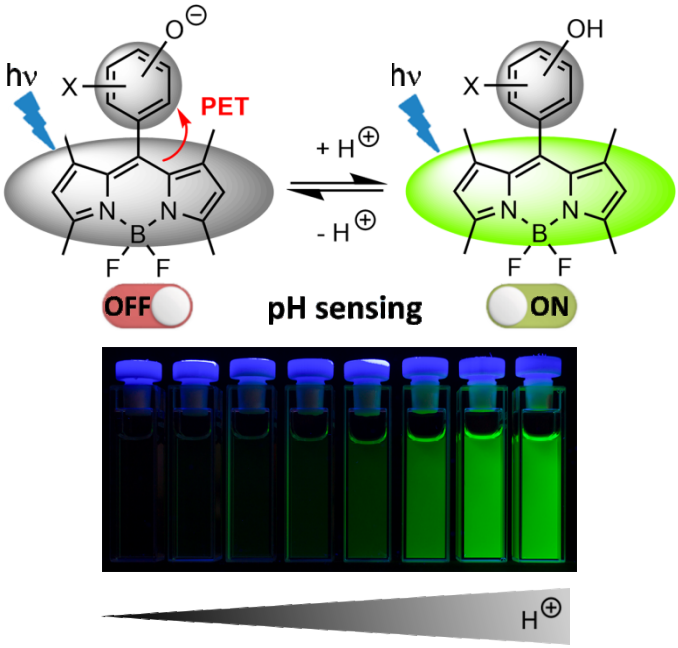

Figure 12: Reprinted with permission from S. Radunz *et al.*.[12] Copyright 2017 Elsevier B.V..

In this publication S. Radunz established the concept, the synthesis and the analytical and spectroscopic characterization of the reported compounds. He performed all experiments and data evaluations as well as he performed the scientific interpretation of the results. The publication was mainly conceived and written by him.

Sensors and Actuators B 251 (2017) 490–494

Contents lists available at ScienceDirect

Sensors and Actuators B: Chemical

journal homepage: www.elsevier.com/locate/snb

Short communication

Broad range ON/OFF pH sensors based on pK_a tunable fluorescent BODIPYs

Sebastian Radunz, Harald Rune Tschiche, Daniel Moldenhauer, Ute Resch-Genger*

Federal Institute for Materials Research and Testing, Richard-Willstaetter-Str. 11, 12489 Berlin, Germany

ARTICLE INFO

Article history:
Received 21 January 2017
Received in revised form 15 May 2017
Accepted 16 May 2017
Available online 18 May 2017

Keywords:
BODIPY
pH
Fluorescence
Sensor
Photoinduced electron transfer

ABSTRACT

A set of highly fluorescent, pH-responsive boron dipyrromethene dyes covering the pH range of 5–12 is presented for broad range pH measurements in mixed aqueous-organic media and polymer matrices. Readout in the intensity domain with low cost and miniaturized instrumentation utilizes reversible protonation induced switching ON of their initially completely quenched fluorescence mediated by photoinduced electron transfer. All dyes, rationally designed to reveal closely matching absorption and emission properties, are accessible via facile two-step reactions in overall yields of up to 20%. By modifying the substitution pattern of the meso-aryl substituent, the pK_a values could be fine-tuned from 6 to 11. Integration of these molecules into polymeric films by a simple mixing procedure yielded reversible and longterm stable pH sensors for naked eye detection.

1. Introduction

Determination of pH values is amongst the most commonly performed analytical measurements in the material and particularly the life sciences. pH presents a crucial parameter for material corrosion [1] and is an important biomarker for medical diagnostics, molecular imaging, and cell biology due to its many roles in enzymatic and tissue activities inside cells like apoptosis [2], multidrug resistance [3], and endocytosis [4]. Electrochemical methods using potentiometric glass pH electrodes are well-established and provide accurate and fast results. However, as they are invasive, they are not suited for measurements in vitro and in vivo e.g., determination of intracellular pH [5]. Optical probes, sensors, and optodes present a straightforward alternative. They offer many advantages like non-destructive, contactless, and very sensitive measurements as well as high spatial resolution in the nanometer range. The basic prerequisite for an optical pH measurement is a pH sensitive indicator dye with different optical properties in its protonated and deprotonated form. This implies (de)protonation-induced changes in the intensity and/or spectral position of its absorption and/or fluorescence or its fluorescence lifetime. The range of application is thereby determined by its pK_a value. Particularly attractive for the design of versatile pH probes enabling the signaling of strongly different pH values and read out with the same, simple, and inexpensive instrumentation is a broad tunability of the pK_a by introduction of electron-donating or electron-withdrawing groups without affecting the spectral properties while maintaining high molar absorption coefficients and fluorescence quantum yields. pH probes have been prepared from a variety of dye classes like xanthenes (e.g., fluoresceins, rhodamines), cyanines, squaraines, and BODIPYs [6,7]. The easily controllable chemical and photophysical diversity of 4,4-difluoro-4-bora-3*a*,4*a*-diaza-*s*-indacenes (BODIPYs) provided by versatile synthetic pathways together with their outstanding thermal and photochemical stability, relatively high molar absorption coefficients and high fluorescence quantum yields makes them ideal candidates for sensor dyes [8–10]. They have been successfully applied as fluorescent sensor for many different ionic analytes like protons and metal ions, typically exploiting analyte-mediated photoinduced electron transfer (PET) for fluorescence signaling [8,11]. In a typical BODIPY probe, the almost perpendicular arrangement between the usually used aryl substituents at meso-position and the BODIPY core decouples electronically the fluorophore subunit and the analyte binding site [12]. This provides the basis for effective and reversible analyte binding-induced fluorescence switching. Introducing pH-sensitive substituents at the meso-aryl unit can enable protonation-mediated PET, the efficiency of which depends on the redox potential of the substituents and the excited singlet state of the BODIPY core. This allows to design pH-sensitive probes which cover large parts of the pH scale with a usual pH response in the range of approximately p$K_a \pm 1$. The acidic pH range is accessible with fluorophores bearing electron donating

* Corresponding author.
E-mail address: ute.resch@bam.de (U. Resch-Genger).

http://dx.doi.org/10.1016/j.snb.2017.05.080
0925-4005/

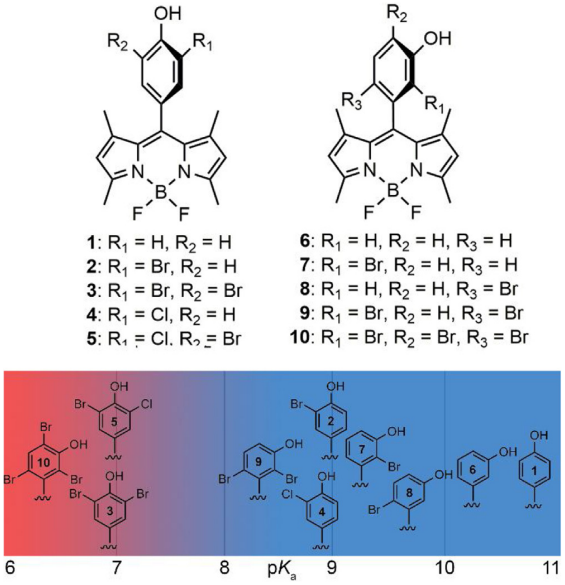

Scheme 1. Top: Chemical structures of the pH sensitive BODIPYs. Bottom: Corresponding pK_a-values in dependence of the degree of halogenation (increasing from right to left). The color gradient from red to blue indicates the increase of the pK_a, which were determined in buffered mixtures of methanol and water (2/1 vol%, 25 mM). (For interpretation of the references to colour in this figure legend, the reader is referred to the web version of this article.)

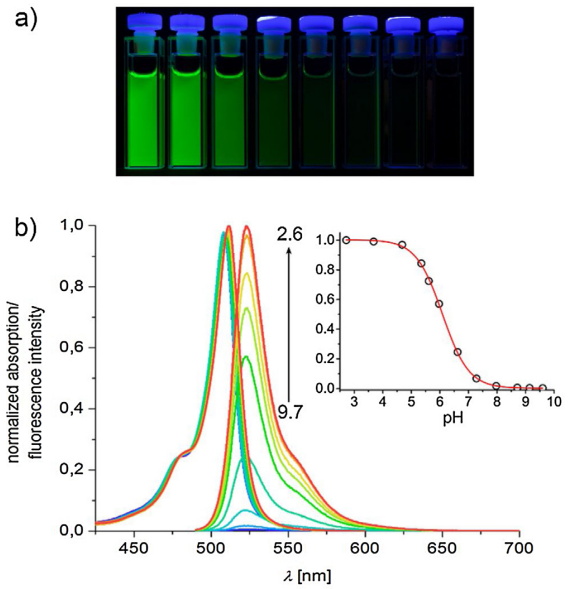

Fig. 1. (a) pH-dependent fluorescence ON/OFF-switching of BODIPY **10** at pH values of 5.35, 5.92, 6.62, 7.26, 7.75, 8.12, 8.30, and 8.60 (photographs from left to right). (b) pH-dependent normalized absorption (left) and fluorescence (right) spectra) of BODIPY **10** in a mixture of methanol and water (2/1 vol%, 25 mM). The inset shows a typical pH titration curve.

amine-containing subunits [13–19], whereas the alkaline pH range requires fluorophores with phenol-containing subunits [20–25]. So far, several pH sensitive BODIPY dyes with different pK_a values have been reported, but the number of easy accessible and highly sensitive BODIPYs with pK_a values in the neutral and near neutral range is rather still limited [8,11,26–28].

2. Results and discussion

In this work, we present a set of BODIPYs accessible via facile two-step reactions in overall yields of up to 20% which cover the pH scale from 5 to 12. An overview of these BODIPYs and their pK_a values is given in Scheme 1; the syntheses and analytical characterization of the dyes by NMR spectroscopy (^{1}H and ^{13}C) and mass spectrometry is detailed in the Supporting Information (ESI). All BODIPYs are non-fluorescent in the unprotonated form and reveal efficient, very fast, and fully reversible PET-triggered ON/OFF-switching of their fluorescence upon protonation/deprotonation (see Fig. 1 and Table S2, ESI), accompanied by minimal spectral shifts in absorption. This enables fluorometric pH sensing and therefore derivation of pK_a values from fluorometric pH-titration experiments (see Figs. S1–S10, ESI). As follows from the photographs in Figs. 1 and 2, all sensor molecules provide a pH response strong enough for naked eye detection.

2.1. pK_A tuning

pK_a tuning is realized by stepwise bromination of the phenolic aryl in meso-position prior to the synthesis of the BODIPY core [29]. Halogenation of phenolic subunits has been already reported for other fluorophores, yielding higher PET efficiencies and being a useful method for tuning of the pK_a [27,30–32]. The pK_a values of the unsubstituted compounds **1** and **5** are 10.75 and 10.31, respectively, and are comparable with previously reported data [24]. Upon stepwise halogenation, remarkable pK_a shifts are obtained

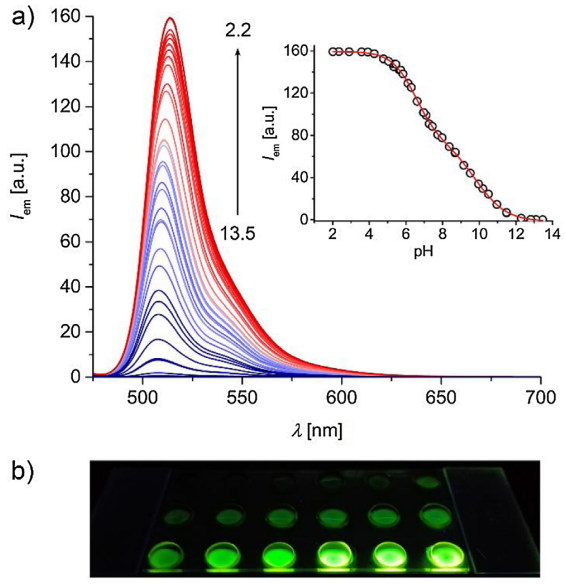

Fig. 2. pH-treatment of broad range sensor, containing a mixture of **1**, **2**, **3** and **10**, in a) buffered aqueous-organic mixed medium (H_2O/MeOH 1/2 vol%) at various pH and b) immobilized in a proton permeable hydrogel (Hydromed D4) starting with pH 12.5 in the upper left corner and ending with pH 4 in the lower right corner (pH increment about 0.5 per well).

as the degree of halogenation strongly influences the acidity of the pH-sensitive hydroxyl group by an inductive effect, thereby withdrawing electron density. Mono-halogenated compounds **2**, **4**, **7**, and **8** show pK_a values of 8.99, 8.93, 9.17, and 9.74, respectively; further bromination leads to more acidic pK_a values of 6.98, 6.94,

Table 1
Overview over the photophysical properties of the synthesized BODIPY dyes.

Dye	ε (λ_{max}) (MeOH) [M^{-1} cm^{-1}]	$\lambda_{em\text{-}acid}$ (MeOH) [nm]	Φ_f (relative) (MeOH) [%][b]	τ_f (MeOH) [ns][c]	k_r [10^8 s^{-1}][c]	k_{nr} [10^8 s^{-1}][d]	pK_a (em)[e]
1	86700 (497)	504.5	0.50 ± 0.03	2.97 ± 0.02	1.68 ± 0.11	1.68 ± 0.09	10.75
2	78000 (499)	507.5	0.54 ± 0.03	3.49 ± 0.02	1.55 ± 0.10	1.32 ± 0.08	8.99
3	86400 (502)[a]	510.5	0.57 ± 0.03[a]	3.69 ± 0.03[a]	1.54 ± 0.09	1.17 ± 0.07	6.98
4	87200 (499)	507.5	0.52 ± 0.03	3.41 ± 0.03	1.52 ± 0.10	1.41 ± 0.08	8.93
5	86300 (502)[a]	510.5	0.56 ± 0.03[a]	3.67 ± 0.02[a]	1.53 ± 0.09	1.20 ± 0.07	6.94
6	93200 (498)	505.5	0.64 ± 0.03	4.29 ± 0.05	1.49 ± 0.08	0.84 ± 0.06	10.31
7	89800 (503)	511.0	0.93 ± 0.03	6.61 ± 0.03	1.41 ± 0.08	0.11 ± 0.07	9.17
8	85700 (503)	511.0	0.91 ± 0.03	6.68 ± 0.02	1.36 ± 0.06	0.13 ± 0.05	9.74
9	82800 (510)[a]	516.5	0.89 ± 0.03[a]	6.58 ± 0.02[a]	1.35 ± 0.07	0.17 ± 0.06	8.28
10	71400 (511)[a]	518.0	0.85 ± 0.03[a]	6.52 ± 0.02[a]	1.30 ± 0.05	0.23 ± 0.04	6.17

[a] For generation of the protonated fluorescent form: further addition of 5 μL conc. HCl to 3 mL sample.
[b] Fluorescence quantum yield (Φ_f) were determined at 25 °C (λ_{ex} = 475 nm).
[c] Mono exponential fit (global analysis f_i (%) = 100.0)).
[d] $k_r = \Phi_f/\tau_f$ and $k_{nr} = (1 - \Phi_f)/\tau_f$.
[e] (MeOH/H_2O 2/1 vol%, 25 mM buffered solution).

and 8.28 for di-halogenated compounds **3**, **5**, and **9**, respectively. As follows from a comparison of **2**–**5** (Table 1), the effect of chloro and bromo substituents on pK_a is clearly negligible compared to the effect of the arene substitution pattern [33]. Substitution in *ortho*-position has a much higher impact on pK_a than substitution in the *para*-position, as exemplarily shown for **7**, **8**, **9**, and **10**, respectively. Tri-brominated compound **10** shows a strong pK_a shift to 6.17. The neutral and near neutral pK_a values of **3**, **5**, **9**, and **10** are particularly favorable for pH-measurements in biological samples in the physiological range.

2.2. Spectroscopic properties

An overview of the spectroscopic properties of the synthesized BODIPY dyes is given in Table 1. All compounds have high molar absorption coefficients ε (>70,000 M^{-1} cm^{-1}) and high fluorescence quantum yields Φ_f (>50%, up to 90%), exceeding those of other previously reported rather similar, but still different pH-sensitive BODIPYs [22,25]. Their fluorescence lifetimes τ_f are in the lower nanosecond range (see Figs. S11–S14, ESI). As desired for our application as broad range pH sensors, they reveal very small spectral shifts in absorption (absorption maxima λ_{abs} of 497–511 nm) and emission (emission maxima λ_{em} of 504–518 nm), despite their different substitution pattern at the meso-aryl unit. The size of the spectral shifts correlates with the inductive effect of the halogen substituents and the substitution pattern. Bromine substituents in 2- and/or 6-position exert a stronger inductive effect on the BODIPY core than bromine substituents in 4-, 3- or 5-position; both substitution pattern lead to smaller spectral shifts compared to halogenation directly at the BODIPY core as reflected by the more pronounced, but still minimal bathochromic shift in absorption and emission maxima [34,35]. The fluorescence of all BODIPY dyes shows a very small Stokes shift as typical for this dye class, which is only slightly affected by halogenation. The substitution pattern, however, influences considerably the fluorescence quantum yield and fluorescence lifetime by an interplay of two competing effects. The higher rigidity of the meso-aryl moiety and the resulting interlocking of the meso-aryl unit between the methyl substituents of the BODIPY plane enhance Φ_f by reducing vibrational movements and thus non-radiative decay pathways [17], whereas the well-studied heavy-atom effect lowers it [36]. Depending on the degree and position of halogenation, the former effect predominates, accounting for the increased Φ_f of all halogenated compounds. Thus, 3-hydroxybenzaldehyde based compounds **7**, **8**, **9**, and **10** are particularly affected (Table 1). For example, bromination in 2-position or 6-position as done for **7** and **8** leads to an increase of Φ_f of up to 30% compared to **6**, in conjunction with a reduction in the non-radiative rate constant k_{nr} by a factor of about 7.5 and 6.5 for **7** and **8**, respectively. For mono- and di-brominated BODIPYs **2** and **3**, only a small increase in Φ_f is observed reflecting the only slightly enhanced rigidity upon halogenation in 3- and/or 5-position. The observed trends in Φ_f indicate that within our BODIPY series, rigidity and steric effects clearly dominate the fluorescence behavior outweighing the only moderate fluorescence quenching by the heavy-atom effect. The small influence of the heavy atom effect is also reflected by the rather similar Φ_f of BODIPYs **2**–**5** bearing chloro and bromo substituents (comparison of **2** and **4** and **3** and **5**, respectively). For the fluorescence lifetimes, which correlates with Φ_f [36], at least a trend is recognizable, i.e., shorter fluorescence lifetimes in dependence of the degree of bromination. A direct comparison of the influence of bromo and chloro substituents on the fluorescence properties of our BODIPYs is, however, hampered by their different sizes, with smaller chloro substituents being less favorable for fluorescence enhancing rigidization. The lifetimes of our BODIPY series follow the same trend as Φ_f, with the longest lifetimes in the range of 4.30–6.70 ns being observed for 3-hydroxybenzaldehyde based compounds **6**–**10**. 4-Hydroxybenzaldehyde based compounds **1**–**5** have shorter fluorescence lifetimes in the range of 3.00–3.70 ns. Only small halogenation-induced changes (<15%) of the radiative decay rates k_f occur within this BODIPY series, whereas k_{nr} values are much stronger affected. The relatively small k_{nr} values found for compounds **7–10** indicate less non-radiative decay pathways due to higher rigidity.

2.3. Photostability

Another crucial parameter for many applications of organic dyes is photostability. Therefore, the photostability of the BODIPY dyes was determined by illumination with visible light (475 nm ± 15 nm) for 18 h (see Fig. S15, ESI), thereby also covering typically used excitation light sources such as the 488 nm Ar^+ laser and the 470 nm laser diode. As measure for dye photostability, we used the change of the initial fluorescence intensity (integral of emission band), This value was also utilized for determining the half-life $t_{1/2}$ by fitting of the exponential decrease in fluorescence (see Table S5, ESI). With exception of **3** and **5**, all compounds show a high photostability (73–88% of the initial fluorescence intensity remaining, $t_{1/2}$ = 2440–5900 min) in comparison to fluorescein 27 (FL27, 48% remaining, 1040 min) and 6-carboxyfluorescein (6-FAM, 22% remaining, 530 min). While $t_{1/2}$ of **7–10** increases from 2440 to 2880 min with an increasing degree of bromination,surprinsingly, $t_{1/2}$ of the corresponding di-halogenated compounds **3** and **5** amounts only to 1100 min. We did not observe the formation of photoproducts from the BODIPYs emitting in the wavelength region of 450–650 nm utilized for pH sensing.

2.4. Broad band pH sensor

The identical spectral properties of the BODIPY dyes together with a dynamic range, which covers the slightly acidic to strongly basic pH scale, allows the design of a broad band pH sensor. For example, mixing of pH probes **1**, **2**, **3**, and **10** yields a pH sensor with a dynamic range from pH 5 to pH 12, providing a double sigmoidal calibration curve (see Fig. 2, Table S4, ESI). Moreover, the combination of these sensor molecules with previously reported BODIPYs bearing PET-active amine-containing subunits in an optimized mixing ratio could yield an universal fluorescence-based indicator covering nearly the whole pH scale with a smooth sigmoidal calibration curve. For ratiometric pH measurements in the fluorescence intensity domain, which eliminate slight modifications in fluorescence intensity resulting from fluctuations in the excitation power density [37], our BODIPYs can be combined with pH-inert fluorophores, for example Nile Red or the NIR dye Itrybe, which can be excited at 475 nm and 500 nm [38], e.g., in polymeric nanoparticles.

In order to evaluate the potential of our BODIPY dyes for use in sensor films and optodes, they were incorporated into a proton permeable hydrogel (see Fig. 2). Subsequently performed protonation studies revealed a fast, strong, and fully reversible pH response visual by naked eye closely matching the behavior observed in water-methanol mixtures. Moreover, long-term exposure of the hydrogels to aqueous buffer solutions of different pH confirmed the absence of dye leaking for both the unprotonated and protonated form, which is ascribed to dye hydrophobicity. This is very promising for the simple fabrication of sensor films as the majority of pH indicators reveal leaking typically in the charged form like for neutral red and bromothymol blue. This requires the covalent attachment of most indicator dyes to e.g., large molecules like dextrans and hence the tedious synthesis of pH-responsive sensor molecules with reactive groups [39]. The chemical environment in the polymer matrix affects the pK_a values of the incorporated dyes slightly (see Table S1, ESI) [13], and very broad pH range pH sensing with naked eye detection is still achieved.

3. Conclusion

In summary, we presented a set of novel highly fluorescent BODIPY dyes with closely matching spectral properties which show pH dependent ON/OFF-switching of their fluorescence in the pH range of 5–12. Tuning of pK_a values is achieved by changing the degree of bromination of the PET-capable phenolic subunits in the meso-position of the BODIPY which considerably affects the fluorescence quantum yields and lifetimes due to sterically induced rigidization outweighing the heavy atom effect. All BODIPYs are accessible by a facile two step synthesis, typically from inexpensive reactands. For example, many of the PET-capable benzaldehyde reactants, especially the derivatives which were used for the synthesis of the broad band pH sensor dyes, are commercial available in a large scale, which makes our dyes even more readily accessible. Furthermore, these BODIPYs can be easily post-functionalized, i.e., to introduce reactive groups for covalent coupling to hydrophilic substituents to enhance their water solubility [11,16,34,40]. Several applications of our pH-responsive BODIPYS are conceivable such as the fabrication of sensor films by simple steric immobilization in polymer matrices as shown here, or the design of pH-responsive nanosensors or bioconjugates after post-functionalization and covalent attachment to nanocarriers like surface-functionalized polymer nanoparticles or biomolecules like antibodies. Also fluoride sensing is possible as reported for phenolic BODIPYs by Wang et al [24].

Acknowledgements

We gratefully acknowledge financial support from the Federal Ministry for Economic Affairs and Energy (grant BMWi-20/14) as well as funding from the Ph.D. program of BAM and the BAM focus area *Material* (projects *Microbial-induced Corrosion* (MIC) and *Polymerdegradation* (PolyComp)).

Appendix A. Supplementary data

Supplementary data associated with this article can be found, in the online version, at http://dx.doi.org/10.1016/j.snb.2017.05.080.

References

[1] G. Muyzer, A.J.M. Stams, The ecology and biotechnology of sulphate-reducing bacteria, Nat. Rev. Microbiol. 6 (6) (2008) 441–454.
[2] A. Ishaque, M. Al-Rubeai, Use of intracellular pH and annexin-V flow cytometric assays to monitor apoptosis and its suppression by bcl-2 over-expression in hybridoma cell culture, J. Immunol. Methods 221 (1–2) (1998) 43–57.
[3] S. Simon, D. Roy, M. Schindler, Intracellular pH and the control of multidrug resistance, Proc. Natl. Acad. Sci. U. S. A. 91 (3) (1994) 1128–1132.
[4] R.A. Gottlieb, J. Nordberg, E. Skowronski, B.M. Babior, Apoptosis induced in Jurkat cells by several agents is preceded by intracellular acidification, Proc. Natl. Acad. Sci. U. S. A. 93 (2) (1996) 654–658.
[5] A. Kotyk, J. Slavik, Intracellular pH and Its Measurement, CRC Press, 2016, pp. 1989.
[6] J. Han, K. Burgess, Fluorescent indicators for intracellular pH, Chem. Rev. 110 (5) (2010) 2709–2728.
[7] R. Wang, C. Yu, F. Yu, L. Chen, C. Yu, Molecular fluorescent probes for monitoring pH changes in living cells, Trends Anal. Chem. 29 (9) (2010) 1004–1013.
[8] N. Boens, V. Leen, W. Dehaen, Fluorescent indicators based on BODIPY, Chem. Soc. Rev. 41 (3) (2012) 1130–1172.
[9] A. Loudet, K. Burgess, BODIPY dyes and their derivatives: syntheses and spectroscopic properties, Chem. Rev. 107 (11) (2007) 4891–4932.
[10] G. Ulrich, R. Ziessel, A. Harriman, The chemistry of fluorescent bodipy dyes: versatility unsurpassed, Angew. Chem. Int. Ed. 47 (7) (2008) 1184–1201.
[11] C. Zhao, W. Zhu, Boron-containing BODIPY chromophore for fluorescent sensing, in: Boron: Sensing, Synthesis and Supramolecular Self-Assembly, The Royal Society of Chemistry, 2016, pp. 202–235, CHAPTER 7.
[12] A. Harriman, L.J. Mallon, G. Ulrich, R. Ziessel, Rapid intersystem crossing in closely-spaced but orthogonal molecular dyads, ChemPhysChem 8 (8) (2007) 1207–1214.
[13] T. Werner, C. Huber, S. Heinl, M. Kollmannsberger, J. Daub, S.O. Wolfbeis, Novel optical pH-sensor based on a boradiaza-indacene derivative, Fresenius' J. Anal. Chem. 359 (2) (1997) 150–154.
[14] Y. Urano, D. Asanuma, Y. Hama, Y. Koyama, T. Barrett, M. Kamiya, T. Nagano, T. Watanabe, A. Hasegawa, P.L. Choyke, H. Kobayashi, Selective molecular imaging of viable cancer cells with pH-activatable fluorescence probes, Nat. Med. 15 (1) (2009) 104–109.
[15] N. Boens, W. Qin, M. Baruah, W.M. De Borggraeve, A. Filarowski, N. Smisdom, M. Ameloot, L. Crovetto, E.M. Talavera, J.M. Alvarez-Pez, Rational design, synthesis, and spectroscopic and photophysical properties of a visible-light-excitable, ratiometric fluorescent near-neutral pH indicator based on BODIPY, Chem. Eur. J. 17 (39) (2011) 10924–10934.
[16] S. Hoogendoorn, A.E.M. Blom, L.I. Willems, G.A. van der Marel, H.S. Overkleeft, Synthesis of pH-activatable red fluorescent BODIPY dyes with distinct functionalities, Org. Lett. 13 (20) (2011) 5656–5659.
[17] J. Bartelmess, W.W. Weare, N. Latortue, C. Duong, D.S. Jones, meso-Pyridyl BODIPYs with tunable chemical, optical and electrochemical properties, New J. Chem. 37 (9) (2013) 2663–2668.
[18] J. Zhang, M. Yang, C. Li, N. Dorh, F. Xie, F.-T. Luo, A. Tiwari, H. Liu, Near-infrared fluorescent probes based on piperazine-functionalized BODIPY dyes for sensitive detection of lysosomal pH, J. Mater. Chem. B 3 (10) (2015) 2173–2184.
[19] Y. Zhang, H. Fang, X. Zhang, S. Wang, G. Xing, 8-(4-aminophenyl)BODIPYs as fluorescent pH probes: facile synthesis, computational study and lysosome imaging, ChemistrySelect 1 (1) (2016) 1–6.
[20] X.-F. Zhang, Fluorescence properties of phenol-modified zinc phthalocyanine that tuned by photoinduced intra-molecular electron transfer and pH values, J. Fluoresc. 21 (4) (2011) 1559–1564.
[21] K.M. Sun, C.K. McLaughlin, D.R. Lantero, R.A. Manderville, Biomarkers for phenol carcinogen exposure act as pH-sensing fluorescent probes, J. Am. Chem. Soc. 129 (7) (2007) 1894–1895.
[22] M. Baruah, W. Qin, N. Basarić, W.M. De Borggraeve, N. Boens, BODIPY-based hydroxyaryl derivatives as fluorescent pH probes, J. Org. Chem. 70 (10) (2005) 4152–4157.

[23] M. Hecht, W. Kraus, K. Rurack, A highly fluorescent pH sensing membrane for the alkaline pH range incorporating a BODIPY dye, Analyst 138 (1) (2013) 325–332.
[24] J. Wang, Y. Hou, C. Li, B. Zhang, X. Wang, Selectivity tune of fluoride ion sensing for phenolic OH-containing BODIPY dyes, Sens. Actuators B 157 (2) (2011) 586–593.
[25] W. Qin, M. Baruah, A. Stefan, M. Van der Auweraer, N. Boens, Photophysical properties of BODIPY-derived hydroxyaryl fluorescent pH probes in solution, ChemPhysChem 6 (11) (2005) 2343–2351.
[26] C.N. Baki, E.U. Akkaya, Boradiazaindacene-appended calix[4] arene: fluorescence sensing of pH near neutrality, J. Org. Chem. 66 (4) (2001) 1512–1513.
[27] W. Qin, M. Baruah, W.M. De Borggraeve, N. Boens, Photophysical properties of an on/off fluorescent pH indicator excitable with visible light based on a borondipyrromethene-linked phenol, J. Photochem. Photobiol. A 183 (1–2) (2006) 190–197.
[28] M. Tian, X. Peng, F. Feng, S. Meng, J. Fan, S. Sun, Fluorescent pH probes based on boron dipyrromethene dyes, Dyes Pigm. 81 (1) (2009) 58–62.
[29] I. Saikia, A.J. Borah, P. Phukan, Use of bromine and bromo-organic compounds in organic synthesis, Chem. Rev. 116 (12) (2016) 6837–7042.
[30] D. Aigner, S.A. Freunberger, M. Wilkening, R. Saf, S.M. Borisov, I. Klimant, Enhancing photoinduced electron transfer efficiency of fluorescent pH-probes with halogenated phenols, Anal. Chem. 86 (18) (2014) 9293–9300.
[31] J. Qi, D. Liu, X. Liu, S. Guan, F. Shi, H. Chang, H. He, G. Yang, Fluorescent pH sensors for broad-range pH measurement based on a single fluorophore, Anal. Chem. 87 (12) (2015) 5897–5904.
[32] M. Strobl, T. Rappitsch, S.M. Borisov, T. Mayr, I. Klimant, NIR-emitting aza-BODIPY dyes – new building blocks for broad-range optical pH sensors, Analyst 140 (21) (2015) 7150–7153.
[33] A. Albert, E.P. Serjeant, Ionization Constants of Acids and Bases a Laboratory Manual, in: Adrien Albert, E.P. Serjeant (Eds.), Wiley: London, Methuen, New York, 1962.
[34] L. Jiao, W. Pang, J. Zhou, Y. Wei, X. Mu, G. Bai, E. Hao, Regioselective stepwise bromination of boron dipyrromethene (BODIPY) dyes, J. Org. Chem. 76 (24) (2011) 9988–9996.
[35] N. Zhao, S. Xuan, F.R. Fronczek, K.M. Smith, M.G.H. Vicente, Stepwise polychlorination of 8-chloro-BODIPY and regioselective functionalization of 2, 3, 5, 6, 8-pentachloro-BODIPY, J. Org. Chem. 80 (16) (2015) 8377–8383.
[36] J.R. Lakowicz, Principles of Fluorescence Spectroscopy, 3rd ed., Springer US, 2006, p XXVI, 954.
[37] C. McDonagh, C.S. Burke, B.D. MacCraith, Optical chemical sensors, Chem. Rev. 108 (2) (2008) 400–422.
[38] T. Behnke, C. Würth, E.-M. Laux, K. Hoffmann, U. Resch-Genger, Simple strategies towards bright polymer particles via one-step staining procedures, Dyes Pigm. 94 (2) (2012) 247–257.
[39] L.C.D. de Rezende, F. da Silva Emery, A review of the synthetic strategies for the development of BODIPY dyes for conjugation with proteins, Orbital: Electron. J. Chem. 5 (1) (2013) 62–83.
[40] N. Zhao, S. Xuan, B. Byrd, F.R. Fronczek, K.M. Smith, M.G.H. Vicente, Synthesis and regioselective functionalization of perhalogenated BODIPYs, Org. Biomol. Chem. 14 (26) (2016) 6184–6188.

Biographies

Sebastian Radunz is working on his PhD in the workgroup of Ute Resch-Genger at the Federal Institute for Materials Research and Testing (BAM) since 2016. His research focus is on the detection of microbial induced corrosion using fluorescent probes and nanosensors. He studied chemistry at the Humboldt-Universität zu Berlin and graduated with his master thesis in organic chemistry and functional materials under supervision of Prof. Stefan Hecht, PhD in 2015.

Harald Rune Tschiche is a postdoctoral fellow in the division *Biophotonics* at the Federal Institute for Materials Research and Testing (BAM). His present research activities include the development of fluorescent sensors and nanosensors. These molecular probes are utilized to get insights into the mode of action microbial induced corrosion processes. He obtained his PhD in 2015 working in the field of nanomedicin, in particular employing FRET-based reporters for the analysis of drug release of polymer conjugates, as well as targeted polymer therapeutics utilizing antibodies.

Daniel Moldenhauer has graduated with his diploma thesis in organic chemistry from TU Bergakademie Freiberg. Afterwards he moved to Friedrich-Alexander-Universität Erlangen-Nürnberg for his PhD. Currently he is a researcher in the division *Biophotonics* of Dr. Ute Resch-Genger at the Federal Institute for Materials Research and Testing (BAM) in Berlin.

Ute Resch-Genger is head of the division *Biophotonics* at the Federal Institute for Materials Research and Testing (BAM). Her present research interests include the photophysics of molecular and nanoscale fluorophores, the rational design of,stimuli-responsive optical probes from different classes of emitters, signal enhancement and multiplexing strategies, optical biomarker analysis, spectroscopic methods for surface group analysis, and traceable methods for the characterization of the signal-relevant optical properties of luminescent materials including the development of fluorescence standards. She is co-chair of the permanent steering committee of the Methods & Applications in Fluorescence (MAF) conference series and member of the editorial advisory board of Bioconjugate Chemistry, the editorial board of MAF, and the scientific committee of the German Biosensor-Symposium.

Broad range ON/OFF pH sensors based on pK_a tunable fluorescent BODIPYs

Sebastian Radunz, Harald Rune Tschiche, Daniel Moldenhauer and Ute Resch-Genger

BAM Federal Institute for Materials Research and Testing, Richard-Willstaetter-Str. 11, 12489 Berlin, Germany. E-mail: ute.resch@bam.de

Electronic Supplementary Information (ESI)

Materials

3-hydroxybenzaldehyde, 4-hydroxybenzaldehyde, 3-chloro-4-hydroxybenzaldehyde, *N*,*N*-diisopropylethylamine, boron trifluoride diethyl etherate, *N*-bromosuccinimide (NBS), silicagel (40 – 63 µm, 230 – 400 mesh), and anhydrous magnesium sulfate were purchased from Sigma Aldrich. 2,4-dimethylpyrrole was bought from ABCR. Deuterated chloroform ($CDCl_3$) and dimethyl sulfoxide (DMSO-d_6) were obtained from Deutero GmbH. Trifluoroacetic acid, methanol (spectroscopic grade) and dichloromethane were purchased from Merck KGaA and *n*-hexane from Carl Roth GmbH, respectively.

Methods

Optical spectroscopy

Absorption measurements were carried out on a calibrated Varian Cary 5000 UV-/VIS-/NIR absorption spectrophotometer with a scan rate of 600 nm/s and a slit width of 2 nm using a baseline correction (air/air) and a solvent sample as reference.

Fluorescence spectra of pH titration experiments were recorded on a calibrated FluoroMax-4P spectrofluorometer from Horiba Jobin Yvon GmbH with an integration time of 0.1 s and slit widths of 1.0 and 1.5 nm for excitation and emission, respectively.

Fluorescence spectra for determination of relative fluorescence quantum yields, following the generally used method,[1] using fluorescein 27 as standard (Lambda Physics; the fluorescence quantum yield of FL27 was determined absolutely to be 0.86 prior to relative measurements), were recorded on a LS-50B luminescence spectrometer from Perkin Elmer with a integration time of 0.1 s and slit widths of 8.0 and 5.0 nm for excitation and emission, respectively (λ_{ex} = 475 nm). Absolute fluorescence quantum yields were determined using a Quantaurus-QY integrating sphere spectrometer C11347-01 from Hamamatsu Photonics K.K. keeping always the absorbance of the sample solutions at the excitation wavelength below 0.1 (λ_{ex} = 475 nm). Determined values of at least five independent measurements for each dye were averaged. To determine the fluorescence quantum yield of the protonated species 5 µl of concentrated HCl (12 M) was added to 3 ml methanolic samples containing BODIPY **3**, **5**, **9** or **10**. The quantum yields have been determined relatively and absolutely and are in good agreement.

Determination of fluorescence lifetimes was carried out with a FLS920 spectrofluorometer from Edinburgh Instruments using a femtosecond supercontinuum laser. The repetition rate was set to 10 MHz. All obtained decay curves were analyzed with the software FAST (Edinburgh Instruments) using mono-exponential fitting parameters to obtain the fluorescence lifetimes.

pH-titration

The pH values of the buffer solutions (borate, citrate) were adjusted with a 780 pH meter using a glass electrode from Deutsche METROHM GmbH & Co. KG and were verified with a pH 211

microprocessor pH meter from Hanna Instruments. The pH meters were calibrated at 25°C with standard buffers of pH 10.01, pH 7.01 and pH 4.01 (Hanna Instruments) in a two-point and three-point calibration for pH 211 microprocessor pH meter and 780 pH meter, respectively.
For the determination of the pK_a-values, 30 – 40 µL of the methanolic stock solutions of the BODIPY dyes (depending on the concentration of the stock solution) diluted with 2 ml methanol, were added to 1 ml buffer. Successively, defined amounts of concentrated HCl were added and the respective absorption and fluorescence emission spectra were collected at the respective pH. pK_a-values were determined from at least 3 independent samples and measurements. Although pK_a-values of pH-sensors bearing phenol groups commonly show negligible sensitivity to low ionic strength, buffer capacity and composition was kept constant for all measurements.[2, 3]
For the broad-range sensor containing dyes **1**, **2**, **3**, and **10**, 10 µl of the stock solution of each dye was mixed and added to 3 ml buffered aqueous-methanolic solution with different pH.

NMR spectroscopy and mass spectrometry
NMR spectroscopic experiments were performed on a Avance II 500 from Bruker at 25 °C using solvent residual proton signals as internal standard (^{1}H: δ($CDCl_3$) = 7.26 ppm, δ(DMSO-d_6) = 2.50 ppm; ^{13}C: δ($CDCl_3$) = 77.16 ppm, δ(DMSO-d_6) = 39.52 ppm). Chemical shifts (δ) are given in parts per million (ppm) relative to tetramethylsilane (TMS).
All samples were measured on an Agilent 6210 ESI-TOF, Agilent Technologies, Santa Clara, CA, USA. Solvent flow rate was adjusted to 4 µL/min, and spray voltage set to 4.000 V, respectively. Drying gas flow rate was set to 15 psi (1 bar). All other parameters were adjusted for maximum abundance of the relative $[M+H]^+$ / $[M-H]^-$

Photostability
For photostability studies, all dye solutions with an initial absorbance of 0.1 were illuminated for 18 h using a 150 W xenon lamp (monochromator set to 475 nm, excitation slit width 15 nm, excitation power 3.2 mW for 475 nm). Light-induced changes were monitored continuously recording fluorescence spectra with a frequency of one spectrum per minute using a CCD spectrometer. To determine the photostability of the protonated species 5 µl of concentrated HCl (12 M) was added to 3 ml methanolic samples containing BODIPY **3**, **5**, **9** or **10**.

Optical sensor film
A mixture containing 0.18 mM (about 1.3 – 2.1 mg/ 10 ml solvent) of indicator dyes **1**, **2**, **3**, and **10** and D4-hydrogel (1000 mg) in 10 ml EtOH/H_2O (8:2 vol%) were used for the preparation of the broad-range pH sensor film.

Experimental Section

Syntheses of substituted hydroxyaryl derivatives **1 – 10** were carried out according a well-established standard protocol for meso-substituted BODIPYs using 2,4-dimethylpyrrole and different aldehydes as reactants.[4-6] It includes the condensation of 2,4-dimethylpyrrole and the corresponding hydroxybenzaldehyde derivate in the presence of trifluoracetic acid (TFA), followed by an oxidation using *p*-chloranil. Subsequent deprotonation with an amine base (e.g., diisopropylethylamine (DIPEA)) and complexation with boron trifluoride etherate ($BF_3 \cdot Et_2O$) yielded the desired products. The sequential one pot reactions were carried out in dichloromethane at room temperature under inert atmosphere.

The different mono-, di-, and tri-bromo-substituted hydroxybenzaldehyde precursors were prepared according to protocols for aromatic bromination reactions using appropriate quantities of NBS following a general procedure 1 (P1).[7] Starting with 4-hydroxybenzaldehyde (**11**) and 3-chloro-4-hydroxybenzaldehyde (**14**) allows to synthesize mono- or di-halogenated benzaldehyde derivatives 3-bromo-4-hydroxybenzaldehyde (**12**), 3,5-dibromo-4-hydroxybenzaldehyde (**13**), and 3-bromo-5-chloro-4-hydroxybenzaldehyde (**15**) by using either one equivalent or a small excess (2.1 eq.) of NBS. Tri-brominated hydroxybenzaldehyde derivate is accessible from unsymmetric 3-hydroxybenzaldehyde (**16**) and with an excess of NBS (3.5 eq.), 2,4,6-tribromo-3-hydroxybenzaldehyde (**20**) was obtained. Mono- and di-halogenated isomers of **16**, in this particular case 2-bromo-3-hydroxybenzaldehyde (**17**), 6-bromo-3-hydroxybenzaldehyde (**18**), and 2,4-dibromo-3-hydroxybenzaldehyde (**19**), were also prepared for this study.

BODIPYs **1** – **10** were synthesized using substituted hydroxybenzaldehyde derivatives **11** – **20**, respectively, following a general procedure (P2; Scheme S1). To obtain the desired products in sufficient purity, it was necessary to run several columns (at least 2 – 3), followed by a final recrystallization. However, all BODIPYs were synthesized in typical yields up to 20%. All synthesized compounds were characterized by NMR spectroscopy (^{1}H, ^{13}C) and mass spectrometry. The pH-sensitive BODIPY dyes were dissolved in MeOH in order to study their spectroscopic properties.

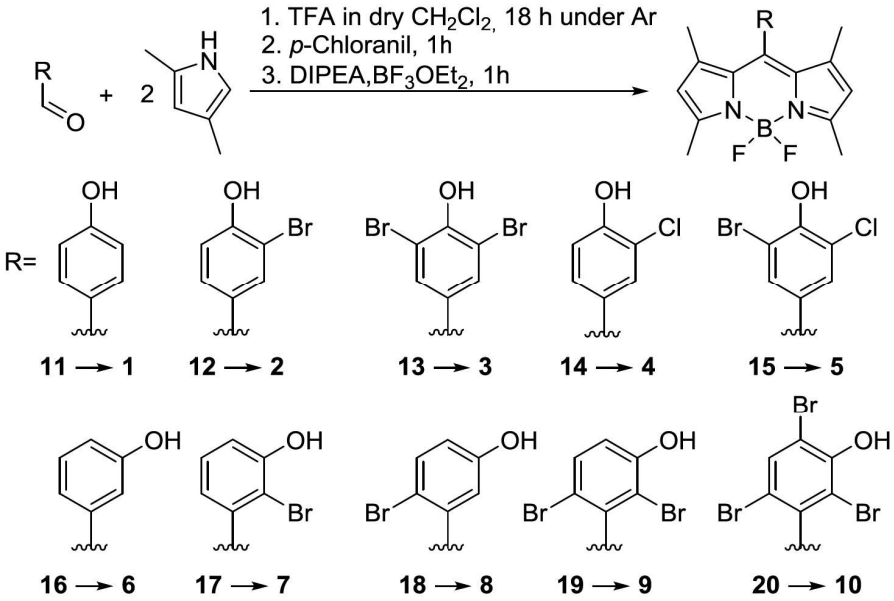

*Scheme S1: Synthetic pathway from aldehydes **11** – **20** to BODIPYs **1** – **10**.*

Bromination of hydroxybenzaldehyde derivatives:
To a stirred solution of the benzaldehyde precursor (25 mmol, 1 eq.) in chloroform (250 ml) an appropriate amount of NBS was added slowly and portion wise over up to 2 hours) Depending on the desired degree of bromination, 1.05 eq., 2.10 eq. or 3.50 eq. of NBS were added for mono-, di- or tri-bromination, respectively. The reaction mixture was stirred at room temperature until complete consumption of the starting reactant (monitored by thin layer chromatography (TLC)). Subsequently, excess bromine was removed by washing with a saturated solution of sodium thiosulfate. The aqueous layer was separated and the residue extracted into chloroform. The organic layers were combined, dried over anhydrous

magnesium sulfate, and concentrated under reduced pressure. The crude product was purified by silica-gel flash column chromatography using dichloromethane (DCM) as eluent.

Synthesis of BODIPYs:
The corresponding aldehyde (2.5 mmol, 1.0 eq.) and 2,4-dimethylpyrrole (5.0 mmol, 2.0 eq.) were dissolved in 150 ml of dry DCM. After degassing by rapid vacuum-argon cycles (5 times), a few drops of TFA (30 µl) were added and the reaction mixture was stirred at room temperature under argon atmosphere in the dark overnight (at least 18 h). *p*-Chloranil (2.5 mmol, 1.0 eq.) was added and the mixture was stirred for additional 60 min. Subsequently, $BF_3 \cdot OEt_2$ (25.0 mmol, 10.0 eq.) and 4.3 ml diisopropylethylamine (DIPEA) (25.0 mmol, 10.0 eq.) were alternately added in 1 ml portions. After stirring for another 60 minutes, the mixture was prepurified by carrying out a short silica-gel flash column chromatography with DCM as eluent. The resulting crude mixture was concentrated under reduced pressure and further purified by silica-gel flash column chromatography using DCM/*n*-hexane (ratio in dependence of product polarity) as eluents. Pure dyes as required for the spectroscopic studies were obtained by recrystallization from chloroform/*n*-hexane.

Synthesis of compounds **12**, **13**, **15**, **17**, **18**, **19** *and* **20**

3-bromo-4-hydroxybenzaldehyde **(12)**
Compound **12** was synthesized according to the procedure mentioned above using 1.05 eq. of NBS. Despite controlled and slow addition of NBS, also formation of di-brominated compound **13** was observed. Purification gave compound **12** as white solid (4.26 g, 85 %) and compound **13** as white solid (0.35 g, 5 %).
^{1}H NMR (500 MHz, $CDCl_3$) [ppm]: δ = 9.83 (s, CHO), 8.04 (d, $1H_{aryl}$), 7.78 (dd, $1H_{aryl}$), 7.16 (d, $1H_{aryl}$), 6.14 (s, OH)
^{13}C NMR (125 MHz, $CDCl_3$) [ppm]: δ = 189.5, 157.5, 134.1, 131.6, 131.2, 116.7, 111.3
ESI-TOF (ESI-): m/z calculated for $C_7H_4Br_1O_2$ $[M\text{-}H]^-$: 198.9395, found 198.9412.

3,5-dibromo-4-hydroxybenzaldehyde **(13)**
Compound **13** was synthesized according to the procedure mentioned above using 2.10 eq. of NBS. Purification gave compound **13** as white solid (6.34 g, 91 %).
^{1}H NMR (500 MHz, $CDCl_3$) [ppm]: δ = 9.80 (s, CHO), 8.00 (s, $2H_{aryl}$), 6.42 (s, OH)
^{13}C NMR (125 MHz, $CDCl_3$) [ppm]: δ = 188.2, 152.2, 133.8, 117.8, 110.9
ESI-TOF (ESI-): m/z calculated for $C_7H_3Br_2O_2$ $[M\text{-}H]^-$: 278.8480, found 278.8528.

3-bromo-5-chloro-4-hydroxybenzaldehyde **(15)**
Compound **15** was synthesized according to the procedure mentioned above using 1.05 eq. of NBS. Purification compound **15** as white solid (5.08 g, 86 %).
^{1}H NMR (500 MHz, $CDCl_3$) [ppm]: δ = 9.81 (s, CHO), 7.97 (d, $1H_{aryl}$), 7.86 (d, $1H_{aryl}$), 6.45 (s, OH)
^{13}C NMR (125 MHz, $CDCl_3$) [ppm]: δ = 188.4, 153.8, 133.2, 130.9, 130.5, 111.2, 110.1
ESI-TOF: not measured

2-bromo-3-hydroxybenzaldehyde **(17)**
Compound **17** was synthesized according to the procedure mentioned above using 1.05 eq. of NBS. Purification by column chromatography on silica gel using DCM as eluent gave several mixed fractions containing different mono- and di-brominated isomers. However, a pure fraction was collected and gave compound **17** as white solid (0.33 g, 66 %, starting with 2.5 mmol aldehyde).

^{1}H NMR (500 MHz, $CDCl_3$) [ppm]: δ = 10.29 (s, CHO), 7.51 (dd, $1H_{aryl}$), 7.36 (td, $1H_{aryl}$), 7.28 (dd, $1H_{aryl}$), 5.97 (s, OH)
^{13}C NMR (125 MHz, $CDCl_3$) [ppm]: δ = 191.3, 153.1, 134.0, 129.0, 122.9, 121.8, 114.1
ESI-TOF (ESI-): m/z calculated for $C_7H_4Br_1O_2$ $[M-H]^-$: 198.9395, found 198.9376.

2-bromo-5-hydroxybenzaldehyde **(18)**
Compound **18** was synthesized by treating an ice-cooled suspension of **16** in DCM slowly with bromine (1.5 eq.). After complete addition of bromine, the reaction mixture was stirred for 4 hours at room temperature. Filtration of the resulting solid and recrystallization from *n*-hexane/chloroform gave white needle shaped crystals (7.6 g, 63 %, starting with 60 mmol aldehyde).
^{1}H NMR (500 MHz, $CDCl_3$) [ppm]: δ = 10.29 (s, CHO), 7.51 (d, $1H_{aryl}$), 7.42 (d, $1H_{aryl}$), 7.01 (dd, $1H_{aryl}$), 6.01 (s, OH)
^{13}C NMR (125 MHz, $CDCl_3$) [ppm]: δ = 192.2, 155.7, 135.0, 134.2, 123.5, 117.9, 115.9
ESI-TOF (ESI-): m/z calculated for $C_7H_4Br_1O_2$ $[M-H]^-$: 198.9395, found 198.9399.

2,6-dibromo-3-hydroxybenzaldehyde **(19)**
Compound **19** was synthesized according to the procedure mentioned above using 2.10 eq. of NBS. Purification by column chromatography on silica gel using DCM as eluent gave several mixed fractions containing different mono- and di-brominated isomers, as well as tribrominated compound **20**. After several columns, a pure fraction was collected and gave compound **19** as white solid (0.87 g, 13 %).
^{1}H NMR (500 MHz, $CDCl_3$) [ppm]: δ = 10.24 (s, CHO), 7.55 (d, $1H_{aryl}$), 7.13 (d, $1H_{aryl}$), 6.17 (s, OH),
^{13}C NMR (125 MHz, $CDCl_3$) [ppm]: δ = 191.1, 153.0, 134.0, 132.1, 121.0, 116.8, 111.5
ESI-TOF (ESI-): m/z calculated for $C_7H_3Br_2O_2$ $[M-H]^-$: 278.8480, found 278.8518.

2,4,6-tribromo-4-hydroxybenzaldehyde **(20)**
Compound **20** was synthesized according to the procedure mentioned above using 3.50 eq. of NBS. Purification gave compound **20** as white solid (6.52 g, 91 %).
^{1}H NMR (500 MHz, $CDCl_3$) [ppm]: δ = 10.17 (s, CHO), 7.85 (s, $1H_{aryl}$), 6.35 (s, OH)
^{13}C NMR (125 MHz, $CDCl_3$) [ppm]: δ = 190.4, 150.3, 136.7, 131.9, 122.6, 115.1, 110.7
ESI-TOF (ESI-): m/z calculated for $C_7H_2Br_3O_2$ $[M-H]^-$: 356.7585, found 356.7667.

Synthesis of compounds **1 – 10**

4,4-difluoro-1,3,5,7-tetramethyl-8-(4-hydroxyphenyl)-bora-3a,4a-diaza-s-indacene **(1)**
Compound **1** was synthesized according to the procedure mentioned above using corresponding aldehyde **11**. Purification by column chromatography on silica gel using DCM as eluent followed by recrystallization gave compound **1** as orange crystals (165 mg, 19 %).
^{1}H NMR (500 MHz, DMSO-d_6) [ppm]: δ = 9.85 (s, OH), 7.11 (m, $2H_{aryl}$), 6.92 (m, $2H_{aryl}$), 6.16 (s, $2H_{pyrrole}$), 2.43 (s, $6H_{methyl}$), 1.42 (s, $6H_{methyl}$)
^{13}C NMR (125 MHz, $CDCl_3$) [ppm]: δ = 158.2, 154.5, 142.8, 131.2, 129.0, 124.2, 121.2, 116.1, 14.2, 14.2
ESI-TOF (ESI+): m/z calculated for $C_{19}H_{20}BF_2N_2O$ $[M+H]^+$: 341.1639, found 341.1643.

4,4-difluoro-1,3,5,7-tetramethyl-8-(3-bromo-4-hydroxyphenyl)-bora-3a,4a-diaza-s-indacene **(2)**
Compound **2** was synthesized according to the procedure mentioned above using corresponding aldehyde **12**. Purification by column chromatography on silica gel using DCM/*n*-hexane (9:1) as eluent followed by recrystallization gave compound **2** as reddish-orange crystals (135 mg, 13 %).
^{1}H NMR (500 MHz, DMSO-d_6) [ppm]: δ = 10.73 (s, OH), 7.51 (d, $1H_{aryl}$), 7.16 (dd, $1H_{aryl}$), 7.11 (d, $1H_{aryl}$), 6.18 (s, $2H_{pyrrole}$), 2.44 (s, $6H_{methyl}$), 1.45 (s, $6H_{methyl}$)
^{13}C NMR (125 MHz, $CDCl_3$) [ppm]: δ = 154.9, 154.9, 142.6, 140.6, 132.1, 131.0, 128.5, 125.8, 121.4, 117.0, 109.9, 14.4, 14.2
ESI-TOF (ESI-): m/z calculated for $C_{19}H_{19}BBrF_2N_2O$ $[M-H]^-$: 417.0586, found 417.0659.

4,4-difluoro-1,3,5,7-tetramethyl-8-(3,5-dibromo-4-hydroxyphenyl)-bora-3a,4a-diaza-s-indacene **(3)**
Compound **3** was synthesized according to the procedure mentioned above using corresponding aldehyde **13**. Purification by column chromatography on silica gel using DCM/*n*-hexane (8:2) as eluent followed by recrystallization gave compound **3** as reddish crystals (262 mg, 21 %).
^{1}H NMR (500 MHz, DMSO-d_6) [ppm]: δ = 10.42 (s, OH), 7.64 (s, $2H_{aryl}$), 6.21 (s, $2H_{pyrrole}$), 2.44 (s, $6H_{methyl}$), 1.48 (s, $6H_{methyl}$)
^{13}C NMR (125 MHz, $CDCl_3$) [ppm]: δ = 155.2, 151.6, 142.5, 138.6, 131.8, 130.9, 127.7, 121.6, 112.5, 14.5, 14.3
ESI-TOF (ESI-): m/z calculated for $C_{19}H_{16}BBr_2F_2N_2O$ $[M-H]^-$: 496.9670, found 496.9742.

4,4-difluoro-1,3,5,7-tetramethyl-8-(3-chloro-4-hydroxyphenyl)-bora-3a,4a-diaza-s-indacene **(4)**
Compound **4** was synthesized according to the procedure mentioned above using corresponding aldehyde **14**. Purification by column chromatography on silica gel using DCM/*n*-hexane (9:1) as eluent followed by recrystallization gave compound **4** as reddish-orange crystals (95 mg, 10 %).
^{1}H NMR (500 MHz, DMSO-d_6) [ppm]: δ = 10.67 (s, OH), 7.38 (dd, $1H_{aryl}$), 7.12 (m, $2H_{aryl}$), 6.18 (s, $2H_{pyrrole}$), 2.44 (s, $6H_{methyl}$), 1.45 (s, $6H_{methyl}$)
^{13}C NMR (125 MHz, $CDCl_3$) [ppm]: δ = 154.9, 153.9, 142.7, 140.7, 131.0, 129.3, 127.8, 125.4, 121.4, 120.5, 117.3, 14.3, 14.2
ESI-TOF (ESI-): m/z calculated for $C_{19}H_{17}BClF_2N_2O$ $[M-H]^-$: 373.1090, found 373.1142.

4,4-difluoro-1,3,5,7-tetramethyl-8-(3-bromo-5-chloro-4-hydroxyphenyl)-bora-3a,4a-diaza-s-indacene **(5)**

Compound **5** was synthesized according to the procedure mentioned above using corresponding aldehyde **15**. Purification by column chromatography on silica gel using DCM/*n*-hexane (8:2) as eluent followed by recrystallization gave compound **5** as reddish crystals (97 mg, 12 %, starting with 1.75 mmol aldehyde).

^{1}H NMR (500 MHz, DMSO-d_6) [ppm]: δ = 10.58 (s, OH), 7.68 (s, $1H_{aryl}$), 7.53 (s, $1H_{aryl}$), 6.21 (s, $2H_{pyrrole}$), 2.44 (s, $6H_{methyl}$), 1.48 (s, $6H_{methyl}$)

^{13}C NMR (125 MHz, $CDCl_3$) [ppm]: δ = 155.2, 150.7, 142.5, 138.7, 131.2, 129.9, 126.9, 122.6, 121.5, 120.6, 112.6, 14.5, 14.2

ESI-TOF (ESI-): m/z calculated for $C_{19}H_{16}BBrClF_2N_2O$ $[M-H]^-$: 451.0196, found 451.0229.

4,4-difluoro-1,3,5,7-tetramethyl-8-(3-hydroxyphenyl)-bora-3a,4a-diaza-s-indacene **(6)**

Compound **6** was synthesized according to the procedure mentioned above using corresponding aldehyde **16**. Purification by column chromatography on silica gel using DCM as eluent followed by recrystallization gave compound **6** as orange crystals (104 mg, 12 %).

^{1}H NMR (500 MHz, DMSO-d_6) [ppm]: δ = 9.81 (s, OH), 7.36 (dd, $1H_{aryl}$), 6.92 (ddd, $1H_{aryl}$), 6.75 (ddd, $1H_{aryl}$), 6.69 (dd, $1H_{aryl}$), 6.17 (s, $2H_{pyrrole}$), 2.44 (s, $6H_{methyl}$), 1.44 (s, $6H_{methyl}$)

^{13}C NMR (125 MHz, $CDCl_3$) [ppm]: δ = 158.3, 154.8, 142.7, 142.0, 135.1, 130.6, 130.5, 121.3, 118.0, 116.1, 114.3, 14.2, 13.8

ESI-TOF (ESI+): m/z calculated for $C_{19}H_{19}BF_2N_2ONa$ $[M+Na]^+$: 363.1456, found 363.1468.

4,4-difluoro-1,3,5,7-tetramethyl-8-(2-bromo-3-hydroxyphenyl)-bora-3a,4a-diaza-s-indacene **(7)**

Compound **7** was synthesized according to the procedure mentioned above using corresponding aldehyde **17**. Purification by column chromatography on silica gel using DCM/*n*-hexane (9:1) as eluent followed by recrystallization gave compound **7** as orange-reddish crystals (54 mg, 9 %, starting with 1.50 mmol aldehyde).

^{1}H NMR (500 MHz, DMSO-d_6) [ppm]: δ = 10.63 (s, OH), 7.37 (dd, $1H_{aryl}$), 7.09 (dd, $1H_{aryl}$), 6.84 (dd, $1H_{aryl}$), 6.17 (s, $2H_{pyrrole}$), 2.45 (s, $6H_{methyl}$), 1.42 (s, $6H_{methyl}$)

^{13}C NMR (125 MHz, $CDCl_3$) [ppm]: δ = 155.2, 155.1, 142.1, 140.2, 136.1, 130.1, 129.7, 121.2, 119.5, 116.7, 109.7, 14.3, 13.2

ESI-TOF (ESI+): m/z calculated for $C_{19}H_{19}BBrF_2N_2O$ $[M+H]^+$: 419.0742, found 419.0733.

4,4-difluoro-1,3,5,7-tetramethyl-8-(2-bromo-5-hydroxyphenyl)-bora-3a,4a-diaza-s-indacene **(8)**

Compound **8** was synthesized according to the procedure mentioned above employing the corresponding aldehyde **18**. Purification by column chromatography on silica gel using DCM/*n*-hexane (9:1) as eluent followed by recrystallization gave compound **8** as orange-redish crystals (110 mg, 10 %, starting with 2.50 mmol aldehyde).

^{1}H NMR (500 MHz, DMSO-d_6) [ppm]: δ = 10.08 (s, OH), 7.54 (d, $1H_{aryl}$), 6.86 (dd, $1H_{aryl}$), 6.75 (d, $1H_{aryl}$), 6.16 (s, $2H_{pyrrole}$), 2.41 (s, $6H_{methyl}$), 1.44 (s, $6H_{methyl}$)

^{13}C NMR (125 MHz, $CDCl_3$) [ppm]: δ = 158.1, 155.4, 142.1, 139.5, 135.3, 134.1, 130.1, 121.4, 118.6, 116.2, 109.8, 14.3, 13.3

ESI-TOF (ESI+): m/z calculated for $C_{19}H_{19}BBrF_2N_2O$ $[M+H]^+$: 419.0742, found 419.0745.

4,4-difluoro-1,3,5,7-tetramethyl-8-(2,6-dibromo-3-hydroxyphenyl)-bora-3a,4a-diaza-s-indacene **(9)**

Compound **9** was synthesized according to the procedure mentioned above using corresponding aldehyde **19**. Purification by column chromatography on silica gel using DCM/*n*-hexane (8:2) as eluent followed by recrystallization gave compound **9** as reddish crystals (75 mg, 6 %).

^{1}H NMR (500 MHz, DMSO-d_6) [ppm]: δ = 10.97 (s, OH), 7.65 (d, $1H_{aryl}$), 7.06 (d, $1H_{aryl}$), 6.19 (s, $2H_{pyrrole}$), 2.46 (s, $6H_{methyl}$), 1.46 (s, $6H_{methyl}$)

^{13}C NMR (125 MHz, $CDCl_3$) [ppm]: δ = 155.6, 155.0, 141.3, 139.0, 135.6, 132.9, 129.5, 121.3, 118.3, 110.9, 110.3, 14.4, 12.9

ESI-TOF (ESI+): m/z calculated for $C_{19}H_{17}BBr_2F_2N_2ONa$ $[M+Na]^+$: 520.9646, found 520.9654.

4,4-difluoro-1,3,5,7-tetramethyl-8-(2,4,6-tribromo-3-hydroxyphenyl)-bora-3a,4a-diaza-s-indacene **(10)**

Compound **10** was synthesized according to the procedure mentioned above using corresponding aldehyde **20**. Purification by column chromatography on silica gel using DCM/*n*-hexane (3:1) as eluent followed by recrystallization gave compound **10** as deep reddish crystals (191 mg, 13 %).

^{1}H NMR (500 MHz, DMSO-d_6) [ppm]: δ = 10.67 (s, OH), 8.12 (s, $1H_{aryl}$), 6.21 (s, $2H_{pyrrole}$), 2.46 (s, $6H_{methyl}$), 1.48 (s, $6H_{methyl}$)

^{13}C NMR (125 MHz, $CDCl_3$) [ppm]: δ = 155.9, 141.2, 138.2, 135.5, 135.1, 129.3, 121.5, 113.8, 113.7, 14.4, 13.1

ESI-TOF (ESI+): m/z calculated for $C_{19}H_{16}BBr_3F_2N_2ONa$ $[M+Na]^+$: 598.8751, found 598.8747.

NMR Spectra

Compound **1**

4,4-difluoro-1,3,5,7-tetramethyl-8-(4-hydroxyphenyl)-bora-3a,4a-diaza-s-indacene

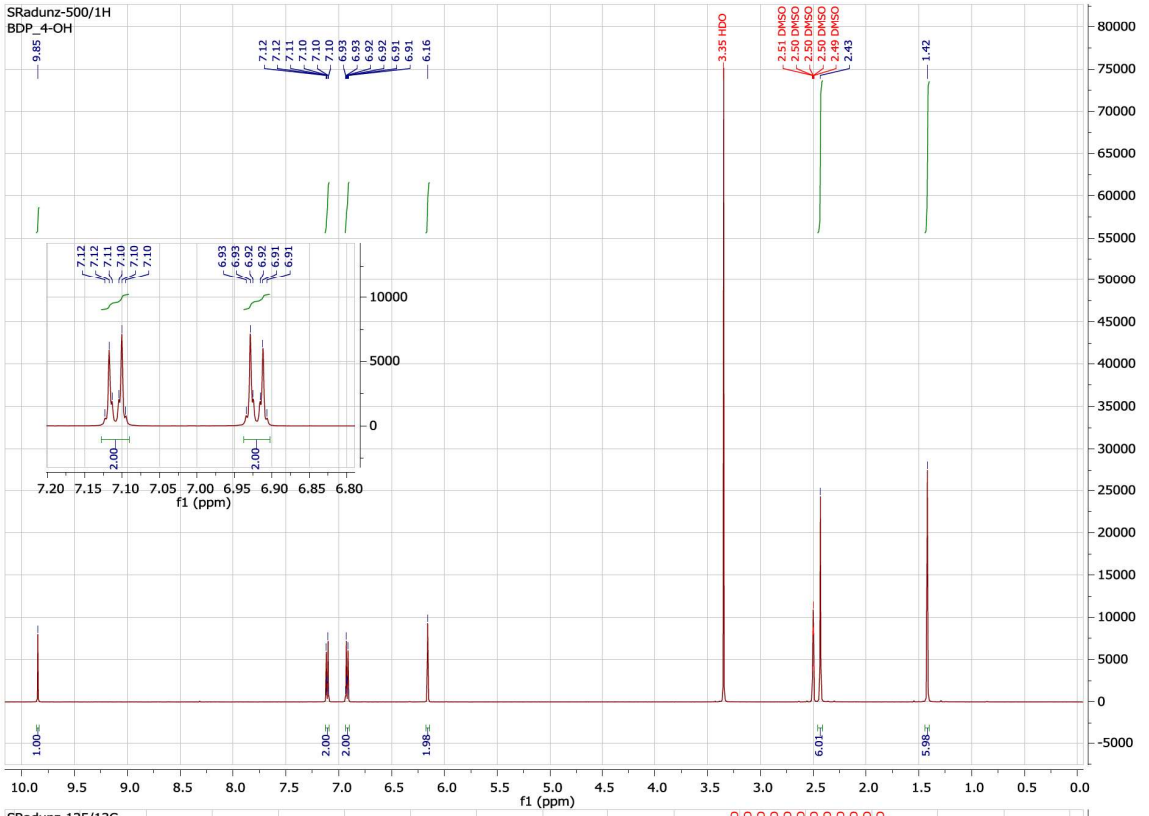

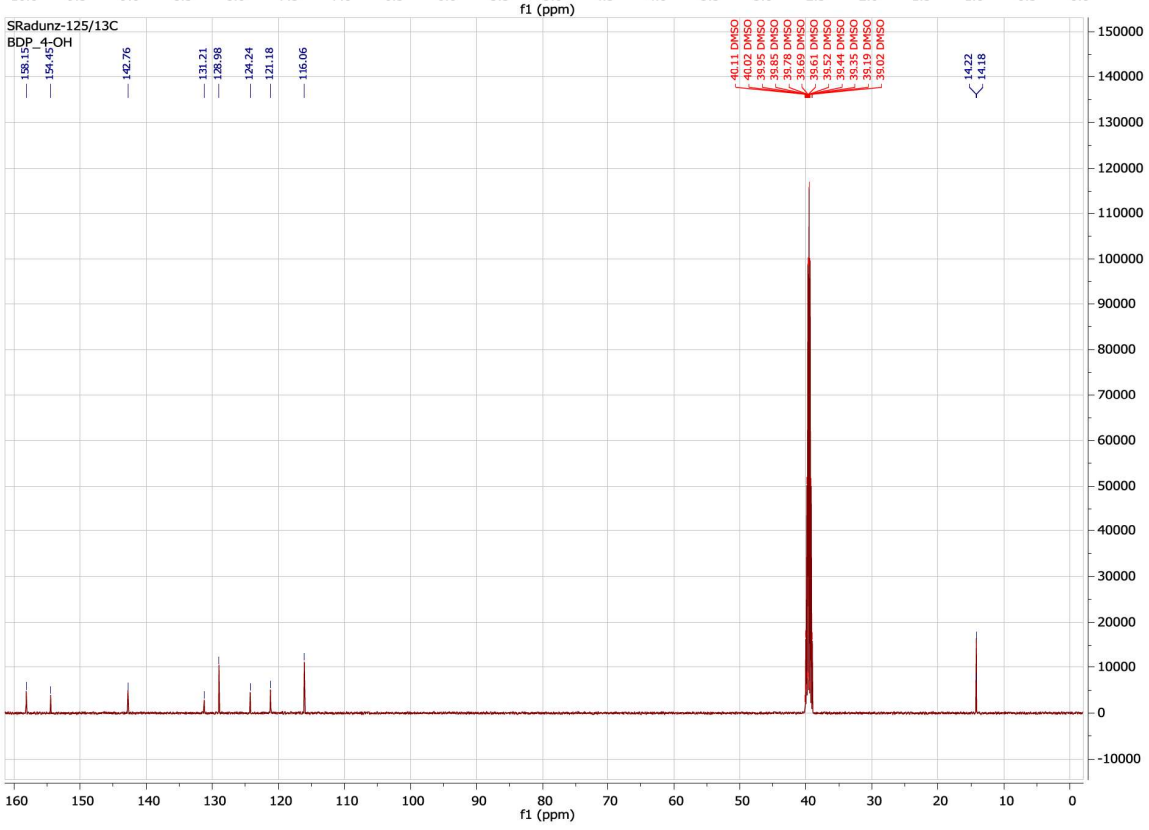

Compound **2**

4,4-difluoro-1,3,5,7-tetramethyl-8-(3-bromo-4-hydroxyphenyl)-bora-3a,4a-diaza-s-indacene

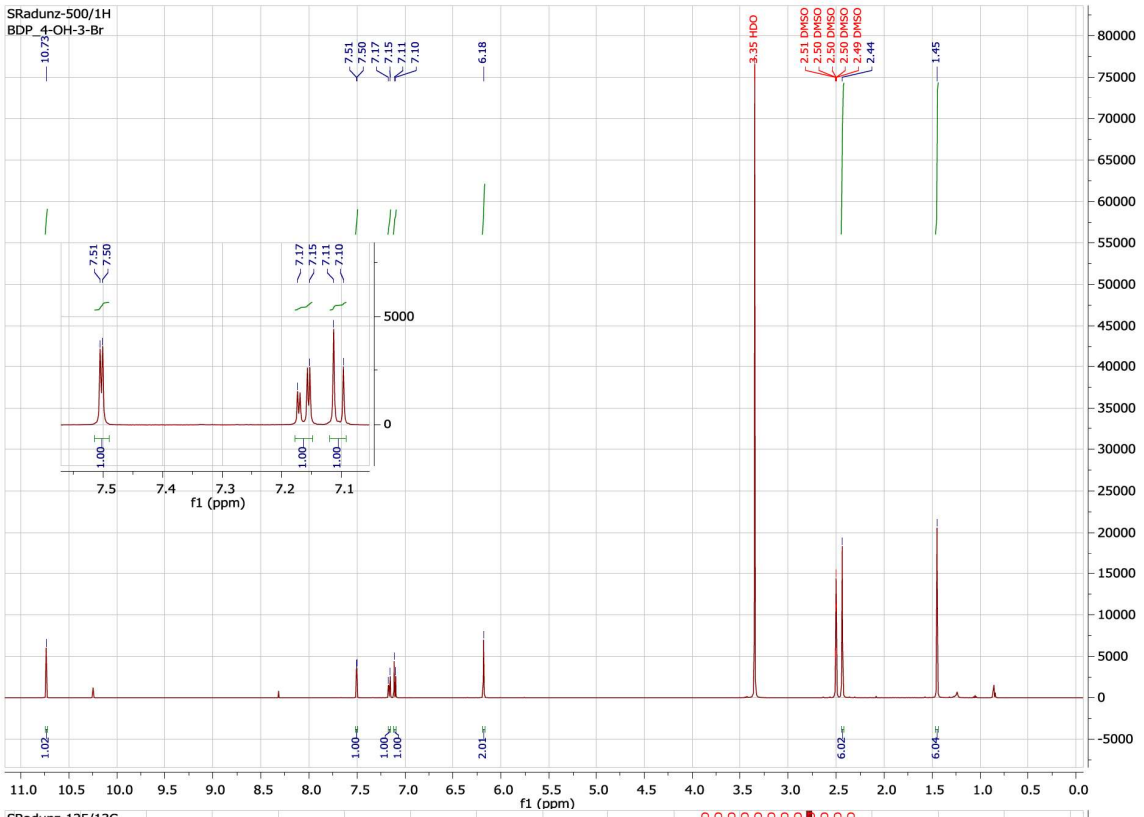

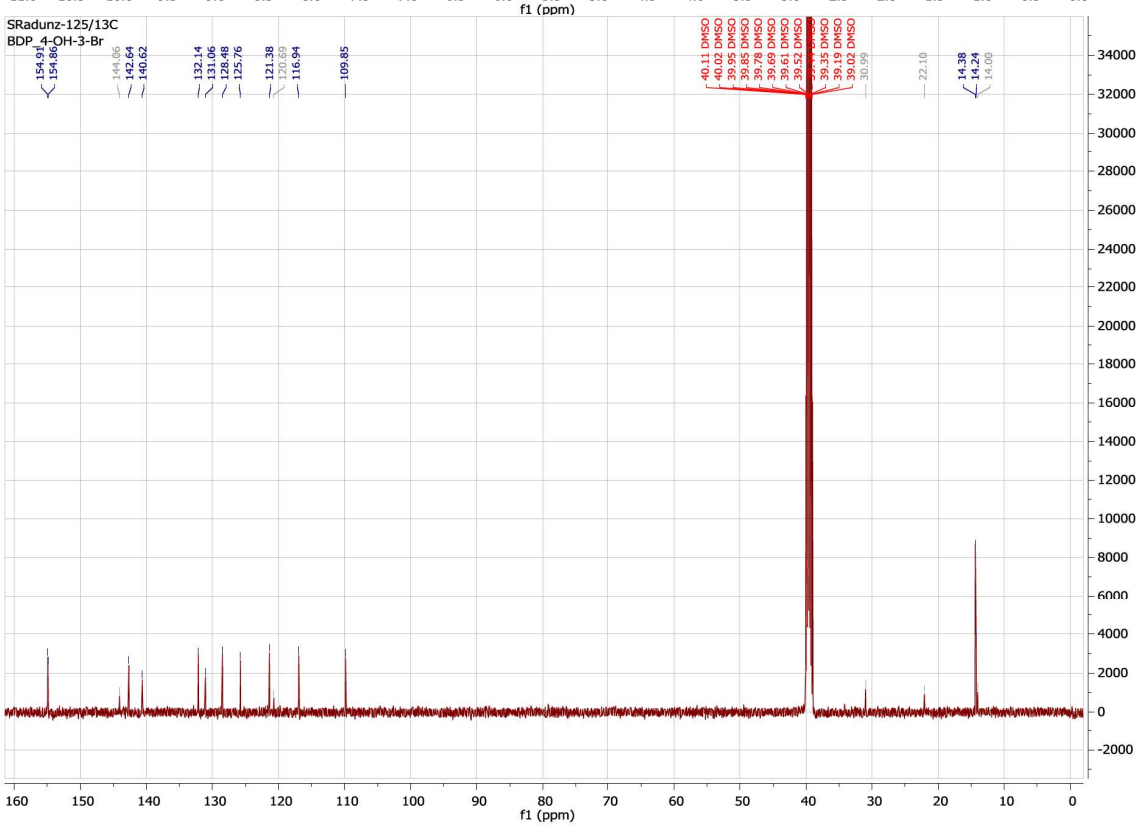

Compound **3**

4,4-difluoro-1,3,5,7-tetramethyl-8-(3,5-dibromo-4-hydroxyphenyl)-bora-3a,4a-diaza-s-indacene

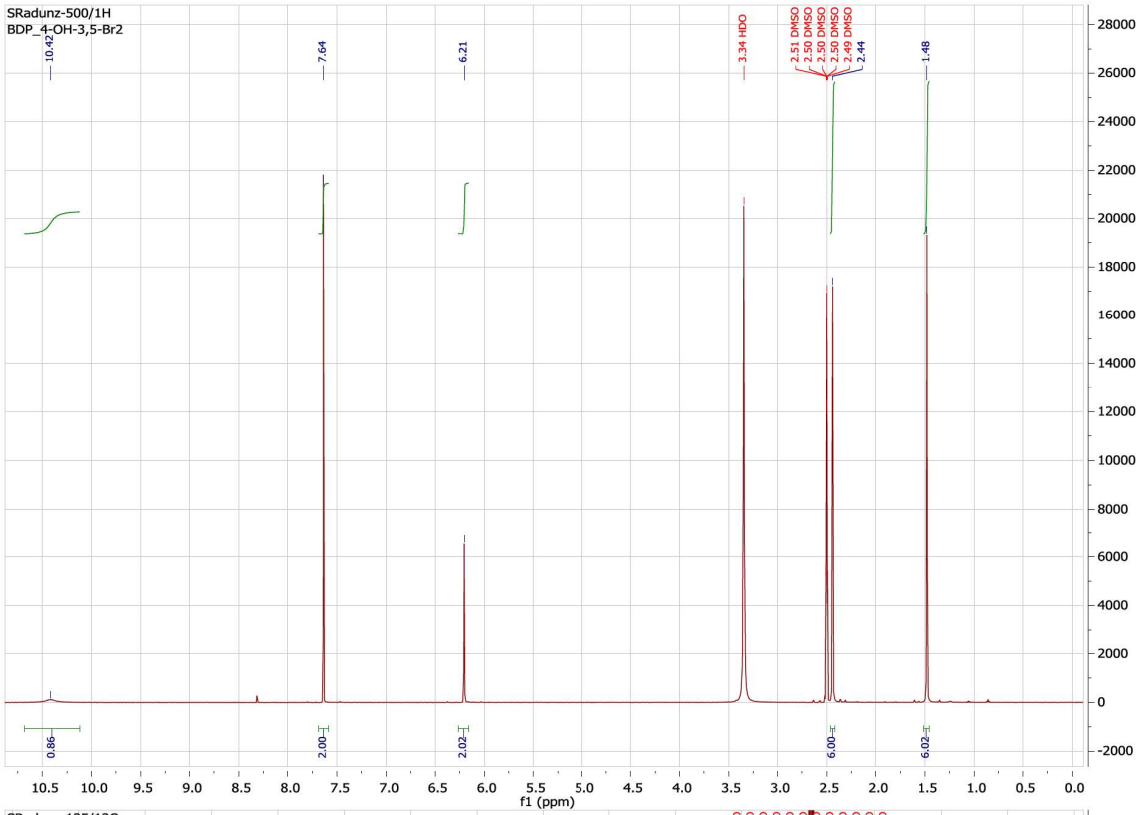

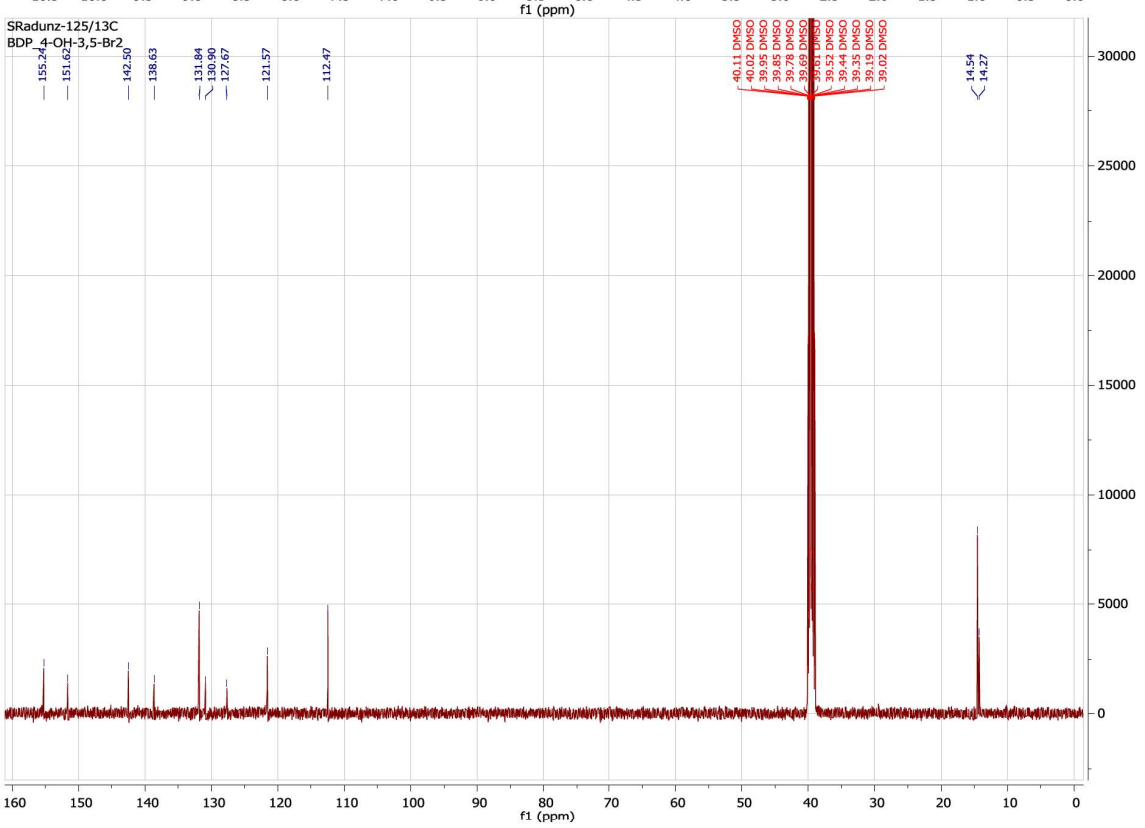

Compound **4**

4,4-difluoro-1,3,5,7-tetramethyl-8-(3-chloro-4-hydroxyphenyl)-bora-3a,4a-diaza-s-indacene

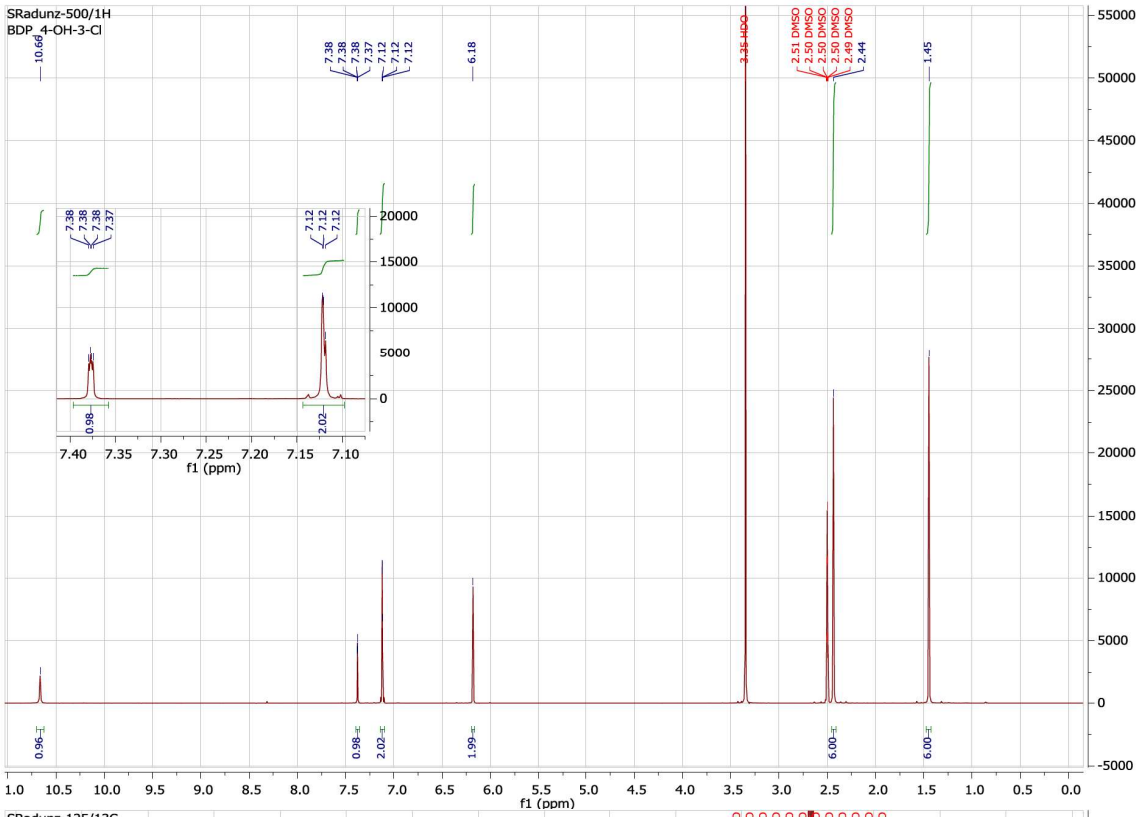

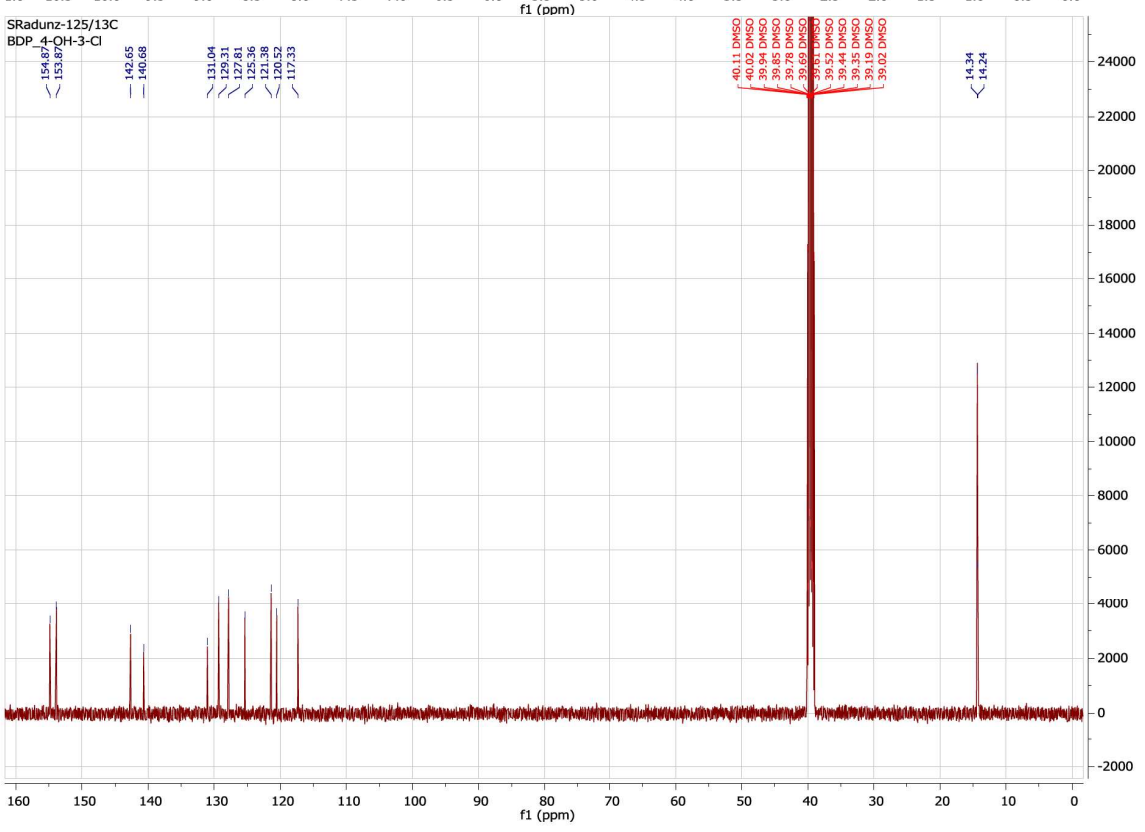

Compound **5**

4,4-difluoro-1,3,5,7-tetramethyl-8-(3-bromo-5-chloro-4-hydroxyphenyl)-bora-3a,4a-diaza-s-indacene

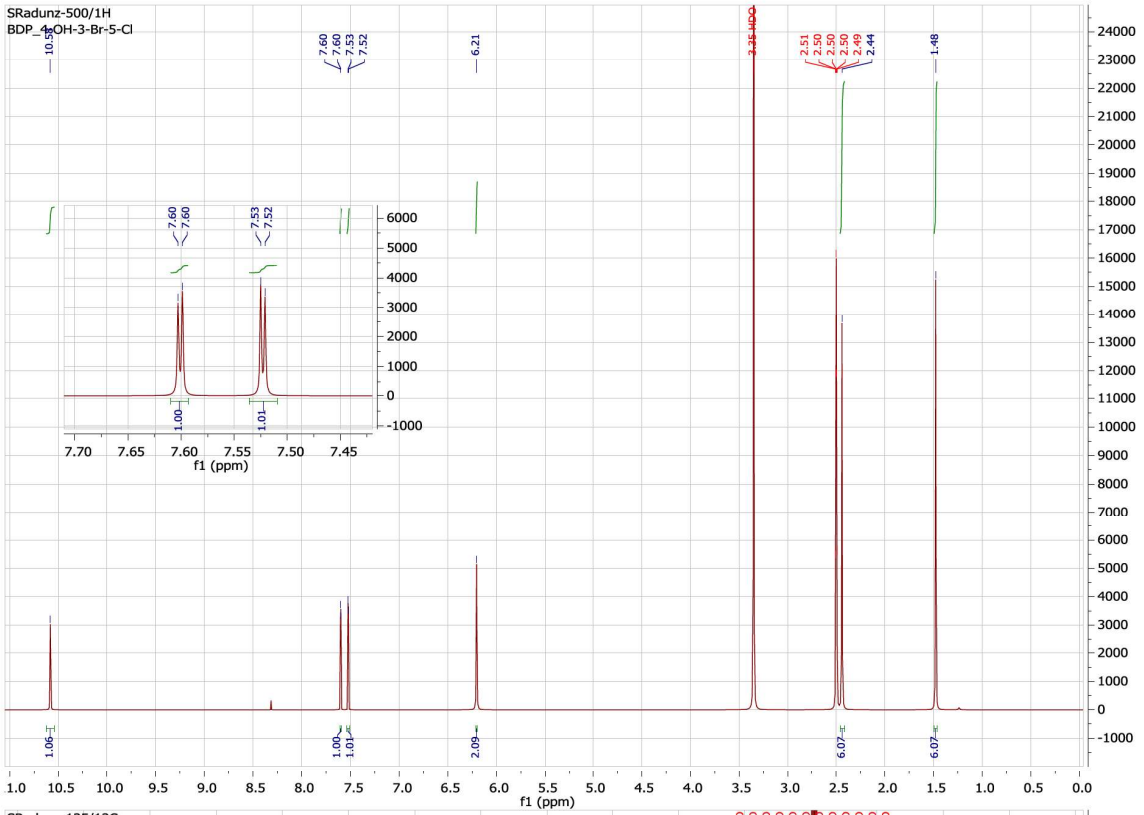

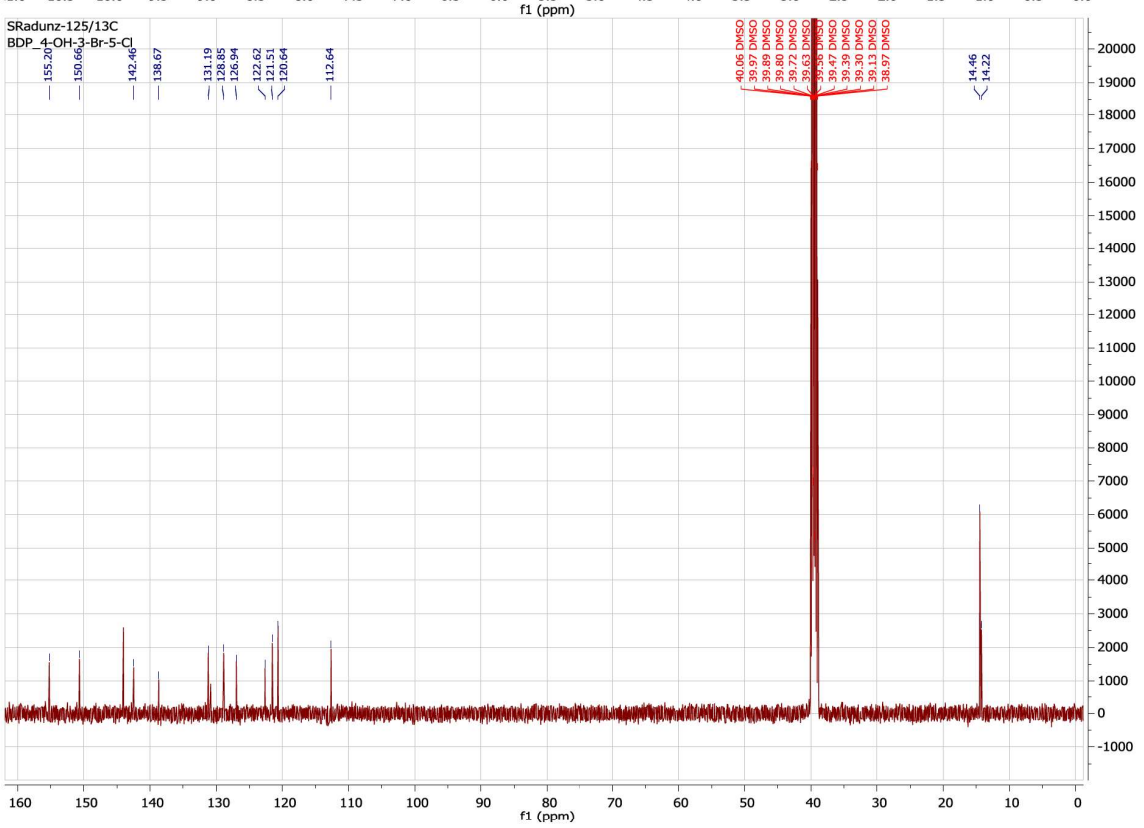

Compound **6**

4,4-difluoro-1,3,5,7-tetramethyl-8-(3-hydroxyphenyl)-bora-3a,4a-diaza-s-indacene

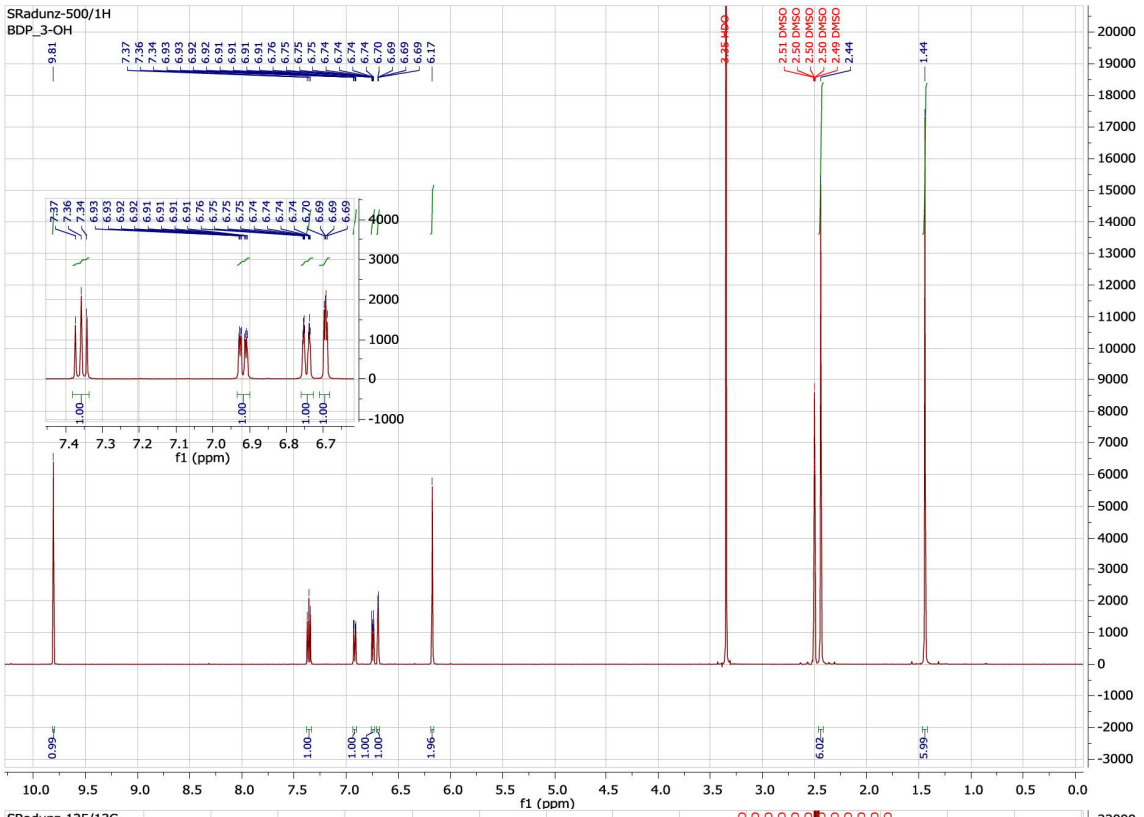

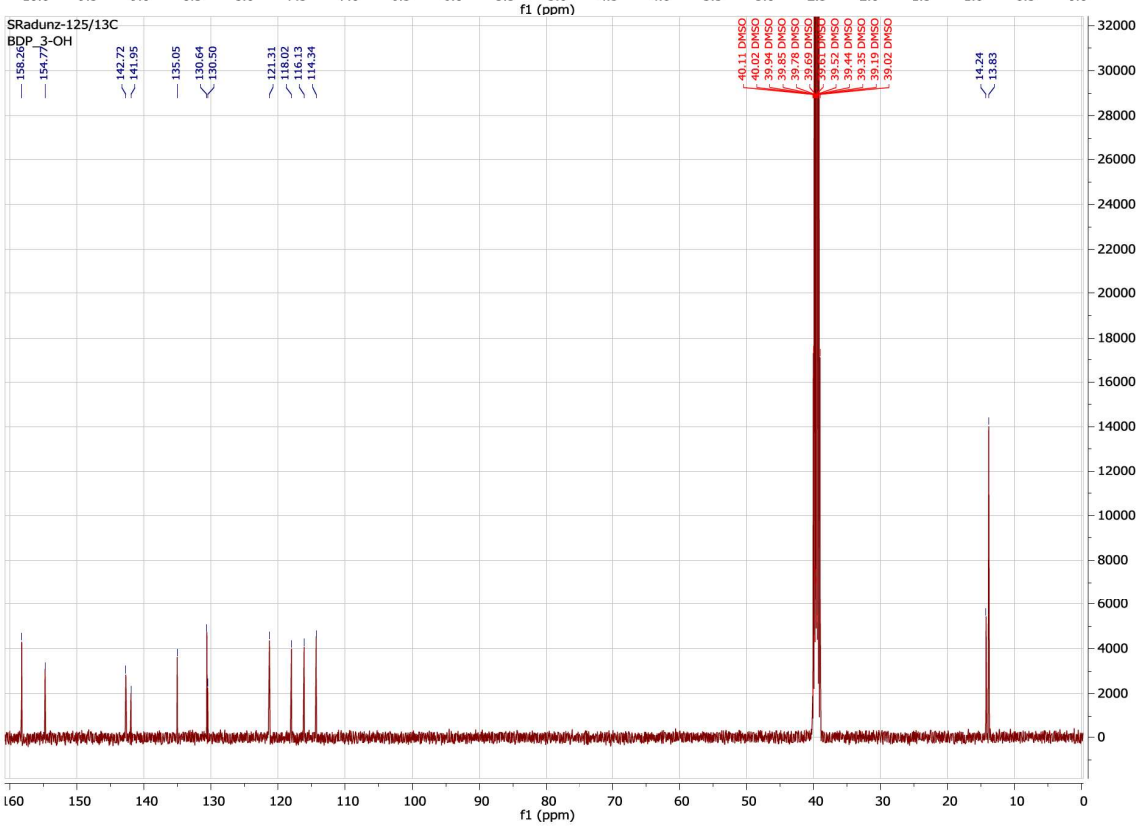

Compound **7**

4,4-difluoro-1,3,5,7-tetramethyl-8-(2-bromo-3-hydroxyphenyl)-bora-3a,4a-diaza-s-indacene

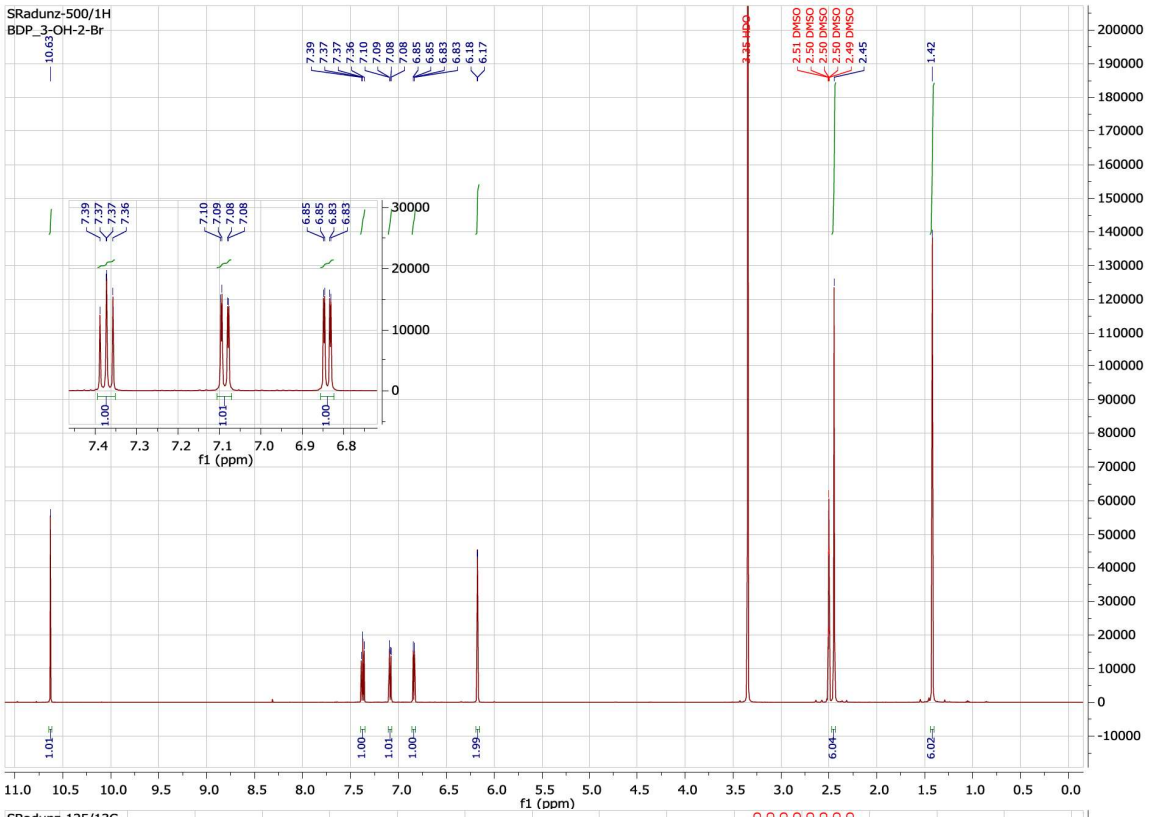

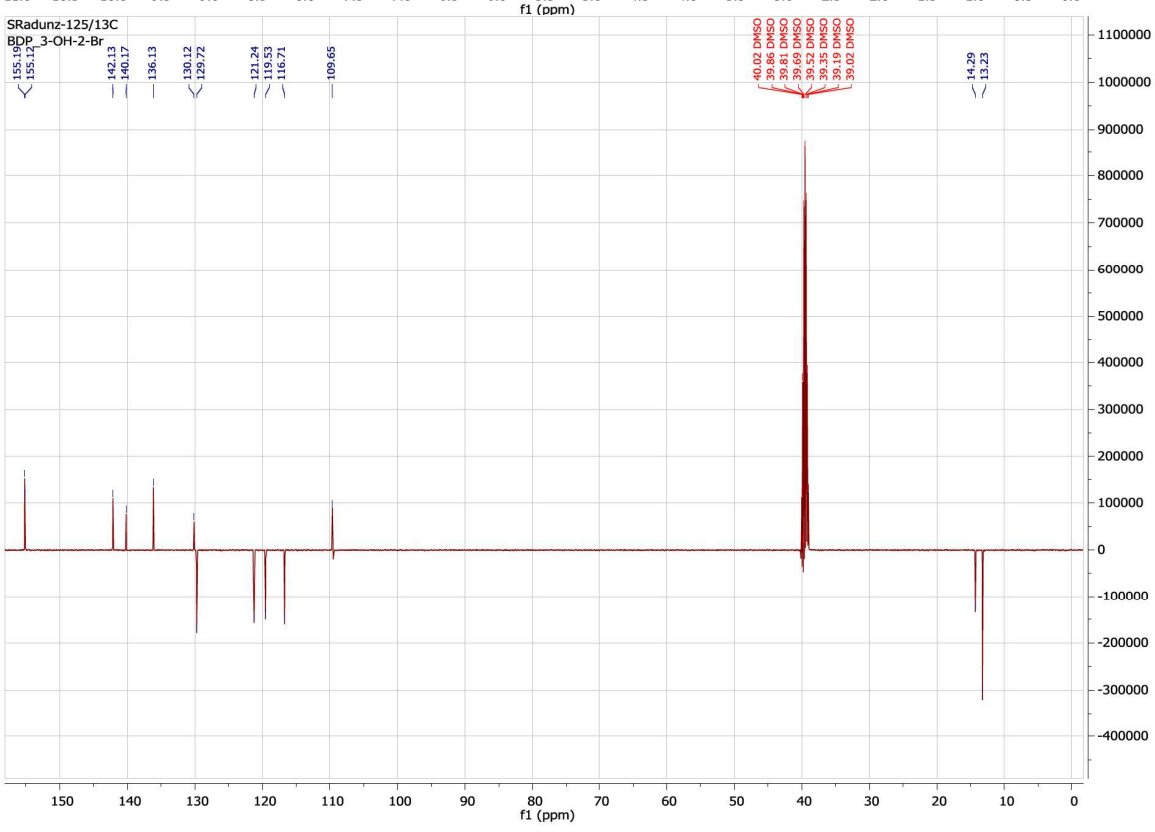

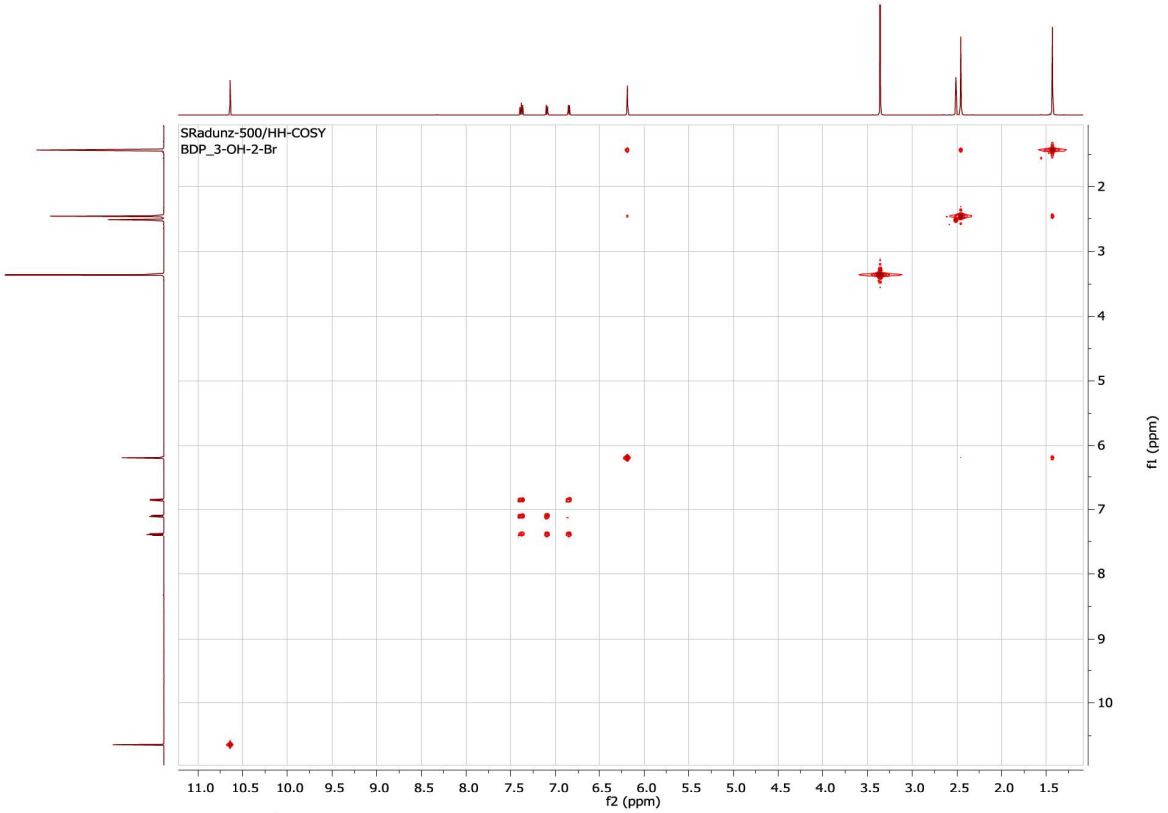
SRadunz-500/HH-COSY
BDP_3-OH-2-Br
f2 (ppm)
f1 (ppm)

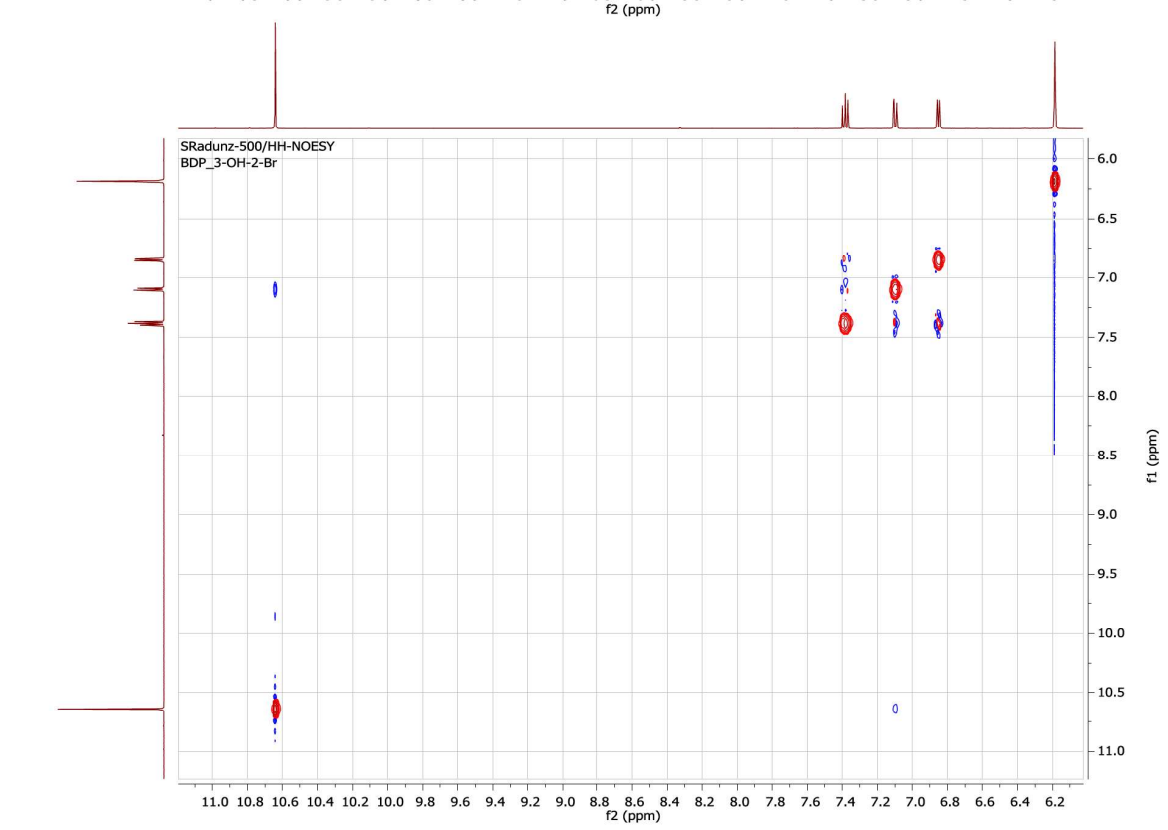
SRadunz-500/HH-NOESY
BDP_3-OH-2-Br
f2 (ppm)
f1 (ppm)

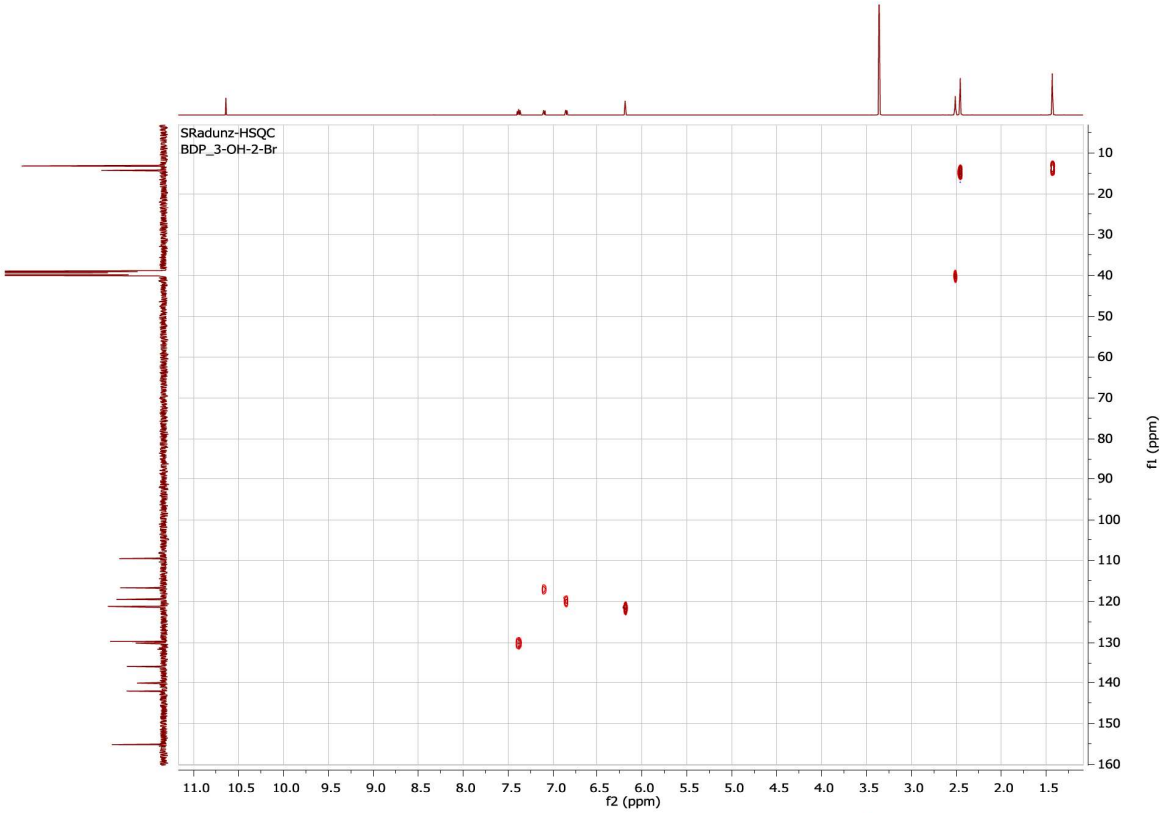
SRadunz-HSQC
BDP_3-OH-2-Br
f2 (ppm)
f1 (ppm)

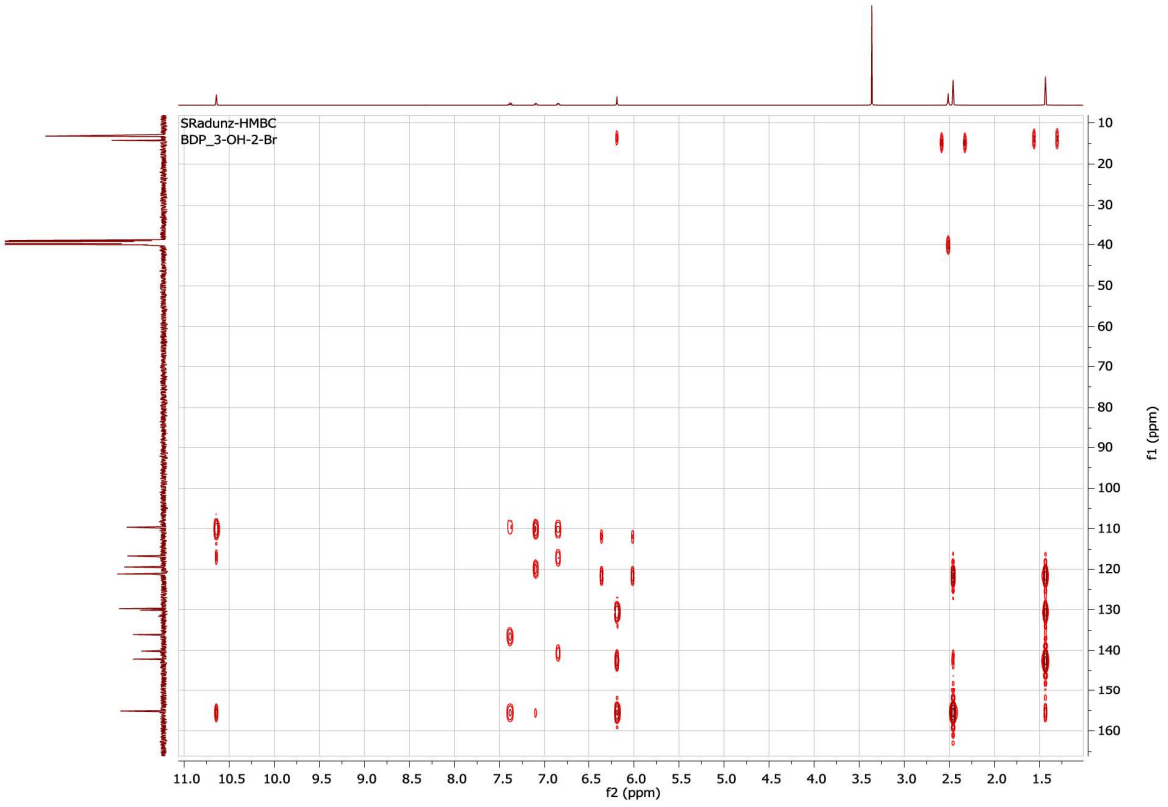
SRadunz-HMBC
BDP_3-OH-2-Br
f2 (ppm)
f1 (ppm)

Compound **8**

4,4-difluoro-1,3,5,7-tetramethyl-8-(2-bromo-5-hydroxyphenyl)-bora-3a,4a-diaza-s-indacene

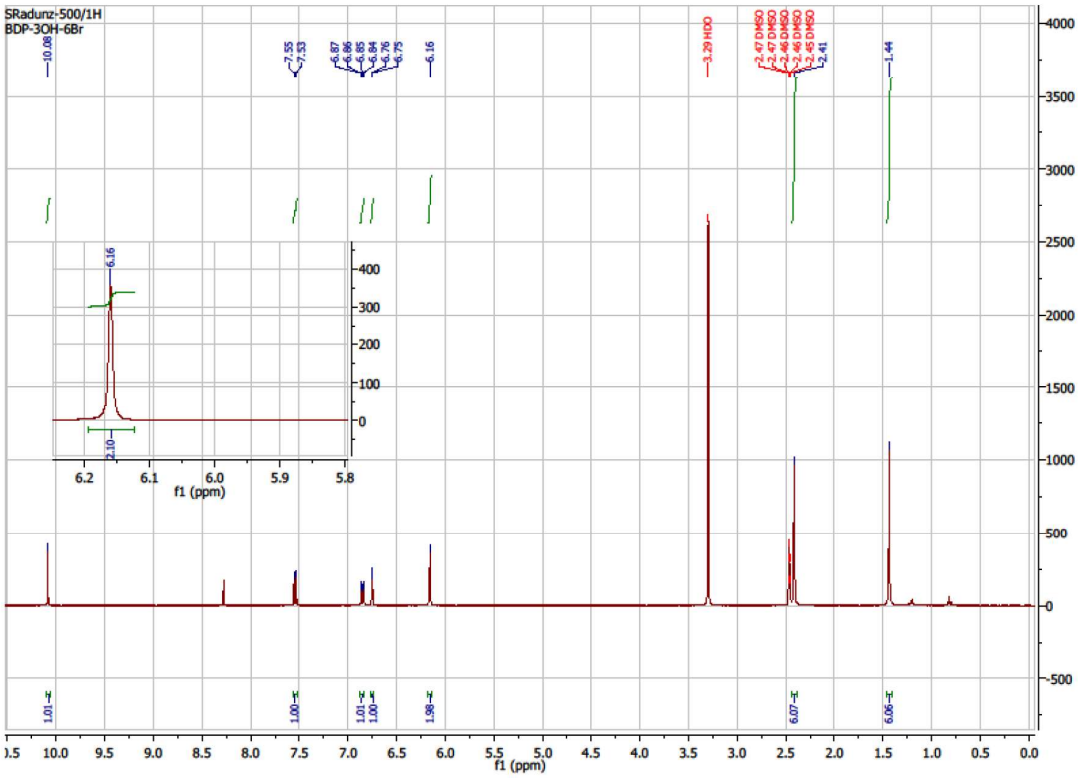

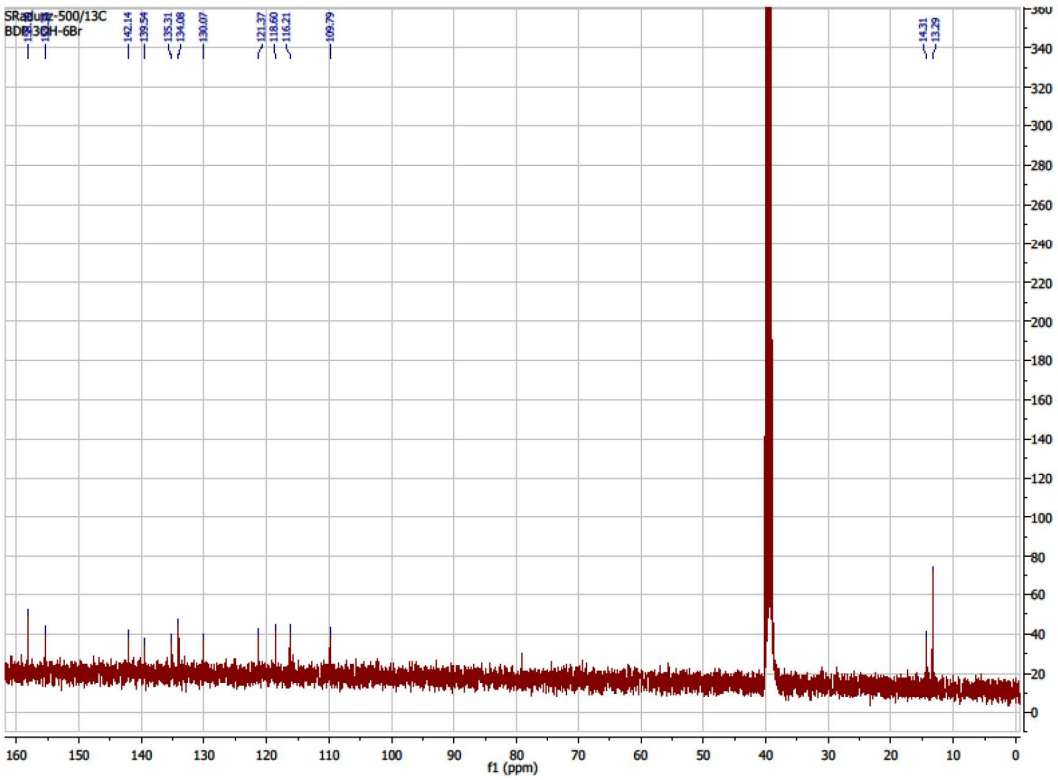

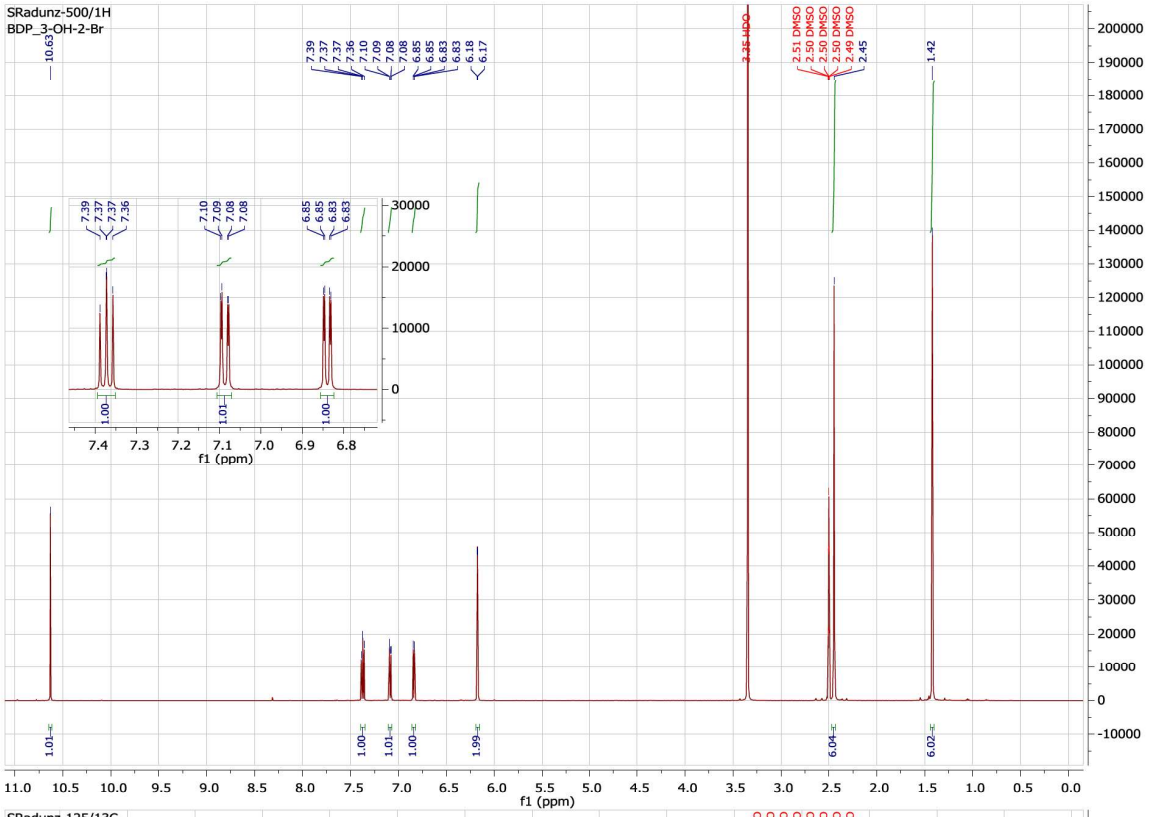
SRadunz-500/1H
BDP_3-OH-2-Br
10.63
7.39
7.37
7.37
7.36
7.10
7.09
7.08
7.08
6.85
6.85
6.83
6.83
6.18
6.17
3.35 HDO
2.51 DMSO
2.50 DMSO
2.50 DMSO
2.50 DMSO
2.49 DMSO
2.45
1.42
1.01
1.00
1.01
1.00
1.99
6.04
6.02
f1 (ppm)

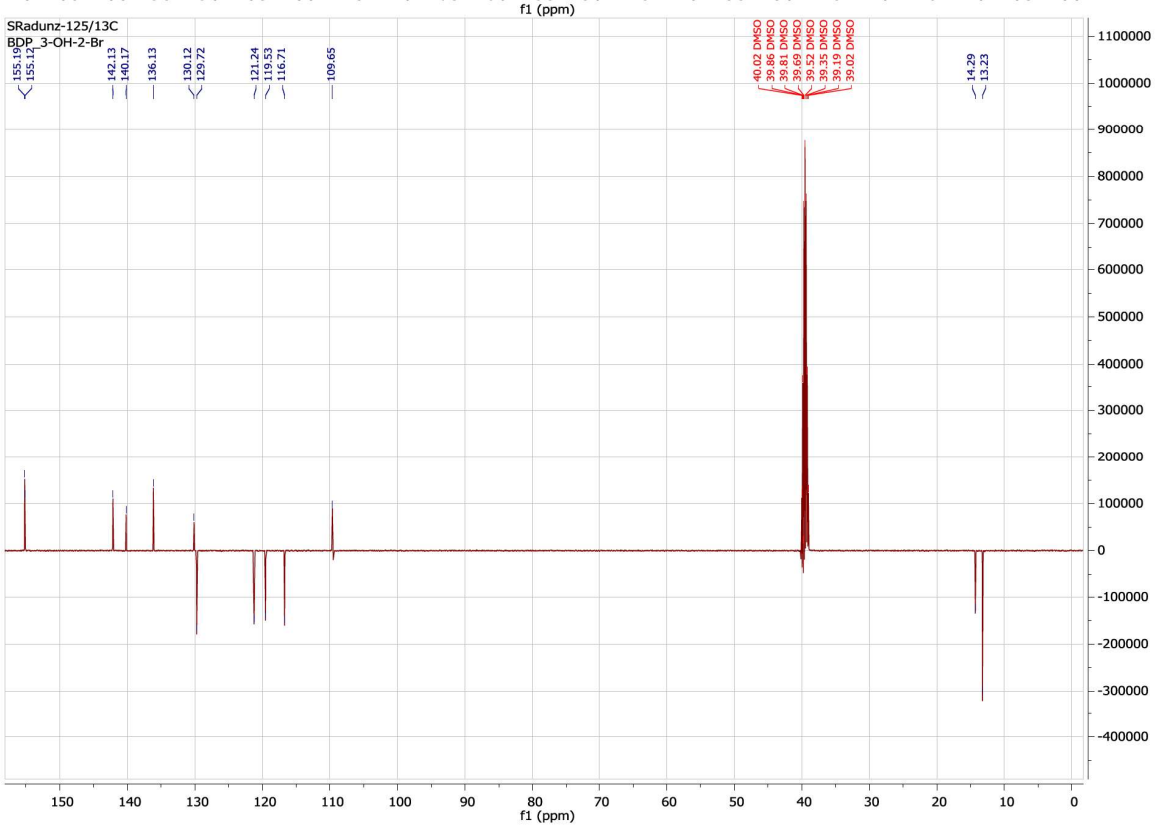
SRadunz-125/13C
BDP_3-OH-2-Br
155.14
155.12
142.13
140.17
136.13
130.12
129.72
121.24
119.53
116.71
109.65
40.02 DMSO
39.86 DMSO
39.81 DMSO
39.69 DMSO
39.52 DMSO
39.35 DMSO
39.19 DMSO
39.02 DMSO
14.29
13.23
f1 (ppm)

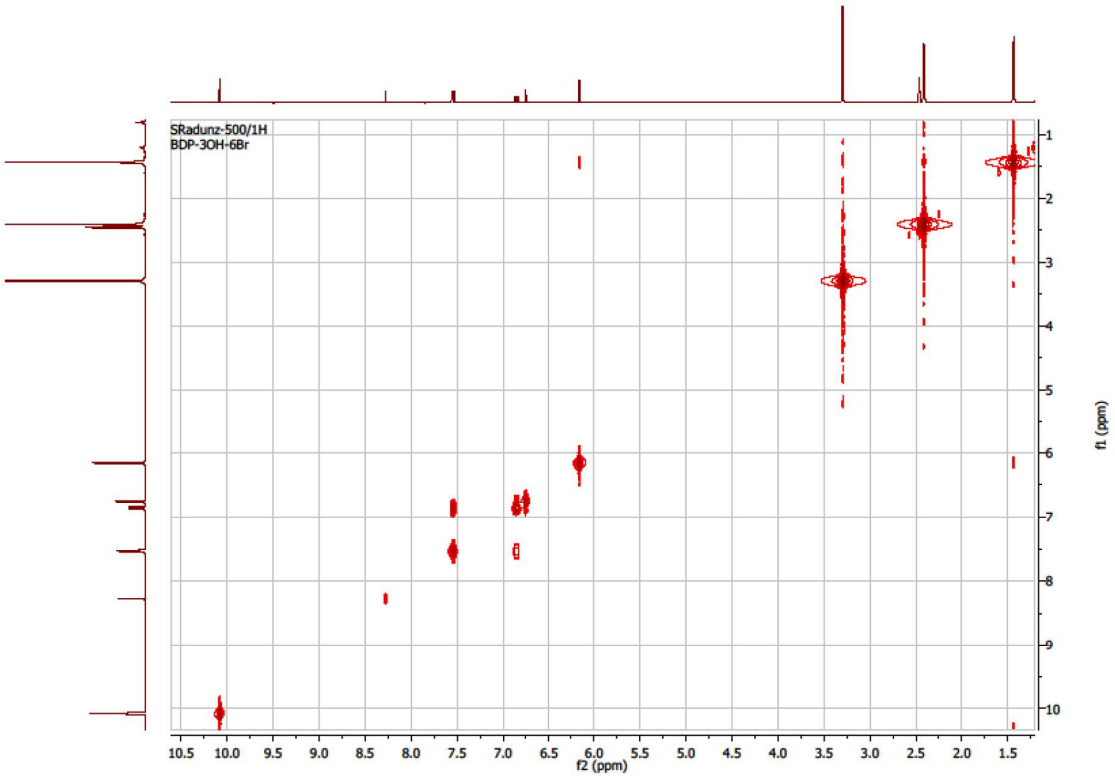
SRadunz-500/1H
BDP-3OH-6Br
f2 (ppm)
f1 (ppm)

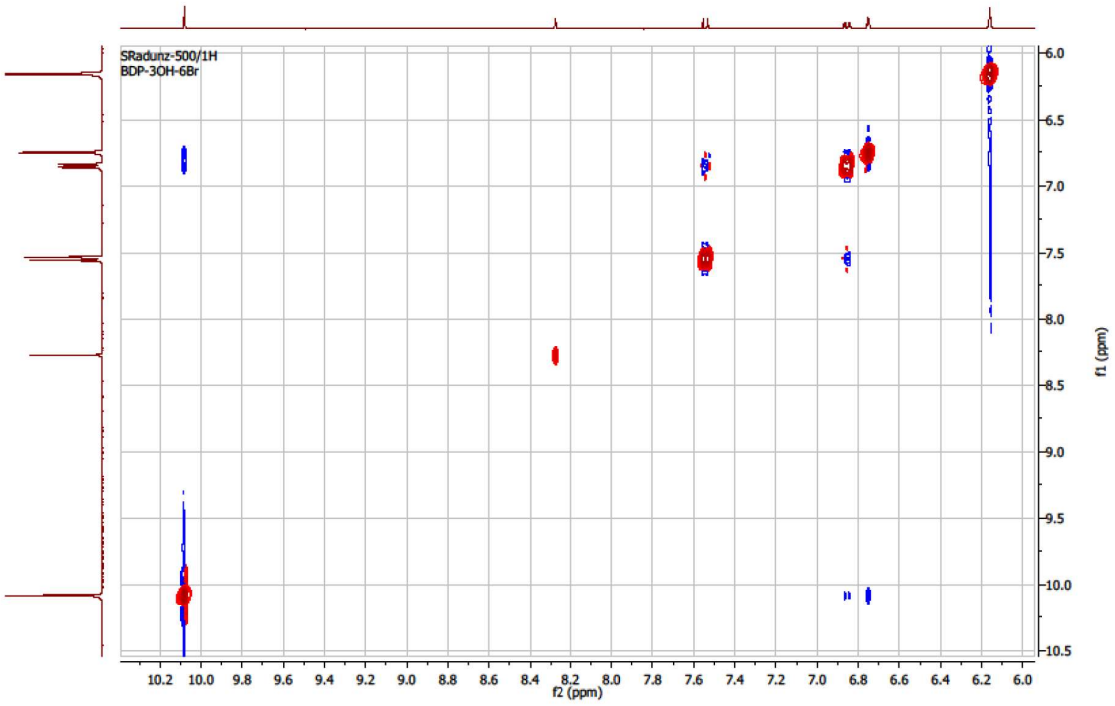
SRadunz-500/1H
BDP-3OH-6Br
f2 (ppm)
f1 (ppm)

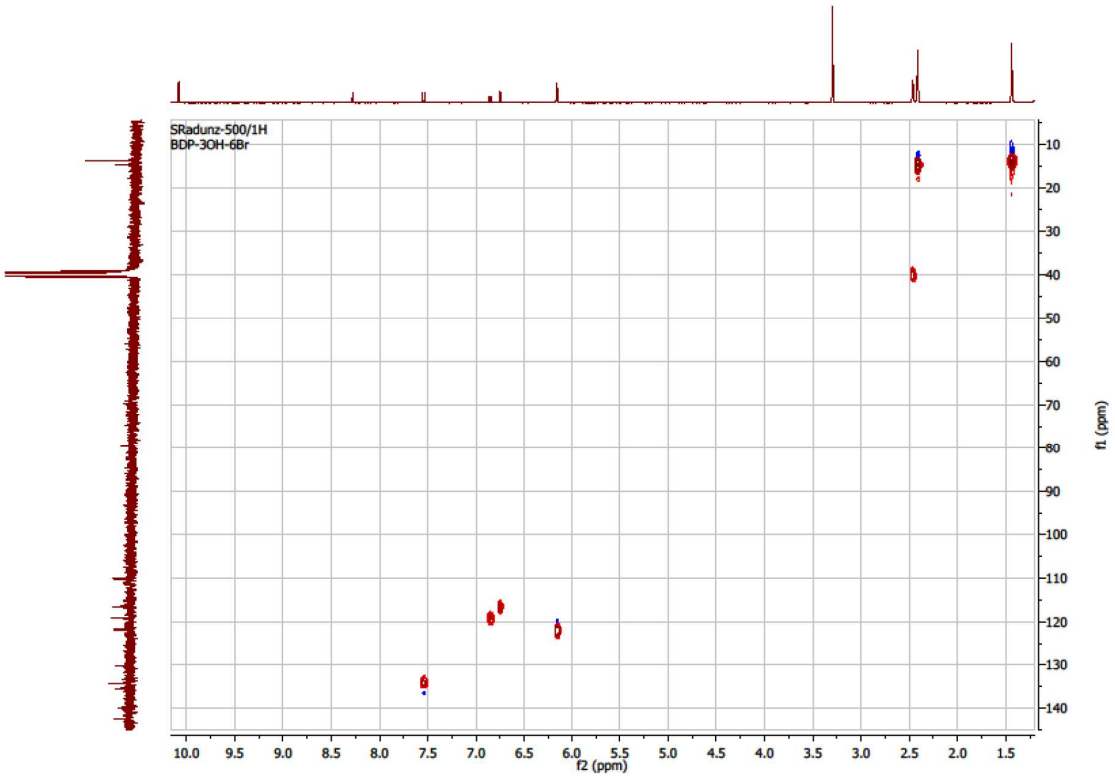
SRadunz-500/1H
BDP-3OH-6Br
f2 (ppm)
f1 (ppm)

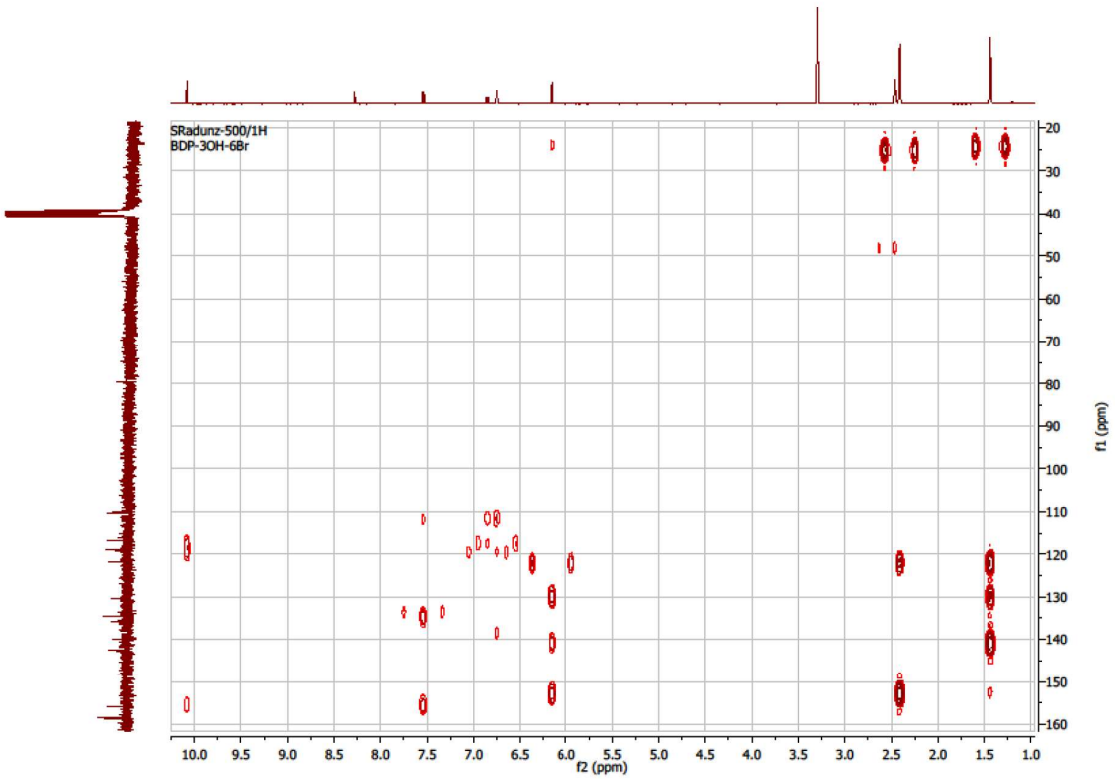
SRadunz-500/1H
BDP-3OH-6Br
f2 (ppm)
f1 (ppm)

Compound **9**

4,4-difluoro-1,3,5,7-tetramethyl-8-(2,6-dibromo-3-hydroxyphenyl)-bora-3a,4a-diaza-s-indacene

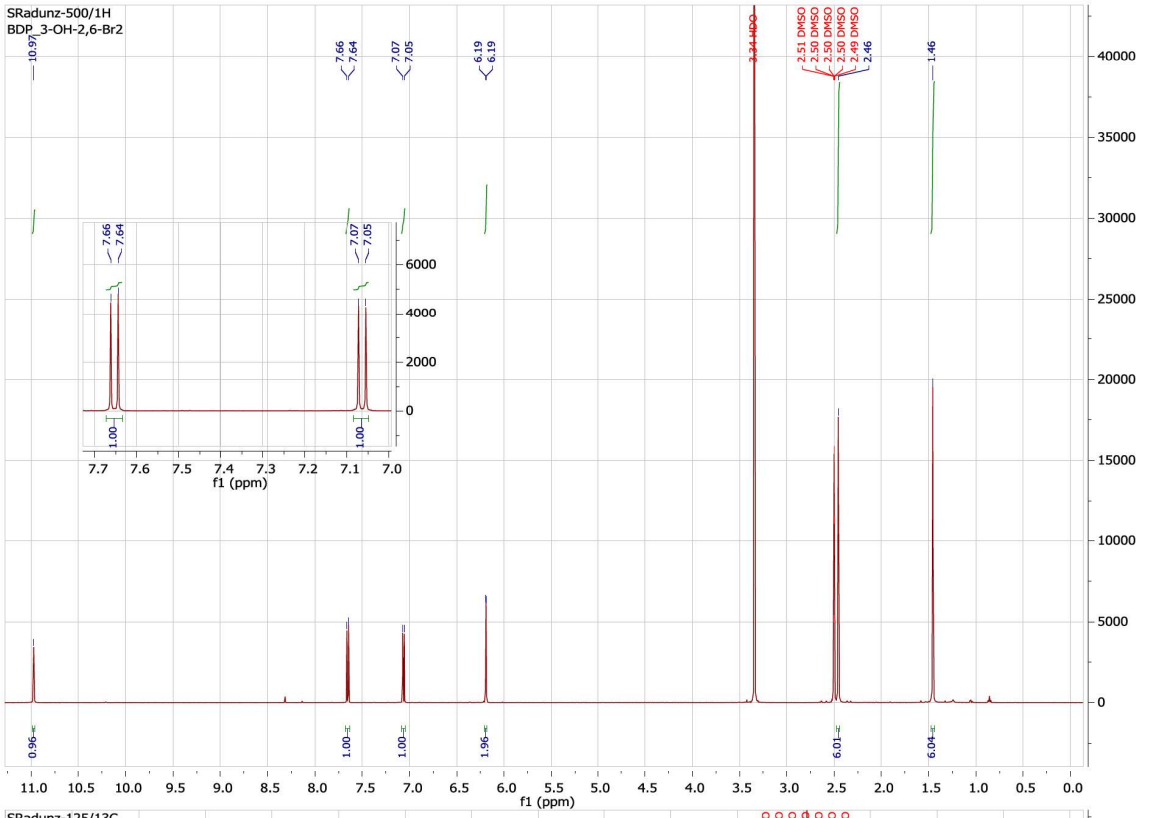

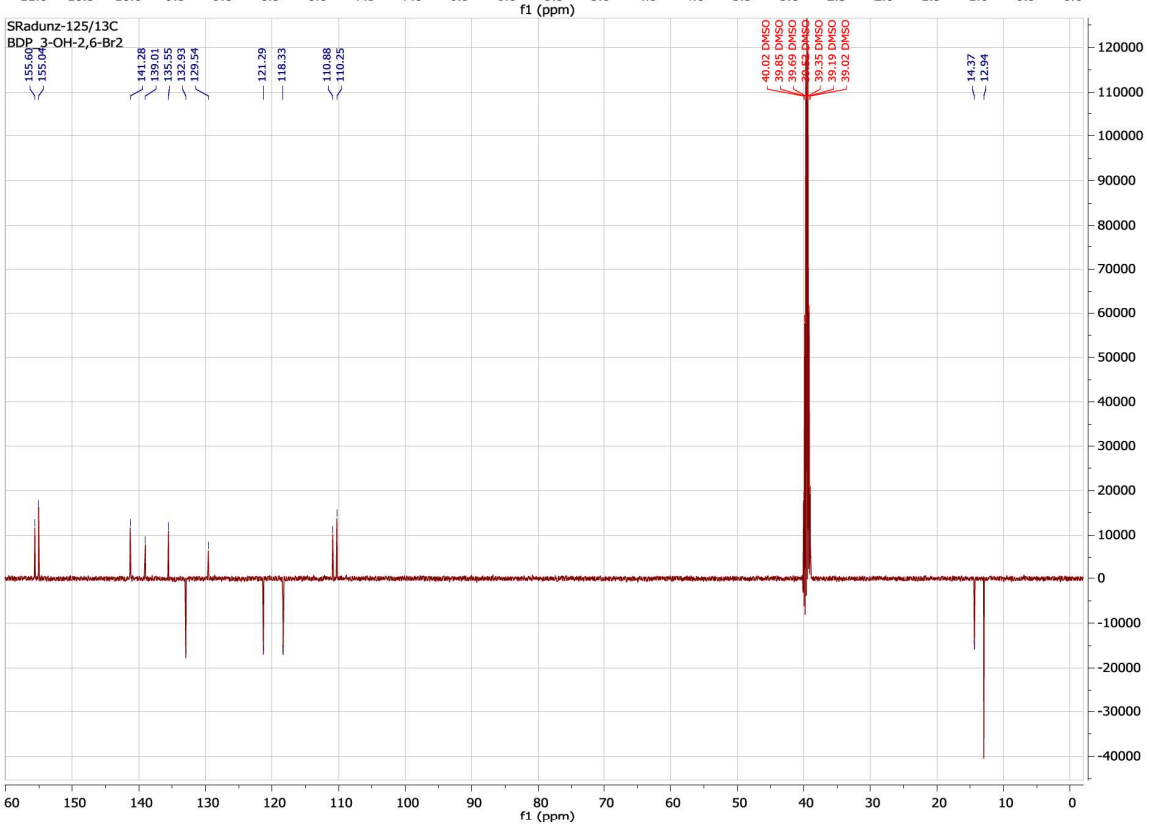

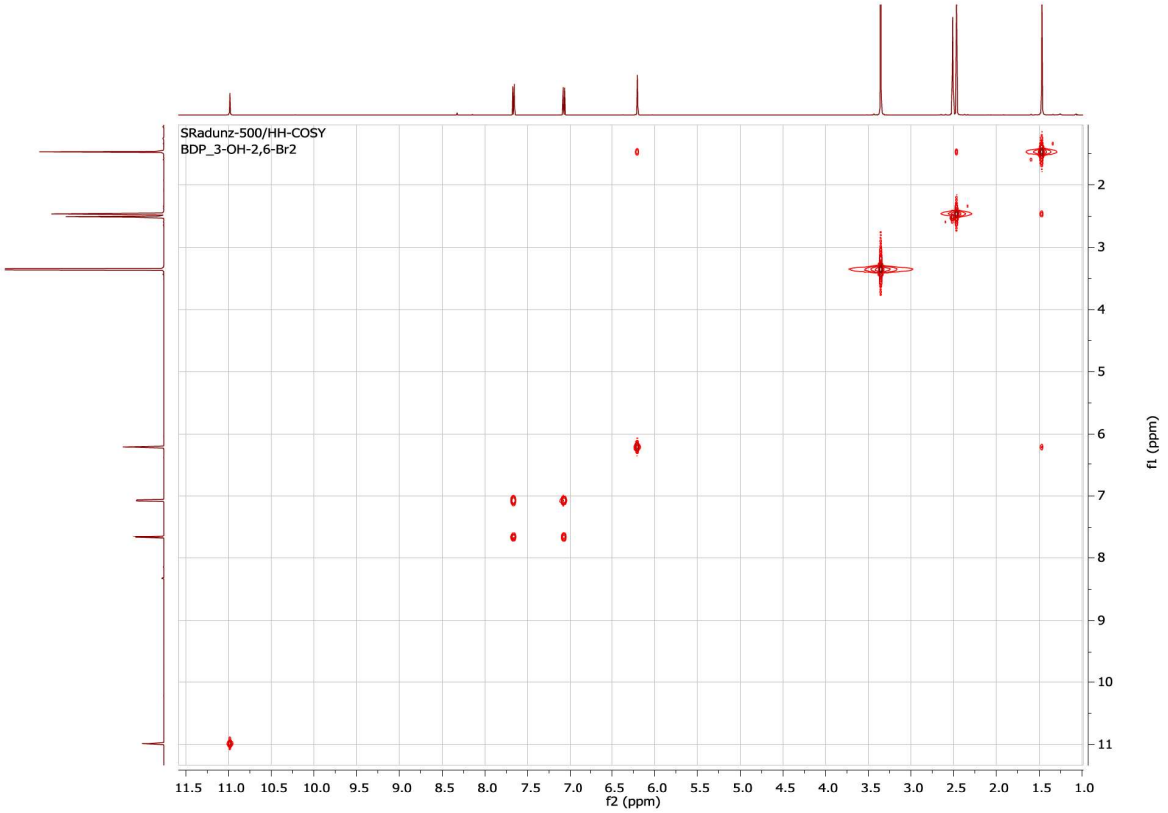
SRadunz-500/HH-COSY
BDP_3-OH-2,6-Br2
f2 (ppm)
f1 (ppm)

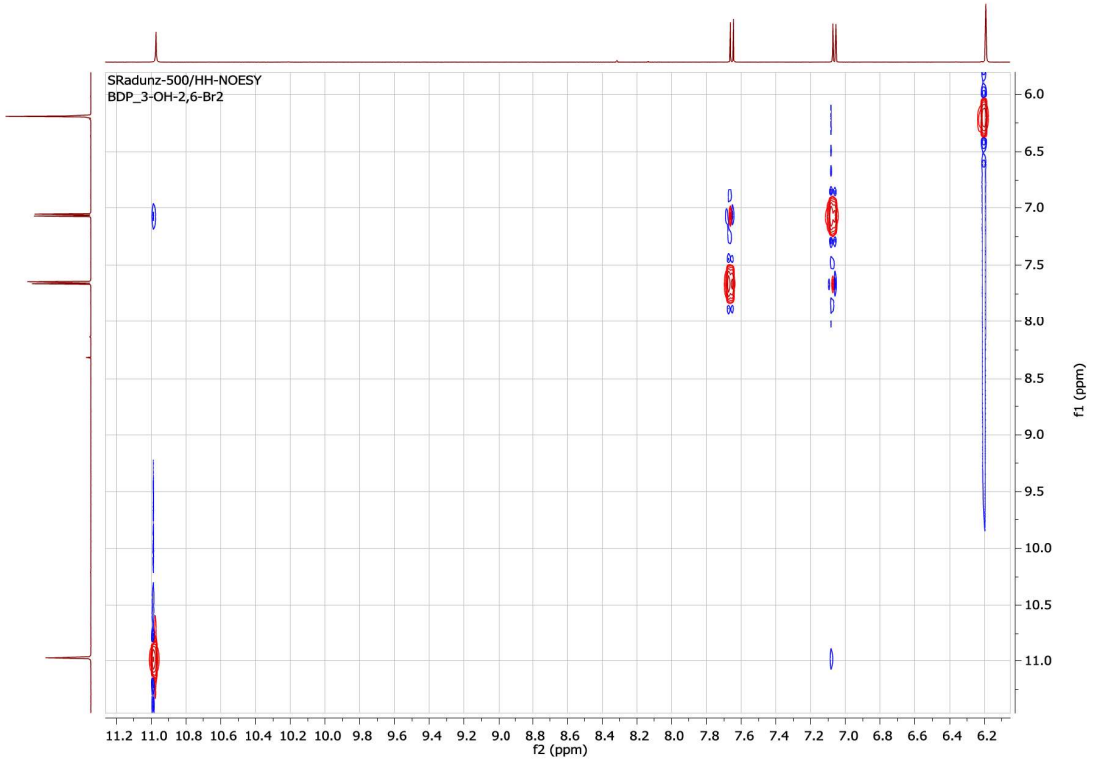
SRadunz-500/HH-NOESY
BDP_3-OH-2,6-Br2
f2 (ppm)
f1 (ppm)

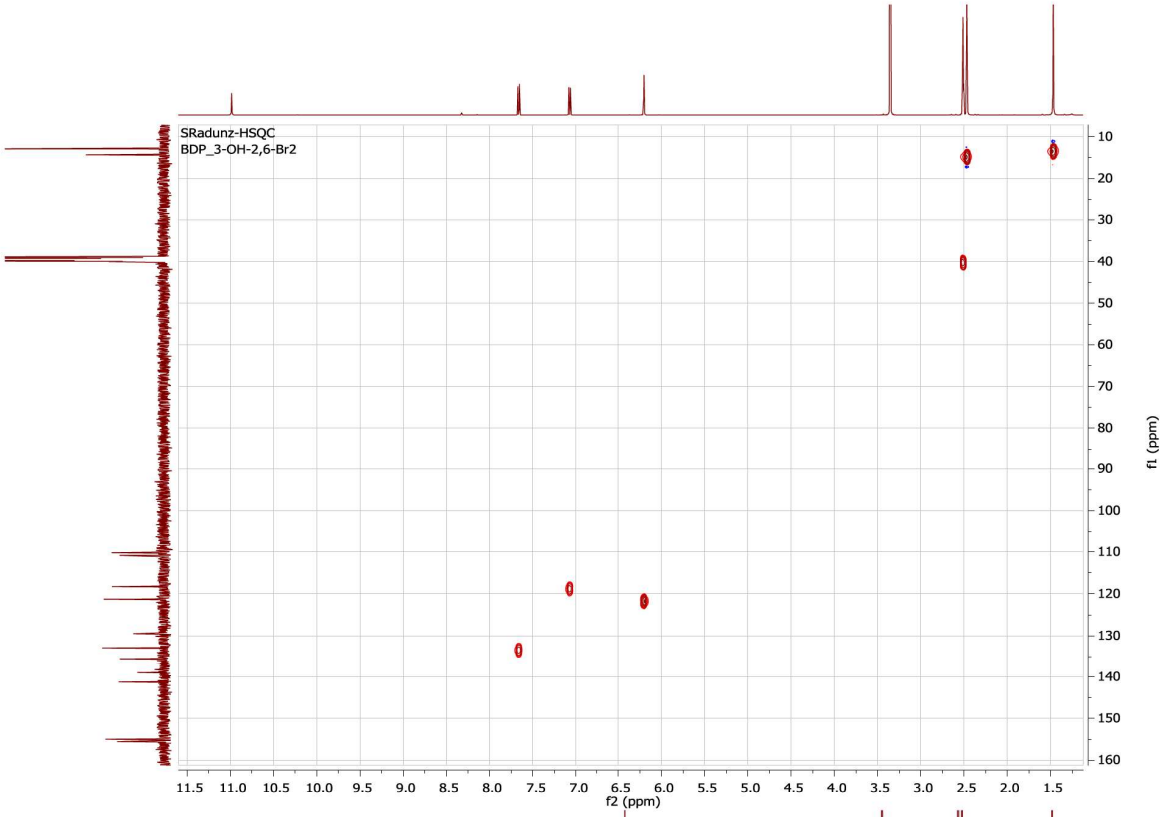
SRadunz-HSQC
BDP_3-OH-2,6-Br2
f2 (ppm)
f1 (ppm)

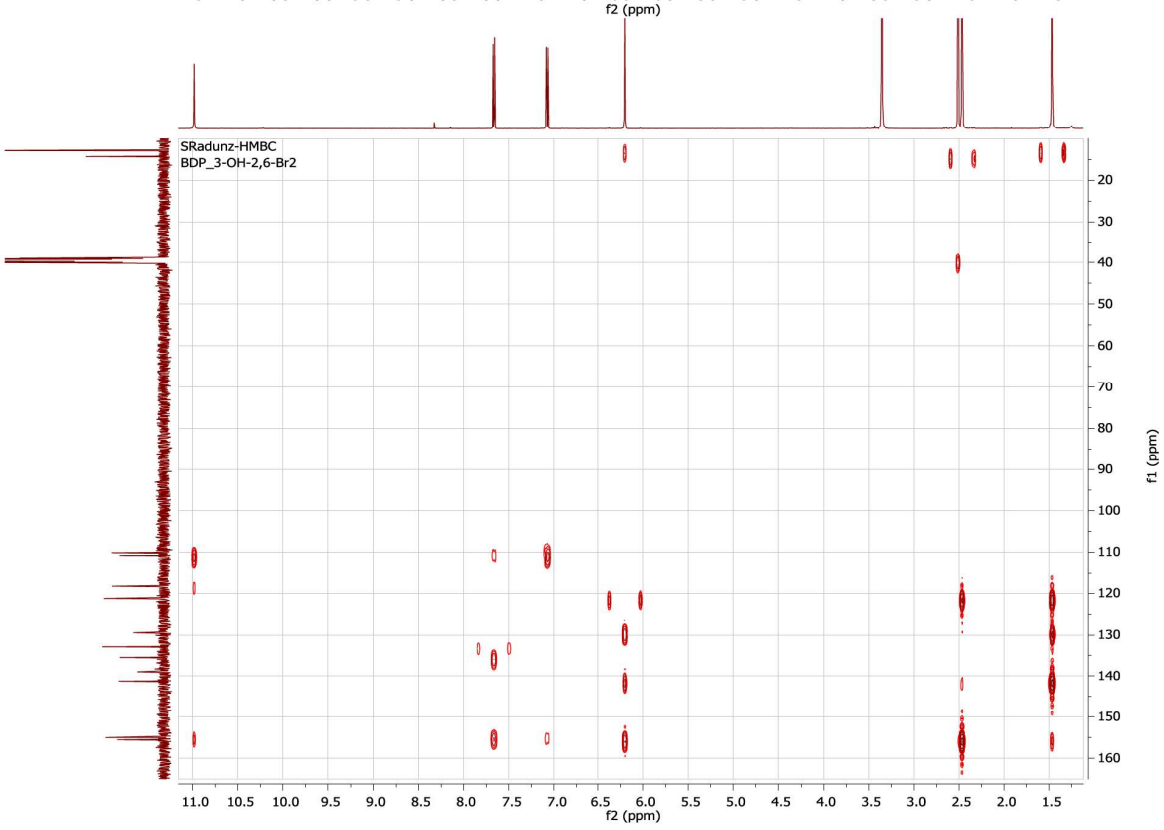
SRadunz-HMBC
BDP_3-OH-2,6-Br2
f2 (ppm)
f1 (ppm)

Compound **10**

4,4-difluoro-1,3,5,7-tetramethyl-8-(2,4,6-tribromo-3-hydroxyphenyl)-bora-3a,4a-diaza-s-indacene

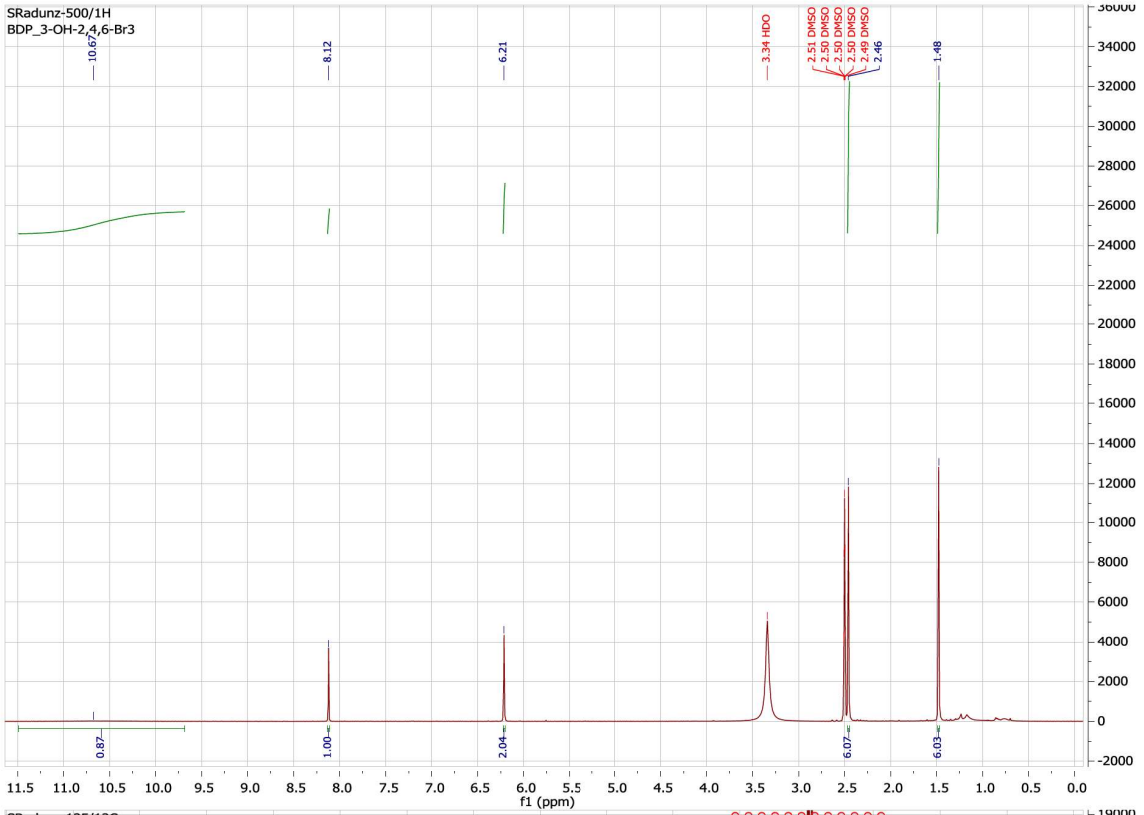

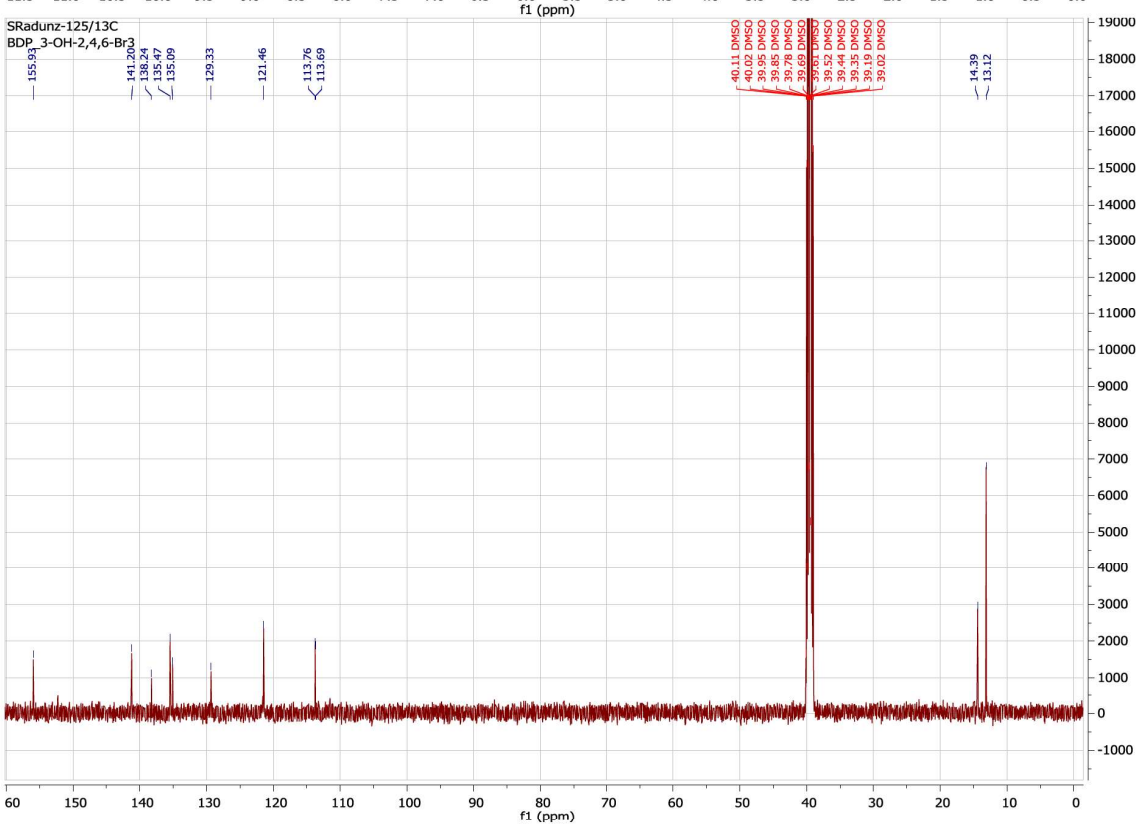

Data and Spectra from Optical Spectroscopy

Table S1: Overview over the photophysical properties of the synthesized BODIPY dyes.

Dye	ε (λ_{max}) (MeOH) [$M^{-1}cm^{-1}$]	$\lambda_{em\text{-}acid}$ (MeOH) [nm]	Φ_f (MeOH) (relative) [%]	Φ_f (MeOH) (absolute) [%]	τ_f (MeOH) [ns][b]	k_r[c] [10^8 s^{-1}]	k_{nr}[c] [10^8 s^{-1}]	pK_a (em)[d]	pK_a (em)[e]
1	86700 (497)	504.5	0.50 ± 0.03	0.46 ± 0.05	2.97 ± 0.02	1.68 ± 0.11	1.68 ± 0.09	10.75	9.90
2	78000 (499)	507.5	0.54 ± 0.03	0.51 ± 0.05	3.49 ± 0.02	1.55 ± 0.10	1.32 ± 0.08	8.99	8.27
3	86400 (502) [a]	510.5	0.57 ± 0.03 [a]	0.54 ± 0.05 [a]	3.69 [a] ± 0.03	1.54 ± 0.09	1.17 ± 0.07	6.98	5.78
4	87200 (499)	507.5	0.52 ± 0.03	0.50 ± 0.05	3.41 ± 0.03	1.52 ± 0.10	1.41 ± 0.08	8.93	8.13
5	86300 (502) [a]	510.5	0.56 ± 0.03 [a]	0.53 ± 0.05 [a]	3.67 [a] ± 0.02	1.53 ± 0.09	1.20 ± 0.07	6.94	6.01
6	93200 (498)	505.5	0.64 ± 0.03	0.60 ± 0.05	4.29 ± 0.05	1.49 ± 0.08	0.84 ± 0.06	10.31	10.08
7	89800 (503)	511.0	0.93 ± 0.05	0.89 ± 0.05	6.61 ± 0.03	1.41 ± 0.08	0.11 ± 0.07	9.17	8.33
8	85700 (503)	511.0	0.91 ± 0.03	0.90 ± 0.05	6.68 ± 0.02	1.36 ± 0.06	0.14 ± 0.05	9.74	9.65
9	82800 (510) [a]	516.5	0.89 ± 0.04 [a]	0.86 ± 0.05 [a]	6.58 [a] ± 0.02	1.35 ± 0.07	0.17 ± 0.06	8.28	7.52
10	71400 (511) [a]	518.0	0.85 ± 0.03 [a]	0.85 ± 0.05 [a]	6.52 [a] ± 0.02	1.30 ± 0.05	0.23 ± 0.04	6.17	5.27

[a] For the protonated form: further addition of 5 µL conc. HCl to 3 ml sample. [b] Mono exponential fit (global analysis f_i (%) = 100.0)).[c] $k_r = \Phi_F / \tau_F$ and $k_{nr} = (1 - \Phi_F) / \tau_F$. [d] (MeOH/H2O 2/1 vol%, 25 mM buffered solution). [e] Incorporated in D4-hydrogel, treated with 25 mM buffer)

Table S2: Fitting parameters using normalized fluorescence emission spectral data λ_{Emmax}.

BODIPY dye	A1	A2	$LOGx_0$	P	R
1	-0.023 ± 0,017	0.999 ± 0,008	10.751 ± 0.025	-0.837 ± 0.038	0.9983
2	0.001 ± 0,001	1.001 ± 0,002	8.987 ± 0.004	-0.886 ± 0.007	0.9999
3	0.005 ± 0,004	1.007 ± 0,004	6.977 ± 0.012	-0.966 ± 0.022	0.9998
4	0.002 ± 0.002	1.006 ± 0.003	8.927 ± 0.007	-0.900 ± 0.011	0.9998
5	0.004 ± 0.002	1.000 ± 0.002	6.939 ± 0.005	-0.965 ± 0.010	0.9999
6	0.006 ± 0.007	1.005 ± 0.005	10.314 ± 0.014	-1.033 ± 0.028	0.9994
7	-0.002 ± 0.008	1.006 ± 0.007	9.172 ± 0.018	-0.871 ± 0.031	0.9991
8	-0.004 ± 0.007	0.999 ± 0.006	9.744 ± 0.014	-0.907 ± 0.025	0.9990
9	-0.002 ± 0.005	0.998 ± 0.004	8.284 ± 0.011	-0.878 ± 0.019	0.9993
10	-0.004 ± 0.007	0.987 ± 0.007	6.170 ± 0.015	-0.970 ± 0.031	0.9984

Table S3: Equations used for sigmoidal curve fitting of pH titration experiments.

Model	Dose response	BiDose response
Equation	$y = A1 + \frac{A2 - A1}{1 + 10^{(LOGx_0 - x)p}}$	$y = A1\,(A2 - A1)\left[\frac{h}{1 + 10^{(LOGx_{01} - x)p1}} + \frac{1 - h}{1 + 10^{(LOGx_{02} - x)p2}}\right]$

*Table S4: Fitting parameters of broad-range sensor containing BODIPY dyes **1**, **2**, **3** and **9**.*

A1	A2	$LOGx_1$	$LOGx_2$	P1	P2	h	R
-1.589 ± 0.904	159.379 ± 0.537	6.532 ± 0.055	9.821 ± 0.092	-0.663 ± 0.030	-0.518 ± 0.039	0.519 ± 0.029	0.9996

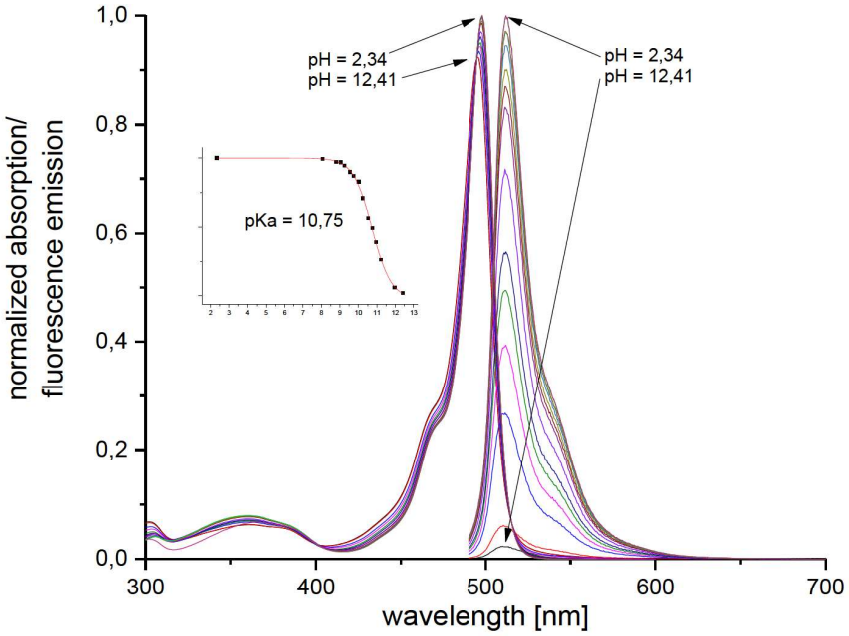

*Figure S1: pH-titration of **1** (6,47 * 10^{-6} mol/l) in a water-methanol mixture (H_2O/MeOH 1/2 vol%) containing buffered (borate-citrate buffer 25 mM).*

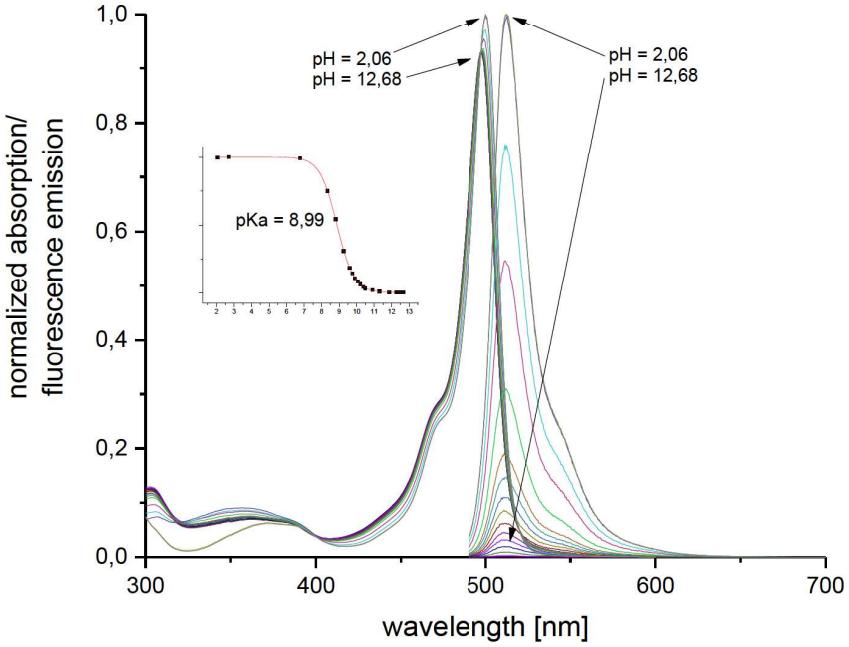

*Figure S2: pH-titration of **2** (5,51 * 10^{-6} mol/l) in a water-methanol mixture (H_2O/MeOH 1/2 vol%) containing buffered (borate-citrate buffer 25 mM).*

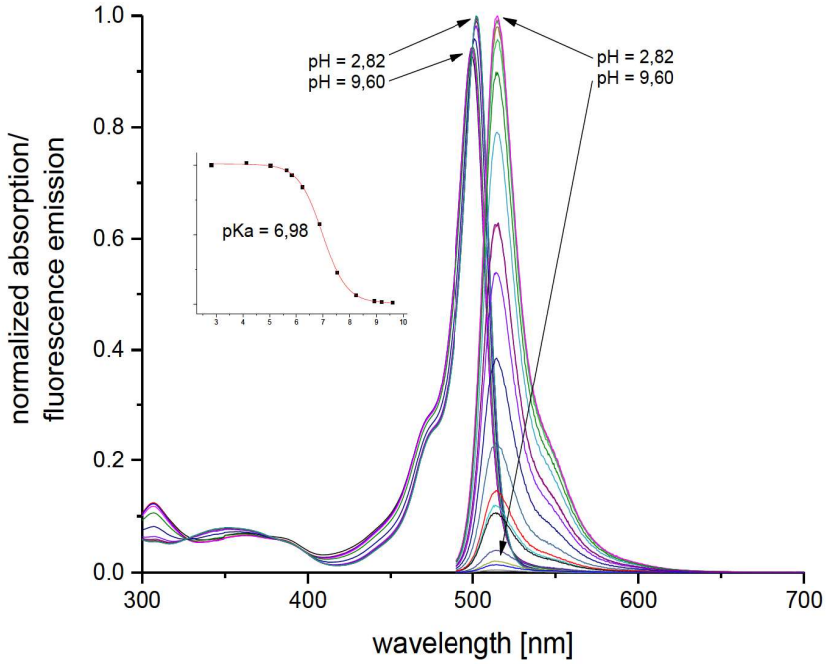

*Figure S3: pH-titration of **3** (4,52 * 10^{-6} mol/l) in a water-methanol mixture (H_2O/MeOH 1/2 vol%) containing buffered (borate-citrate buffer 25 mM).*

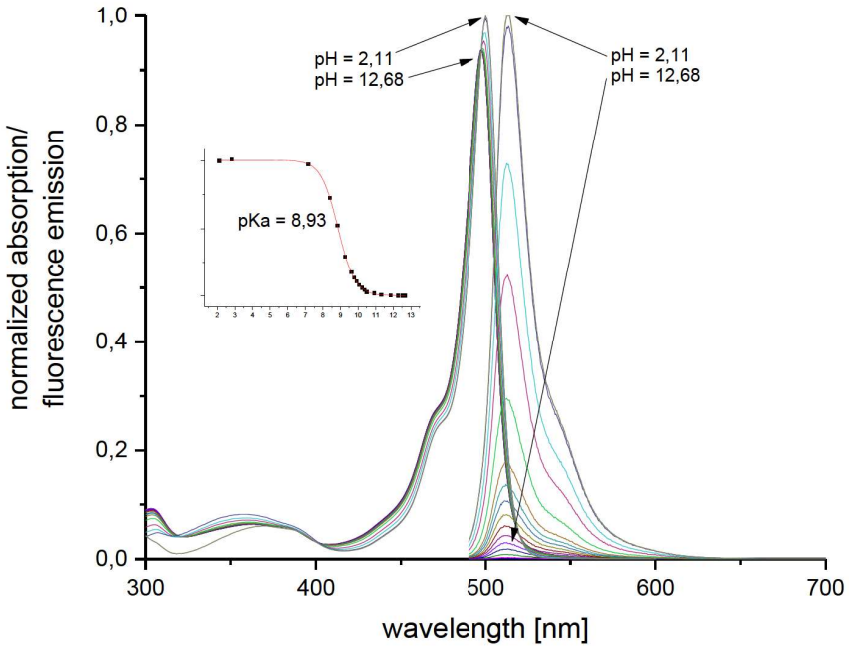

*Figure S4: pH-titration of **4** (5,74 * 10^{-6} mol/l) in a water-methanol mixture (H_2O/MeOH 1/2 vol%) containing buffered (borate-citrate buffer 25 mM).*

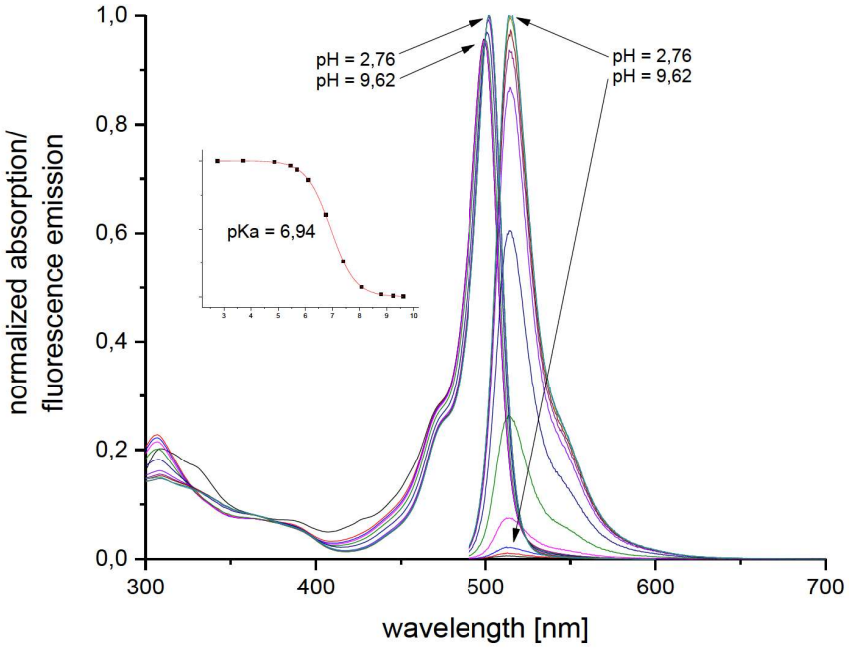

*Figure S5: pH-titration of **5** (6,68 * 10^{-6} mol/l) in a water-methanol mixture (H_2O/MeOH 1/2 vol%) containing buffered (borate-citrate buffer 25 mM).*

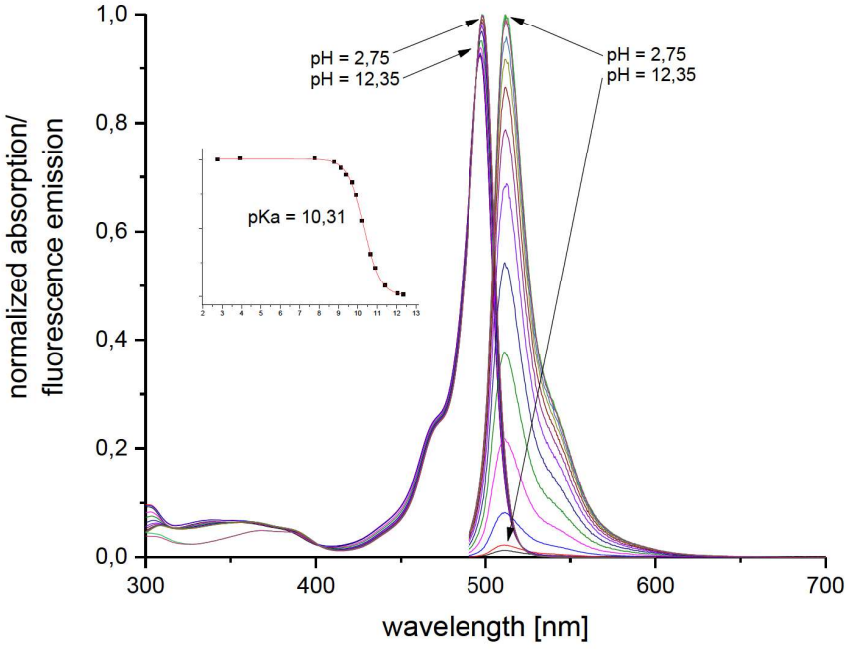

*Figure S6: pH-titration of **6** (7,26* 10^{-6} mol/l) in a water-methanol mixture (H_2O/MeOH 1/2 vol%) containing buffered (borate-citrate buffer 25 mM).*

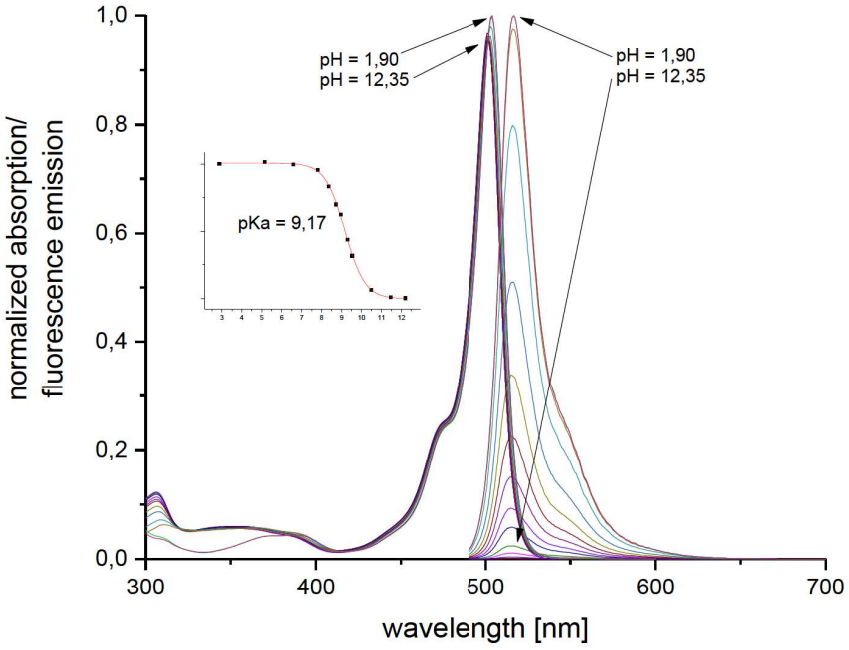

*Figure S7: pH-titration of **7** (6,18 * 10^{-6} mol/l) in a water-methanol mixture (H_2O/MeOH 1/2 vol%) containing buffered (borate-citrate buffer 25 mM).*

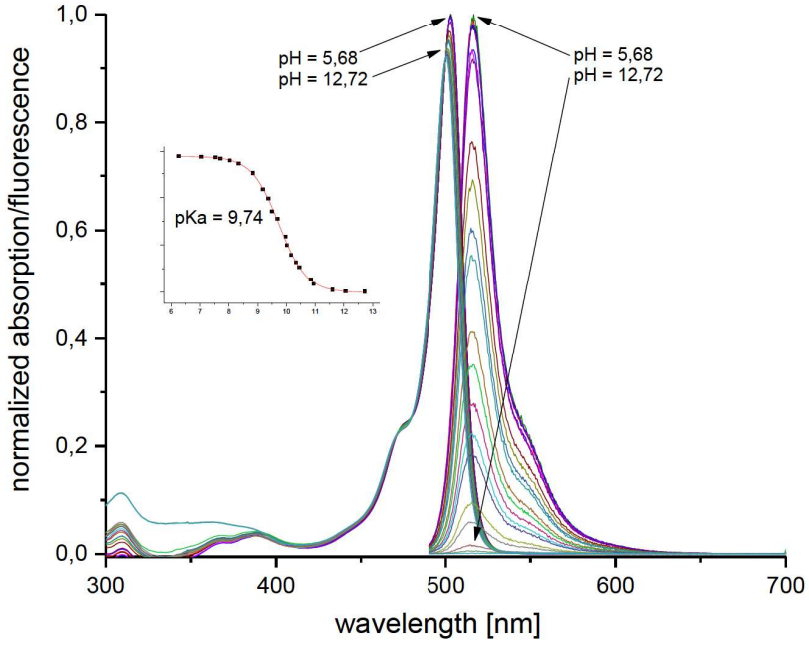

*Figure S8: pH-titration of **8** (7,41 * 10^{-6} mol/l) in a water-methanol mixture (H_2O/MeOH 1/2 vol%) containing buffered (borate-citrate buffer 25 mM).*

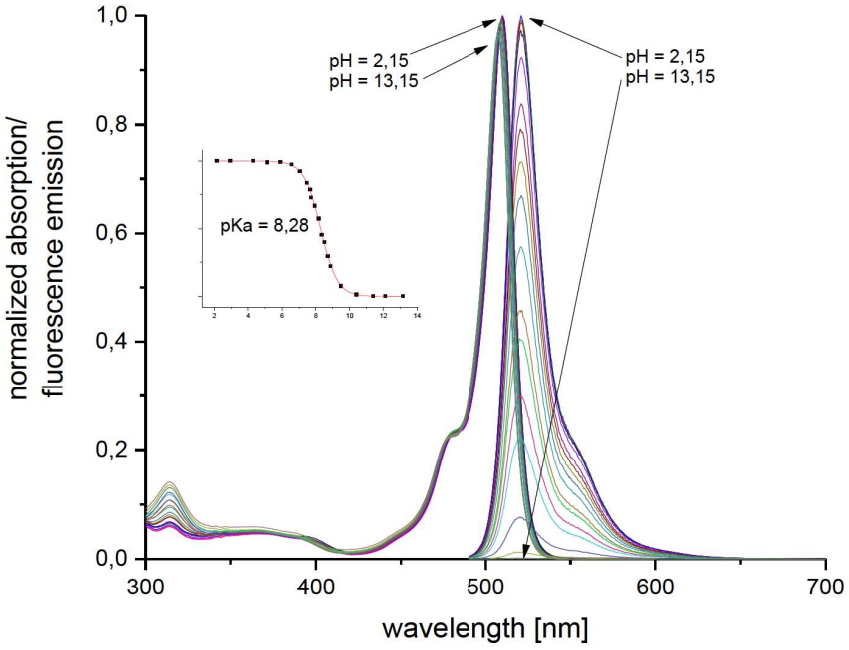

*Figure S9: pH-titration of **9** (4,36 * 10^{-6} mol/l) in a water-methanol mixture (H_2O/MeOH 1/2 vol%) containing buffered (borate-citrate buffer 25 mM).*

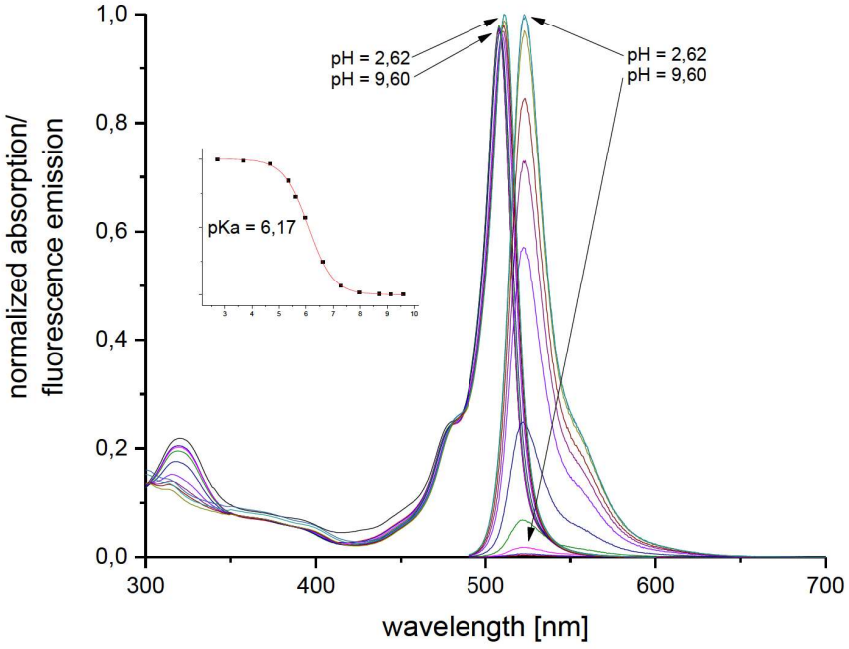

Figure S 1

*Figure S10: pH-titration of **10** (4,59 * 10^{-6} mol/l) in a water-methanol mixture (H_2O/MeOH 1/2 vol%) containing buffered (borate-citrate buffer 25 mM).*

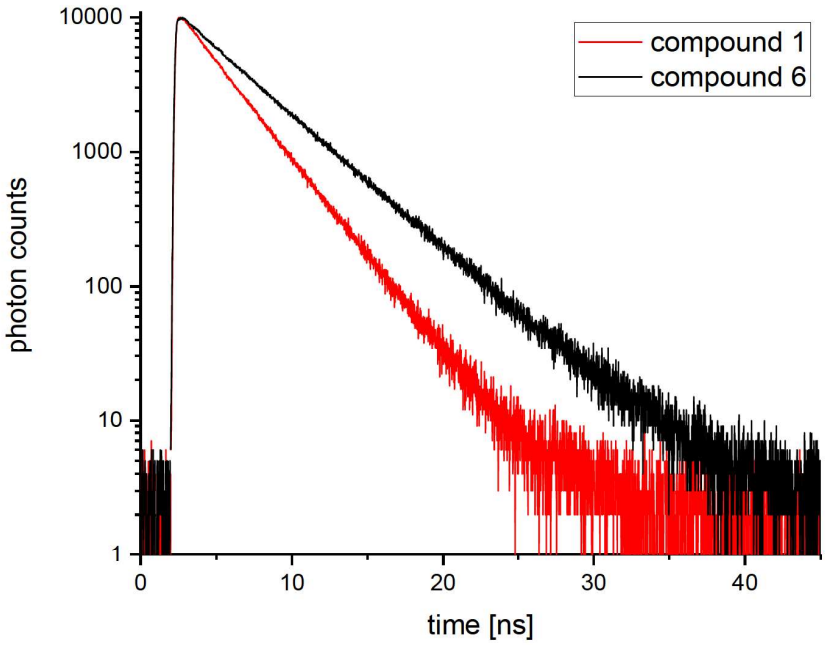

*Figure S11: Fluorescence decay curves of unhalogenated compounds **1** and **6**.*

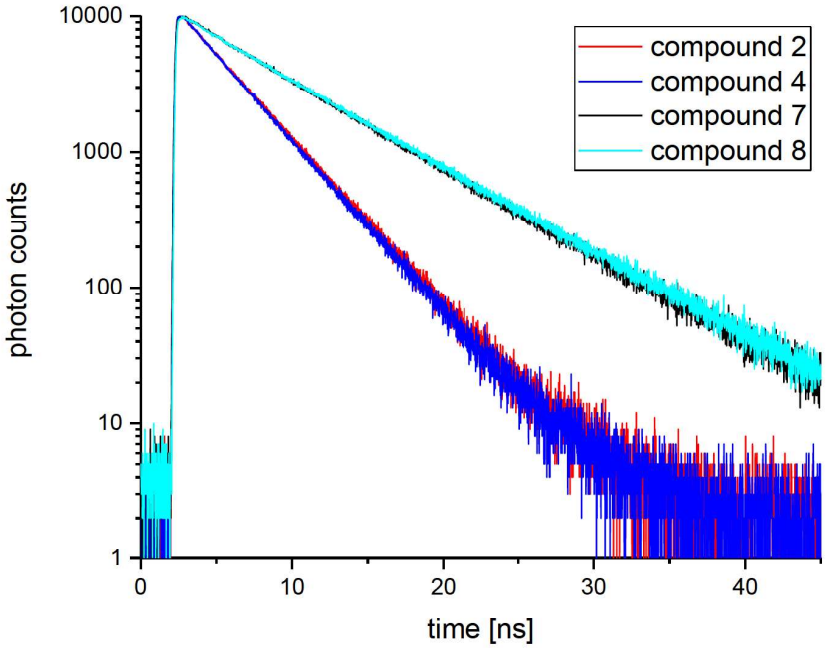

*Figure S12: Fluorescence decay curves of mono-halogenated compounds **2**, **4**, **7** and **8**.*

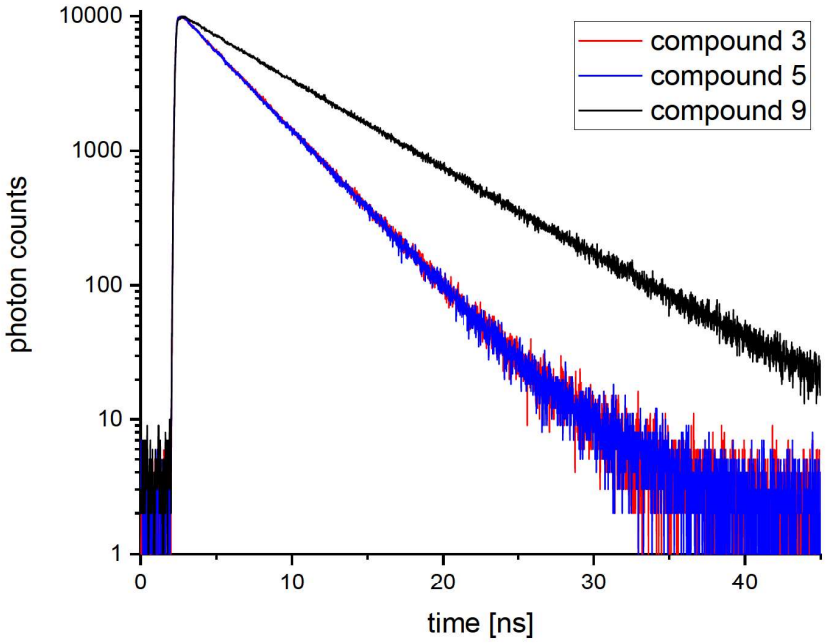

*Figure S13: Fluorescence decay curves of di-halogenated compounds **3**, **5** and **9**.*

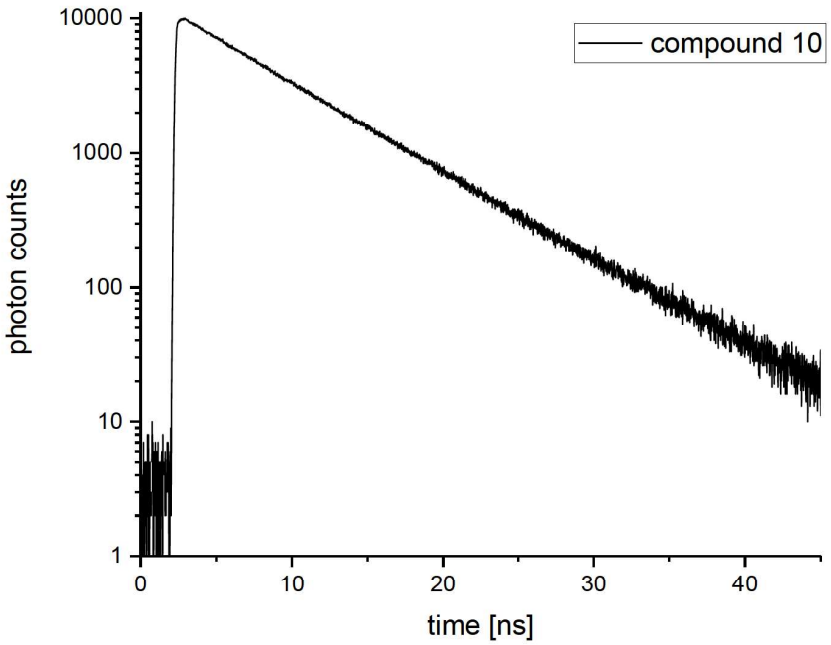

*Figure S14 Fluorescence decay curve of tri-halogenated compound **10**.*

Photostability

Table S5: Half-life of the dyes upon illumination.

dye	$t_{1/2}$ [min]
1	5296
2	5142
3	1097
4	5878
5	1105
6	3687
7	2442
8	2564
9	2572
10	2879
FL27	1041
6-FAM	532

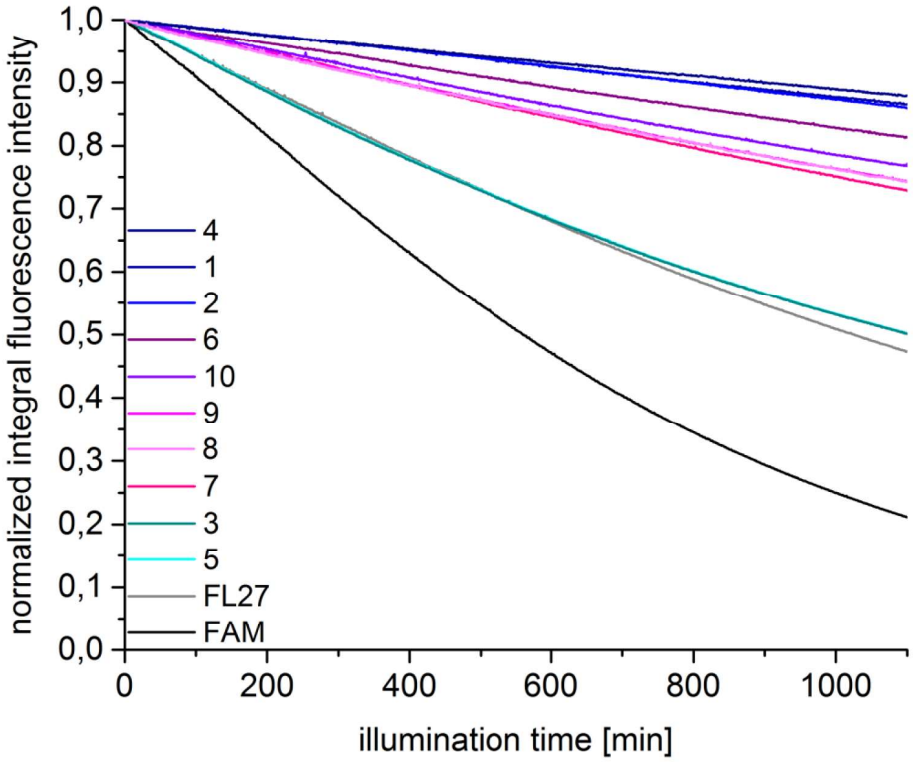

*Figure S15: Photostability of compounds **1** – **10** compared to fluoresceins FL27 and 6-FAM.*

1 C. Würth, M. Grabolle, J. Pauli, M. Spieles and U. Resch-Genger, *Nat. Protocols*, 2013, **8**, 1535-1550.
2 M. Baruah, W. Qin, N. Basarić, W. M. De Borggraeve and N. Boens, *J. Org. Chem.*, 2005, **70**, 4152-4157.
3 T. Werner, C. Huber, S. Heinl, M. Kollmannsberger, J. Daub and S. O. Wolfbeis, *Fresenius' J. Anal. Chem.*, 1997, **359**, 150-154.
4 L. C. D. de Rezende and F. da Silva Emery, *Orbital: Electron. J. Chem.*, 2013, **5**, 62-83.
5 N. Boens, V. Leen and W. Dehaen, *Chem. Soc. Rev.*, 2012, **41**, 1130-1172.
6 A. Loudet and K. Burgess, *Chem. Rev.*, 2007, **107**, 4891-4932.
7 I. Saikia, A. J. Borah and P. Phukan, *Chem. Rev.*, 2016, **116**, 6837-7042.

2.2 Temperature- and Structure-Dependent Optical Properties and Photophysics of BODIPY Dyes

Sebastian Radunz, Werner Kraus, Florian Bischoff, Harald Rune Tschiche, Ute Resch-Genger*

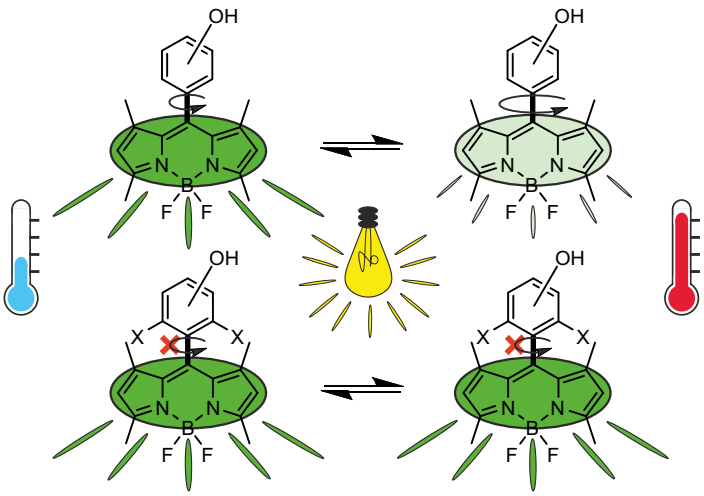

Figure 13: Reprinted with permission from S. Radunz *et al.*.[257] Copyright 2020 American Chemical Society

In this publication S. Radunz established the concept, the synthesis and the analytical and spectroscopic characterization of the reported compounds. He performed most experiments and data evaluations as well as he performed most of the scientific interpretation of the results. The publication was mainly conceived and written by him.

The following articles is reproduced with permission from S. Radunz, W. Kraus, F. A. Bischoff, F. Emmerling, H. R. Tschiche, U. Resch-Genger, *The Journal of Physical Chemistry A* **2020**, *124*, 1789–1797. Copyrigth 2020 American Chemical Society.

THE JOURNAL OF PHYSICAL CHEMISTRY A

pubs.acs.org/JPCA Article

Temperature- and Structure-Dependent Optical Properties and Photophysics of BODIPY Dyes

Sebastian Radunz, Werner Kraus, Florian A. Bischoff, Franziska Emmerling, Harald Rune Tschiche, and Ute Resch-Genger*

Cite This: J. Phys. Chem. A 2020, 124, 1787−1797 Read Online

ACCESS | Metrics & More | Article Recommendations | Supporting Information

ABSTRACT: We report on the temperature- and structural-dependent optical properties and photophysics of a set of boron dipyrromethene (BODIPY) dyes with different substitution patterns of their meso-aryl subunit. Single-crystal X-ray diffraction analysis of the compounds enabled a classification of the dyes into a sterically hindered and a unhindered group. The steric hindrance refers to a blocked rotational motion of the aryl subunit around the bond connecting this moiety to the meso-position of the BODIPY core. The energy barriers related to this rotation were simulated by DFT calculations. As follows from the relatively low rotational barrier calculated to about 17 kcal/mol, a free rotation is only possible for sterically unhindered compounds. Rotational barriers of more than 40 kcal/mol determined for the sterically hindered compounds suggest an effective freezing of the rotational motion in these molecules. With the aid of temperature-dependent spectroscopic measurements, we could show that the ability to rotate directly affects the optical properties of our set of BODIPY dyes. This accounts for the strong temperature dependence of the fluorescence of the sterically unhindered compounds which show a drastic decrease in fluorescence quantum yield and a significant shortening in fluorescence lifetime upon heating. The optical properties of the sterically hindered compounds, however, are barely affected by temperature. Our results suggest a nonradiative deactivation of the first excited singlet state of the sterically unhindered compounds caused by a conical intersection of the potential energy surfaces of the ground and first excited state which is accessible by rotation of the meso-subunit. This is in good agreement with previously reported deactivation mechanisms. In addition, our results suggest the presence of a second nonradiative depopulation pathway of the first excited singlet state which is particularly relevant for the sterically hindered compounds.

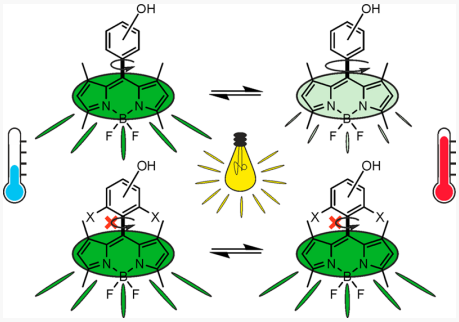

INTRODUCTION

After their first discovery by Treibs and Kreuzer in 1968,[1] 4-bora-3a,4a-diaza-*s*-indacenes (BODIPYs) have become an important class of dyes particularly for the life sciences.[2−7] The continuous development of this class of dyes in the last decades resulted in a steady improvement of synthetic procedures with still ongoing research.[8,9] As a consequence, many new BODIPYs are meanwhile available for applications such as fluorescent probes and sensors,[10−13] bioimaging,[4,6,14] photosensitizers for photodynamic therapy (PDT),[3,15−18] building blocks for artificial photosynthetic models,[19,20] and dye-sensitized solar cells.[21] Advantages of BODIPYs are their high structural versatility in combination with their nowadays comparative ease of preparation and their remarkable photophysical properties such as high molar absorption coefficients, high fluorescence quantum yields (Φ_{Fl}), and high photostability.[2,7,22] At the core of many BODIPY-related studies is the correlation between their structural and photophysical properties,[23−25] aiming, e.g., at the design of sensor molecules or dyes with a bright emission in a specific spectral window, particularly in the long wavelength region. The photophysical properties of most organic dyes including BODIPYs, e.g., their absorption and fluorescence features, are sensitive to their microenvironment. This comprises parameters like temperature, solvent polarity (solvatochromism), solvent proticity (H-bonding capability), and viscosity, which can be exploited for sensing applications.[26−28] Moreover, dyes can also respond to neutral or ionic analytes, although this commonly requires the introduction of a target-specific recognition moiety.[10,29,30] The responsivity to environmental parameters is always associated with structural parameters of the dyes and the underlying photophysical processes.[10] In an early study by Kee and coworkers, a correlation between the photodynamics and optical properties and the size or steric bulkiness of the meso-aryl substituent of the BODIPY was described.[31] These authors found higher Φ_{Fl} and longer lifetimes (τ_{Fl}) for BODIPYs with

Received: December 23, 2019
Revised: February 7, 2020
Published: February 10, 2020

https://dx.doi.org/10.1021/acs.jpca.9b11859
J. Phys. Chem. A 2020, 124, 1787−1797

bulky meso-substituents. This effect was ascribed to the hindrance of the intramolecular rotation of the meso-aryl group eventually blocking a nonradiative deactivation channel. These findings led to the design of BODIPY-based molecular rotors that can signal viscosity changes on the microscopic level by changes in emission intensity and fluorescence lifetime, enabling optical measurements of viscosity changes, e.g., in living cells.[28,32,33] In a recent study, we introduced a phenolic subunit at the meso-position of the BODIPY core, capable of undergoing a photoinduced electron transfer (PET). This leads to a family of pH-sensitive fluorophores.[11,12] These dyes show a highly efficient pH-controlled quenching of the fluorescence associated with the deprotonation of the hydroxyl group as well as substitution-degree- and pattern-dependent pK_a values. In our previous study, we additionally noticed a remarkable impact of the substitution pattern on the photophysical properties or parameters Φ_{Fl} and τ_{Fl} with higher Φ_{Fl} and longer τ_{Fl} resulting for the dyes with a bulky meso-subunit.[11] This encouraged us to perform an in depth study with extensive structural analysis of these molecules using single-crystal diffraction analysis, temperature-dependent measurements of the photophysical properties, and computational calculations of rotational motions and rotational barriers. These results were then combined to derive a model for the excited state kinetics of our dyes.

EXPERIMENTAL SECTION

Materials. 3-Hydroxybenzaldehyde, 4-hydroxybenzaldehyde, *p*-chloranil, *N*,*N*-diisopropylethylamine (DIPEA), boron trifluoride diethyl etherate, *N*-bromosuccinimide (NBS), and silica gel (40−63 μm, 230−400 mesh) were purchased from Sigma-Aldrich. 2,4-Dimethylpyrrole was bought from ABCR. Deuterated chloroform ($CDCl_3$) was obtained from Deutero GmbH. Trifluoroacetic acid (TFA) and dichloromethane (DCM) were purchased from Merck KGaA, and chloroform, *n*-hexane, and ethanol, from Carl Roth GmbH, respectively. Fluorescein 27 used as a reference for the relative quantum yield measurements was purchased from Lambda Physics. All reagents and solvents employed for dye synthesis and characterization were used without further purification.

Synthesis. The syntheses as well as the analytical characterization of the pH-sensitive BODIPY dyes and their precursor hydroxybenzaldehyde derivatives have been reported previously by our group.[11] However, the synthesis of the dyes was further optimized using ethanol as a cosolvent which drastically increased the reaction yields up to 60% (see the Supporting Information).[12,34,35] Crystals for single-crystal X-ray structure determination were obtained by recrystallization of the dyes from chloroform/*n*-hexane mixtures.

Single-Crystal X-ray Diffraction Analysis. Single-crystal X-ray diffraction studies were carried out on a D8 Venture diffractometer (Bruker AXS, Germany) equipped with a Photon 100 area detector. Data collection was done at 150 ± 2 K. An IμS X-ray source with a multilayer optic monochromated Mo Kα1 (λ = 0.71073 Å) radiation source operating at 50 kV and 1 mA was used. An empirical absorption correction was applied by using Bruker SADABS,[36] and the data reduction was performed with the Bruker SAINT program.[37] Structures were solved by direct methods with Bruker SHELXTL[38] and refined by full-matrix least-squares on F2 using SHELXS/L.[39,40] Anisotropic thermal parameters were employed for non-hydrogen atoms. The hydrogen atoms were treated isotropically with U_{iso} = 1.2 × U_{eq} of the parent atom.

Crystal structures of **1**−**10** (CCDC 1969036−1969045) are provided in the Supporting Information. These data can also be obtained free of charge from The Cambridge Crystallographic Data Centre via www.ccdc.cam.ac.uk/data_request/cif. For **8**, the disordered solvent (*n*-hexane) was removed using Squeeze.[41]

Computational Details. All calculations were performed using the TURBOMOLE program package.[42] Structural optimizations of the BODIPYs in dependence of the dihedral angle (θ) of the aryl subunit attached to the meso-position of the core were performed using density functional theory with the BP functional[43,44] and the split-valence basis set def2-SV(P).[45] All stationary states (minima and transition structures) were confirmed by a vibrational analysis. Convergence criteria were 10^{-6} E_h for the energy change and 10^{-3} E_h/a_0 for the gradient. The convergence level with respect to the used basis set size and functional was exemplarily verified by performing a calculation with def2-TZVPP,[45] which showed only minor numerical deviations.

Optical Spectroscopy. All optical measurements were performed in absolute ethanol with concentrations of the BODIPY dyes of 5 × 10^{-6} mol/L using 10 mm quartz cuvettes (Hellma, QS cells).

Absorption measurements were carried out on a calibrated Varian Cary 5000 UV-/VIS-/NIR absorption spectrophotometer equipped with a 6 × 6 Peltier-thermostated multicell holder. All spectra were measured with a scan rate of 600 nm/s and a slit width of 2 nm using a baseline correction (solvent/air).

Steady-state fluorescence measurements utilized for the determination of the temperature-dependent Φ_{Fl} were performed on a calibrated FLS920 spectrofluorometer from Edinburgh Instruments equipped with a Peltier-based temperature-controlled cuvette holder, as well as a Xe900 450 W continuous xenon arc lamp and a femtosecond supercontinuum laser. The excitation wavelength for each dye was set to match the isosbestic point of the respective absorption spectra derived from previously done temperature-dependent absorption measurements. For steady-state measurements, all spectra were measured three times with an integration time of 0.1 s and slit widths of 3 and 6 nm for excitation and emission, respectively. The calibrated FLS920 spectrofluorometer from Edinburgh Instruments was also used for time-resolved fluorescence measurements. For time-resolved fluorescence measurements, the repetition rate was set to 10 MHz and all obtained decay curves were analyzed with the software FAST (Edinburgh Instruments) using monoexponential fitting parameters to obtain τ_{Fl}. Temperature-dependent measurements of fluorescence emission spectra and fluorescence decay kinetics were done in a temperature range from 5 to 70 °C in 5 K steps with 7.5 min of temperature equilibration prior to each measurement.

Φ_{Fl} values of the BODIPY dyes were determined at 20 °C and averaged over at least five independent samples following the generally used method for relative Φ_{Fl} measurements.[46] Fluorescein 27 was employed as a quantum yield standard (Lambda Physics; Φ_{Fl27} = 0.86). Data evaluation was performed according to eq 1

https://dx.doi.org/10.1021/acs.jpca.9b11859
J. Phys. Chem. A 2020, 124, 1787−1797

$$\Phi_{Fl,x} = \Phi_{Fl,st}\frac{F_x}{F_{st}}\frac{f_{st}}{f_x}\frac{{n_x}^2}{{n_{st}}^2} \quad (1)$$

with $\Phi_{Fl,st}$ representing the quantum yield of the reference dye, F the integral photon flux, f the absorption factor, and n the refractive index of the solvent, respectively. Subsequently, Φ_{Fl} values of the BODIPY dyes were calculated for the temperatures in the range 5−70 °C using the Φ_{Fl} values determined at 20 °C as a reference. To determine the fluorescence features of the protonated species, 5 μL of concentrated HCl (12 M) was added to 3 mL of ethanolic samples containing the BODIPY dyes **3**, **5**, **9**, and **10**.

RESULTS AND DISCUSSION

A set of BODIPY dyes (see Figure 1) with pH-controllable fluorescence was synthesized according to literature procedures.[11] These dyes are structurally very similar. They also possess similar photophysical properties, e.g., absorption and emission, as they have an identical chromophore core. However, as the dyes differ in the substitution pattern of their meso-subunit with respect to the position of the hydroxyl group and additional substituents, these pH-responsive fluorophores reveal very different pK_a values. This is related to changes in the acidity of the hydroxyl group, which is controlled by the position and number of the substituents at the meso-aryl group. Additionally, the position and degree of substitution of this moiety affect the photophysical properties of these dyes, leading to slight shifts in absorption and emission and more pronounced changes in Φ_{Fl} and τ_{Fl}. These BODIPY fluorophores can be classified into two groups, i.e., sterically unhindered and sterically hindered dyes, based upon the substitution-pattern-dependent impact on the photophysical properties.

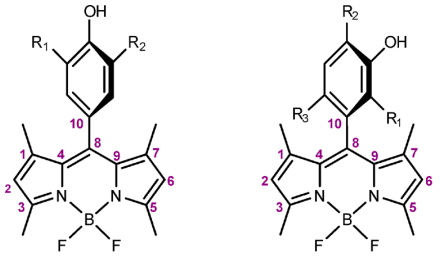

1: R_1 = H, R_2 = H
2: R_1 = Br, R_2 = H
3: R_1 = Br, R_2 = Br
4: R_1 = Cl, R_2 = H
5: R_1 = Cl, R_2 = Br
6: R_1 = H, R_2 = H, R_3 = H
7: R_1 = Br, R_2 = H, R_3 = H
8: R_1 = H, R_2 = H, R_3 = Br
9: R_1 = Br, R_2 = H, R_3 = Br
10: R_1 = Br, R_2 = Br, R_3 = Br

Figure 1. Studied BODIPY dyes with different substitution patterns.

Single-Crystal X-ray Structure Analysis. The crystal structures of BODIPY **1**−**10** were determined by single-crystal X-ray diffraction analysis. Selected crystallographic data and structural refinement parameters are listed in Table S1. The observed geometric parameters of all crystal structures are generally comparable with data previously reported for other BODIPY-based compounds.[47,48] All compounds crystallize in a monoclinic space group. While **10** crystallizes in the space group $C2/c$ and **7** and **9** crystallize in Cc, all other compounds (**1**−**6** and **8**) crystallize in $P2_1/n$ or $P2_1/c$.

The BODIPY skeleton/chromophore core formed by three conjugated heterocyclic rings is almost planar, with a root-mean-square (rms) deviation ranging from 0.0134 (for **7**) to 0.0804 (for **10**); see Table 1. The tetrahedral coordination of the boron atom with the two fluorine atoms being perpendicularly oriented with respect to the dipyrrin plane is slightly distorted.[49]

The average B−N bond length amounts to 1.535(5) Å, indicating that all compounds possess single B−N bonds. The two B−N distances are virtually identical, implying the expected delocalization of the positive charge. The average B−F bond length is 1.396(5) Å, and the average N−B−N and F−B−F angles are 107.42(3) and 108.09(3)°, respectively. The biggest difference in the B−F bond lengths with 1.380(2) and 1.420(4) Å is found between **2**/**6** and **1**, respectively. Except for **7**, no hydrogen bonds are present in the crystal structure of the dyes. **7** is the only compound containing water molecules in the crystal lattice. The water molecules form hydrogen bonds to the hydroxyl groups of the meso-aryl. These findings confirm the pronounced structural similarity of the BODIPY, especially for the chromophore core leading to similar photophysical properties.

The main difference between the members of this dye family is the substitution pattern of the meso-subunit attached to C8 of the BODIPY core with varying substituents like the hydroxy group either at the meso- or para-position and different Br or

Table 1. Selected Crystallographic Values for the BODIPY Dyes

dye	distance C8−C10 (Å)	dihedral angle θ meso-aryl−BODIPY core (deg)	root mean square (rms) of meso-aryl	root mean square (rms) of BODIPY core	shortest π−π ring distance, cg−cg (Å)
1	1.492(4)	88.826(0.076)	0.0060	0.0514	4.56
2	1.485(2)	79.723(0.048)	0.0048	0.0434	4.49
	1.486(3)	67.360(0.045)	0.0078	0.0379	
3	1.486(2)	85.979(0.045)	0.0019	0.0569	4.13
4	1.489(2)	80.154(0.049)	0.0059	0.0371	3.88
	1.489(3)	68.499(0.047)	0.0066	0.0313	
5	1.5000(7)	87.777(0.059)	0.0021	0.0496	4.198
6	1.480(6)	89.863(0.110)	0.0060	0.0174	4.19
	1.497(6)	84.086(0.130)	0.0065	0.0426	
	1.496(6)	86.316(0.117)	0.0058	0.0500	
7	1.484(4)	83.703(0.086)	0.0092	0.0134	4.342
8	1.491(3)	81.045(0.061)	0.0042	0.0331	4.24
9	1.485(9)	83.402(0.135)	0.0031	0.0456	4.24
10	1.490(3)	76.232(0.067)	0.0048	0.0804	3.8557

https://dx.doi.org/10.1021/acs.jpca.9b11859
J. Phys. Chem. A 2020, 124, 1787−1797

Cl atoms at varying positions (see Figure 2a and see Figure S1). For some dyes, the substituents are disordered over two positions in the crystal lattice; e.g., the position of Cl and Br is disordered in the ratio of 1/3 to 2/3 for **5**, while two positions of the hydroxyl oxygen O1 with ratios of 0.3/0.7 and 0.2/0.8 can be observed for **6** and **10**, respectively (see Figure S1). The meso-aryl group is strongly twisted out of the BODIPY plane, with dihedral angles θ ranging from 67.360(2) to 89.863(1)° (see Table 1). θ is closest to 90° for the non-halogenated compounds **1** and **6** as well as for dyes **3** and **5** with a symmetrically substituted meso-subunit, while all derivates with an unsymmetrically substituted meso-aryl group show smaller dihedral angles. θ is also influenced by the packing of the dye molecules in the crystal lattice. For example, for compound **2**, there are two conformers in the asymmetric unit with values for θ of 68.49 and 80.15°. This is also the case for **4**, revealing two conformers with θ of 67.36 and 79.72°. The crystal lattice of compound **6** contains even three conformers with θ of 84.09, 86.32, and 89.86°. As expected, the C−C distance between C8 and C10 is not influenced by θ and, hence, matches for dyes **2**−**10** (see Table 1). The packing of the molecule is always stabilized by π−π-interactions between the pyrrole rings of the BODIPYs. There are different packing motifs, exemplarily shown for compounds **1** and **7** (see Figure 2). In one motif, the BODIPY molecules are arranged inversely in dimers with a sandwich-like π−π-stacking with dimer−dimer interactions occurring in a head-to-tail fashion by additional X−H···π-ring interactions; see, e.g., compound **1** in Figure 2b. Alternatively, the dye molecules are arranged in chain-like structures with all molecules pointing into the same direction in a parallel displaced π−π-stacking. An example presents compound **7** (see Figure 2c). While the inversely arranged sandwich-like π−π-stacking occurs mostly for compounds **1**, **3**, **5**, and **6** with a θ value close to 90°, the parallelly displaced π−π-stacking seems to be typical for dyes with an unsymmetrically substituted meso-aryl group, that reveal a more pronounced distortion of θ like **2**, **7**, **8**, and **9**. An exception is compound **10**, as its crystal packing motif presents a mixture of both types of packing motifs previously described, with inversely arranged parallelly displaced π−π-stacked molecules, which additionally are stabilized by intramolecular methyl-H···π-meso-aryl interactions (see Figure S2). Furthermore, this packing motif shows the strongest π−π interactions, as indicated by the shortest plane-to-plane distance between the pyrrole rings of about 3.85 Å observed within this series. The plane-to-plane distances differ for all dyes with values ranging from 3.85 to 4.56 Å for **10** and **1**, respectively. With a value of 3.88 Å, the plane-to-plane distance obtained for **4** is the second smallest value within this series and is attributed to a much denser packing enabled by the Cl substituent which is smaller than the Br substituents. While the crystal packing and plane-to-plane distance are clearly not only different for compound **10**, with a value of 0.0804, this compound also possesses the largest rms of the BODIPY core. The spatially demanding, twisted meso-subunit and the stabilizing inter- and intramolecular interactions obviously lead to a propeller-like distortion of the BODIPY core with an angle of 11.894°(0.143) between the two pyrrole rings (see Figure S2). For comparison, this angle amounts only to 3.220°(0.150) and 1.156°(0.240) for **1** and **7**, respectively.

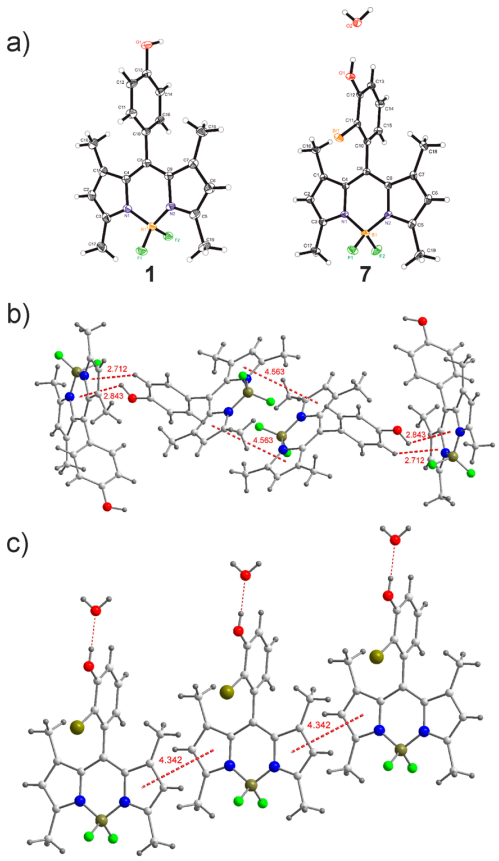

Figure 2. (a) Crystal structure of compounds **1** and **7** determined by single-crystal X-ray structure analysis. (b) Sandwich-like head-to-tail crystal packing of compound **1**. (c) Parallel displaced crystal packing of compound **7**. Color-coding: white - carbon, gray - hydrogen, red - oxygen, blue - nitrogen, green - fluorine, brown - boron, olive - bromine.

Based on these data, the unsymmetrically substituted compounds **7**, **8**, **9**, and **10** are classified as being sterically hindered, as their meso-subunit is always substituted in the ortho-position to C10. This is expected to drastically decrease the degree of freedom of the meso-aryl subunit by the sterically demanding substituents in terms of interactions with the methyl groups of the BODIPY core. All symmetrically substituted compounds **2**, **3**, **4**, and **5** as well as the non-halogenated compounds **1** and **6** are assigned to the sterically unhindered class of BODIPY dyes, since the meso-subunit of these fluorophores is only substituted in the meta- and para-position to C10. This substitution pattern is favorable for a rotation along the C8−C10 axis. In the hypothetical case of deprotonated methyl groups attached to C1 and C7 at the BODIPY core, a unhindered rotation of the meso-subunit seems to be feasible for all compounds classified as sterically unhindered (**1**−**6**), as the shortest distance between the ortho-carbons of the meso-subunit and the methyl carbon is 2.129 Å (non-binding). If the meso-aryl group is substituted in the ortho-position, e.g., with bromine, as is the case for the sterically hindered BODIPY molecules, the spatial demand of the substituent inhibits a free rotation. For example, a minimum θ of 48.2° was determined for **7**.[50] Although the deprotonation of the methyl groups and a completely rigid

https://dx.doi.org/10.1021/acs.jpca.9b11859
J. Phys. Chem. A 2020, 124, 1787−1797

molecule during rotation of the meso-subunit present only assumptions, we could nevertheless classify the dye molecules of our BODIPY series here appropriately using structural parameters.

DFT Calculations. To verify our assumptions and classifications, we performed computational calculations of the rotation of the aryl subunit in the meso-position of the BODIPY core including rotational barriers and molecular motions. These calculations were done exemplarily for dyes **1**, **3**, **6**, **7**, **8**, and **9**. The results of these calculations revealed a distinct energetic minimum (E_{min}) at a dihedral angle θ of about 90° between the meso-aryl subunit and the BODIPY core plane for all molecules. Compound **6**, however, presents an exception, as its E_{min} is found for a smaller θ of 83° (see Table 2). As shown for the rigid structures obtained by single-crystal diffraction analysis, a rotation of the meso-subunit along the C8−C10 axis is only possible for the sterically unhindered dyes **1**−**6**, as discussed in the previous section. As these previously made assumptions were only hypothetical ones, without a chemistry basis, they were neglected for the DFT calculations. The actual rotation of the meso-subunit of all dyes starts from the energetic minimum with an out-of-plane motion of the meso-aryl subunit and a bulging motion of the BODIPY core, as exemplarily shown for compound **1** in Figure 3. These motions minimize the interactions between the methyl groups at positions C1 and C7 and the meso-subunit during the rotation around the bond connecting both moieties. As a result, θ is lowered to around 14° for the transition state (see Figure 3b). Furthermore, the previously planar BODIPY core is drastically bulged. For compound **1** as well as for compounds **6** and **9**, an additional intermediate state with a slightly different geometry compared to this transition state can be observed (see Figure 3c). The size of the rotational barrier is determined by two opposite effects: (1) delocalization of π-electrons and (2) steric effects. The enhanced delocalization of π-electrons of the BODIPY core and the meso-aryl subunit during the rotational motion contributes to a stabilization of the system with decreasing θ, whereas the bulging motion destabilizes the π-system by distortion of the BODIPY core plane. However, steric effects caused by the spatial proximity of the methyl groups at positions C1 and C7 and the meso-aryl subunit are predominant, as supported by the effects accompanying the attachment of bulky substituents in the 2- and 6-position at the meso-aryl subunit. This substitution pattern drastically increases the steric hindrance for a rotational motion and, thus, the energetic barrier to be overcome by this motion. For all dyes, a very broad transition "area" with a defined energetic maximum of the transition state (TS) in dependence of θ was calculated. Furthermore, additional intermediate states (IS) with lower energies than the transition structures have been identified for **1** and **6** as well as **9** (see Table S2). However, their presence does not affect the rotational movement, since with values of 0.3, 0.2, and 2.6 kcal/mol the energy differences to the transition states are very small for **1**, **6**, and **9**. While the relative energy differences between the energetic minima and transition states are quite similar for **1**, **3**, and **6** with values of 16.4, 16.7, and 18. kcal/mol, they drastically differ from the values of 42.3, 38.2, and 49.2 kcal/mol calculated for **7**, **8**, and **9**. This verifies our previously made classification of the dyes into sterically hindered and unhindered compounds. This classification can also be made with respect to θ in the transition state. For dyes **1**, **3**, and **6** with unhindered rotation, the value for θ is around 13−14° in their transition state, whereas θ is between 30 and 40° for the transition state of **7**, **8**, and **9**. This is attributed to steric effects related to the substitution pattern. Assuming first order reaction kinetics for the rotation and applying the Eyring equation from transition state theory, half-life times $t_{1/2}$ for the rotation at different temperatures can be calculated (see Table 2).[51] For **1**, **3**, and **6**, the $t_{1/2}$ values calculated for a temperature of 20 °C are on the time scale of seconds, indicating a unhindered rotation of the meso-aryl group. In contrast, the $t_{1/2}$ values calculated for **7**, **8**, and **9** are on the order of 10^{17} s, rendering a rotation on a measurable time scale very unlikely.[52] Obviously, substituents at the 2- and 6-position that increase the rotational barrier from around 17 kcal/mol to

Table 2. Calculated Relative Energies of the Transition (TS1) and Intermediate (IS) States and Corresponding θ of BODIPY Compounds 1, 3, 6, 7, 8, and 9

	relative energy (kcal mol^{-1})		dihedral angle θ (deg)			$t_{1/2}$[a] (s) (20 °C)
dye	E_{TS}	E_{IS}	min	TS1	IS	min → TS1
1	16.4	16.1	90	14	3	0.2
3	16.7		90	14		0.3
6	18.2	18.0	83	13	3	4.3
7	42.3		89	34		3.9×10^{18}
8	38.2		89	29		3.1×10^{15}
9	49.2	46.6	90	39	11	5.1×10^{23}

[a]Half-life calculated assuming first order reaction kinetics $t_{1/2} = \frac{\ln(2)}{k}$, with $k = \kappa\frac{k_B T}{h}e^{-\Delta G/RT}$ from the Eyring equation with k_B = Boltzmann constant, T = 293.15 K, h = Planck constant, κ = 1 (transmission coefficient), and R = gas constant.

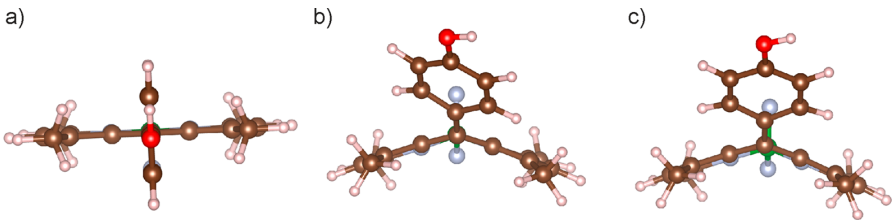

Figure 3. (a) Calculated energetic minimum (min) of the structure of **1** showing a planar BODIPY core plane and a perpendicular standing meso-aryl subunit. (b) Rotational motion results in a bulged BODIPY core and an out-of-plane meso-aryl subunit for the calculated transition state of **1**. (c) Calculated intermediate state of structure **1**. Color-coding: brown - carbon, misty rose - hydrogen, red - oxygen, green - boron, light blue - fluorine, powder blue - nitrogen.

https://dx.doi.org/10.1021/acs.jpca.9b11859
J. Phys. Chem. A 2020, 124, 1787−1797

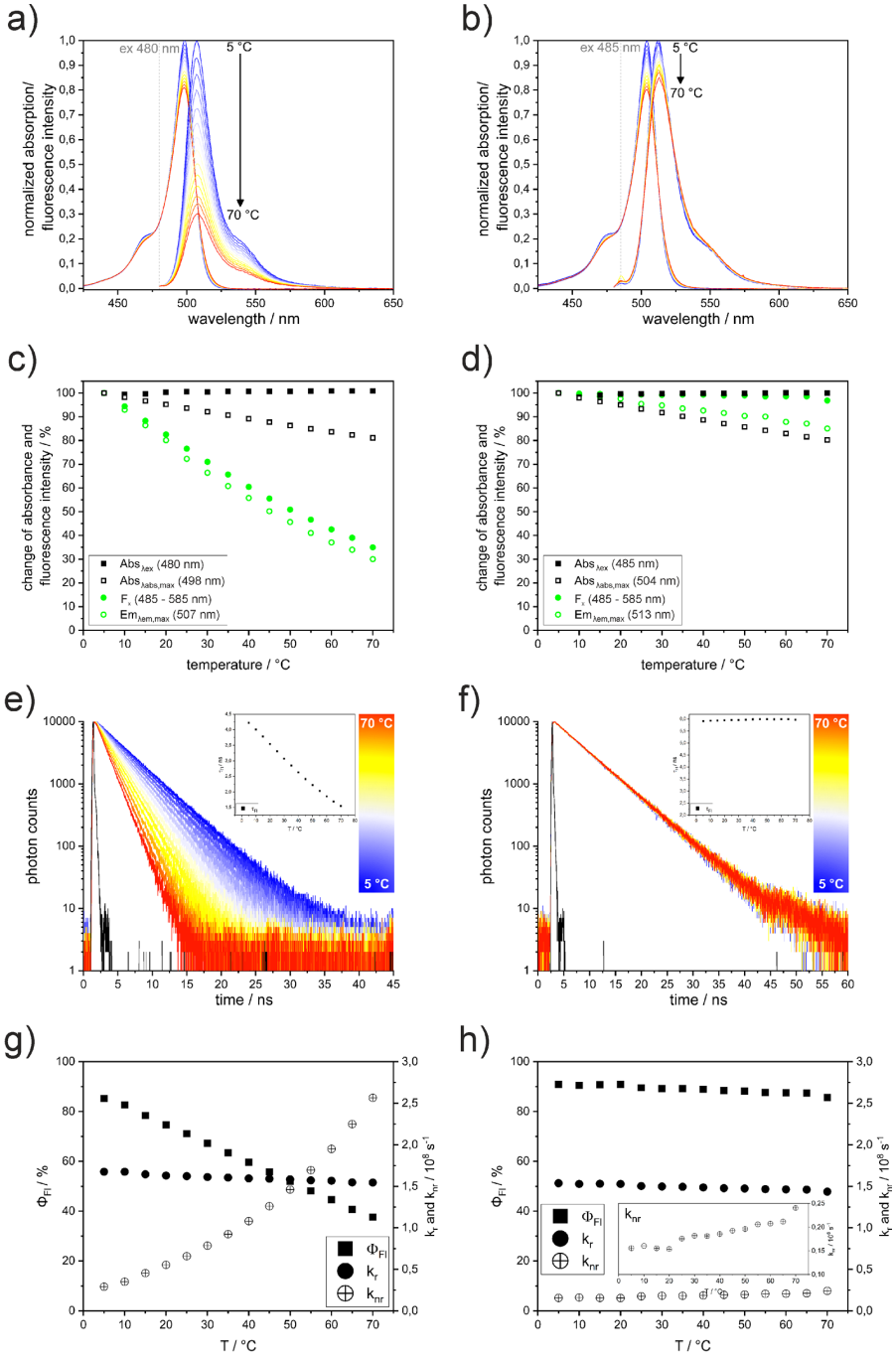

Figure 4. (a, b) Temperature-dependent normalized absorption and normalized fluorescence intensity of non-sterically hindered compound **1** upon excitation at 480 nm and sterically hindered compound **7** upon excitation at 485 nm, respectively. (c, d) Changes (in percentage) of the absorbance (black squares) at the excitation wavelength and the absorption maximum (full and open symbols) and changes of the fluorescence intensity in percentage (green circles) for the emission maximum and for integrated emission intensities (open and full symbols) in dependence of the temperature for **1** and **7**. (e, f) Fluorescence decay curves for **1** and **7** in dependence of the temperature (the black line represents the instrument response function (IRF)). The inset shows the monoexponentially fitted fluorescence decay kinetics as a function of temperature. (g, h) Temperature dependence of the fluorescence quantum yield Φ_{Fl}, radiative rate constant k_r, and nonradiative decay constant k_{nr} for **1** and **7**. The latter two quantities were calculated according to eq 9.

https://dx.doi.org/10.1021/acs.jpca.9b11859
J. Phys. Chem. A 2020, 124, 1787−1797

Table 3. Temperature-Dependent Photophysical Properties Fluorescence Quantum Yield and Fluorescence Lifetime for Dyes 1−10, Rate Constants for the Radiative and Nonradiative Deactivation of the First Excited State S_1 (Calculated According to Eq 9) as Well as Activation Energies Calculated for Nonradiative Deactivation

	Φ_{Fl} (EtOH) (%)			τ_{Fl} (EtOH, 20 °C) (ns)						
dye	5 °C	20 °C	70 °C	5 °C	20 °C	70 °C	k_r (10^8 s^{-1})	k_{nr} (20 °C) (10^8 s^{-1})	$E_A(\Phi_{Fl})$[a] (kcal mol^{-1})	$E_A(\tau_{Fl})$[b] (kcal mol^{-1})
1	72 ± 3	59 ± 3	24 ± 3	4.22 ± 0.03	3.54 ± 0.03	1.54 ± 0.03	1.63 ± 0.06	1.16 ± 0.05	6.02 ± 0.30	5.92 ± 0.30
2	73 ± 3	60 ± 3	25 ± 3	4.33 ± 0.03	3.72 ± 0.03	1.75 ± 0.03	1.56 ± 0.07	1.07 ± 0.06	6.08 ± 0.30	5.87 ± 0.29
3	69 ± 3	58 ± 3	17 ± 3	4.30 ± 0.03	3.66 ± 0.03	1.91 ± 0.03	1.43 ± 0.11	1.15 ± 0.05	6.47 ± 0.32	6.02 ± 0.22
4	69 ± 3	59 ± 3	24 ± 3	4.27 ± 0.03	3.65 ± 0.03	1.68 ± 0.03	1.55 ± 0.07	1.12 ± 0.07	5.91 ± 0.30	5.94 ± 0.30
5	69 ± 3	58 ± 3	19 ± 3	4.34 ± 0.03	3.67 ± 0.03	1.85 ± 0.03	1.48 ± 0.09	1.15 ± 0.05	6.16 ± 0.31	6.05 ± 0.23
6	85 ± 3	75 ± 3	38 ± 3	4.58 ± 0.03	4.58 ± 0.03	4.58 ± 0.03	1.60 ± 0.04	0.55 ± 0.02	6.54 ± 0.33	6.44 ± 0.32
7	91 ± 3	91 ± 3	86 ± 3	5.91 ± 0.03	5.95 ± 0.03	5.97 ± 0.03	1.49 ± 0.04	0.15 ± 0.01	1.47 ± 0.29	[c]
8	90 ± 3	90 ± 3	83 ± 3	5.96 ± 0.03	5.98 ± 0.03	5.95 ± 0.03	1.45 ± 0.05	0.18 ± 0.01	1.49 ± 0.30	[c]
9	89 ± 3	87 ± 3	75 ± 3	5.83 ± 0.03	5.85 ± 0.03	5.84 ± 0.03	1.45 ± 0.05	0.21 ± 0.01	2.74 ± 0.55	[c]
10	88 ± 3	87 ± 3	78 ± 3	5.91 ± 0.03	5.94 ± 0.03	5.94 ± 0.03	1.42 ± 0.04	0.22 ± 0.01	1.84 ± 0.37	[c]

[a]Determined using eq 6. [b]Determined using eq 8. [c]Could not be determined by fitting.

more than 40 kcal/mol effectively freeze the respective BODIPY molecules.

Temperature-Dependent Optical Properties. Vibrational and rotational relaxation-induced internal conversion (IC) is one of the main nonradiative processes depopulating the excited singlet state of organic dyes, thereby competing with fluorescence emission and intersystem crossing.[53] IC is temperature-dependent, as temperature can considerably influence the kinetics of vibrational and rotational modes by changing the Boltzmann distribution of different states. This temperature dependence of IC largely accounts also for the temperature dependence of the radiative process fluorescence. Commonly, Φ_{Fl} increases with decreasing temperature. The size of such effects largely depends on the structural properties of the fluorophores. Flexible structures are more prone to strong temperature effects than rigid chromophore structures, particularly if rotations of these flexible structures are involved in nonradiative deactivation pathways. This has been utilized for fluorescence-based temperature measurements, e.g., utilizing rhodamine B.[54]

As derived in the previous sections, our fluorescent BODIPYs can be divided into dyes with sterically hindered and unhindered rotation of the meso-aryl group based upon the substitution pattern of this moiety. This should lead to different temperature sensitivities of the optical properties of both groups, with a higher temperature sensitivity being expected for the sterically unhindered group. For this group of dyes, an increase in temperature can favor rotational motions, thereby enhancing nonradiative deactivation by IC. To verify this assumption, we performed temperature-dependent absorption as well as steady-state and time-resolved fluorescence measurements.

As exemplarily shown in Figure 4, sterically unhindered compound **1** and sterically hindered compound **7** both show temperature-dependent changes of their optical properties. The size of these effects is, however, considerably affected by the substitution pattern of the meso-aryl subunit. As shown in Figure 4a and b, the absorption spectra reveal a slight broadening with increasing temperature. This is also reflected by isosbestic points at 480 and 507 nm and at 485 and 512 nm for **1** and **7**, respectively. For both compounds, the absorbance at the respective absorption maximum, i.e., at 498 nm for **1** and 504 nm for **7**, obtained at 70 °C is reduced to 80% of the value measured at 5 °C (see Figure 4c and d). As is to be expected, all dyes reveal similar temperature-dependent changes in absorption (see Figures S4−S11). On the contrary, both classes of BODIPY dyes display a considerably different temperature dependence of their fluorescence intensity, as exemplarily shown for **1** and **7** in Figure 4. While the fluorescence intensity at the emission maximum as well as the integrated fluorescence emission (F_x) of dye **1** are strongly temperature dependent with an overall decrease of the emission intensity at 70 °C to about 30% of its maximum value at 5 °C (see Figure 4c), the fluorescence of **7** is barely affected by temperature. At 70 °C, the maximum fluorescence intensity of **7** decreases to about 85% of its value obtained at 5 °C. However, when considering the temperature-induced broadening of the fluorescence by calculating integral fluorescence intensities (see Figure 4d), it becomes obvious that the overall fluorescence intensity remains constant, as can be seen by negligible changes in F_x.

Since all temperature-dependent measurements were performed in absolute ethanol, which shows small temperature-dependent changes of its refractive index, and the temperature-dependent absorption spectra of the dyes reveal isosbestic points, the determination of the temperature dependence of Φ_{Fl} (eq 1) can be simplified by using changes in fluorescence intensities upon excitation at the isosbestic point of the absorption spectra and, hence, always at the same absorbance and absorption factor. Temperature-dependent Φ_{Fl} values were calculated according to eq 2

$$\Phi_{Fl,x}(T) = \Phi_{Fl,x}(20\ °C)\frac{F_x(T)}{F_x(20\ °C)}\frac{n_x^2(T)}{n_x^2(20\ °C)} \quad (2)$$

with $\Phi_{Fl,x}(20\ °C)$ representing the quantum yield of the dye determined at 20 °C relative to a reference dye, F_x is the integrated fluorescence emission, and n is the refractive index of the solvent. As shown in Table 3, the relatively determined Φ_{Fl} values of the dyes in ethanol are in the same range and show similar trends as the Φ_{Fl} values of the dyes obtained in methanol in a previous study.[11] Again, the classification of the dyes in two groups is confirmed. The sterically unhindered dyes show Φ_{Fl} values ranging from 58 to 75% for compounds **1**, **2**, **3**, **4**, **5**, and **6** at 20 °C, whereas the sterically hindered dyes **7**, **8**, **9**, and **10** show Φ_{Fl} values of 87−91% at 20 °C. Furthermore, the Φ_{Fl} values of the former are very sensitive to temperature. As exemplarily shown for **1** in Figure 4g (see

https://dx.doi.org/10.1021/acs.jpca.9b11859
J. Phys. Chem. A 2020, 124, 1787−1797

Table 3 for all other dyes), the heating-induced decrease of Φ_{Fl} from about 72% at 5 °C to 24% at 70 °C is obvious. For the sterically hindered dye **7**, only a minimal temperature-dependent decrease of Φ_{Fl} from 91% at 5 °C to 86% at 70 °C (see Figure 4h) occurs. In both cases, the decrease of Φ_{Fl} with increasing temperature reveals a linear correlation. However, for dyes with a higher degree of substitution, namely, **3**, **5**, **9**, and **10**, a deviation from this linear trend is observed at higher temperatures (see Figures S4−S11). This behavior is tentatively ascribed to enhanced contributions of nonradiative depopulation processes favored by additional vibration modes from the additional substituents. A decomposition of the dyes leading to a decrease in fluorescence can be excluded, as the heating-induced decrease in fluorescence intensity is completely reversible, with the initial fluorescence being completely restored upon cooling.

Time-resolved fluorescence measurements displayed the same trend of the temperature-dependent changes. As shown exemplarily for **1** in Figure 4e), a significantly faster fluorescence decay is obtained for increasing temperatures, leading to a 3-fold reduction of τ_{Fl}, derived from mono-exponentially fitted decay kinetics, from 4.3 ns at 5 °C to 1.5 ns at 70 °C. Contrary, for **7**, the decay kinetics and subsequently τ_{Fl} remain constant with τ_{Fl} = 6 ns observed at room and higher temperatures (see Figure 4f). While the fluorescence decay kinetics of the sterically unhindered dyes **1**−**6** are considerably sped up by temperature, yielding faster decays at higher temperatures, no changes occur for the sterically hindered dyes **7**−**10** (see Table 3 and Figures S4−S11).

Excited-State Kinetics. The results from the steady-state and time-resolved fluorescence measurements confirm that the rotation of the meso-aryl subunit plays an important role in the nonradiative deactivation of the first excited state S_1 of our and related BODIPY dyes. Several studies showed that the structure of the relaxed excited state S_1 of meso-aryl substituted BODIPY dyes is similar to the structure of the transition state of the ground state S_0 obtained by rotation of the meso-aryl subunit (see Figure 3b).[31,55−58] Thus, rotation of the meso-aryl group probably facilitates the access to a conical intersection of the potential energy surfaces (PES) of S_1 and S_0. We hence derived the rate constant for the radiative (k_r) and nonradiative (k_{nr}) deactivation processes for each dye from the measured temperature-dependent fluorescence data as well as the activation energy (ΔE_A) for the nonradiative decay from S_1 to S_0. The latter defines the energetic barrier for nonradiative IC, which we assume to be the main contribution to the nonradiative depopulation of S_1. We exclude other processes like charge transfer (CT), intersystem crossing (ISC), and photoinduced electron transfer (PET). CT is not likely for our type of BODIPY dyes. Although heavy atoms like Br are present in our dyes, a major contribution from ISC as a deactivation pathway is unlikely as the chromophore core and substituted meso-subunit are electronically decoupled.[59] Furthermore, PET can be neglected, as it does not occur under acidic conditions used for our studies.

In the absence of external quenchers, Φ_{Fl} is related to the rate constants of the radiative and nonradiative deactivation processes of the first excited singlet state, as described in eq 3

$$\Phi_{Fl} = \frac{k_r}{k_r + \sum k_i} \tag{3}$$

where k_r is the rate constant for radiative deactivation, i.e., fluorescence, and $\sum k_i$ represents the sum of the rate constants of all processes i that can nonradiatively deactivate the excited singlet state such as IC, ISC, CT, and PET.[53] It has been found that $\sum k_i$ usually takes the form

$$\sum k_i = k_1 + k_2 \tag{4}$$

with $k_2 = A e^{-(\Delta E_A/RT)}$.

Here, k_1 represents all remaining temperature-independent nonradiative rate constants and k_2 the temperature-dependent components. The latter can be written in the common Arrhenius form. As mentioned above, the activation energy ΔE_A is equivalent to the energy required to go from the lowest vibrational level of S_1 to the point of a conical intersection with S_0 on the PES. Combining and rearranging eqs 3 and 4 leads to

$$\frac{1}{\Phi_{Fl}} - 1 - c_1 = c_2 \times e^{-(\Delta E_A/RT)} \tag{5}$$

with $c_1 = \frac{k_1}{k_r}$ and $c_2 = \frac{A}{k_r}$.

Finally, taking the natural logarithm gives eq 6

$$\ln\left(\frac{1}{\Phi_{Fl}} - 1 - c_1\right) = \ln(c_2) - \frac{\Delta E_A}{RT} \tag{6}$$

Once Φ_{Fl} is known as a function of T, eq 4 can be solved by an iterative determination of c_1 using the method of least-squares. This results in a straight line for a plot of $\ln\left(\frac{1}{\Phi_{Fl}} - 1 - c_1\right)$ versus $\frac{1}{T}$.

However, no significant improvements of the fit of our data were obtained for $c_1 \neq 0$ ($k_1 \ll k_r$). This suggests that only temperature-dependent components contribute to the radiationless deactivation of the excited singlet state.

Equation 6 can also be expressed using τ_{Fl}, thereby exploiting the relationship between τ_{Fl} and the rate constants of all processes depopulating the excited singlet state. This yields eq 8.

$$\tau_{Fl} = \frac{1}{k_r + \sum k_i} \tag{7}$$

Combining eqs 4 and 7 followed by rearranging and taking the natural logarithm gives

$$\ln\left(\frac{1}{\tau_{Fl}} - c_3\right) = \ln(A) - \frac{\Delta E_A}{RT} \tag{8}$$

with $c_3 = k_r + k_1$.

Once τ_{Fl} is known as a function of T, c_3 can be determined iteratively following the same algorithm as that used for eq 6. As could be already shown for the Φ_{Fl}, also τ_{Fl} is governed only by temperature-dependent nonradiative processes. Thus, $k_1 = 0$ ($k_1 \ll k_r$) and $c_3 = k_r$.

The radiative and nonradiative decay rates k_r and $k_{nr} = \sum k_i$, can be calculated by combining eqs 3 and 8 to

$$k_r = \frac{\Phi_{Fl}}{\tau_{Fl}} \quad \text{and} \quad k_{nr} = \frac{1 - \Phi_{Fl}}{\tau_{Fl}} \tag{9}$$

The calculated values for k_r and k_{nr} are given in Table 3 (for detailed temperature-dependent k_{nr} values, see Table S3). These data are exemplarily shown for compounds **1** and **7** in Figure 4g and h. For all dyes of this series, the k_r values show

https://dx.doi.org/10.1021/acs.jpca.9b11859
J. Phys. Chem. A 2020, 124, 1787−1797

only a minor temperature dependency and the values are in the same range of (1.4−1.6) × 10^8 s^{-1} at 20 °C with values slightly lowered by around 15% in total resulting upon heating (5−70 °C). However, major differences can be observed for k_{nr}. k_{nr} values for the sterically hindered compounds **7**−**10** are calculated to about 0.2 × 10^8 s^{-1} at 20 °C, while values for sterically unhindered compounds **1**−**5** are about 1.1 × 10^8 s^{-1} (0.6 × 10^8 s^{-1} for **6**) at 20 °C. Furthermore, a notable temperature dependency of k_{nr} can be observed, which is far more pronounced for sterically unhindered compounds, as exemplarily shown for **1** in Figure 4g. In this case, k_{nr} increases from 0.7 × 10^8 s^{-1} at 5 °C to 4.9 × 10^8 s^{-1} at 70 °C (>5-fold). For the sterically hindered compounds, only a minor increase of k_{nr} occurs upon heating, as exemplarily shown for **7** in Figure 4h. For **7**, k_{nr} rises from 0.16 × 10^8 s^{-1} at 5 °C to 0.24 × 10^8 s^{-1} at 70 °C.

Equations 6 and 8 enable the determination of the activation energy ΔE_A for the nonradiative deactivation of the first exited state S_1 using the experimentally determined quantities Φ_{Fl} and τ_{Fl}. As summarized in Table 3, ΔE_A calculated from Φ_{Fl} and from τ_{Fl} data amounts to about 6 kcal/mol for the sterically unhindered BODIPY derivatives **1**−**6**. The sterically hindered dyes **7**−**10** have an activation energy ΔE_A of around 3 kcal/mol, which could only be derived from Φ_{Fl} as the temperature-dependent changes of τ_{Fl} are too small, and thus, the fits do not give reliable results. However, neither the ΔE_A of 3 kcal/mol nor that of 6 kcal/mol are real barriers, as these values are even lower than the rotational barriers of the meso-subunit determined for the sterically unhindered compounds (see Table 1). The corresponding fitting parameters for ΔE_A can be found in Table S4. Apparently, a direct comparison of the activation energies of both BODIPY groups is not really appropriate, as our results suggest that the nonradiative depopulation of the first excited singlet state can involve two different pathways. As already mentioned previously, a free rotational motion of the meso-aryl subunit for sterically unhindered compounds makes a nonradiative deactivation due to a high structural similarity of the transition state of S_0 and the relaxed excited state of S_1 likely.[31,55−58] Therefore, access to a conical intersection of both PES, which shows an energy barrier of around 6 kcal/mol for the transition from S_1 to the TS of S_0, is feasible for **1**−**6**. However, this pathway is not accessible for sterically hindered compounds **7**−**10**, as the steric hindrance prevents them from reaching the relaxed excited state of S_1. Nonetheless, nonradiative depopulation processes occur also in this BODIPY group albeit to a lesser extent. This finding accompanied by a smaller value for ΔE_A ($S_1 \rightarrow S_0$) of around 1.5−2.8 kcal/mol indicates the presence of another nonradiative deactivation pathway of S_1 for BODIPY dyes. This additional pathway shows only a slight temperature dependency (see Figure 4h, inlet) and is probably also accessible for compounds **1**−**6** but superimposed by the pathways involving the TS of S_0. The mechanism of the second pathway seems to be related to vibrational motions of the BODIPY plane, as k_{nr} is in the same order of magnitude for the sterically hindered dyes but not affected by the substitution pattern of the meso-aryl. This process is most likely connected with a bulging of the core plane that participates in the rotational motion of the meso-subunit for the sterically unhindered derivatives. Thus, this bulging could also take place for the sterically hindered compounds with an increasing amplitude in dependence of temperature possibly enabling this additional deactivation pathway.

CONCLUSION AND OUTLOOK

The results of our combined structural and photophysical study of a family of 10 BODIPY dyes consisting of two building blocks, an identical chromophore core, and a differently substituted aryl meso-subunit confirm a strong correlation of both properties. From the crystal structures of the compounds determined by single-crystal X-ray diffraction analysis, a first classification of the BODIPY family into sterically unhindered and sterically hindered derivatives was made utilizing crystal structure-related parameters like the dihedral angle θ between the core plane and the meso-aryl subunit as well as the crystal packing motif.

These findings were supported by DFT calculations simulating the rotation of the meso-subunit. This rotation is only possible for the sterically unhindered BODIPYs, which do not have substituents in the ortho-position to the meso-aryl carbon (C10) binding to the core. Upon substitution at the ortho-position, the meso-aryl group becomes too bulky to pass the methyl groups attached to the core, effectively freezing this rotational motion. The rotational motion of the meso-subunit involves a bulging of the core plane, easily accessible for the sterically unhindered compounds, as indicated by the rotational barrier, which was derived by calculating the structures of transition and intermediate states as well as their corresponding energies.

Temperature-dependent measurements of the absorption and fluorescence properties of our dyes revealed that the substitution pattern of the meso-aryl subunit and sterical constraints introduced by bulky substituents control the size of the achievable fluorescence quantum yields and the temperature dependence of their fluorescence. We attribute these effects to the rotation of the meso-aryl subunit enabling a deactivation of the first excited state S_1 via a conical intersection of the excited and ground state potential energy surfaces. This conical intersection is only accessible for sterically unhindered compounds, as only these BODIPYS can reach the relaxed excited state of S_1 by rotation. Access to this state is not possible for the sterically hindered dyes. However, a small temperature-dependent nonradiative rate constant was observed, suggesting the presence of an additional nonradiative deactivation pathway of the first excited state. The exact nature of this process is currently assessed.

ASSOCIATED CONTENT

Supporting Information

The Supporting Information is available free of charge at https://pubs.acs.org/doi/10.1021/acs.jpca.9b11859.

Crystal structures and selected crystallographic structure refinement parameters; temperature-dependent spectra of absorption, emission, and fluorescence decay; calculated energies of the compounds; derived decay rates; and fitting parameters for activation energies for nonradiative decay (PDF)

AUTHOR INFORMATION

Corresponding Author

Ute Resch-Genger − *Department 1 − Analytical Chemistry; Reference Materials, Federal Institute for Materials Research and Testing (BAM), 12489 Berlin, Germany;* orcid.org/0000-0002-0944-1115; Email: ute.resch@bam.de

https://dx.doi.org/10.1021/acs.jpca.9b11859
J. Phys. Chem. A 2020, 124, 1787−1797

Authors

Sebastian Radunz − *Department 1 − Analytical Chemistry; Reference Materials, Federal Institute for Materials Research and Testing (BAM), 12489 Berlin, Germany*

Werner Kraus − *Department 1 − Analytical Chemistry; Reference Materials, Federal Institute for Materials Research and Testing (BAM), 12489 Berlin, Germany*

Florian A. Bischoff − *Department of Chemistry, Humboldt-Universität zu Berlin, 12489 Berlin, Germany;* orcid.org/0000-0002-7717-3183

Franziska Emmerling − *Department 1 − Analytical Chemistry; Reference Materials, Federal Institute for Materials Research and Testing (BAM), 12489 Berlin, Germany; Department of Chemistry, Humboldt-Universität zu Berlin, 12489 Berlin, Germany;* orcid.org/0000-0001-8528-0301

Harald Rune Tschiche − *Department 7 − Chemicals and Product Safety, German Federal Institute for Risk Assessment (BfR), 10589 Berlin, Germany*

Complete contact information is available at: https://pubs.acs.org/10.1021/acs.jpca.9b11859

Notes

The authors declare no competing financial interest.

■ ACKNOWLEDGMENTS

We gratefully acknowledge financial support from the internal BAM project MIC (microbiologically influenced corrosion) and from the Ph.D. program of BAM.

■ REFERENCES

(1) Treibs, A.; Kreuzer, F.-H. Difluorboryl-Komplexe von Di- und Tripyrrylmethenen. *Justus Liebigs Ann. Chem.* **1968**, *718*, 208−223.

(2) Loudet, A.; Burgess, K. BODIPY Dyes and Their Derivatives: Syntheses and Spectroscopic Properties. *Chem. Rev.* **2007**, *107* (11), 4891−4932.

(3) Bertrand, B.; Passador, K.; Goze, C.; Denat, F.; Bodio, E.; Salmain, M. Metal-based BODIPY Derivatives as Multimodal Tools for Life Sciences. *Coord. Chem. Rev.* **2018**, *358*, 108−124.

(4) Kolemen, S.; Akkaya, E. U. Reaction-based BODIPY Probes for Selective Bio-imaging. *Coord. Chem. Rev.* **2018**, *354*, 121−134.

(5) Antina, E. V.; Bumagina, N. A. Tetraaryl-substituted Aza-BODIPY: Synthesis, Spectral Properties, and Possible Applications (Microreview). *Chem. Heterocycl. Compd.* **2017**, *53* (1), 39−41.

(6) Kowada, T.; Maeda, H.; Kikuchi, K. BODIPY-based Probes for the Fluorescence Imaging of Biomolecules in Living Cells. *Chem. Soc. Rev.* **2015**, *44* (14), 4953−4972.

(7) Ulrich, G.; Ziessel, R.; Harriman, A. The Chemistry of Fluorescent Bodipy Dyes: Versatility Unsurpassed. *Angew. Chem., Int. Ed.* **2008**, *47* (7), 1184−1201.

(8) Pereira, N. A. M.; Pinho e Melo, T. M. V. D. Recent Developments in the Synthesis of Dipyrromethanes. A Review. *Org. Prep. Proced. Int.* **2014**, *46* (3), 183−213.

(9) Nascimento, B. F. O.; Lopes, S. M. M.; Pineiro, M.; Pinho e Melo, T. M. V. D. Current Advances in the Synthesis of Valuable Dipyrromethane Scaffolds: Classic and New Methods. *Molecules* **2019**, *24* (23), 4348.

(10) Boens, N.; Leen, V.; Dehaen, W. Fluorescent Indicators Based on BODIPY. *Chem. Soc. Rev.* **2012**, *41* (3), 1130−1172.

(11) Radunz, S.; Tschiche, H. R.; Moldenhauer, D.; Resch-Genger, U. Broad Range ON/OFF pH Sensors Based on pKa Tunable Fluorescent BODIPYs. *Sens. Actuators, B* **2017**, *251*, 490−494.

(12) Radunz, S.; Andresen, E.; Würth, C.; Koerdt, A.; Tschiche, H. R.; Resch-Genger, U. Simple Self-Referenced Luminescent pH Sensors Based on Upconversion Nanocrystals and pH-Sensitive Fluorescent BODIPY Dyes. *Anal. Chem.* **2019**, *91* (12), 7756−7764.

(13) Gotor, R.; Ashokkumar, P.; Hecht, M.; Keil, K.; Rurack, K. Optical pH Sensor Covering the Range from pH 0−14 Compatible with Mobile-Device Readout and Based on a Set of Rationally Designed Indicator Dyes. *Anal. Chem.* **2017**, *89* (16), 8437−8444.

(14) Lee, J.-S.; Kang, N.-y.; Kim, Y. K.; Samanta, A.; Feng, S.; Kim, H. K.; Vendrell, M.; Park, J. H.; Chang, Y.-T. Synthesis of a BODIPY Library and Its Application to the Development of Live Cell Glucagon Imaging Probe. *J. Am. Chem. Soc.* **2009**, *131* (29), 10077−10082.

(15) Kamkaew, A.; Lim, S. H.; Lee, H. B.; Kiew, L. V.; Chung, L. Y.; Burgess, K. BODIPY Dyes in Photodynamic Therapy. *Chem. Soc. Rev.* **2013**, *42* (1), 77−88.

(16) Kue, C. S.; Ng, S. Y.; Voon, S. H.; Kamkaew, A.; Chung, L. Y.; Kiew, L. V.; Lee, H. B. Recent Strategies to Improve Boron Dipyrromethene (BODIPY) for Photodynamic Cancer Therapy: an Updated Review. *Photochem. Photobiol. Sci.* **2018**, *17* (11), 1691−1708.

(17) Turksoy, A.; Yildiz, D.; Akkaya, E. U. Photosensitization and Controlled Photosensitization with BODIPY Dyes. *Coord. Chem. Rev.* **2019**, *379*, 47−64.

(18) Jung, H. S.; Han, J.; Shi, H.; Koo, S.; Singh, H.; Kim, H.-J.; Sessler, J. L.; Lee, J. Y.; Kim, J.-H.; Kim, J. S. Overcoming the Limits of Hypoxia in Photodynamic Therapy: A Carbonic Anhydrase IX-Targeted Approach. *J. Am. Chem. Soc.* **2017**, *139* (22), 7595−7602.

(19) Liu, J.-Y.; Huang, Y.; Menting, R.; Röder, B.; Ermilov, E. A.; Ng, D. K. P. A Boron Dipyrromethene−phthalocyanine Pentad as an Artificial Photosynthetic Model. *Chem. Commun.* **2013**, *49* (29), 2998−3000.

(20) Meng, L.-B.; Li, D.; Xiong, S.; Hu, X.-Y.; Wang, L.; Li, G. FRET-capable Supramolecular Polymers Based on a BODIPY-bridged Pillar[5]arene Dimer with BODIPY Guests for Mimicking the Light-harvesting System of Natural Photosynthesis. *Chem. Commun.* **2015**, *51* (22), 4643−4646.

(21) Bessette, A.; Hanan, G. S. Design, Synthesis and Photophysical Studies of Dipyrromethene-based Materials: Insights into Their Applications in Organic Photovoltaic Devices. *Chem. Soc. Rev.* **2014**, *43* (10), 3342−3405.

(22) Bañuelos, J. BODIPY Dye, the Most Versatile Fluorophore Ever? *Chem. Rec.* **2016**, *16* (1), 335−348.

(23) Burghart, A.; Kim, H.; Welch, M. B.; Thoresen, L. H.; Reibenspies, J.; Burgess, K.; Bergström, F.; Johansson, L. B. Å. 3,5-Diaryl-4,4-difluoro-4-bora-3a,4a-diaza-s-indacene (BODIPY) Dyes: Synthesis, Spectroscopic, Electrochemical, and Structural Properties. *J. Org. Chem.* **1999**, *64* (21), 7813−7819.

(24) Burghart, A.; Thoresen, L. H.; Chen, J.; Burgess, K.; Bergström, F.; Johansson, L. B. Å. Energy Transfer Cassettes Based on BODIPY Dyes. *Chem. Commun.* **2000**, No. 22, 2203−2204.

(25) Kim, H.; Burghart, A.; Welch, M. B.; Reibenspies, J.; Burgess, K. Synthesis and Spectroscopic Properties of a New 4-Bora-3a,4a-diaza-s-indacene (BODIPY®) Dye. *Chem. Commun.* **1999**, *18*, 1889−1890.

(26) Ogle, M. M.; Smith McWilliams, A. D.; Ware, M. J.; Curley, S. A.; Corr, S. J.; Martí, A. A. Sensing Temperature in Vitro and in Cells Using a BODIPY Molecular Probe. *J. Phys. Chem. B* **2019**, *123* (34), 7282−7289.

(27) Wang, D.; Miyamoto, R.; Shiraishi, Y.; Hirai, T. BODIPY-Conjugated Thermoresponsive Copolymer as a Fluorescent Thermometer Based on Polymer Microviscosity. *Langmuir* **2009**, *25* (22), 13176−13182.

(28) Levitt, J. A.; Kuimova, M. K.; Yahioglu, G.; Chung, P.-H.; Suhling, K.; Phillips, D. Membrane-Bound Molecular Rotors Measure Viscosity in Live Cells via Fluorescence Lifetime Imaging. *J. Phys. Chem. C* **2009**, *113* (27), 11634−11642.

(29) Han, J.; Burgess, K. Fluorescent Indicators for Intracellular pH. *Chem. Rev.* **2010**, *110* (5), 2709−2728.

(30) Zhao, C.; Zhu, W. Boron-Containing BODIPY Chromophore for Fluorescent Sensing. *Boron: Sensing, Synthesis and Supramolecular Self-Assembly*; Royal Society of Chemistry: 2016; Chapter 7, pp 202−235.

(31) Kee, H. L.; Kirmaier, C.; Yu, L.; Thamyongkit, P.; Youngblood, W. J.; Calder, M. E.; Ramos, L.; Noll, B. C.; Bocian, D. F.; Scheidt, W. R.; Birge, R. R.; Lindsey, J. S.; Holten, D. Structural Control of the Photodynamics of Boron−Dipyrrin Complexes. *J. Phys. Chem. B* **2005**, *109* (43), 20433−20443.
(32) Kuimova, M. K.; Yahioglu, G.; Levitt, J. A.; Suhling, K. Molecular Rotor Measures Viscosity of Live Cells via Fluorescence Lifetime Imaging. *J. Am. Chem. Soc.* **2008**, *130* (21), 6672−6673.
(33) Alamiry, M. A. H.; Benniston, A. C.; Copley, G.; Elliott, K. J.; Harriman, A.; Stewart, B.; Zhi, Y.-G. A Molecular Rotor Based on an Unhindered Boron Dipyrromethene (Bodipy) Dye. *Chem. Mater.* **2008**, *20* (12), 4024−4032.
(34) Lindsey, J. S.; Wagner, R. W. Investigation of the Synthesis of Ortho-substituted Tetraphenylporphyrins. *J. Org. Chem.* **1989**, *54* (4), 828−836.
(35) Bartelmess, J.; Weare, W. W.; Latortue, N.; Duong, C.; Jones, D. S. Meso-Pyridyl BODIPYs with Tunable Chemical, Optical and Electrochemical Properties. *New J. Chem.* **2013**, *37* (9), 2663−2668.
(36) Sheldrick, G. M. *SADABS, Program for Empirical Absorption Correction of Area Detector Data*; University of Göttingen: Göttingen, Germany, 2002.
(37) *SAINT*; Bruker Analytical X-ray Instruments Inc.: Madison, WI, 1998.
(38) *APEX2*; Bruker Analytical X-ray Instruments Inc.: Madison, WI, 2001.
(39) Sheldrick, G. M. *SHELXS/L-97, Programs for Crystal Structure Determination*; University of Göttingen: Göttingen, Germany, 1997.
(40) Sheldrick, G. M. A Short History of SHELX. *Acta Crystallogr., Sect. A: Found. Crystallogr.* **2008**, *64*, 112−122.
(41) van der Sluis, P.; Spek, A. L. BYPASS: an Effective Method for the Refinement of Crystal Structures Containing Disordered Solvent Regions. *Acta Crystallogr., Sect. A: Found. Crystallogr.* **1990**, *46* (3), 194−201.
(42) *TURBOMOLE V7.0 2015*; A Development of University of Karlsruhe and Forschungszentrum Karlsruhe GmbH; 1989−2007, TURBOMOLE GmbH, since 2007, available from http://www.turbomole.com.
(43) Perdew, J. P. Density-functional Approximation for the Correlation Energy of the Inhomogeneous Electron Gas. *Phys. Rev. B: Condens. Matter Mater. Phys.* **1986**, *33* (12), 8822−8824.
(44) Becke, A. D. Density-functional Exchange-energy Approximation with Correct Asymptotic Behavior. *Phys. Rev. A: At., Mol., Opt. Phys.* **1988**, *38* (6), 3098−3100.
(45) Weigend, F.; Ahlrichs, R. Balanced Basis Sets of Split Valence, Triple Zeta Valence and Quadruple Zeta Valence Quality for H to Rn: Design and Assessment of Accuracy. *Phys. Chem. Chem. Phys.* **2005**, *7* (18), 3297−3305.
(46) Würth, C.; Grabolle, M.; Pauli, J.; Spieles, M.; Resch-Genger, U. Relative and Absolute Determination of Fluorescence Quantum Yields of Transparent Samples. *Nat. Protoc.* **2013**, *8* (8), 1535−1550.
(47) Picou, C. L.; Stevens, E. D.; Shah, M.; Boyer, J. H. Structure of 4,4-Difluoro-1,3,5,7,8-pentamethyl-3a,4a-diaza-4-bora-*s*-indacene. *Acta Crystallogr., Sect. C: Cryst. Struct. Commun.* **1990**, *46*, 1148−1150.
(48) Wang, D.-C.; He, C.; Fan, J.-L.; Huang, W.-W.; Peng, X.-J. 8-(4-Bromophenyl)-4,4-difluoro-1,3,5,7-tetramethyl-4-bora-3a.4a-diaza-*s*-indacene. *Acta Crystallogr., Sect. E: Struct. Rep. Online* **2007**, *63*, o2900.
(49) Hecht, M.; Kraus, W.; Rurack, K. A Highly Fluorescent pH Sensing Membrane for the Alkaline pH Range Incorporating a BODIPY Dye. *Analyst* **2013**, *138* (1), 325−332.
(50) Kraus, W.; Nolze, G. POWDER CELL - A Program for the Representation and Manipulation of Crystal Structures and Calculation of the Resulting X-ray Powder Patterns. *J. Appl. Crystallogr.* **1996**, *29* (3), 301−303.
(51) IUPAC. *Compendium of Chemical Terminology*, 2nd ed. (the "Gold Book"); Blackwell Scientific Publications: Oxford, U.K., 1997.
(52) Planck Collaboration.. Planck 2015 results. *Astron. Astrophys.* **2016**, *594*, A13.
(53) Lakowicz, J. R. *Principles of Fluorescence Spectroscopy*, 3rd ed.; Springer: 2006; pp XXVI, 954.
(54) Jaque, D.; Vetrone, F. Luminescence Nanothermometry. *Nanoscale* **2012**, *4* (15), 4301−4326.
(55) Prlj, A.; Vannay, L.; Corminboeuf, C. Fluorescence Quenching in BODIPY Dyes: The Role of Intramolecular Interactions and Charge Transfer. *Helv. Chim. Acta* **2017**, *100* (6), No. e1700093.
(56) Lou, Z.; Hou, Y.; Chen, K.; Zhao, J.; Ji, S.; Zhong, F.; Dede, Y.; Dick, B. Different Quenching Effect of Intramolecular Rotation on the Singlet and Triplet Excited States of Bodipy. *J. Phys. Chem. C* **2018**, *122* (1), 185−193.
(57) Li, F.; Yang, S. I.; Ciringh, Y.; Seth, J.; Martin, C. H.; Singh, D. L.; Kim, D.; Birge, R. R.; Bocian, D. F.; Holten, D.; Lindsey, J. S. Design, Synthesis, and Photodynamics of Light-Harvesting Arrays Comprised of a Porphyrin and One, Two, or Eight Boron-Dipyrrin Accessory Pigments. *J. Am. Chem. Soc.* **1998**, *120* (39), 10001−10017.
(58) Laine, M.; Barbosa, N. A.; Wieczorek, R.; Melnikov, M. Y.; Filarowski, A. Calculations of BODIPY Dyes in the Ground and Excited States Using the M06-2X and PBE0 Functionals. *J. Mol. Model.* **2016**, *22* (11), 260.
(59) Radunz, S.; Wedepohl, S.; Röhr, M.; Calderon, M.; Tschiche, H. R.; Resch-Genger, U. pH Activatable Singlet Oxygen Generating BODIPYs for Photodynamic Therapy and Bioimaging. *J. Med. Chem.* **2020**, DOI: 10.1021/acs.jmedchem.9b01873.

Temperature- and Structural-Dependent Optical Properties and Photophysics of BODIPY Dyes

Sebastian Radunz,[a] Werner Kraus,[a] Florian A. Bischoff,[b] Franziska Emmerling,[a,b] Harald Rune Tschiche[c] and Ute Resch-Genger[a]*

[a] Department 1 – Analytical Chemistry; Reference Materials, Federal Institute for Materials Research and Testing (BAM), Richard-Willstaetter-Str. 11, 12489 Berlin, Germany. E-mail: ute.resch@bam.de
[b] Department of Chemistry, Humboldt-Universität zu Berlin, Brook-Taylor-Straße 2, 12489 Berlin, Germany.
[c] Department of Chemical and Product Safety, German Federal Institute for Risk Assessment (BfR), Max-Dohrn-Str. 8-10, 10589 Berlin, Germany.

Electronic Supplementary Information (ESI)

Experimental Section

Synthesis of fluorescent pH sensitive BODIPYs:
The corresponding aldehyde (2.5 mmol, 1.0 eq.) and 2,4-dimethylpyrrole (5.0 mmol, 2.0 eq.) were dissolved in 140 ml dry DCM and 10 ml dry EtOH. After degassing by rapid vacuum-argon cycles (5 times), a few drops of TFA (30 µl) were added and the reaction mixture was stirred at room temperature under argon atmosphere in the dark overnight. *p*-Chloranil (2.5 mmol, 1.0 eq.) was added and the mixture was stirred for additional 60 min. Prior addition of $BF_3 \cdot OEt_2$ (25.0 mmol, 10.0 eq.) and 4.3 ml diisopropylethylamine (DIPEA) (25.0 mmol, 10.0 eq.), the DCM/EtOH solvent mixture was removed under reduced pressure and replaced by 100 ml of dry DCM to avoid a reaction between $BF_3 \cdot OEt_2$ and EtOH. After portionwise addition, the reaction mixture was stirred for 60 minutes. Subsequently, the reaction mixture was prepurified by carrying out a short silica-gel flash column chromatography with DCM as eluent. The resulting crude mixture was concentrated under reduced pressure and further purified by

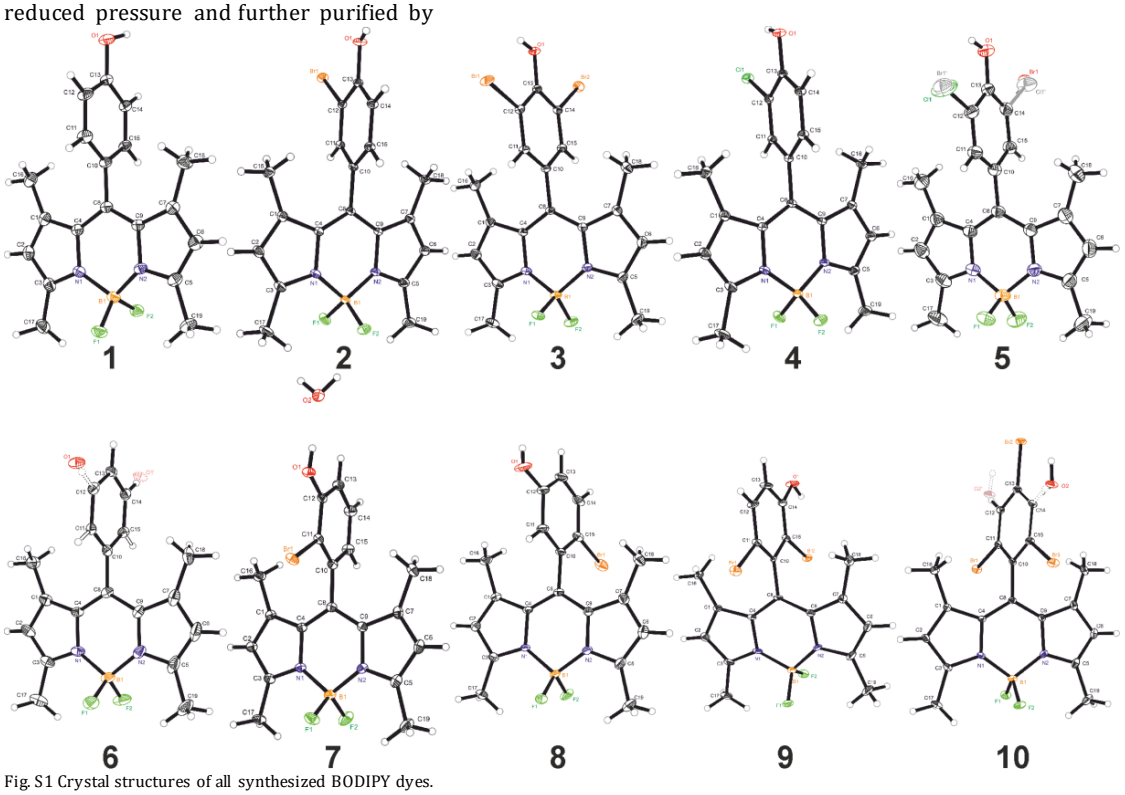

Fig. S1 Crystal structures of all synthesized BODIPY dyes.

Table S1. Selected crystallographic data and structure refinement parameters.

Compound reference	1	2	3	4	5	6	7	8	9	10
Chemical formula	$C_{19}H_{19}BF_2N_2O$	$C_{19}H_{18}BBrF_2N_2O$	$C_{19}H_{17}BBr_2FN_2O$	$C_{19}H_{18}BClF_2N_2O$	$C_{19}H_{17}BBrClF_2N_2O$	$C_{19}H_{18}BF_2N_2O$	$C_{19}H_{20}BBrF_2N_2O_2$	$C_{19}H_{18}BBrF_2N_2O$	$C_{19}H_{17}BBr_2FN_2O$	$C_{19}H_{16}BBr_3F_2N_2O$
Formula Mass /g mol^{-1}	340.17	419.07	497.97	374.61	452.51	339.16	437.09	419.07	497.97	576.88
Crystal system	monoclinic	monoclinic	monoclinic	monoclinic	monoclinic	monoclinic	monoclinic	monoclinic	monoclinic	monoclinic
a /Å	13.8943	16.0546	12.6348	15.8689	12.6330	13.8906	11.4965	7.0391	13.4725	26.5236
b/Å	9.6155	13.4873	10.6680	13.4387	10.7186	25.8723	8.9786	14.1435	19.8851	10.3333
c/Å	13.8974	16.4137	15.1098	16.2719	15.1341	14.1900	18.2352	20.8508	7.4708	17.5893
α/°	90	90	90	90	90	90	90	90	90	90
β/°	113.810	96.9234	107.3285	95.8495	107.1048	91.0486	91.431	91.1289	109.6622	125.3134
γ/°	90	90	90	90	90	90	90	90	90	90
Unit cell volume /Å^3	1698.7	3528.2	1944.18	3452.0	1958.64	5098.8	1881.68	2075.45	1884.74	3933.8
Temperature /K	150(2)	150(2)	150(2)	150(2)	297(2)	150(2)	150(2)	150(2)	150(2)	150(2)
Space group	*P*21/*n*	*P*21/*n*	*P*21/*n*	*P*21/*n*	*P*21/*n*	*P*21/*c*	*Cc*	*P*21/*n*	*Cc*	*C*2/*c*
No. of formula units per unit cell, Z	4	8	4	8	4	12	4	4	4	8
Absorption coefficient, μ/mm^{-1}	0.097	2.361	4.199	0.252	2.264	0.097	2.220	2.007	4.332	6.184
No. of reflections measured	29038	107330	74846	92931	42661	130154	27890	67769	30356	101847
No. of independent reflections	4224	10821	9966	11048	4887	12704	4698	6364	6201	13128
R_{int}	0.1955	0.0933	0.1082	0.1039	0.1257	0.1993	0.0936	0.1050	0.1371	0.0817
Final R_1 values ($I > 2\sigma(I)$)	0.0736	0.0407	0.0459	0.0628	0.0440	0.1276	0.0335	0.0569	0.0546	0.0628
Final $wR(F^2)$ values ($I > 2\sigma(I)$)	0.1696	0.0986	0.1120	0.1494	0.1111	0.2203	0.0852	0.1203	0.1181	0.1156
Final R_1 values (all data)	0.1274	0.0520	0.0739	0.0878	0.0654	0.1943	0.0342	0.0719	0.0775	0.1054
Final $wR(F^2)$ values (all data)	0.1989	0.1060	0.1252	0.1640	0.1268	0.2431	0.0859	0.1272	0.1455	0.1287
Goodness of fit on F^2	1.034	1.022	1.013	1.051	1.074	1.222	1.044	1.085	1.071	1.084
CCDC number	1969036	1969037	1969038	1969039	1969040	1969041	1969042	1969043	1969044	1969045

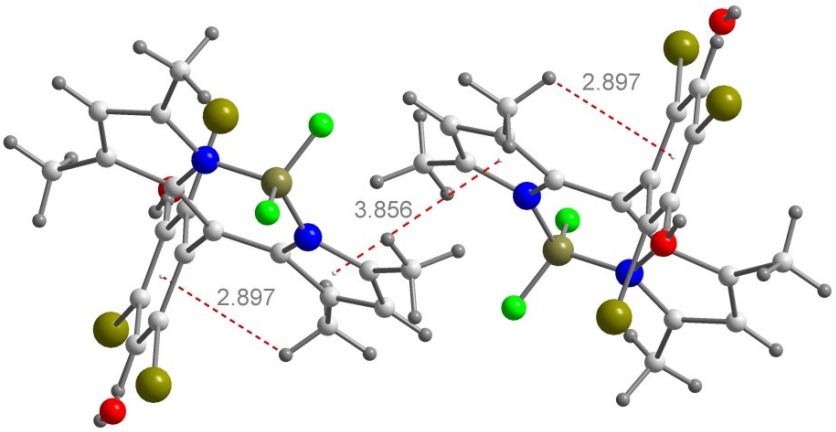

Fig. S2 Crystal packing and stabilizing inter- and intramolecular interactions.

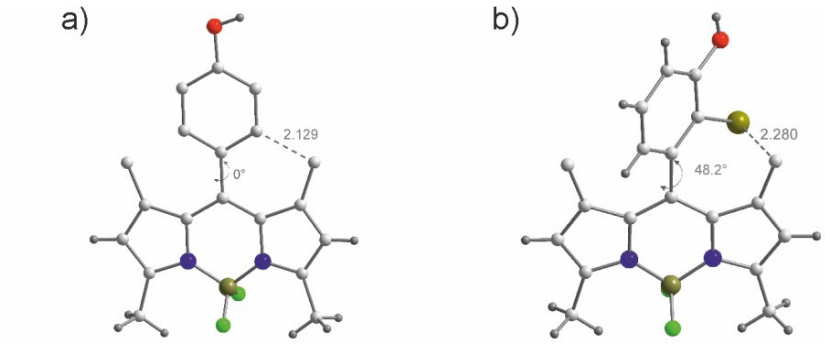

*Fig. S3 Hypothetical rotation of the meso-aryl along the C8-C10 axis of BODIPY **1** and **7**.*

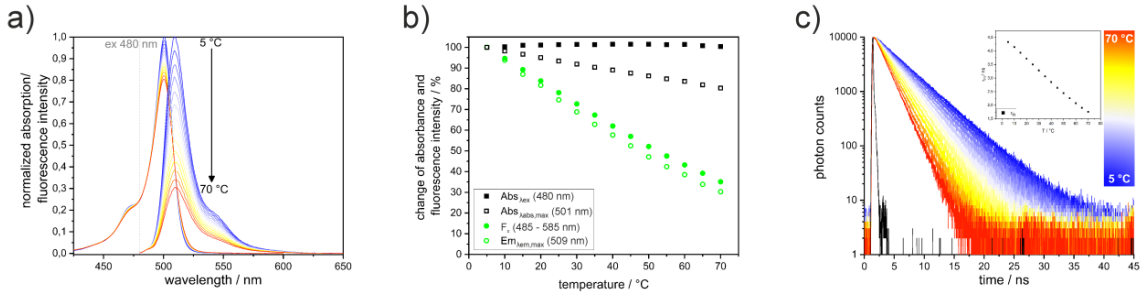

Fig. S4 a) Temperature-dependent normalized absorption and normalized fluorescence intensity of non-sterically hindered compound **2** upon excitation at 480 nm. b) Percentage changes of the absorbance (black squares) at excitation wavelength and at maximum absorbance (full and open symbols, respectively), and percentage changes of the fluorescence intensity (green circles) for integrated emission intensity and at emission maximum (full and open symbols, respectively) in dependence of temperature for compound **2**. c) Fluorescence decay curves for compound **2** in dependence of the temperature (black line represents the instrument response function (IRF)). The inset shows the mono exponential fitted fluor escence lifetime as function of temperature.

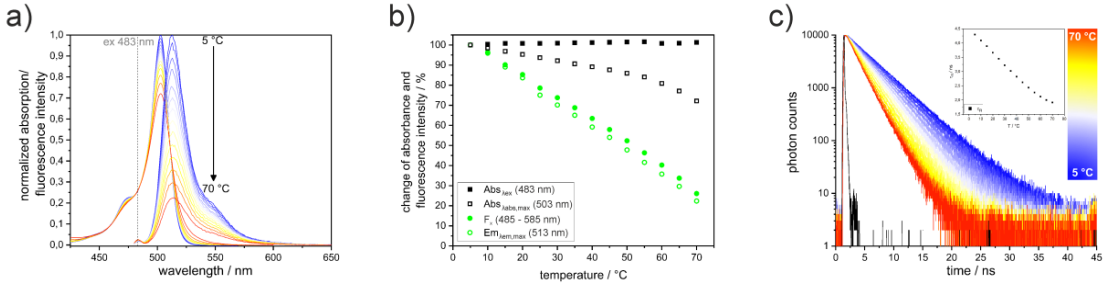

Fig. S5 a) Temperature-dependent normalized absorption and normalized fluorescence intensity of non-sterically hindered compound **3** upon excitation at 483 nm. b) Percentage changes of the absorbance (black squares) at excitation wavelength and at maximum absorbance (full and open symbols, respectively), and percentage changes of the fluorescence intensity (green circles) for integrated emission intensity and at emission maximum (full and open symbols, respectively) in dependence of temperature for compound **3**. c) Fluorescence decay curves for compound **3** in dependence of the temperature (black line represents the instrument response function (IRF)). The inset shows the mono exponential fitted fluor escence lifetime as function of temperature.

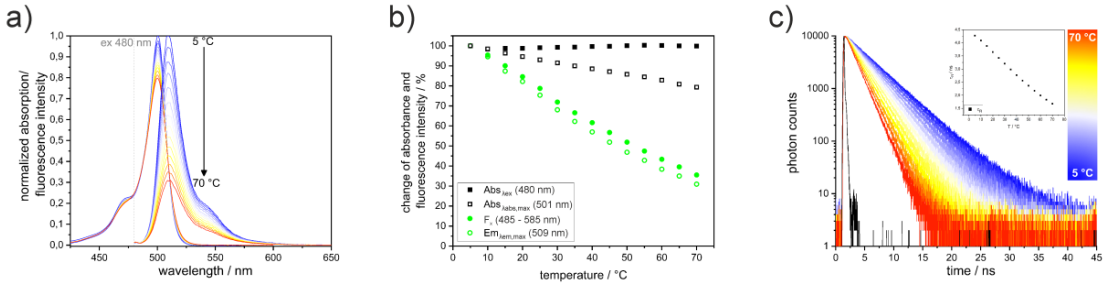

Fig. S6 a) Temperature-dependent normalized absorption and normalized fluorescence intensity of non-sterically hindered compound **4** upon excitation at 480 nm. b) Percentage changes of the absorbance (black squares) at excitation wavelength and at maximum absorbance (full and open symbols, respectively), and percentage changes of the fluorescence intensity (green circles) for integrated emission intensity and at emission maximum (full and open symbols, respectively) in dependence of temperature for compound **4**. c) Fluorescence decay curves for compound **4** in dependence of the temperature (black line represents the instrument response function (IRF)). The inset shows the mono exponential fitted fluorescence lifetime as function of temperature.

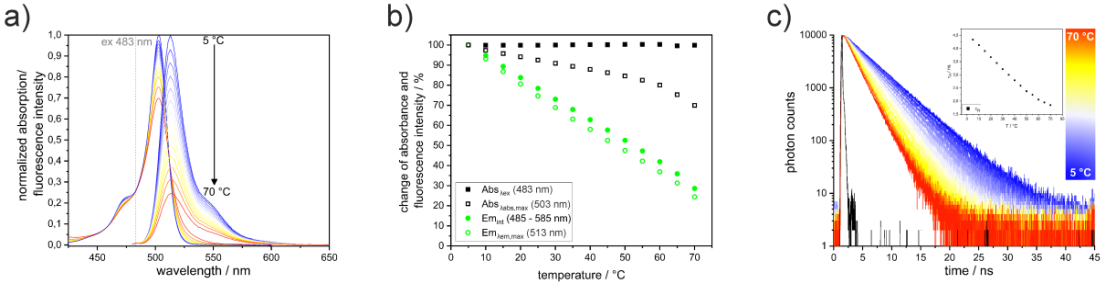

Fig. S7 a) Temperature-dependent normalized absorption and normalized fluorescence intensity of non-sterically hindered compound **5** upon excitation at 483 nm. b) Percentage changes of the absorbance (black squares) at excitation wavelength and at maximum absorbance (full and open symbols, respectively), and percentage changes of the fluorescence intensity (green circles) for integrated emission intensity and at emission maximum (full and open symbols, respectively) in dependence of temperature for compound **5**. c) Fluorescence decay curves for compound **5** in dependence of the temperature (black line represents the instrument response function (IRF)). The inset shows the mono exponential fitted fluorescence lifetime as function of temperature.

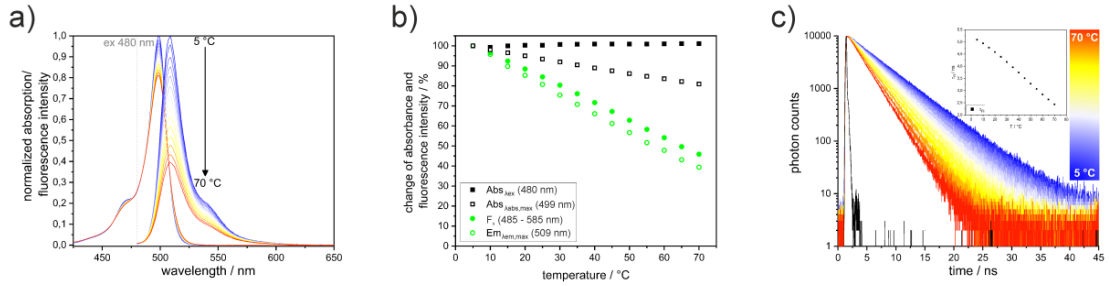

Fig. S8 a) Temperature-dependent normalized absorption and normalized fluorescence intensity of non-sterically hindered compound **6** upon excitation at 480 nm. b) Percentage changes of the absorbance (black squares) at excitation wavelength and at maximum absorbance (full and open symbols, respectively), and percentage changes of the fluorescence intensity (green circles) for integrated emission intensity and at emission maximum (full and open symbols, respectively) in dependence of temperature for compound **6**. c) Fluorescence decay curves for compound **6** in dependence of the temperature (black line represents the instrument response function (IRF)). The inset shows the mono exponential fitted fluorescence lifetime as function of temperature.

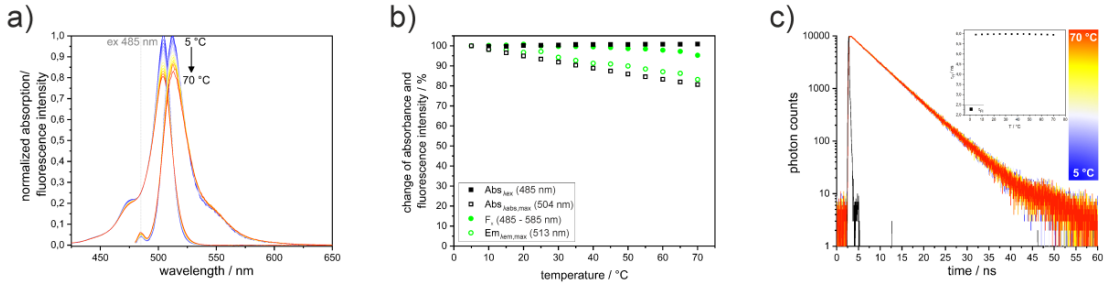

Fig. S9 a) Temperature-dependent normalized absorption and normalized fluorescence intensity of sterically hindered compound **8** upon excitation at 485 nm. b) Percentage changes of the absorbance (black squares) at excitation wavelength and at maximum absorbance (full and open symbols, respectively), and percentage changes of the fluorescence intensity (green circles) for integrated emission intensity and at emission maximum (full and open symbols, respectively) in dependence of temperature for compound **8**. c) Fluorescence decay curves for compound **8** in dependence of the temperature (black line represents the instrument response function (IRF)). The inset shows the mono exponential fitted fluorescence lifetime as function of temperature.

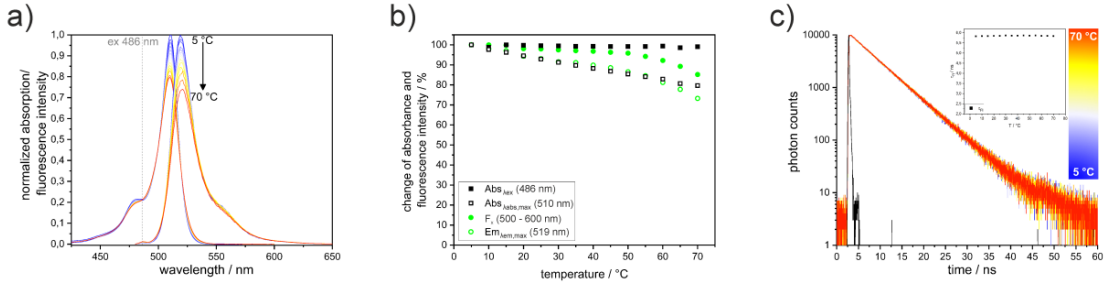

Fig. S10 a) Temperature-dependent normalized absorption and normalized fluorescence intensity of sterically hindered compound **9** upon excitation at 486 nm. b) Percentage changes of the absorbance (black squares) at excitation wavelength and at maximum absorbance (full and open symbols, respectively), and percentage changes of the fluorescence intensity (green circles) for integrated emission intensity and at emission maximum (full and open symbols, respectively) in dependence of temperature for compound **9**. c) Fluorescence decay curves for compound **9** in dependence of the temperature (black line represents the instrument response function (IRF)). The inset shows the mono exponential fitted fluorescence lifetime as function of temperature.

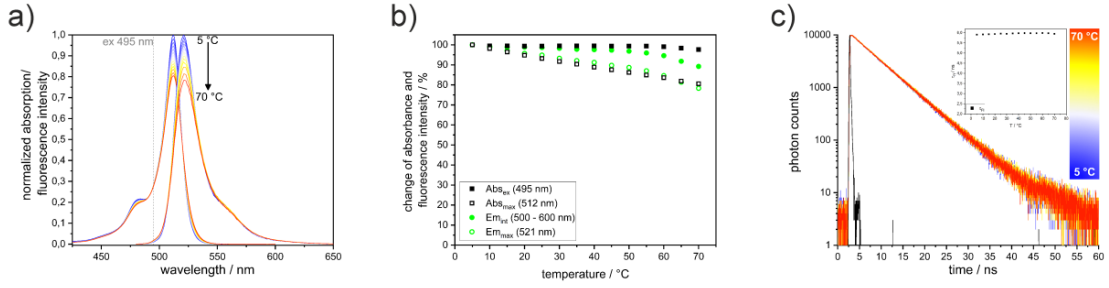

Fig. S11 a) Temperature-dependent normalized absorption and normalized fluorescence intensity of sterically hindered compound **10** upon excitation at 495 nm. b) Percentage changes of the absorbance (black squares) at excitation wavelength and at maximum absorbance (full and open symbols, respectively), and percentage changes of the fluorescence intensity (green circles) for integrated emission intensity and at emission maximum (full and open symbols, respectively) in dependence of temperature for compound **10**. c) Fluorescence decay curves for compound **10** in dependence of the temperature (black line represents the instrument response function (IRF)). The inset shows the mono exponential fitted fluorescence lifetime as function of temperature.

Table S2. Calculated absolute and relative energies of the minimum (min1, min2), the transition (TS1, TS2) and intermediate (IS) states and corresponding dihedral angles of BODIPY compounds **1**, **3**, **6**, **7**, **8** and **9**.

Dye	*absolute energy / E_h (relative energy / kcalmol^{-1})*					*dihedral angle[a] / °*					*$t_{1/2}$[b] / s (20 °C)*
	min 1	TS 1	IS	TS 2	min 2	min 1	TS 1	IS	TS 2	min 2	*min->TS1*
1	0	16.4	16.1	16.4	0	90	14	3	-14	-90	0.2
3	0	16.7	-	-	0.03	90	14			-93	0.3
6	0	12.9	12.7	12.8	0	40	13	3	-13	-40	$4.8 * 10^{-4}$
7	0	42.3	-	-	0		34				$3.9 * 10^{18}$
8	0	38.2	-	-	0.3	89	29			-92	$3.1 * 10^{15}$
9	0	49.2	46.6	49.2	0	90	39	10.5	-39	-90	$5.1 * 10^{23}$

[a] Dihedral angle determined by....

[b] Half-life calculated assuming first order reaction kinetics $t_{1/2} = \frac{\ln(2)}{k}$, with $k = \kappa \frac{k_B T}{h} e^{-\frac{\Delta G}{RT}}$ from Eyring equation with k_B = Boltzmann constant, T = 293.15 K, h = Planck constant, κ = 1 (transmission coefficient) and R = gas constant.

Table S3. Temperature-dependent non-radiative decay rates k_{nr}.

Dye	k_{nr} (T) / 10^8 s^{-1}		
	5 °C	20 °C	70 °C
1	0.66 ± 0.05	1.16 ± 0.05	4.91 ± 0.05
2	0.62 ± 0.06	1.07 ± 0.06	4.29 ± 0.06
3	0.72 ± 0.05	1.15 ± 0.05	4.32 ± 0.05
4	0.71 ± 0.07	1.12 ± 0.07	4.53 ± 0.07
5	0.71 ± 0.05	1.15 ± 0.05	4.36 ± 0.05
6	0.29 ± 0.02	0.55 ± 0.02	2.57 ± 0.02
7	0.15 ± 0.01	0.15 ± 0.01	0.24 ± 0.01
8	0.18 ± 0.01	0.18 ± 0.01	0.30 ± 0.01
9	0.18 ± 0.01	0.21 ± 0.01	0.43 ± 0.01
10	0.20 ± 0.01	0.22 ± 0.01	0.37 ± 0.01

Table S4..Fitting parameters fot the determination of ΔE_A for non-radiative decay of the first exited state S_1

Dye	$\frac{\Delta E_A}{R}$ (Φ_{Fl}) / K[a]	$E_A(\Phi_{Fl})$ / kcalmol^{-1}[a]	ln (c2) (Φ_{Fl})[a]	R^2 (Φ_{Fl})	$\frac{\Delta E_A}{R}$ (τ_{Fl}) / K[b]	$E_A(\tau_{Fl})$ / kcalmol^{-1}[b]	ln (A) (τ_{Fl})	c_3 (τ_{Fl})/ 10^8 s^{-1}*	R^2 (τ_{Fl})
1	-3030 ± 19	6.02 ± 0.30	9,97 ± 0,06	0,999	-2981 ± 13	5.92 ± 0.30	7,94 ± 0,04	1,75	0,999
2	-3058 ± 12	6.08 ± 0.30	10,00 ± 0,04	0,999	-2956 ± 11	5.87 ± 0.29	7,68 ± 0,03	1,78	0,999
3	-3255 ± 133	6.47 ± 0.32	10,79 ± 0,43	0,979	-3029 ± 10	6.02 ± 0.22	7,94 ± 0,03	1,78	0,999
4	-2972 ± 30	5.91 ± 0.30	9,80 ± 0,10	0,999	-2989 ± 19	5.94 ± 0.30	7,84 ± 0,06	1,79	0,999
5	-3101 ± 100	6.16 ± 0.31	10,26 ± 0,32	0,987	-3046 ± 7	6.05 ± 0.23	8,02 ± 0,02	1,78	0,998
6	-3289 ± 32	6.54 ± 0.33	10,11 ± 0,11	0,999	-3241 ± 28	6.44 ± 0.32	8,02 ± 0,09	1,70	0,999
7	-739 ± 56	1.47 ± 0.29	0,21± 0,18	0,927	-[c]		-[c]	-[c]	-[c]
8	-751 ± 67	1.49 ± 0.30	0,52 ± 0,21	0,913	-[c]		-[c]	-[c]	-[c]
9	-1380 ± 109	2.74 ± 0.55	2,68 ± 0,44	0,895	-[c]		-[c]	-[c]	-[c]
10	-927 ± 71	1.84 ± 0.37	1,27 ± 0,27	0,909	-[c]		-[c]	-[c]	-[c]

[a] iteratively determined following eq. 6 with $c_1 = 0$
[b] iteratively determined following eq. 8
[c] could not be determined

1. S. Radunz, H. R. Tschiche, D. Moldenhauer, U. Resch-Genger, *Sensors and Actuators B: Chemical* 2017, **251**, 490-494.

2.3 pH-Activatable Singlet Oxygen-Generating Boron-dipyrromethenes (BODIPYs) for Photodynamic Therapy and Bioimaging

Sebastian Radunz, Stefanie Wedepohl, Mathilde Röhr, Marcelo Calderón, Harald Rune Tschiche*, Ute Resch-Genger*

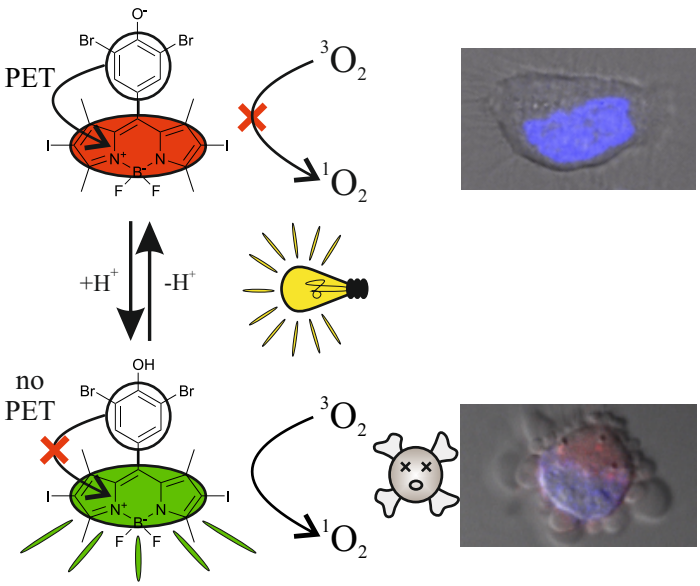

Figure 14: Reprinted with permission from S. Radunz *et al.*. [13] Copyright 2020 American Chemical Society.

In this publication S. Radunz established the concept, parts of the synthesis and parts of the analytical and spectroscopic characterization of the reported compounds. He performed only a few experiments but most of the data evaluation as well as he performed most of the scientific interpretation of the results. The publication was mainly conceived and written by him.

Journal of Medicinal Chemistry

pubs.acs.org/jmc Article

pH-Activatable Singlet Oxygen-Generating Boron-dipyrromethenes (BODIPYs) for Photodynamic Therapy and Bioimaging

Sebastian Radunz, Stefanie Wedepohl, Mathilde Röhr, Marcelo Calderón, Harald Rune Tschiche,* and Ute Resch-Genger*

Cite This: https://dx.doi.org/10.1021/acs.jmedchem.9b01873 Read Online

ACCESS | Metrics & More | Article Recommendations | Supporting Information

ABSTRACT: Singlet oxygen can severely damage biological tissue, which is exploited in photodynamic therapy (PDT). In PDT, the effective range is limited by the distribution of the photosensitizer (PS) and the illuminated area. However, no distinction is made between healthy and pathological tissue, which can cause undesired damage. This encouraged us to exploit the more acidic pH of cancerous tissue and design pH-controllable singlet oxygen-generating boron-dipyrromethene (BODIPY) dyes. A pH sensitivity of the dyes is achieved by the introduction of an electronically decoupled, photoinduced electron transfer (PET)-capable subunit in meso-position of the BODIPY core. To favor triplet-state formation as required for singlet oxygen generation, iodine substituents were introduced at the chromophore core. The resulting pH-controlled singlet oxygen-generating dyes with pK_a values in the physiological range were subsequently assessed regarding their potential as pH-controlled PS for PDT. Using HeLa cells, we could successfully demonstrate markedly different pH-dependent cytotoxicities upon illumination.

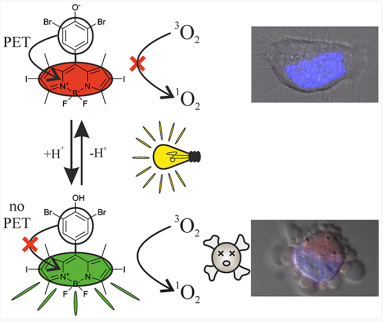

INTRODUCTION

Photodynamic therapy (PDT) has emerged as a very promising therapy for the treatment of a variety of cancers. This easily applicable, low invasive, and local method utilizes three individually nontoxic components, namely, the photosensitizer (PS), molecular oxygen in its ground triplet state ($^3O_2$), and light, that must be all simultaneously present. The light-activated PS is able to transfer energy to surrounding $^3O_2$, which results in the formation of singlet oxygen ($^1O_2$) and eventually reactive oxygen species (ROS).[1] The presence of a PS is essential as $^1O_2$ is not produced by light alone due to the spin- and symmetry-forbidden transition from $^3O_2$ to $^1O_2$.[2] The generated $^1O_2$ and ROS can induce highly localized cellular damage because of their low half-life due to strong reactivity,[3] which eventually leads to cell death by apoptotic and/or necrotic processes. Low side effects, a controllable range of performance, and a good selectivity of PDT rely on the increased accumulation of the PS in diseased tissue in conjunction with the local application of light.[4,5] Therefore, PDT is used for the treatment of several precancerous and malignant diseases as well as for inflammatory dermatitis and has been approved by the Food and Drug Administration (FDA) for the treatment of several forms of cancer and age-related macular degeneration.[6−10] Nevertheless, a better local control of PDT is still desired to keep damage to healthy tissue as low as possible.

The first generation of PS utilized for PDT was mostly porphyrin derivatives. However, they possess several drawbacks such as a challenging synthesis, rather unfavorable solubilities, and high dark toxicities.[11] Therefore, the search for new PS for PDT is ongoing, focusing on other promising dye classes. Although boron-dipyrromethene (BODIPY) dyes have shown to be suitable for PDT purposes over the last years,[12] they have gained substantial new attention only recently.[13−16] Particularly advantageous of this dye class is the high versatility and comparative ease of preparation together with their remarkable photophysical properties such as high molar absorption coefficients, high fluorescence quantum yields, and high photostability.[17−19] BODIPY dyes have already been successfully utilized as fluorescent probes and sensors for ionic and neutral analytes,[20] e.g., for pH,[21−23] for cell imaging,[24] as building blocks for artificial photosynthetic models,[25,26] and for dye-sensitized solar cells.[27] To increase the application potential of these highly fluorescent dyes for PDT, the population of the excited triplet state must be favored, thus increasing the quantum yield for singlet oxygen generation (ϕ_Δ). This is commonly achieved by introducing heavy halogens such as bromine and iodine substituents at the BODIPY core, thereby increasing the intersystem crossing rate from the first excited singlet state S_1 to the excited triplet state

Received: November 27, 2019
Published: January 22, 2020

T_1 of the dyes by the enhanced spin−orbit coupling.[28−33] As fluorescence and intersystem crossing (ISC) compete in the deactivation of the S_1 state, the fluorescence quantum yield (ϕ_f) of the dye is typically reduced in favor of an increased ϕ_Δ. However, the fluorescence is usually not completely quenched, which enables dual use as PS for PDT and as reporter for fluorescence imaging in theranostic applications.

In this study, we exploited the strategy of increasing ϕ_Δ by the introduction of iodine substituents at the BODIPY core in combination with the design concept of pH control of the optical properties derived from our previously reported BODIPYs.[21,23] These dyes feature on/off-switchable fluorescence due to a meso-substituted phenolic subunit that can efficiently deactivate the S_1 state via a photoinduced electron transfer (PET) in its deprotonated form. Thereby, we aim to selectively produce singlet oxygen solely in cancerous tissues which are known to be slightly more acidic than healthy ones.[34] As the PET-capable meso-subunit and the chromophore core are electronically decoupled, both features, singlet oxygen generation and pH sensitivity, can be combined. So far, only very few examples of BODIPY-based pH-activatable PS for selective PDT have been reported;[35−37] however, only PET-capable building blocks with amino groups have been used until now.[36−40] Phenolic PET-capable moieties as used by us, however, enable to cover a broader pH range and provide a better pK_a tunability,[21,22] which could be beneficial, e.g., for addressing different cell compartments specifically. In the following, we present the synthesis of these dyes, their spectroscopic properties, and the assessment of their potential for dual use as PS for PDT and as optical reporter for bioimaging.

RESULTS AND DISCUSSION

Synthesis and Characterization of pH-Sensitive Singlet Oxygen-Generating Molecules. Prior to the synthesis of pH-sensitive singlet oxygen-generating molecules, pH-responsive fluorescent precursor dyes **1a**, **1b**, and **1c** were prepared following our published procedure (see Scheme S1, Supporting Information (SI)).[21,23] The degree of substitution as well as the substitution pattern of the electronically decoupled phenolic meso-subunit allow a tuning of the pK_a value and control the photophysical properties ϕ_f and fluorescence lifetime (τ_f), while the spectral position of the absorption and emission maxima are only minimally affected.[21] For this study, we used **1a−c** as precursor dyes as we aimed at derivatives with pK_a values in the physiological range (**1b, c**) suitable for biomedical applications. One compound with a basic pK_a, in this case, dye **1a**, was chosen as the precursor dye for an "always-on" control probe, which is assumed to always show singlet oxygen production upon illumination, as the pK_a value is expected to be more basic than the pH conditions in cells.

As ISC is mainly responsible for an effective generation of singlet oxygen, we introduced iodine substituents at the core of the precursor BODIPYs at 2- and 6-positions. While a substitution at the core should affect all photophysical properties, the pH sensitivity of the dyes controlled by the phenolic meso-substituent should remain unchanged, as the fluorophore core and the subunit are electronically decoupled. Iodination was done using respective equivalents of *N*-iodosuccinimide (NIS) to obtain mono- or diiodinated derivates **2a−c** and **3a−c**, respectively (see Figure 1), in reasonable yields (<20%). The chemical structure of all dyes

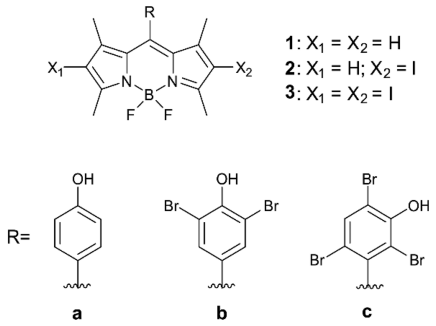

Figure 1. Chemical structures of the pH-sensitive BODIPY dyes.

synthesized was confirmed by NMR spectroscopy and mass spectrometry (see the Experimental Section). Subsequently, the photophysical properties and the capability of pH-controlled singlet oxygen generation of the dyes as well as the utilization as PDT agents were studied.

An overview of the spectroscopic properties of the synthesized BODIPY dyes is given in Table 1. All compounds have high molar absorption coefficients ε (>90 000 M^{-1} cm^{-1}) with a slight increase of ε upon iodination (see Table 1). As exemplarily shown in Figure 2a for the dyes with 3,5-dibromo-4-hydroxyphenyl as meso-substituent (**1b−3b**), a bathochromic shift of the absorption maximum from 501 to 515 to 534 nm for **1b**, **2b**, and **3b**, respectively, as well as of the emission maximum from 511 to 530 to 550 nm for **1b**, **2b**, and **3b**, respectively, is observed in dependence of the degree of substitution. Such a shift is typically observed upon introduction of auxochromes such as halogens. Iodination-induced red shifts in absorption in the same order of magnitude were also observed for **1a−3a** and **1c−3c** (see Table 1 and Figure S1, SI), while there are also differences in dependence of the substitution degree and pattern of the meso-subunit, as reported earlier.[21] Eventually, iodine substitution directly at the chromophore core has an overall stronger impact on the absorption and emission maxima than the substitution degree and pattern of the meso-substituent. To confirm the pH dependence of the optical properties of our BODIPYs, pH titrations were performed. In Figure 2b, a pH titration is exemplarily shown for compound **3b** in the pH range of 4.5−8.2. As can be seen, only minor changes can be observed in absorption while the fluorescence intensity is drastically decreased at more basic pH values throughout the titration. Under basic conditions, the fluorescence is completely switched off due to a highly efficient photoinduced electron transfer (PET). A pK_a value of 6.4 ± 0.1 for **3b** was derived by sigmoidal curve fitting (see Figure 2b, inset). This value is close to that of the precursor dye **1b** and the monoiodinated compound **2b**. The small differences are ascribed to iodination-induced changes in the electron density of the chromophore cores, which consequently lead to changes in the electron density of the meso-subunit directly affecting the acidity of the pH-sensitive hydroxyl group. For all compounds, a pH-dependent on/off switching of their fluorescence was observed. The pK_a values, however, differ drastically depending on the degree of substitution in meso-position ranging from 10.9−10.6 for **1a−3a**, respectively, to 5.9−5.4 for **1c−3c**, respectively (see Table 1). These findings as well as the derived pK_a values are in a good agreement with previously reported data.[21,23] The experimental data and the

https://dx.doi.org/10.1021/acs.jmedchem.9b01873
J. Med. Chem. XXXX, XXX, XXX−XXX

Table 1. Photophysical Properties of the Synthesized BODIPY Dyes

dye	$\varepsilon \times 10^{-3}$ (ACN) (M^{-1} cm^{-1})	$\lambda_{abs,max}$ (ACN) (nm)	$\lambda_{em,max}$ (ACN) (nm)	ϕ_f/%	$\phi_{\Delta dir}$/% (λ_{ex} = 532 nm)	$\phi_{\Delta ind}$/% (λ_{ex} = 532 nm)	pK_a[c]
1a	93 ± 7	497	506	59 ± 2	1 ± 2[a]	[b]	10.9 ± 0.1
2a	96 ± 8	509	524	3 ± 3	57 ± 7	56 ± 9	10.8 ± 0.1
3a	102 ± 4	528	543	2 ± 2	63 ± 11	58 ± 7	10.6 ± 0.2
1b	92 ± 5	501	511	64 ± 5	3 ± 3[a]	[b]	6.5 ± 0.1
2b	97 ± 5	515	530	3 ± 2	57 ± 5	60 ± 7	6.4 ± 0.2
3b	99 ± 6	534	550	2 ± 1	59 ± 8	63 ± 8	6.4 ± 0.1
1c	91 ± 3	510	518	91 ± 2	3 ± 3[a]	[b]	5.9 ± 0.2
2c	94 ± 3	525	539	5 ± 2	84 ± 8	89 ± 8	5.5 ± 0.1
3c	96 ± 4	546	562	2 ± 1	90 ± 9	92 ± 8	5.4 ± 0.1

[a] λ_{ex} = 510 nm, **3c** was used as a reference. [b] Not determined as absorption at λ_{ex} = 510 nm is too low. [c] pK_a corrected with respect to acetonitrile (ACN) content.

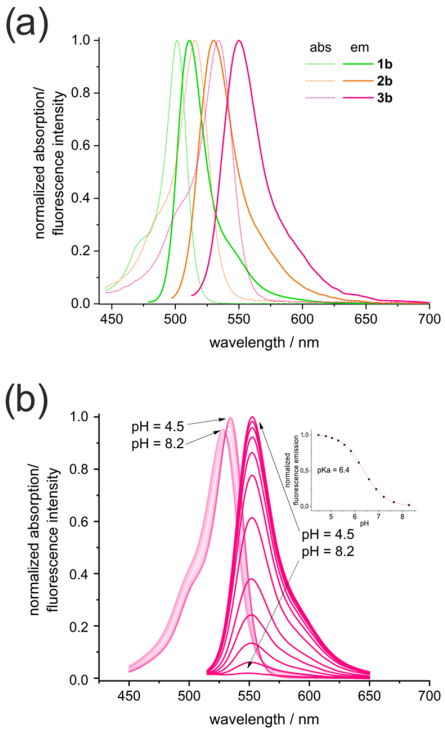

Figure 2. (a) Absorption and emission spectra of compounds **1b**, **2b**, and **3b** in ACN. (b) pH-dependent normalized absorption and fluorescence of BODIPY **3b** in a mixture of ACN and water (2/1 v/v, 25 mM buffered). The inset shows the normalized integrated fluorescence intensity depending on pH and the corresponding sigmoidal curve fit.

corresponding sigmoidal fits and fitting parameters can be found in the SI (Figure S2 and Table S2). These results confirm that the pH sensitivity of the dyes' fluorescence is retained upon iodination and that the pK_a values are only marginally affected by substitution at the chromophore core.

Subsequently, we studied the impact of iodination on ϕ_f as well as on ϕ_Δ. As shown in Table 1, the precursor dyes show high ϕ_f values of 59, 64, and 91% for **1a**, **1b**, and **1c**, respectively. ϕ_f for **1c** is outstanding and differs drastically from the ϕ_f values of **1a** and **1b** because the sterically hindered meso-subunit minimizes possible nonradiative deactivation pathways caused by internal conversion. Here, it is noteworthy to mention that ϕ_f is defined as the quotient of the rate constant for spontaneous emissions (k_r) and the sum of the rate constant for radiative (k_r) and nonradiative processes (k_{nr}) depopulating the first excited singlet state. The latter one is mainly governed by internal conversion (k_{IC}) and intersystem crossing (k_{ISC}), but other processes like charge transfer (CT) or PET can also contribute, depending on the internal and external conditions. In our case, CT and PET can be neglected as CT is not likely for our dyes and PET does not occur under acidic conditions as demonstrated by our measurements. Yet alone, by comparing the ϕ_f values of **1a**, **1b**, and **1c**, we can make assumptions regarding the contribution of k_{IC} as well as a rough benchmark for the maximum value of ϕ_Δ. By introducing a sterically hindered meso-substituent, an increase of ϕ_f for **1c** of roughly 30% is observed compared to **1a** and **1b**, which can most likely be attributed to a decrease of k_{IC}. Thus, we can assume for **1a** and **1b** that k_{IC} equals the main contribution to k_{nr} and that it is expected to remain in the same order of magnitude after iodine substitution at the core, defining an upper limit for ϕ_Δ considering the values for ϕ_f. As k_{nr} is assumed to remain constant, any changes of ϕ_f upon iodination are most likely caused by an increase of ϕ_Δ. As highlighted in Table 1 mono- and diiodination strongly decrease ϕ_f of the dyes **2a**–**c** and **3a**–**c** to the lower single-digit range (<5%). However, we did not observe significant differences between mono- and diiodination, both revealing exceptionally efficient fluorescence quenching. Subsequently, we determined ϕ_Δ values for our BODIPYs by an indirect method using 1,3-diphenylisobenzofuran (DPBF) as singlet oxygen quencher (yielding $\phi_{\Delta ind}$) as well as by utilizing a direct method of recording the luminescence intensity of singlet oxygen generated in situ (yielding $\phi_{\Delta dir}$). As exemplarily shown in Figure 3a, the concentration changes of DPBF (derived from the absorbance measured at the absorption maximum of 411 nm) upon illumination of **3b** with λ_{ex} = 532 nm can be observed depending upon the illumination time. While the absorbance of DPBF is drastically decreased due to the reaction with the generated singlet oxygen, the absorbance of **3b** remains constant. This indicates highly efficient quenching of singlet oxygen by DPBF and furthermore an overall good photostability of the BODIPY as **3b** neither decomposes nor shows photobleaching at least in the given time frame. The latter was verified by separate illumination of all compounds showing no changes in their absorbance upon illumination (see Figure S3a, exemplarily for **3b**, SI). For the determination of ϕ_Δ, the logarithm of the ratio of the initial and time-dependent concentrations of DFBF $\ln([DPBF]_0/[DPBF])$ was plotted in dependence of t. From the observed linear dependence (see Figure 3a, inset), we derived a depletion rate k (see eq 3). k

https://dx.doi.org/10.1021/acs.jmedchem.9b01873
J. Med. Chem. XXXX, XXX, XXX−XXX

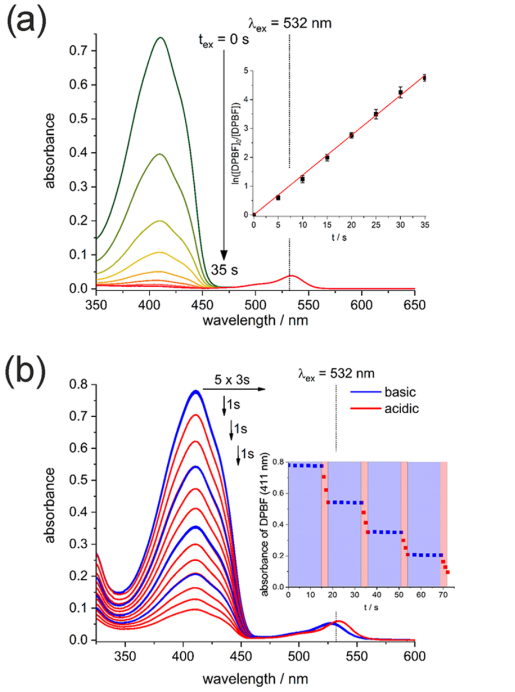

Figure 3. (a) Absorption spectra showing the decomposition of DPBF by singlet oxygen upon stepwise (7 x 5s) illumination of **3b** with a 532 nm laser diode. The inset shows the dependence of the DPBF concentration ([DPBF]) on illumination time. (b) Time-dependent changes in absorbance of DPBF upon illumination at λ_{ex} = 532 nm in the presence of **3b** and varying pH conditions (pH 10.5–2.5). The inset shows the illumination time- and pH-dependent changes in absorbance of DPBF derived from the absorption spectra.

was then utilized to relatively determine ϕ_Δ using rose bengal as a reference following eq 2. In comparison, the direct method exploits the integrated luminescence intensity F of the singlet oxygen emission at 1270 nm (see Figure S4, SI) to relatively determine ϕ_Δ (see eq 1). Directly and indirectly determined ϕ_Δ values of all synthesized compounds are given in Table 1.

While $\phi_{\Delta ind}$ could not be determined for the precursor dyes **1a–c** as they do not absorb at 532 nm, the output wavelength of our laser diode, $\phi_{\Delta dir}$ of **1a–c** was obtained using an excitation wavelength λ_{ex} of 510 nm and **3c** as reference. As to be expected, the precursor dyes for **1a**, **1b**, and **1c** show virtually no singlet oxygen generation ($\phi_{\Delta dir}$ of 1, 3, and 3%) with the singlet oxygen luminescence not being well distinguishable from background noise of the detector. This is astonishing as bromine is usually also capable of increasing k_{ISC} by enhanced spin–orbit coupling, however with a lower efficiency than iodine.[29,30] The negligible impact of the bromination at the meso-position of our dyes is ascribed to the electronically decoupled chromophore core and meso-subunit. However, iodination at the chromophore core has a huge impact on ϕ_Δ for mono-/diiodinated derivatives **2a–c** and **3a–c**. As can be seen from Table 1, ϕ_Δ values drastically increase up to roughly 60% for **2a,b** and **3a,b**, and up to roughly 90% for **2c** and **3c**. The values obtained for both determination methods used are in a very good agreement. However, no significant differences result for mono- and diiodination, considering the uncertainty of our measurements.

The obtained values for ϕ_Δ for the iodinated derivatives are in the same order of magnitude like the ϕ_f values for the corresponding precursor dyes. This has been already shown for similar systems, and these results confirm a highly efficient shift of the deactivation pathway of the excited singlet state from fluorescence to ISC by attaching heavy atoms at the chromophore core.[12,41] Considering rate constants, this proves that $k_{ISC} > k_r$ for our dyes. We furthermore deduce from our pH titration experiments that $k_{PET} > k_r$ and $k_{PET} < k_r$ for basic and acidic conditions, respectively. Conclusively, this leads to $k_{PET} > k_{ISC} > k_r$ and $k_{ISC} > k_r > k_{PET}$ for basic and acidic conditions, respectively, which is mandatory for the desired pH-controlled singlet oxygen generation. To verify this assumption for our dyes, we performed a stepwise illumination at λ_{ex} = 532 nm under varying pH conditions and illumination times. As exemplarily shown for **3b** in Figure 3b, no changes in the absorbance of DPBF at 411 nm can be observed under basic conditions for five illumination intervals, each equaling an illumination for 3 s. The singlet oxygen generation is most likely quenched due to PET, as observed for fluorescence. However, strong changes of the absorbance of DPBF at 411 nm occur under acidic conditions for illumination in intervals of 1 s. This process can be repeated until complete DPBF consumption, while singlet oxygen is only produced under acidic conditions, as shown in the inset of Figure 3b. With the aid of negative controls examined at basic and acidic conditions without illumination (see Figure S3b, SI), we demonstrated that changes in DPBF absorption are exclusively caused by the reaction with photochemically generated singlet oxygen. Although ϕ_Δ values for mono- and diiodinated compounds are the same, we focused on the diiodinated compounds for the evaluation of our dyes as photosensitizers, as they are synthetically accessible in better yields and do show higher extinction coefficients at the excitation wavelength (532 nm).

Evaluation of Modified BODIPY Dyes as Photosensitizers. As the singlet oxygen generation can be controlled by pH, we tested the ability of our compounds to be utilized as PS for PDT. Therefore, we incubated HeLa cells with various concentrations of **3a** and **3b** and determined the cell viability after treatment of the cells with or without illumination with λ_{ex} = 532 nm. As can be seen in Figure 4a, both compounds show a low dark cytotoxicity with IC_{50} values of >10 and 8.5 μM for **3a** and **3b**, respectively. Upon illumination, however, the cytotoxicity of the dyes is drastically increased by several orders of magnitude. The IC_{50} value after 24 h incubation followed by 30 min of illumination of the non-pH-sensitive probe **3a** was determined to be 2 nM, and an IC_{50} value of around 70 nM was obtained for our pH-sensitive probe **3b**. Despite their similar chemical structures and similar ϕ_Δ values, both compounds show different cytotoxicities, which are tentatively attributed to the different activation of singlet oxygen generation with regard to intracellular pH. As the dyes might accumulate in different cell compartments with different local microenvironments and pH values, the singlet oxygen generation rate of the pH-sensitive compound **3b** can particularly be affected, while the singlet oxygen generation rate of the non-pH-sensitive compound **3a** remains unaffected. Therefore, we aimed at gaining a first insight into the cellular uptake and accumulation capability as well as cellular reactions upon incubation and light excitation using live-cell imaging. Cellular imaging revealed that our BODIPYs enter the cells and distribute quickly within minutes (see SI, Figures 4b and

https://dx.doi.org/10.1021/acs.jmedchem.9b01873
J. Med. Chem. XXXX, XXX, XXX–XXX

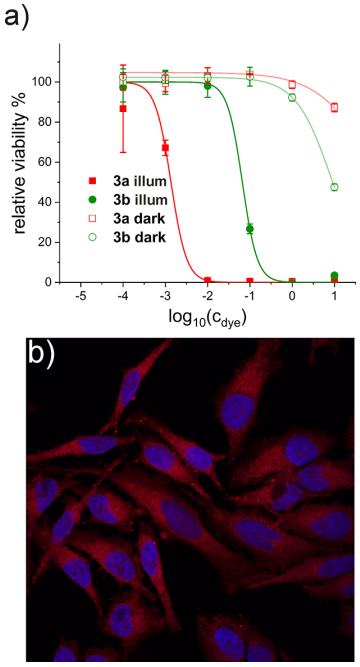

Figure 4. (a) Cell viability of HeLa cells in full medium depending on dye concentration of compounds **3a** (red) and **3b** (green) upon illumination with λ_{ex} = 532 nm (irr) and without illumination (dark). Illumination was performed with 532 nm irradiation for 30 min. Cell viabilities were determined by 3-(4,5-dimethylthiazol-2-yl)-2,5-diphenyltetrazolium bromide (MTT) test after a further 24 h of incubation. (b) Confocal laser scanning microscopy (CLSM) pictures (blue and red channels merged) of fixed HeLa cells incubated with 1 μM compound **3b**. The nuclei were stained with 4′,6-diamidino-2-phenylindole (DAPI). The blue channel shows the fluorescence of DAPI, and the red channel shows the fluorescence of the dye.

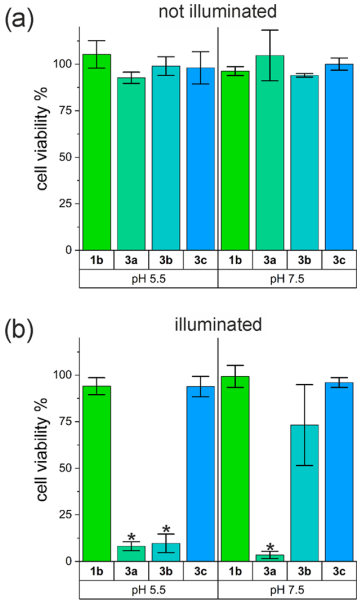

Figure 5. (a) Dark cytotoxicity of compounds **1b** and **3a**–**c** as well as (b) cytotoxicity upon illumination with λ_{ex} = 532 nm studied with HeLa cells at different adjusted pH values. The cells were incubated with a dye concentration of 0.1 μM for 24 h. Illumination was performed with a 532 nm laser diode for 5 min. Cell viabilities were determined by the MTT test after a further 24 h of incubation. (* Compared with not illuminated samples, unpaired *t*-test, $p < 0.05$.).

S6), which is favorable for PDT agents. During live-cell imaging and simultaneous illumination of the HeLa cells incubated with the always-on probe **3a**, we observed massive cell death as evident by membrane blebbing and detachment (see SI, Figure S7). This observation underlines the strong cytotoxicity of this compound due to the illumination-mediated ROS production.

With these results, we could demonstrate the applicability of both dyes as PS in PDT. To confirm that the differences in cytotoxicity upon illumination are caused by different singlet oxygen production rates in response to pH, we adjusted the intracellular pH of the HeLa cells to 5.5 or 7.5 prior illumination with a λ_{ex} = 532 nm laser diode to avoid ambiguity caused by a possibly different distribution of the dyes in the various cellular compartments. We also optimized the duration of illumination from 30 to 5 min to avoid saturation of our readout signals. While a chemically similar precursor dye **1b** was used as control showing no singlet oxygen generation, **3a** was used as always-on probe as its pK_a value is far more basic than the adjusted pH values. We expected **3b** and **3c** to reveal different toxicities at different pH values since their pK_a values are in the pH range used and singlet oxygen generation at pH 5.5 is assumed to be higher than that at pH 7.5. As can be seen for a dye concentration of 0.1 μM (Figure 5a), the cell viability is not affected as long as the cells are not illuminated. Only at higher concentrations with IC_{50} values >1 or >10 μM for **3b** and **3c** or **1b** and **3a**, respectively (see SI, Table 2 and Figure S5), we observed cytotoxicity under dark conditions. However, upon illumination with a λ_{ex} = 532 nm laser diode, we observed drastically increased concentration-dependent cytotoxicities of the dyes **3a**–**c** with IC_{50} values in the nanomolar range (see Table 2). For the negative control **1b**, illumination did not lead to an increase in cytotoxicity, which is consistent with the inability of this dye to absorb at λ_{ex} = 532 nm and to generate singlet oxygen. The positive control probe **3a** shows a drastically increased toxicity upon illumination with a several orders of magnitude decreased IC_{50} value of about 10–20 nM. As expected, no pH-dependent differences in cytotoxicity of **3a** were observed as the adjusted pH values are more acidic than the pK_a value of **3a**. Also, a drastically higher cytotoxicity upon illumination with an IC_{50} value of about 30 nM was observed for the pH-controllable dye **3b**, but only under acidic conditions at pH 5.5. At pH 7.5, a 5-fold increase of IC_{50} to about 150 nM occurred, which we attribute to a lowered singlet oxygen generation caused by the deactivation of the compound. Compound **3c** did not reveal a significant pH dependence of its cytotoxicity, which is ascribed to its too acidic pK_a. As can be noted in Figure 5b for a concentration of 0.1 μM, pH-dependent differences in cell viability result only for **3b**. While **1b** and **3c** affect the cell viability neither at pH 5.5 nor at pH 7.5, the positive control **3a** shows a strong cytotoxicity for both conditions. Compound **3b**, however, is strongly cytotoxic particularly under acidic conditions at pH 5.5 and less cytotoxic at pH 7.5. Compound **3c** shows an IC_{50} of about 1 μM in its off state at pH 7.5, which slightly

https://dx.doi.org/10.1021/acs.jmedchem.9b01873
J. Med. Chem. XXXX, XXX, XXX–XXX

Table 2. Calculated IC_{50} Values of the Different Compounds Determined by Sigmoidal Curve Fitting of the Concentration-Dependent Cell Viabilities for Given Conditions[a,b]

conditions	1b	3a	3b	3c
illum, fm	n.d.	2 ± 10 nM	70 ± 40 nM[d]	n.d.
illum, pH 5.5	>10 μM[c]	20 ± 10 nM	30 ± 20 nM	480 ± 230 nM
illum, pH 7.5	>10 μM[c]	10 ± 10 nM	150 ± 60 nM	1.0 ± 0.2 μM
no illum, fm	n.d.	>10 μM[c]	8.5 ± 1.7 μM	n.d.
no illum, pH 5.5	>10 μM[c]	>10 μM[c]	3.6 ± 1.5 μM	4.4 ± 1.7 μM
no illum, pH 7.5	>10 μM[c]	>10 μM[c]	7.9 ± 2.2 μM	9.3 ± 5.5 μM

[a]The results represent mean ± CI (CI: confidence interval 95%). [b]fm = full medium. [c]IC_{50} out of the measured concentration range. [d]Illumination time of 30 min.

decreases to 500 nM at pH 5.5. This increase in toxicity is smaller than the increase observed for **3b**. This observation is tentatively ascribed to **3c** not being completely activated at pH 5.5. However, a quantitative statement with respect to the percentage of on-/off-switched molecules is not possible as the pK_a values of the dyes can differ from the values determined in cuvette experiments as the pK_a values depend considerably on the respective chemical environment, which is more complex on the cellular level. Nonetheless, the pH-dependent cytotoxic ROS production controllable by illumination can be clearly observed for **3b** and **3c** at different pH values. We determined a roughly 5-fold decrease of the IC_{50} for **3b** upon adjusting the pH to 5.5. This is less than expected from the cuvette experiments where we observed a pronounced on/off switching of the singlet oxygen generation (see Figure 3a,b). This might be due to the accumulation or localization of dye molecules in various cell components not heavily influenced by changes in intracellular pH, resulting in a constant presence of on-switched dyes. Furthermore, this could also explain the much higher toxicity of the pH-controllable dyes upon illumination at a pH of 7.5 compared to the derived dark cytotoxicity (see Table 2), as we could exclude cell death induced by laser light-induced phototoxicity alone. The cytotoxicities of our dyes determined for illumination versus dark conditions are in a good agreement with reports from similar, structurally not complex, and not pH-sensitive systems reported earlier.[12,16] Moreover, the light-induced cytotoxicities in the lower-digit nanomolar range outperform most of the reported BODIPY-based PS. Even in the pH-controlled off state, the cytotoxicity of **3b** and **3c** is still higher or at least comparable to the cytotoxicity of structurally more complex systems,[12,13] which renders them potent PS. However, no comparison of the advantages of the pH-controlled cytotoxicity of our BODIPYS can be made as there are presently no data available for pH-controlled BODIPY-based singlet oxygen generators.

CONCLUSIONS

In this study, we described the successful synthesis and analytical and photophysical characterization of pH-activatable fluorescent singlet oxygen-generating BODIPY dyes, which can be used as photosensitizers (PS) for photodynamic therapy (PDT) and as reporters for bioimaging. Using precursor dyes with a pH-switchable fluorescence, the capability of singlet oxygen generation was introduced by iodine substituents at the 2- and 6-position of the chromophore core, which is electronically decoupled from the pH-responsive phenolic meso-subunit. This rational design concept yields dyes revealing pH-induced fluorescence quenching by photo-induced electron transfer (PET), originating from the phenolic moiety of the dyes, that is not affected by iodination, as a prerequisite to additionally quench intersystem crossing of the iodinated compounds depending on pH. Consequently, these new dyes show a pH-dependent singlet oxygen generation. Moreover, we could realize pH-activatable singlet oxygen-generating dyes with different pK_a values as our dye design provides pK_a tunability by the substitution pattern of the phenolic meso-subunit. Evaluation of the applicability of our compounds as PS for PDT in cell studies with a cultured HeLa cell line revealed a drastic difference in cytotoxicity for PS-treated cells upon illumination compared to dark conditions. These experiments showed almost complete eradication of the cell population after illumination for 5 min for dye concentrations exceeding 0.1 μM. Moreover, we could show that the pH control of the optical features, and thereby also the singlet oxygen production of our compounds can provide the basis for pH-dependent cytotoxicity. This was demonstrated for one dye with a pK_a value of 6.4 that reveals increased ISC and hence a on-switched singlet oxygen generation at lower pH values. These results underline the considerable application potential of our pH-controllable, singlet oxygen-generating BODIPY derivatives as PS in PDT, which could lead to a safer and more targeted PDT. Future research will be focused on the improvement of application-relevant properties like water solubility and the bathochromic shift of the absorption and emission bands of our BODIPY dyes.[42,43]

EXPERIMENTAL SECTION

Materials. 3-Hydroxybenzaldehyde, 4-hydroxybenzaldehyde, *p*-chloranil, *N*,*N*-diisopropylethylamine (DIPEA), boron trifluoride diethyl etherate, *N*-bromosuccinimide (NBS), *N*-iodosuccinimide (NIS), silica gel (40−63 μm, 230−400 mesh), rose bengal, and 1,3-diphenylisobenzofuran (DPBF) were purchased from Sigma-Aldrich. 2,4-Dimethylpyrrole was bought from ABCR. Deuterated chloroform ($CDCl_3$) was obtained from Deutero GmbH. Trifluoroacetic acid (TFA), acetonitrile (ACN), dichloromethane (DCM), and chloroform were purchased from Merck KGaA, and *n*-hexane and petroleum ether (40−60 °C, PE) were obtained from Carl Roth GmbH. The dyes rhodamine 6G and fluorescein 27 used as references for the relative quantum yield measurements were purchased from Lambda Physics.

Synthesis. The synthesis as well as analytical and optical characterizations of the noniodinated pH-sensitive BODIPY dyes (**1a−c**) and their precursor hydroxybenzaldehyde derivatives have been reported previously by our group.[21] For this study, 4-hydroxybenzaldehyde, 3,5-dibromo-4-hydroxybenzaldehyde, and 2,4,6-tribromo-4-hydroxybenzaldehyde were used as precursors for **1a**, **1b**, and **1c**, respectively. The synthetic procedure was meanwhile slightly modified to increase the reaction yield (see SI, Scheme 1).[21,23,44,45] The precursor dyes were further used to synthesize a set of mono- and diiodinated pH-sensitive singlet oxygen-generating BODIPYs (**2a−c**, **3a−c**) using *N*-iodosuccinimide (NIS).[29,46] All

https://dx.doi.org/10.1021/acs.jmedchem.9b01873
J. Med. Chem. XXXX, XXX, XXX−XXX

compounds subjected to biological assays were of >95% purity (ultra performance liquid chromatography—UPLC). All reagents and solvents employed for the synthesis and characterization were used without further purification.

BODIPYs 1a–c. For the synthesis, the corresponding aldehyde (2.5 mmol, 1.0 equiv) and 2,4-dimethylpyrrole (5.0 mmol, 2.0 equiv) were dissolved in 140 mL of dry DCM and 10 mL of dry EtOH. After degassing by rapid vacuum–argon cycles (five times), a few drops of TFA (30 μL) were added and the reaction mixture was stirred at room temperature under argon atmosphere in the dark overnight. *p*-Chloranil (2.5 mmol, 1.0 equiv) was added, and the mixture was stirred for additional 60 min. Prior to the addition of $BF_3{\cdot}OEt_2$ (25.0 mmol, 10.0 equiv) and 4.3 mL of diisopropylethylamine (DIPEA) (25.0 mmol, 10.0 equiv), the DCM/EtOH solvent mixture was removed under a reduced pressure and replaced by 100 mL of dry DCM to avoid the reaction between $BF_3{\cdot}OEt_2$ and EtOH. After portionwise addition, the reaction mixture was stirred for 60 min. Subsequently, the reaction mixture was prepurified by carrying out short silica gel flash column chromatography with DCM as eluent. The resulting crude mixture was concentrated under reduced pressure and further purified by silica gel flash column chromatography using DCM/petroleum ether (9:1, 2:1, and 3:1 for **1a**, **1b**, and **1c**, respectively) as eluents. Pure dyes as required for the spectroscopic studies were obtained by recrystallization from chloroform/n-hexane. For detailed analytical characterization, see the literature.[21] UPLC traces can be found in the SI (see Figures S8–S10).

*4,4-Difluoro-1,3,5,7-tetramethyl-8-(4-hydroxyphenyl)-bora-3a,4a-diaza-s-indacene (**1a**).* Yield 49%; UPLC: > 99% purity; ^{1}H NMR (500 MHz, DMSO-d_6) [ppm]: δ = 9.85 (s, OH), 7.11 (m, $2H_{aryl}$), 6.92 (m, $2H_{aryl}$), 6.16 (s, $2H_{pyrrole}$), 2.43 (s, $6H_{methyl}$), 1.42 (s, $6H_{methyl}$); ^{13}C NMR (125 MHz, DMSO-d_6) [ppm]: δ = 158.2, 154.5, 142.8, 131.2, 129.0, 124.2, 121.2, 116.1, 14.2, 14.2; MS (ESI-TOF): m/z calculated for $C_{19}H_{20}BF_2N_2O^+$ $[M + H]^+$: 341.1639; found: 341.1643.

*4,4-Difluoro-1,3,5,7-tetramethyl-8-(3,5-dibromo-4-hydroxyphenyl)-bora-3a,4a-diaza-s-indacene (**1b**).* Yield 41%; UPLC: >99% purity; ^{1}H NMR (500 MHz, DMSO-d_6) [ppm]: δ = 10.42 (s, OH), 7.64 (s, $2H_{aryl}$), 6.21 (s, $2H_{pyrrole}$), 2.44 (s, $6H_{methyl}$), 1.48 (s, $6H_{methyl}$); ^{13}C NMR (125 MHz, DMSO-d_6) [ppm]: δ = 155.2, 151.6, 142.5, 138.6, 131.8, 130.9, 127.7, 121.6, 112.5, 14.5, 14.3; MS (ESI-TOF): m/z calculated for $C_{19}H_{16}BBr_2F_2N_2O^-$ $[M - H]^-$: 496.9670; found: 496.9742.

*4,4-Difluoro-1,3,5,7-tetramethyl-8-(2,4,6-tribromo-3-hydroxyphenyl)-bora-3a,4a-diaza-s-indacene (**1c**).* Yield 60%; UPLC: >97% purity; ^{1}H NMR (500 MHz, DMSO-d_6) [ppm]: δ = 10.67 (s, OH), 8.12 (s, $1H_{aryl}$), 6.21 (s, $2H_{pyrrole}$), 2.46 (s, $6H_{methyl}$), 1.48 (s, $6H_{methyl}$) ^{13}C NMR (125 MHz, DMSO-d_6) [ppm]: δ = 155.9, 141.2, 138.2, 135.5, 135.1, 129.3, 121.5, 113.8, 113.7, 14.4, 13.1; MS (ESI-TOF): m/z calculated for $C_{19}H_{16}BBr_3F_2N_2ONa^+$ $[M + Na]^+$: 598.8751; found: 598.8747.

*BODIPYs **2a–c**.* A respective amount of NIS (1.1 equiv) was added slowly in small portions to a cooled solution (0 °C) of BODIPY **1a–c** (1 equiv) in 100 mL of DCM. After complete addition of NIS, the reaction mixture was stirred for 30 min. Then, the reaction mixture was washed with deionized water and subsequently dried over $MgSO_4$. Purification was performed by column chromatography in the dark using DCM/petroleum ether (PE) (1/1, v/v) as eluents followed by recrystallization by chloroform/*n*-hexane. ^{1}H NMR spectra and UPLC traces can be found in the SI (see Figures S8–S16).

*4,4-Difluoro-2-iodo-1,3,5,7-tetramethyl-8-(4-hydroxyphenyl)-bora-3a,4a-diaza-s-indacene (**2a**).* Yield 20%; UPLC: >99% purity; ^{1}H NMR (500 MHz, $CDCl_3$) [ppm]: δ = 6.97 (d, $2H_{aryl}$), 6.88 (d, $2H_{aryl}$), 5.97 (s, $1H_{pyrrole}$), 2.53 (s, $3H_{methyl}$), 2.47 (s, $3H_{methyl}$), 1.39 (s, $6H_{methyl}$); δ = 157.6, 155.4, 150.3, 145.2, 143.6, 137.1, 136.6, 132.5, 132.0, 131.2, 129.0, 121.9, 84.7, 17.3, 15.9, 15.2, 15.0; MS (ESI-TOF): m/z calculated for $C_{19}H_{18}BF_2IN_2NaO^+$ $[M + Na]^+$: 489.0423; found: 489.0442.

*4,4-Difluoro-2-iodo-1,3,5,7-tetramethyl-8-(3,5-dibromo-4-hydroxyphenyl)-bora-3a,4a-diaza-s-indacene (**2b**).* Yield 18%; UPLC: >96% purity; ^{1}H NMR (500 MHz, $CDCl_3$) [ppm]: δ = 7.41 (s, $2H_{aryl}$), 6.07 (s, $1H_{pyrrole}$), 2.62 (s, $3H_{methyl}$), 2.55 (s, $3H_{methyl}$), 1.60 (s, $3H_{methyl}$), 1.53 (s, $3H_{methyl}$); ^{13}C NMR (125 MHz, $CDCl_3$) [ppm]: δ = 158.7, 155.5, 150.4, 144.7, 143.0, 137.3, 131.9, 131.7, 130.9, 129.2, 122.7, 110.7, 84.8, 17.4, 15.8, 15.3, 14.9; MS (ESI-TOF): m/z calculated for $C_{19}H_{16}BBr_2F_2IN_2NaO^+$ $[M + Na]^+$: 644.8633; found: 644.8617.

*4,4-Difluoro-2-iodo-1,3,5,7-tetramethyl-8-(2,4,6-tribromo-3-hydroxyphenyl)-bora-3a,4a-diaza-s-indacene (**2c**).* Yield 34%; UPLC: >99% purity; ^{1}H NMR (500 MHz, $CDCl_3$) [ppm]: δ = 7.88 (s, $1H_{aryl}$), 6.11 (s, $1H_{aryl}$), 6.08 (s, $1H_{pyrrole}$), 2.65 (s, $3H_{methyl}$), 2.58 (s, $3H_{methyl}$), 1.53 (s, $3H_{methyl}$), 1.52 (s, $3H_{methyl}$); ^{13}C NMR (125 MHz, $CDCl_3$) [ppm]: δ = 159.4, 155.9, 150.3, 143.5, 141.8, 137.0, 136.2, 135.7, 130.5, 129.1, 122.6, 113.5, 111.5, 111.1, 84.7, 16.1, 15.8, 15.0, 13.9; MS (ESI-TOF): m/z calculated for $C_{19}H_{14}BBr_3F_2IN_2O^-$ $[M - H]^-$: 698.7762; found: 698.7727.

*BODIPYs **3a–c**.* NIS (2.2 equiv) was added slowly in small portions to a stirred solution of BODIPY **1a–c** (1 equiv) in 100 mL of DCM. After complete addition of the NIS, the reaction mixture was stirred for further 60 min. Then, the reaction mixture was washed with deionized water and subsequently dried over $MgSO_4$. Purification was performed by column chromatography in the dark using DCM/petroleum ether (PE) (1/1, v/v) as eluents followed by recrystallization by chloroform/*n*-hexane. ^{1}H NMR spectra and UPLC traces can be found in the SI (see Figures S8–S16).

*4,4-Difluoro-2,6-diiodo-1,3,5,7-tetramethyl-8-(4-hydroxyphenyl)-bora-3a,4a-diaza-s-indacene (**3a**).* Yield 23%; UPLC: >95% purity; ^{1}H NMR (500 MHz, $CDCl_3$) [ppm]: δ = 7.04 (d, $2H_{aryl}$), 6.98 (d, $2H_{aryl}$), 2.63 (s, $6H_{methyl}$), 1.48 (s, $6H_{methyl}$); ^{13}C NMR (125 MHz, $CDCl_3$) [ppm]: δ = 158.2, 156.3, 145.5, 142.2, 131.8, 129.0, 125.4, 116.3, 85.3, 17.0, 15.8; MS (ESI-TOF): m/z calculated for $C_{19}H_{17}BF_2I_2N_2NaO^+$ $[M + Na]^+$: 614.9389; found: 614.9417.

*4,4-Difluoro-2,6-diiodo-1,3,5,7-tetramethyl-8-(3,5-dibromo-4-hydroxyphenyl)-bora-3a,4a-diaza-s-indacene (**3b**).* Yield 67%; UPLC: >98% purity; ^{1}H NMR (500 MHz, $CDCl_3$) [ppm]: δ = 7.40 (s, $2H_{aryl}$), 2.64 (s, $6H_{methyl}$), 1.54 (s, $6H_{methyl}$); ^{13}C NMR (125 MHz, $CDCl_3$) [ppm]: δ = 157.7, 150.6, 145.0, 137.1, 131.6, 131.3, 129.1, 110.8, 86.2, 17.7, 16.1; MS (ESI-TOF): m/z calculated for $C_{19}H_{14}BBr_2F_2I_2N_2O^-$ $[M - H]^-$: 746.7624; found: 746.7636.

*4,4-Difluoro-2,6-diiodo-1,3,5,7-tetramethyl-8-(2,4,6-tribromo-3-hydroxyphenyl)-bora-3a,4a-diaza-s-indacene (**3c**).* Yield 27%; UPLC: >96% purity; ^{1}H NMR (500 MHz, $CDCl_3$) [ppm]: δ = 7.89 (s, $1H_{aryl}$), 6.12 (s, $1H_{phenolic}$), 2.66 (s, $6H_{methyl}$), 1.53 (s, $6H_{methyl}$); ^{13}C NMR (125 MHz, $CDCl_3$) [ppm]: δ = 158.2, 150.4, 143.8, 136.8, 136.0, 135.8, 129.7, 113.3, 111.4, 111.3, 86.1, 16.3, 16.1; MS (ESI-TOF): m/z calculated for $C_{19}H_{13}BBr_3F_2I_2N_2O^-$ $[M - H]^-$: 824.6729; found: 824.6687.

Optical Spectroscopy. Absorption measurements were carried out on a calibrated Varian Cary 5000 UV–vis–NIR absorption spectrophotometer with a scan rate of 600 nm/s and a slit width of 2 nm using a baseline correction (air/air) and a solvent sample as a reference. Fluorescence spectra of pH titration experiments were recorded on a calibrated LS-50B luminescence spectrometer from PerkinElmer with an integration time of 0.1 s and slit widths of 8.0 and 8.0 nm for excitation and emission, respectively. Fluorescence spectra required for the relative determination of fluorescence quantum yields (ϕ_f), following the generally used method,[47] using fluorescein 27 or rhodamine 6G as standards (λ_{ex} = 480 or 495 nm), were recorded on a calibrated FLS920 spectrofluorometer from Edinburgh Instruments. For these measurements, an integration time of 0.1 s and slit widths of 2 and 6 nm were employed for excitation and emission, respectively. The resulting values and relative standard deviations were derived from at least five independent measurements of each dye. To determine the fluorescence quantum yield of the protonated dye species, 2.5 μL of HCl (12 M) was added to 3 mL of a dye containing acetonitrilic samples. All measurements were carried out in Hellma quartz cuvettes (QS, 10 × 10 mm^2).

Fluorometric pH Titration. The pH values of the buffer solutions (borate/citrate) were adjusted with a 780 pH meter using a glass electrode from Deutsche METROHM GmbH & Co. KG and were

https://dx.doi.org/10.1021/acs.jmedchem.9b01873
J. Med. Chem. XXXX, XXX, XXX–XXX

verified with a pH 211 microprocessor pH meter from Hanna Instruments. These pH meters were calibrated at 25 °C with standard buffers of pH = 10.01, 7.01, and 4.01 (Hanna Instruments) in three-point and two-point calibrations, respectively. For the determination of pK_a values, the respective volumes of the dye stock solutions diluted in 2 mL of acetonitrile were added to 1 mL of buffer ($\lambda_{abs} \approx 0.1$). Successively, defined volumes of concentrated HCl were added and the absorption and fluorescence emission spectra of the dye solutions were recorded for the respective pH values. The pK_a values were determined from at least three independent samples and measurements. Although the pK_a values of pH sensors bearing phenol groups commonly show negligible sensitivity to a low ionic strength, the buffer capacity and composition were kept constant for all measurements.[48,49]

Determination of Quantum Yields for Singlet Oxygen Generation. The quantum yield for the singlet oxygen generation (ϕ_Δ) of all dyes was determined relatively using a direct and an indirect method for quantifying the amount of produced singlet oxygen upon excitation of the dyes. For both methods, rose bengal was used as standard (ϕ_Δ = 0.53 in ACN[50]). For the direct method, the generated singlet oxygen was quantified by its phosphorescence emission at 1270 nm upon excitation of the dyes at 510 or 532 nm (xenon lamp, excitation wavelength (λ_{ex}) chosen dependent on the absorption (λ_{abs}) of the studied dyes).[51] The absorbance of each dye at the respective λ_{ex} was kept around 0.5. The emission spectra were recorded on a calibrated FLS920 spectrofluorometer from Edinburgh Instruments with an integration time of 2 s and slit widths of 15 and 15 nm for excitation and emission, respectively. All measurements were repeated five times. A long-pass filter (1035 nm) was used on the emission side to remove interfering signals. The obtained emission curves were used to calculate ϕ_Δ following eq 1[31]

$$\Phi_\Delta = \Phi_\Delta^{ref} \times \frac{F}{F_{ref}} \times \frac{f^{ref}}{f} \quad (1)$$

with

$$F = \int_{\lambda_{em}} I(\lambda_{em}) \times \lambda_{em} d\lambda_{em}$$

and

$$f = \int_{\lambda_{ex}-1/2\Delta\lambda_{ex}}^{\lambda_{ex}+1/2\Delta\lambda_{ex}} 1 - 10^{-A_{\lambda_{ex}}} d\lambda_{ex}$$

While F represents the integral photon flux calculated from the emission intensity I[47] of the generated singlet oxygen, f is the absorption factor and ϕ_Δ^{ref} is the singlet oxygen quantum yield of the reference PS rose bengal.

For the indirect method, the singlet oxygen generation was quantified by using 1,3-diphenylisobenzofuran (DPBF) as singlet oxygen quencher.[51,52] As DPBF can be used for both colorimetric and fluorometric quantification of singlet oxygen generation, we only used the colorimetric approach monitoring the decrease of the absorbance of DPBF at 410 nm upon quenching of singlet oxygen produced by excitation of the dyes. Therefore, the absorbance of DPBF was set to a value of about 0.8 at λ_{abs} and the absorbance of the respective dye was set to values of 0.03−0.05 at λ_{ex}. Subsequently, the samples were illuminated stepwise using a 532 nm laser diode (100 mW, Roithner Lasertechnik GmbH). The initial laser power of 100 mW was adjusted with regard to the experiments and finally scaled down to around 15 mW using gray filters (T92%, T80%, T70%, T60%, and T50%). After each illumination step, an absorption spectrum was collected. Finally, ϕ_Δ was calculated as described in the literature following eq 2[31,53,54]

$$\Phi_\Delta = \Phi_\Delta^{ref} * \frac{k}{k_{ref}} * \frac{f^{ref}}{f} \quad (2)$$

The rate constants k were determined assuming pseudo-first-order kinetics

$$kt = \ln \frac{[DPBF]_0}{[DPBF]} \quad (3)$$

All measurements were carried out in acetonitrile acidified with 2.5 μL of HCl (12 M), and a total volume of approximately 3 mL was used. Each singlet oxygen quantum yield was determined from three independent measurements using five samples for each compound.

NMR Spectroscopy and Mass Spectrometry. NMR spectroscopy experiments were performed on an Avance II 500 from Bruker at 25 °C using solvent residual proton signals as internal standard (^{1}H: $\delta(CDCl_3)$ = 7.26 ppm; ^{13}C: $\delta(CDCl_3)$ = 77.16 ppm). Chemical shifts (δ) are given in parts per million (ppm) relative to tetramethylsilane (TMS).

For mass spectrometry, all samples were measured on an Agilent 6210 ESI-TOF (Agilent Technologies, Santa Clara, CA). The solvent flow rate was adjusted to 4 μL/min, and the spray voltage set to 4.000 V. Drying gas flow rate was set to 15 psi (1 bar). All other parameters were adjusted for the maximum abundance of the relative $[M + H]^+$/$[M - H]^-$.

Purity of the Compounds. The purity of the compounds was determined by UPLC using an analytical Aquity H UPLC-ESI-MS system from Waters on a C-18 column (1.7 μm, 2.1 × 50 mm; pore size, 130 Å; flow rate, 0.5 mL/min; 50 °C; detection at 280 nm). As a mobile phase, mixtures of water (A) and acetonitrile (B) (gradient 5−90% ACN content) with 0.1% TFA were used. The compounds were characterized by electrospray ionization mass spectrometry (ESI-MS) with a VL quadrupole mass spectrometer in the positive-scan mode.

Cell Culture. HeLa cells (DSMZ no. ACC-57) were obtained from Leibnitz Institute DSMZ—German Collection of Microorganisms and Cell Cultures and routinely cultured in RPMI 1640 medium with 10% FBS (FBS Superior, Merck), 1% penicillin/streptomycin (Thermo Fisher Scientific), and 1% MEM nonessential amino acids (Merck) at 37 °C and 5% CO_2.

PDT in Cell Culture and Viability Tests. 1.5 × 10^5 cells/mL were seeded into transparent flat-bottom 96-well plates (Sarstedt) at 100 μL/well and grown overnight. The next day, the medium was removed and replaced with 100 μL/well of 10-fold serial dilutions of the test compounds in duplicates in full medium. The test compounds were first solubilized in DMSO to give a 10 mM stock solution. Subsequently, the stock solution was diluted in DMSO to a dye concentration of 1 mM. Further dilution was done using cell culture medium, yielding a starting concentration of 10 μM with a final DMSO concentration of 0.1% in cell culture. Solution handling and incubation were done in the dark. After 24 h of incubation at 37 °C, the supernatant was removed and the cells were washed 2× with 200 μL/well PBS. The pH of the cells was adjusted by incubating the cells with buffer solutions of pH 5.5 or 7.5 containing 10 μM of each Nigericin and Valinomycin for 5 min at 37 °C (Intracellular pH Calibration Buffer Kit, Thermo Fisher Scientific). Subsequently, the plates were illuminated for 5 min using a 532 nm laser diode (100 mW, Roithner Lasertechnik GmbH). The laser beam was increased to a circular area of roughly 100 cm^2 by optical lenses covering the 96-well plate yielding a power intensity of around 1 mW/cm^2. After illumination, the cells were washed again 2× with 200 μL/well PBS and fresh medium was added. After overnight incubation, the supernatant was removed and replaced with 100 μL/well fresh medium containing 10 μL of MTT (5 mg/mL solution in PBS, Merck) and incubated for 4 h at 37 °C. The supernatant was removed and formazan crystals were solubilized in a solution of isopropanol with 0.04 M HCl. The absorbance at 570 nm was measured in a Tecan Infinite M200 Pro microplate reader. Relative viabilities were calculated by dividing average absorbance values of wells containing treated cells by the values of wells containing untreated cells (100% control). All tests were repeated two times (n = 2) independently in duplicates. An unpaired t-test was performed to verify statistical significance at a confidence level of 95% ($p > 0.05$).

https://dx.doi.org/10.1021/acs.jmedchem.9b01873
J. Med. Chem. XXXX, XXX, XXX−XXX

■ ASSOCIATED CONTENT

Supporting Information

The Supporting Information is available free of charge at https://pubs.acs.org/doi/10.1021/acs.jmedchem.9b01873.

Figures of pH titration experiments of the dyes in solution as well as corresponding fitting parameters; figures of cell viabilities and corresponding fits and fitting parameters for IC_{50} values; pictures of live-cell imaging; and UPLC traces and ^1H NMR spectra of all new compounds (PDF)

Molecular formula strings (CSV)

■ AUTHOR INFORMATION

Corresponding Authors

Harald Rune Tschiche − *Department of Chemical and Product Safety, German Federal Institute for Risk Assessment (BfR), 10589 Berlin, Germany*; Email: Harald.Tschiche@bfr.bund.de

Ute Resch-Genger − *Division Biophotonics, Federal Institute for Materials Research and Testing (BAM), 12489, Germany*; orcid.org/0000-0002-0944-1115; Email: ute.resch@bam.de

Authors

Sebastian Radunz − *Division Biophotonics, Federal Institute for Materials Research and Testing (BAM), 12489, Germany*

Stefanie Wedepohl − *Institute of Chemistry and Biochemistry, Freie Universität Berlin, 14195 Berlin, Germany*

Mathilde Röhr − *Division Biophotonics, Federal Institute for Materials Research and Testing (BAM), 12489, Germany*

Marcelo Calderón − *Institute of Chemistry and Biochemistry, Freie Universität Berlin, 14195 Berlin, Germany; POLYMAT and Applied Chemistry Department, Faculty of Chemistry, University of the Basque Country UPV/EHU, 20018 Donostia-San Sebastián, Spain; Basque Foundation for Science, Ikerbasque, 48013 Bilbao, Spain;* orcid.org/0000-0002-2734-9742

Complete contact information is available at: https://pubs.acs.org/10.1021/acs.jmedchem.9b01873

Notes

The authors declare no competing financial interest.

■ ACKNOWLEDGMENTS

The authors gratefully acknowledge financial support from the internal BAM project MIC (microbiologically influenced corrosion) and from the Ph.D. program of BAM. They furthermore gratefully acknowledge financial support from the Bundesministerium für Bildung und Forschung (BMBF) through the NanoMatFutur award (ThermoNanogele, 13N12561) and from grant RE1203/23-1 of the German Research Council (DFG). They would also like to acknowledge the assistance of the Core Facility BioSupraMol supported by the DFG.

■ ABBREVIATIONS

PDT, photodynamic therapy; PS, photosensitizer; BODIPY, boron-dipyrromethene; PET, photoinduced electron transfer; ROS, reactive oxygen species; ϕ_Δ, quantum yields for singlet oxygen generation; ISC, intersystem crossing; ϕ_f, fluorescence quantum yield; τ_f, fluorescence lifetime; ACN, acetonitrile; NIS, *N*-iodosuccinimid; DPBF, 1,3-diphenylisobenzofuran; CT, charge transfer; DIPEA, *N*,*N*-diisopropylethylamine; TFA, trifluoroacetic acid; DCM, dichloromethane; EtOH, ethanol; PE, petroleum ether

■ REFERENCES

(1) DeRosa, M. C.; Crutchley, R. J. Photosensitized singlet oxygen and its applications. *Coord. Chem. Rev.* **2002**, *233*−*234*, 351−371.

(2) Kearns, D. R. Physical and chemical properties of singlet molecular oxygen. *Chem. Rev.* **1971**, *71*, 395−427.

(3) Moan, J.; Berg, K. The photodegradation of porphyrins in cells can be used to estimate the lifetime of singlet oxygen. *Photochem. Photobiol.* **1991**, *53*, 549−553.

(4) Rogers, G. S. Continuous low-irradiance photodynamic therapy: A new therapeutic paradigm. *J. Natl. Compr. Cancer Network* **2012**, *10*, 14−17.

(5) Castano, A. P.; Demidova, T. N.; Hamblin, M. R. Mechanisms in photodynamic therapy: part one-photosensitizers, photochemistry and cellular localization. *Photodiagn. Photodyn. Ther.* **2004**, *1*, 279−293.

(6) Neubert, T.; Lehmann, P. Bowen's disease - a review of newer treatment options. *Ther. Clin. Risk Manage.* **2008**, *4*, 1085−1095.

(7) Ericson, M. B.; Wennberg, A.-M.; Larkö, O. Review of photodynamic therapy in actinic keratosis and basal cell carcinoma. *Ther. Clin. Risk Manage.* **2008**, *4*, 1−9.

(8) Shishkova, N.; Kuznetsova, O.; Berezov, T. Photodynamic therapy for gynecological diseases and breast cancer. *Cancer Biol. Med.* **2012**, *9*, 9−17.

(9) Riddle, C. C.; Terrell, S.; Menser, M.; Aires, D.; Schweiger, E. A review of photodynamic therapy (PDT) for the treatment of acne vulgaris. *J. Drugs Dermatol.* **2009**, *8*, 1010−1019.

(10) Enk, C. D.; Nasereddin, A.; Alper, R.; Dan-Goor, M.; Jaffe, C. L.; Wulf, H. C. Cutaneous leishmaniasis responds to daylight-activated photodynamic therapy: proof of concept for a novel self-administered therapeutic modality. *Br. J. Dermatol.* **2015**, *172*, 1364−1370.

(11) Bonnett, R. Photosensitizers of the porphyrin and phthalocyanine series for photodynamic therapy. *Chem. Soc. Rev.* **1995**, *24*, 19−33.

(12) Kamkaew, A.; Lim, S. H.; Lee, H. B.; Kiew, L. V.; Chung, L. Y.; Burgess, K. BODIPY dyes in photodynamic therapy. *Chem. Soc. Rev.* **2013**, *42*, 77−88.

(13) Kue, C. S.; Ng, S. Y.; Voon, S. H.; Kamkaew, A.; Chung, L. Y.; Kiew, L. V.; Lee, H. B. Recent strategies to improve boron dipyrromethene (BODIPY) for photodynamic cancer therapy: an updated review. *Photochem. Photobiol. Sci.* **2018**, *17*, 1691−1708.

(14) Turksoy, A.; Yildiz, D.; Akkaya, E. U. Photosensitization and controlled photosensitization with BODIPY dyes. *Coord. Chem. Rev.* **2019**, *379*, 47−64.

(15) Jung, H. S.; Han, J.; Shi, H.; Koo, S.; Singh, H.; Kim, H.-J.; Sessler, J. L.; Lee, J. Y.; Kim, J.-H.; Kim, J. S. Overcoming the limits of hypoxia in photodynamic therapy: A carbonic anhydrase IX-targeted approach. *J. Am. Chem. Soc.* **2017**, *139*, 7595−7602.

(16) Agazzi, M. L.; Ballatore, M. B.; Durantini, A. M.; Durantini, E. N.; Tomé, A. C. BODIPYs in antitumoral and antimicrobial photodynamic therapy: An integrating review. *J. Photochem. Photobiol., C* **2019**, *40*, 21−48.

(17) Ulrich, G.; Ziessel, R.; Harriman, A. The chemistry of fluorescent BODIPY dyes: versatility unsurpassed. *Angew. Chem., Int. Ed.* **2008**, *47*, 1184−1201.

(18) Loudet, A.; Burgess, K. BODIPY dyes and their derivatives: Syntheses and spectroscopic properties. *Chem. Rev.* **2007**, *107*, 4891−4932.

(19) Bañuelos, J. BODIPY dye, the most versatile fluorophore ever? *Chem. Rec.* **2016**, *16*, 335−348.

(20) Boens, N.; Leen, V.; Dehaen, W. Fluorescent indicators based on BODIPY. *Chem. Soc. Rev.* **2012**, *41*, 1130−1172.

(21) Radunz, S.; Tschiche, H. R.; Moldenhauer, D.; Resch-Genger, U. Broad range ON/OFF pH sensors based on pKa tunable fluorescent BODIPYs. *Sens. Actuators, B* **2017**, *251*, 490−494.
(22) Gotor, R.; Ashokkumar, P.; Hecht, M.; Keil, K.; Rurack, K. Optical pH sensor covering the range from pH 0−14 compatible with mobile-device readout and based on a set of rationally designed indicator dyes. *Anal. Chem.* **2017**, *89*, 8437−8444.
(23) Radunz, S.; Andresen, E.; Würth, C.; Koerdt, A.; Tschiche, H. R.; Resch-Genger, U. Simple self-referenced luminescent pH sensors based on upconversion nanocrystals and pH-sensitive fluorescent BODIPY dyes. *Anal. Chem.* **2019**, *91*, 7756−7764.
(24) Kowada, T.; Maeda, H.; Kikuchi, K. BODIPY-based probes for the fluorescence imaging of biomolecules in living cells. *Chem. Soc. Rev.* **2015**, *44*, 4953−4972.
(25) Liu, J.-Y.; Huang, Y.; Menting, R.; Röder, B.; Ermilov, E. A.; Ng, D. K. P. A boron dipyrromethene−phthalocyanine pentad as an artificial photosynthetic model. *Chem. Commun.* **2013**, *49*, 2998−3000.
(26) Meng, L.-B.; Li, D.; Xiong, S.; Hu, X.-Y.; Wang, L.; Li, G. FRET-capable supramolecular polymers based on a BODIPY-bridged pillar[5]arene dimer with BODIPY guests for mimicking the light-harvesting system of natural photosynthesis. *Chem. Commun.* **2015**, *51*, 4643−4646.
(27) Bessette, A.; Hanan, G. S. Design, synthesis and photophysical studies of dipyrromethene-based materials: insights into their applications in organic photovoltaic devices. *Chem. Soc. Rev.* **2014**, *43*, 3342−3405.
(28) Atilgan, S.; Ekmekci, Z.; Dogan, A. L.; Guc, D.; Akkaya, E. U. Water soluble distyryl-boradiazaindacenes as efficient photosensitizers for photodynamic therapy. *Chem. Commun.* **2006**, *42*, 4398−4400.
(29) Gorbe, M.; Costero, A. M.; Sancenón, F.; Martínez-Máñez, R.; Ballesteros-Cillero, R.; Ochando, L. E.; Chulvi, K.; Gotor, R.; Gil, S. Halogen-containing BODIPY derivatives for photodynamic therapy. *Dyes Pigm.* **2019**, *160*, 198−207.
(30) Lincoln, R.; Durantini, A. M.; Greene, L. E.; Martínez, S. R.; Knox, R.; Becerra, M. C.; Cosa, G. meso-Acetoxymethyl BODIPY dyes for photodynamic therapy: improved photostability of singlet oxygen photosensitizers. *Photochem. Photobiol. Sci.* **2017**, *16*, 178−184.
(31) Rey, Y. P.; Abradelo, D. G.; Santschi, N.; Strassert, C. A.; Gilmour, R. Quantitative profiling of the heavy-atom effect in BODIPY dyes: correlating initial rates, atomic numbers, and 1O2 quantum yields. *Eur. J. Org. Chem.* **2017**, *2017*, 2170−2178.
(32) Yogo, T.; Urano, Y.; Ishitsuka, Y.; Maniwa, F.; Nagano, T. Highly efficient and photostable photosensitizer based on BODIPY chromophore. *J. Am. Chem. Soc.* **2005**, *127*, 12162−12163.
(33) Zou, J.; Yin, Z.; Ding, K.; Tang, Q.; Li, J.; Si, W.; Shao, J.; Zhang, Q.; Huang, W.; Dong, X. BODIPY derivatives for photodynamic therapy: influence of configuration versus heavy atom effect. *ACS Appl. Mater. Interfaces* **2017**, *9*, 32475−32481.
(34) Gerweck, L. E.; Seetharaman, K. Cellular pH gradient in tumor versus normal tissue: Potential exploitation for the treatment of cancer. *Cancer Res.* **1996**, *56*, 1194−1198.
(35) Li, X.; Kolemen, S.; Yoon, J.; Akkaya, E. U. Activatable photosensitizers: agents for selective photodynamic therapy. *Adv. Funct. Mater.* **2017**, *27*, No. 1604053.
(36) Xue, F.; Wei, P.; Ge, X.; Zhong, Y.; Cao, C.; Yu, D.; Yi, T. A pH-responsive organic photosensitizer specifically activated by cancer lysosomes. *Dyes Pigm.* **2018**, *156*, 285−290.
(37) Xiong, H.; Zhou, K.; Yan, Y.; Miller, J. B.; Siegwart, D. J. Tumor-activated water-soluble photosensitizers for near-infrared photodynamic cancer therapy. *ACS Appl. Mater. Interfaces* **2018**, *10*, 16335−16343.
(38) McDonnell, S. O.; Hall, M. J.; Allen, L. T.; Byrne, A.; Gallagher, W. M.; O'Shea, D. F. Supramolecular photonic therapeutic agents. *J. Am. Chem. Soc.* **2005**, *127*, 16360−16361.
(39) Agazzi, M. L.; Durantini, J. E.; Gsponer, N. S.; Durantini, A. M.; Bertolotti, S. G.; Durantini, E. N. Light-harvesting antenna and proton-activated photodynamic effect of a novel BODIPY−fullerene C60 dyad as potential antimicrobial agent. *ChemPhysChem* **2019**, *20*, 1110−1125.
(40) Lai, Y.-C.; Su, S.-Y.; Chang, C.-C. Special reactive oxygen species generation by a highly photostable BODIPY-based photosensitizer for selective photodynamic therapy. *ACS Appl. Mater. Interfaces* **2013**, *5*, 12935−12943.
(41) Durantini, A. M.; Heredia, D. A.; Durantini, J. E.; Durantini, E. N. BODIPYs to the rescue: Potential applications in photodynamic inactivation. *Eur. J. Med. Chem.* **2018**, *144*, 651−661.
(42) Hoogendoorn, S.; Blom, A. E. M.; Willems, L. I.; van der Marel, G. A.; Overkleeft, H. S. Synthesis of pH-activatable red fluorescent BODIPY dyes with distinct functionalities. *Org. Lett.* **2011**, *13*, 5656−5659.
(43) Sutter, A.; Elhabiri, M.; Ulrich, G. Fluorescent pH-responsive probes based on water-soluble boron-dipyrromethene (BODIPY) derivatives, featuring long-wavelength emission. *Chem. - Eur. J.* **2018**, *24*, 11119−11130.
(44) Lindsey, J. S.; Wagner, R. W. Investigation of the synthesis of ortho-substituted tetraphenylporphyrins. *J. Org. Chem.* **1989**, *54*, 828−836.
(45) Bartelmess, J.; Weare, W. W.; Latortue, N.; Duong, C.; Jones, D. S. meso-Pyridyl BODIPYs with tunable chemical, optical and electrochemical properties. *New J. Chem.* **2013**, *37*, 2663−2668.
(46) Lu, H.; Wang, Q.; Gai, L.; Li, Z.; Deng, Y.; Xiao, X.; Lai, G.; Shen, Z. Tuning the solid-state luminescence of BODIPY derivatives with bulky arylsilyl groups: synthesis and spectroscopic properties. *Chem. - Eur. J.* **2012**, *18*, 7852−7861.
(47) Würth, C.; Grabolle, M.; Pauli, J.; Spieles, M.; Resch-Genger, U. Relative and absolute determination of fluorescence quantum yields of transparent samples. *Nat. Protoc.* **2013**, *8*, 1535−1550.
(48) Baruah, M.; Qin, W.; Basarić, N.; De Borggraeve, W. M.; Boens, N. BODIPY-Based hydroxyaryl derivatives as fluorescent pH probes. *J. Org. Chem.* **2005**, *70*, 4152−4157.
(49) Werner, T.; Huber, C.; Heinl, S.; Kollmannsberger, M.; Daub, J.; Wolfbeis, S. O. Novel optical pH-sensor based on a boradiazaindacene derivative. *Fresenius' J. Anal. Chem.* **1997**, *359*, 150−154.
(50) Epelde-Elezcano, N.; Martínez, V.; Pena-Cabrera, E.; Gomez Duran, C.; Lopez Arbeloa, I.; Lacombe, S. Modulation of singlet oxygen generation in halogenated BODIPY dyes by substitution at their meso position: Towards a solvent-independent standard in the vis region. *RSC Adv.* **2016**, *6*, 41991−41998.
(51) You, Y. Chemical tools for the generation and detection of singlet oxygen. *Org. Biomol. Chem.* **2018**, *16*, 4044−4060.
(52) Krieg, M. Determination of singlet oxygen quantum yields with 1,3-diphenylisobenzofuran in model membrane systems. *J. Biochem. Biophys. Methods* **1993**, *27*, 143−149.
(53) Hu, W.; Zhang, X.-F.; Lu, X.; Lan, S.; Tian, D.; Li, T.; Wang, L.; Zhao, S.; Feng, M.; Zhang, J. Attaching electron donating groups on the meso-phenyl and meso-naphthyl make aryl substituted BODIPYs act as good photosensitizer for singlet oxygen formation. *J. Lumin.* **2018**, *194*, 185−192.
(54) Wang, P.; Qin, F.; Zhang, Z.; Cao, W. Quantitative monitoring of the level of singlet oxygen using luminescence spectra of phosphorescent photosensitizer. *Opt. Express* **2015**, *23*, 22991−23003.

https://dx.doi.org/10.1021/acs.jmedchem.9b01873
J. Med. Chem. XXXX, XXX, XXX−XXX

pH Activatable Singlet Oxygen Generating Boron-dipyrromethenes (BODIPYs) for Photodynamic Therapy and Bioimaging

Sebastian Radunz,[a] Stefanie Wedepohl,[b] Mathilde Röhr,[a] Marcelo Calderon,[b,c,d] Harald Rune Tschiche,*[e] and Ute Resch-Genger*[a]

[a] *Division Biophotonics, BAM Federal Institute for Materials Research and Testing, Richard-Willstaetter-Str. 11, 12489 Berlin, Germany*
[b] *Institute of Chemistry and Biochemistry, Freie Universität Berlin, Takustr. 3, 14195 Berlin, Germany*
[c] *POLYMAT and Applied Chemistry Department, Faculty of Chemistry, University of the Basque Country UPV/EHU, Paseo Manuel de Lardizabal 3, 20018 Donostia-San Sebastián, Spain.*
[d] *Basque Foundation for Science, IKERBASQUE, 48013 Bilbao, Spain.*
[e] *Department of Chemical and Product Safety, German Federal Institute for Risk Assessment (BfR), Max-Dohrn-Str. 8-10, 10589 Berlin, Germany*

Supplementary Information (SI)

Table of Contents:

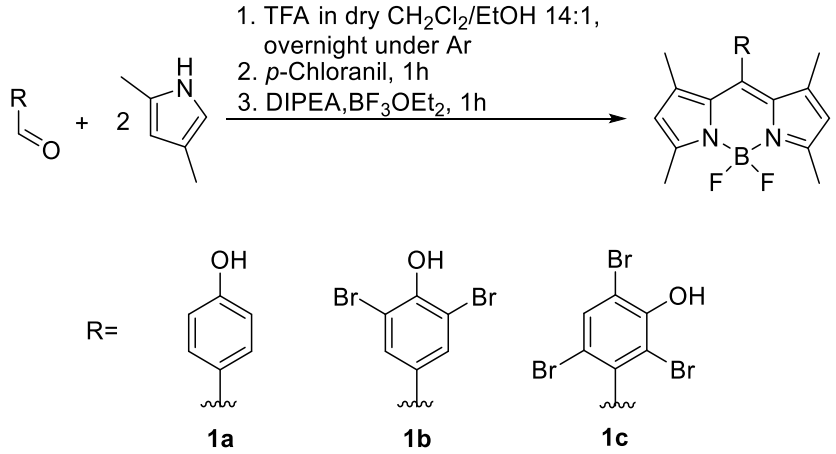

Scheme S1. Three-step reaction scheme of the synthesis of BODIPY dyes **1a-c** using the corresponding benzaldehyde derivatives.

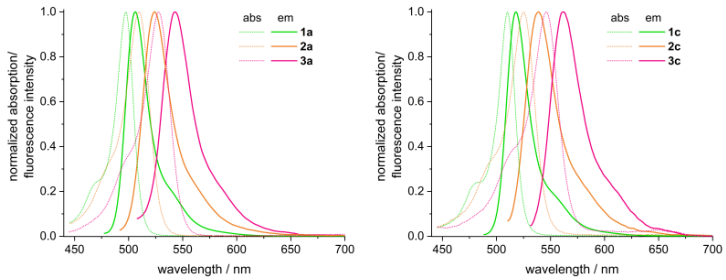

Figure S1. Normalized absorption and fluorescence emission spectra of parent BODIPYs **1a** (left) and **1c** (right) and their respective mono- and diiodated derivates **2a** and **2c** as well as **3a** and **3c**, respectively.

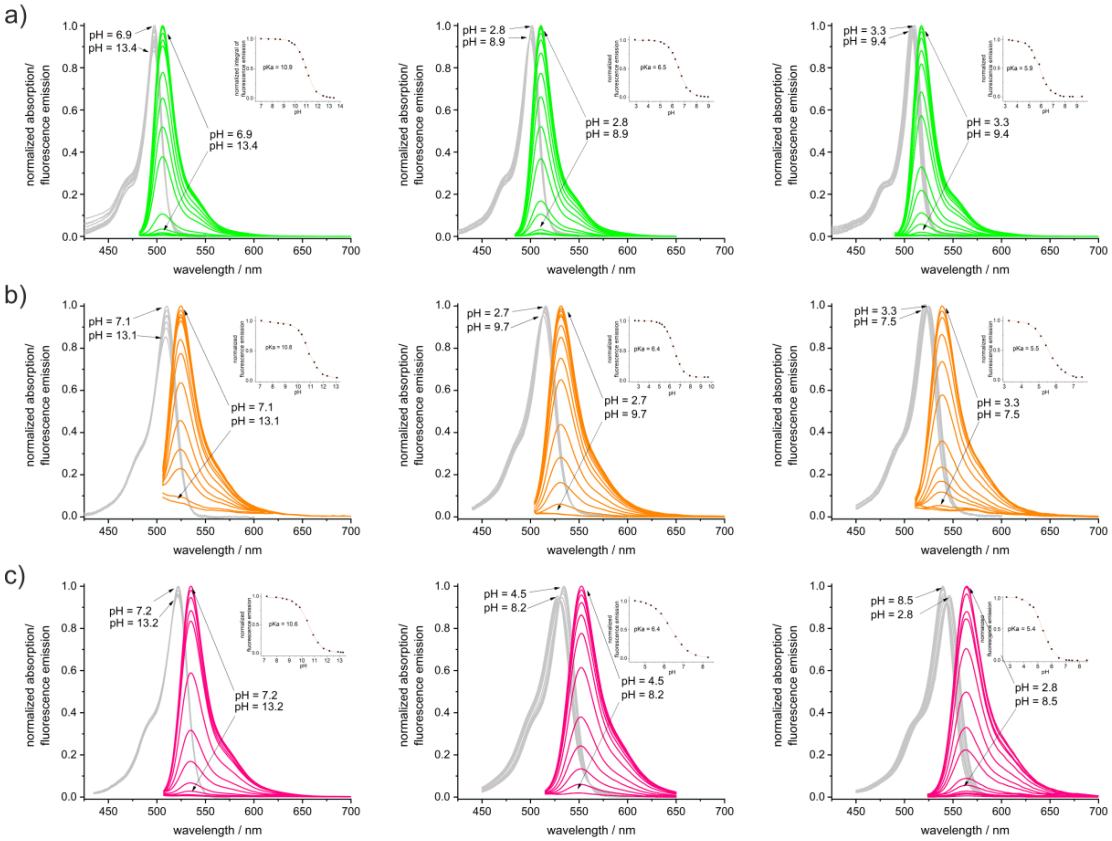

Figure S2. pH-dependent normalized absorption an fluorescence spectra of parent dyes (a) **1a-c**, left to right), monoiodated (b) **2a-c**, left to right) and diiodated (c) **3a-c**, left to right) photosensitizers in ACN/H_2O (2/1 v/v, 25 mM buffered). The insets show the normalized integrated fluorescence intensity in dependence of pH and the corresponding sigmoidal curve fit and pK_a value for the respective compound.

Table S1. Equation used for the sigmoidal curve fitting of pH titration experiments.

Model	Equation
Dose response	$y = A1 + \frac{A2 - A1}{1 + 10^{(LOGx_0 - x)p}}$

Table S2. Sigmoidal fitting parameters[a] of the normalized integrated fluorescence emissions of the BODIPYs from pH titration in solution (ACN/H_2O, 2/1 v/v, buffered 25 mM).

dye	A1	A2	$LOGx_0$	P	R
1a	0.003 ± 0.006	0.986 ± 0.004	10.90 ± 0.01	-0.951 ± 0.028	0.999
2a	0.061 ± 0.015	0.976 ± 0.009	10.82 ± 0.03	-0.966 ± 0.054	0.998
3a	0.000 ± 0.008	0.997 ± 0.005	10.64 ± 0.03	-0.912 ± 0.031	0.999
4a	0.008 ± 0.005	0.982 ± 0.006	10.55 ± 0.02	-0.886 ± 0.025	0.999
1b	0.004 ± 0.004	0.991 ± 0.003	6.53 ± 0.01	-1.043 ± 0.021	0.999
2b	0.066 ± 0.001	0.997 ± 0.001	6.42 ± 0.01	-0.989 ± 0.006	0.999
3b	0.004 ± 0.002	1.012 ± 0.013	6.36 ± 0.01	-0.963 ± 0.007	0.999
1c	0.000 ± 0.009	0.995 ± 0.011	5.89 ± 0.02	-0.973 ± 0.045	0.999
2c	0.024 ± 0.006	1.003 ± 0.007	5.53 ± 0.01	-1.028 ± 0.028	0.999
3c	0.008 ± 0.008	0.996 ± 0.012	5.35 ± 0.02	-1.053 ± 0.056	0.998

[a] fitting parameters for fits shown in the insets of Fig. 2, and S2.

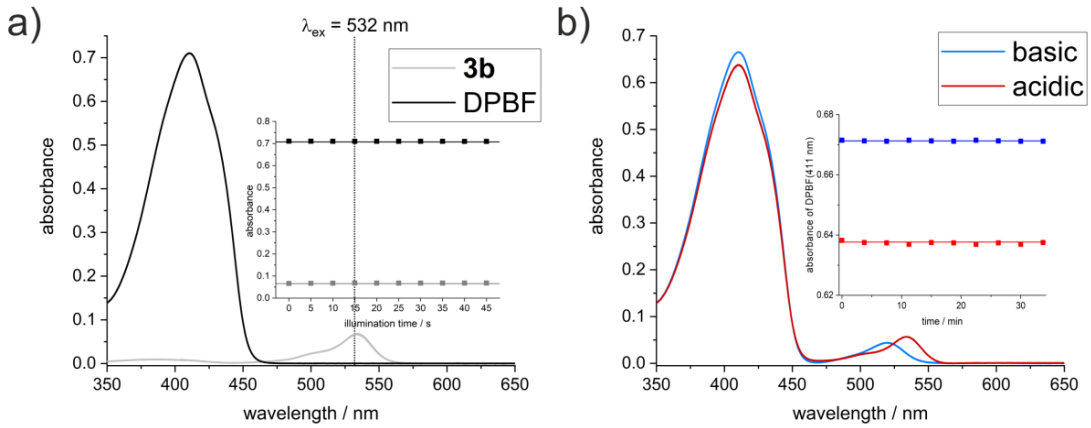

Figure S3. a) Absorption spectra of separate irradiation of DPBF and **3b** in ACN/H_2O (2/1 v/v, buffered 25 mM) with λ_{ex} = 532 nm for a total of 45 s in 5 s increments. b) Multiple absorption spectra of basic (blue) and an acidic (red) mixtures of DPBF and **3b** in ACN/H_2O (2/1 v/v, buffered 25 mM) measured in a time range of roughly 35 min indicating no chemical decomposition without external irradiation.

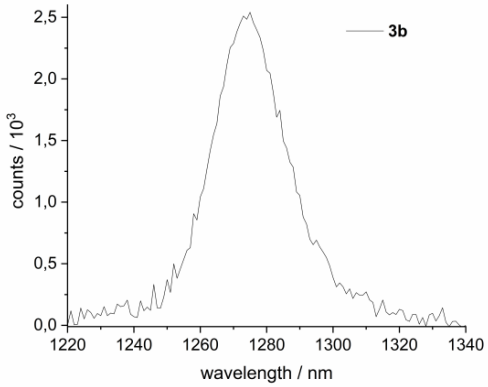

Figure S4. Luminescence spectra of singlet oxygen generated by irradiation of **3b** at λ_{ex} = 532 nm.

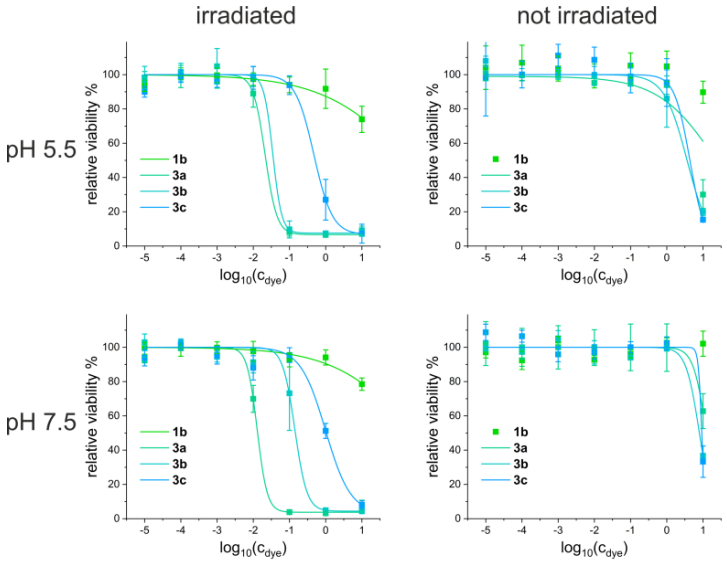

Figure S5. Relative cell viability of HeLa cells in dependence of dye concentrations (logarithmic scale) for irradiated (left) and not irradiated (right) samples with different adjusted pH values 5.5 and 7.5, top and bottom, respectively.

Table S3. Sigmoidal fitting parameters of the cell viability in dependence of dye concentration used for incubation of the HeLa cells for photo cytotoxicity studies. Fitting parameters for fits shown in Fig S5.

a) irradiated at pH 5.5

dye	A1	A2	$LOGx_0$	P	R
1b	0*	100*	2.299 ± 0.753	-0.365 ± 0.129	0.604
3a	6.645 ± 0.415	100*	-1.672 ± 0.073	-2.661 ± 0.464	0.997
3b	7.545 ± 0.413	100*	-1.460 ± 0.111	-3.535 ± 0.826	0.999
3c	6.695 ± 10.447	100*	-0.326 ± 0.292	-1.699 ± 0.967	0.926

**fixed parameter*

b) irradiated at pH 7.5

dye	A1	A2	$LOGx_0$	P	R
1b	0*	100*	2.449 ± 0.373	-0.399 ± 0.084	0.934
3a	3.728 ± 2.479	100*	-1.891 ± 0.306	-3.122 ± 8.105	0.997
3b	4.372 ± 1.965	100*	-0.852 ± 0.224	-2.599 ± 2.014	0.996
3c	3.083 ± 7.418	100*	-0.003 ± 0.102	-1.257 ± 0.484	0.991

**fixed parameter*

c) not irradiated at pH 5.5

dye	A1	A2	$LOGx_0$	P	R
1b	n.d.	n.d.	n.d.	n.d.	n.d.
3a	0*	100*	1.380 ± 0.918	-0.545 ± 0.210	0.631
3b	0*	100*	0.561 ± 0.229	-1.380 ± 0.714	0.990
3c	0*	100*	0.638 ± 0.220	-2.052 ± 1.248	0.991

**fixed parameter*

d) not irradiated at pH 7.5

dye	A1	A2	$LOGx_0$	P	R
1b	n.d.	n.d.	n.d.	n.d.	n.d.
3a	0*	100*	1.093 ± 0.082	-2.445 ± 2.149	0.997
3b	0*	100*	0.899 ± 0.120	-2.363 ± 2.754	0.971
3c	0*	100*	0.966 ± 0.396	-8.997 ± 1.064	0.833

**fixed parameter*

100

Confocal Laser scanning microscopy

$1x10^5$ cells/mL were seeded at 0.5 mL/well into 24 well plates (Sarstedt) containing microscope cover slips (0,17 mm) and grown over night. The next day, compounds were added yielding a final concentration of 1 µM in full medium and incubated for 24 h. Then, the supernatant was removed and cells were washed 3x with PBS. Cells on slides were fixed with 10% neutral buffered formalin for 20 minutes followed by 3 washing steps with PBS. Nuclei were stained with DAPI (2.5 µg/mL in PBS) for 30 minutes and the objects were washed again 3x with PBS before mounting them onto microscope slides using ProTaqs MountFluor (Quartett GmbH) mounting medium. After drying overnight, images were acquired on a Leica SP8 confocal laser scanning microscope using LASX software.

For live cell imaging, cells were seeded at $1x10^5$ cells/mL in 300 µL medium into µ-slide 8 well slides (ibiTreat, ibidi) the day before imaging. The microscope was equilibrated to 37°C using a custom fit heating chamber. Nuclei were stained with Hoechst 33258 in medium. Compounds were added with a final concentration of 1 µM. Subsequently, 1 image per minute was recorded for 8 minutes upon continuous excitation with λ_{ex} = 405 nm and λ_{ex} = 514 nm using corresponding emission channels at λ_{em} = 410 – 447 nm and λ_{em} = 520 – 603 nm, respectively, as well as the transmission channel.

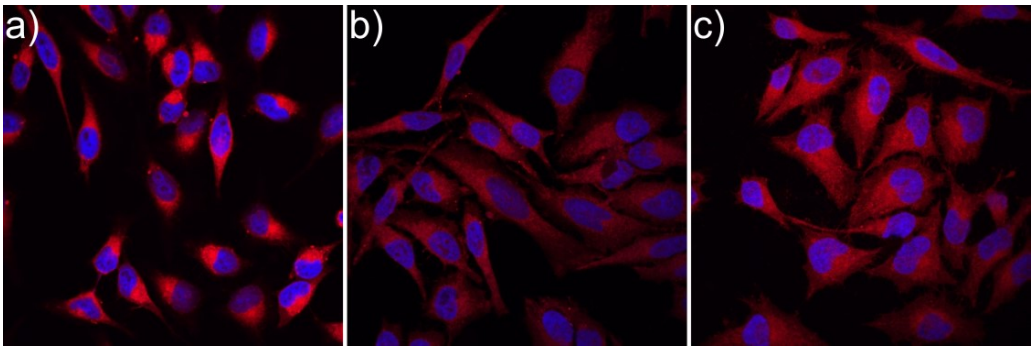

Figure S6. CLSM pictures (blue and red channel merged) of fixed HeLa cells incubated with 1 µM photosensitizers **3a**, **3b**, and **3c** (a), b) and c), respectively). Nuclei were stained with DAPI. The blue channel shows the fluorescence of DAPI, the red channel shows the fluorescence of the PS.

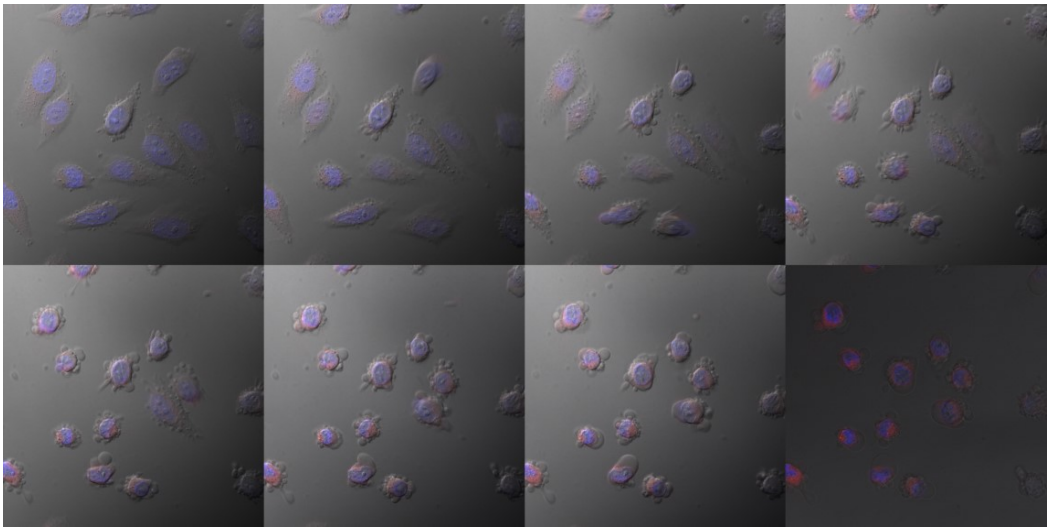

Figure S7. Live cell imaging of HeLa cells during uptake and irradiation of **3a**. Pictures were taken every minute starting at 1 min after incubation to a total of 8 min of irradiation (from upper left to bottom right). Nuclei were stained with Hoechst. Pictures show merged channels (blue, red, transmission).

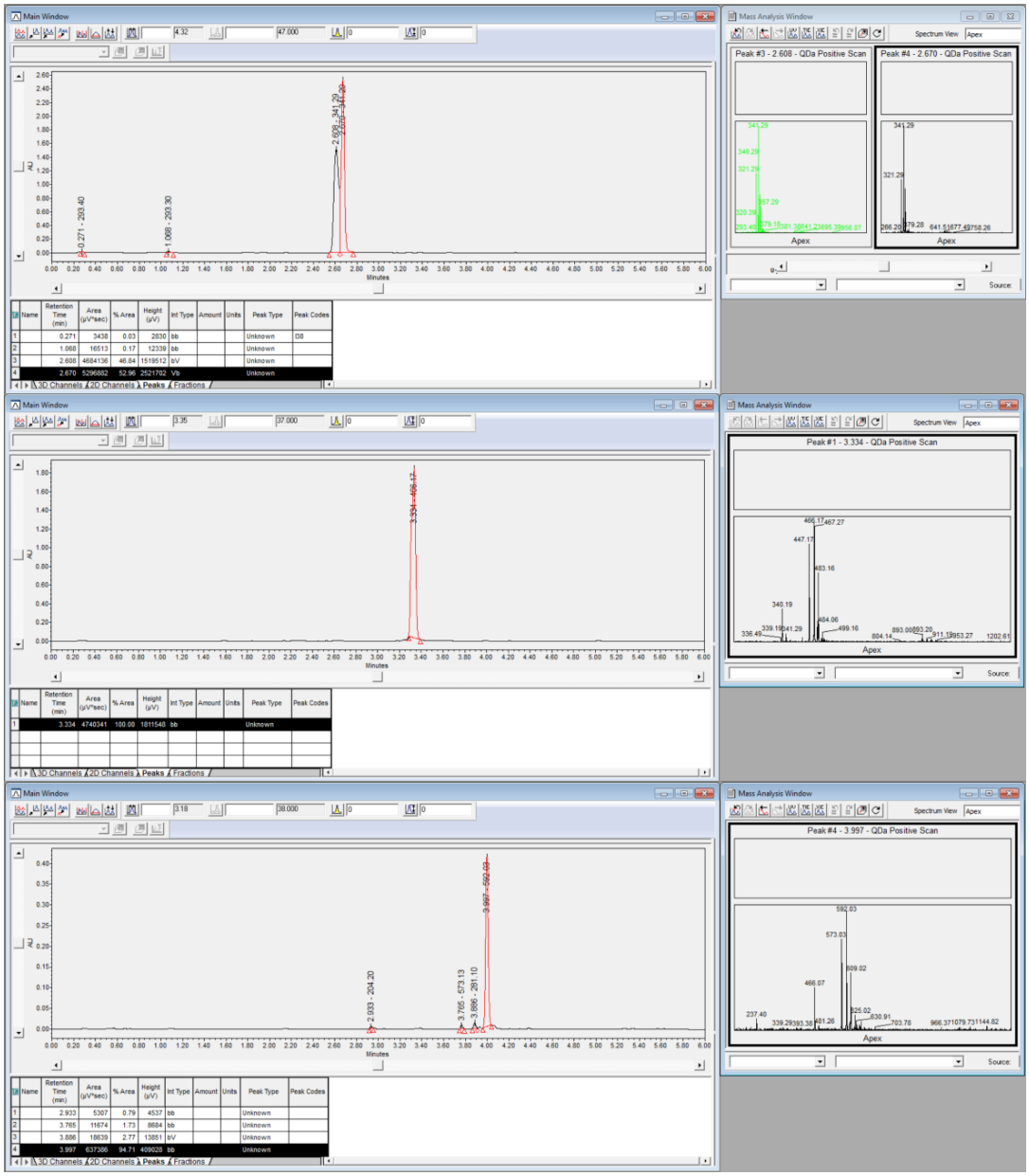

Figure S8. UPLC chromatogram of compounds **1a**, **2a**, and **3a** (top to bottom) and corresponding ESI/MS spectra.

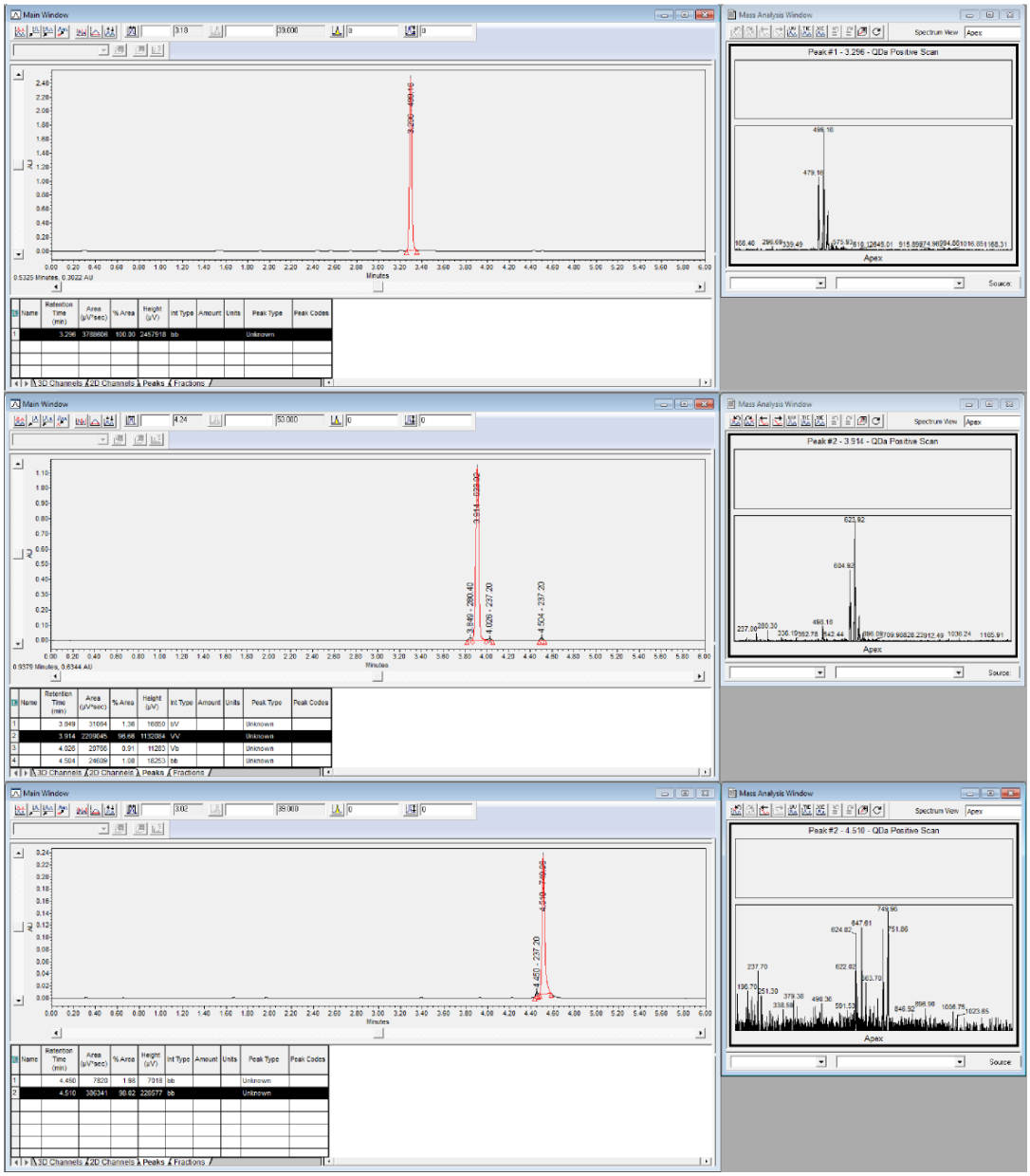

Figure S9. UPLC chromatogram of compounds **1b**, **2b**, and **3b** (top to bottom) and corresponding ESI/MS spectra.

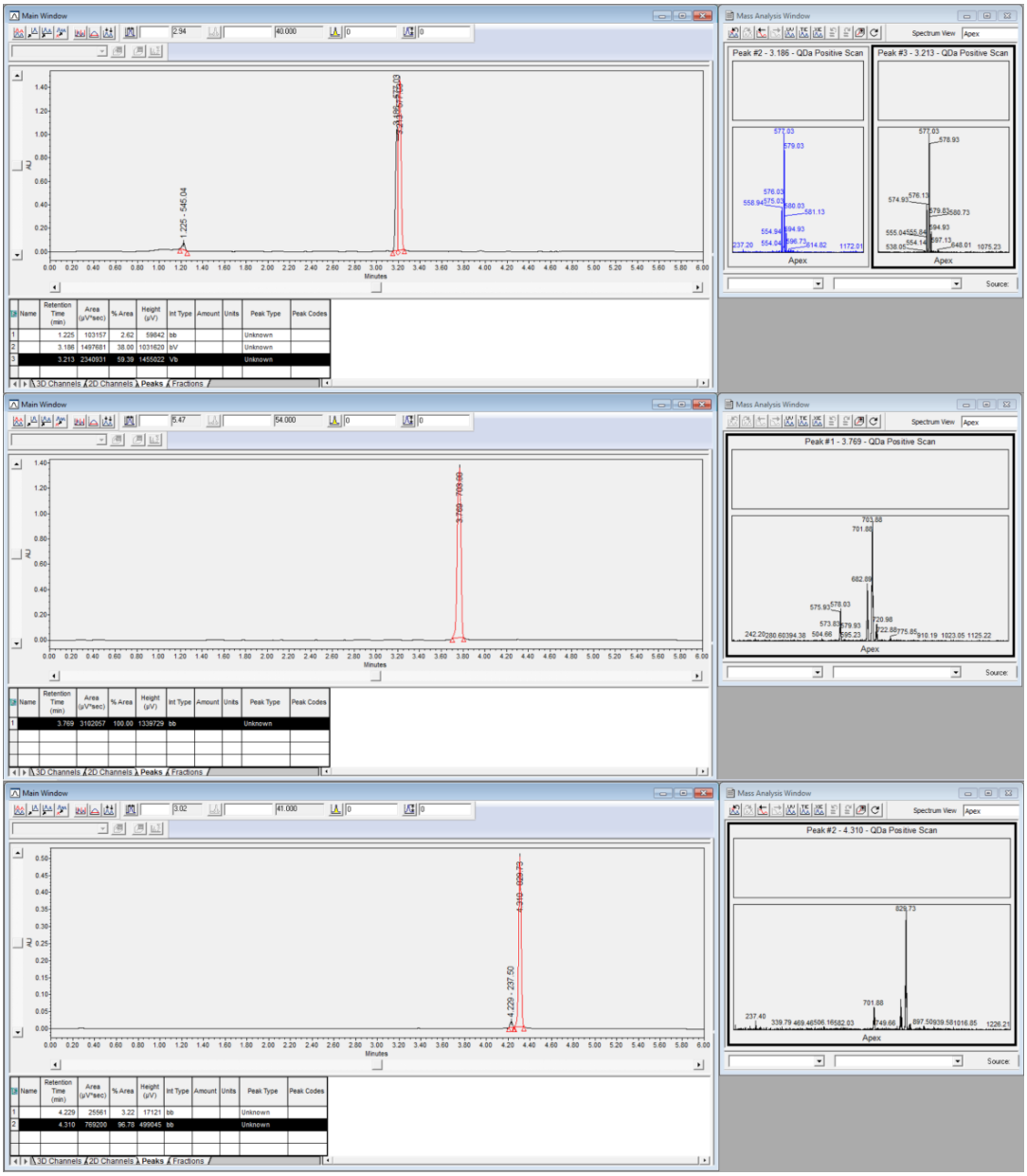

Figure S10. UPLC chromatogram of compounds **1c**, **2c**, and **3c** (top to bottom) and corresponding ESI/MS spectra.

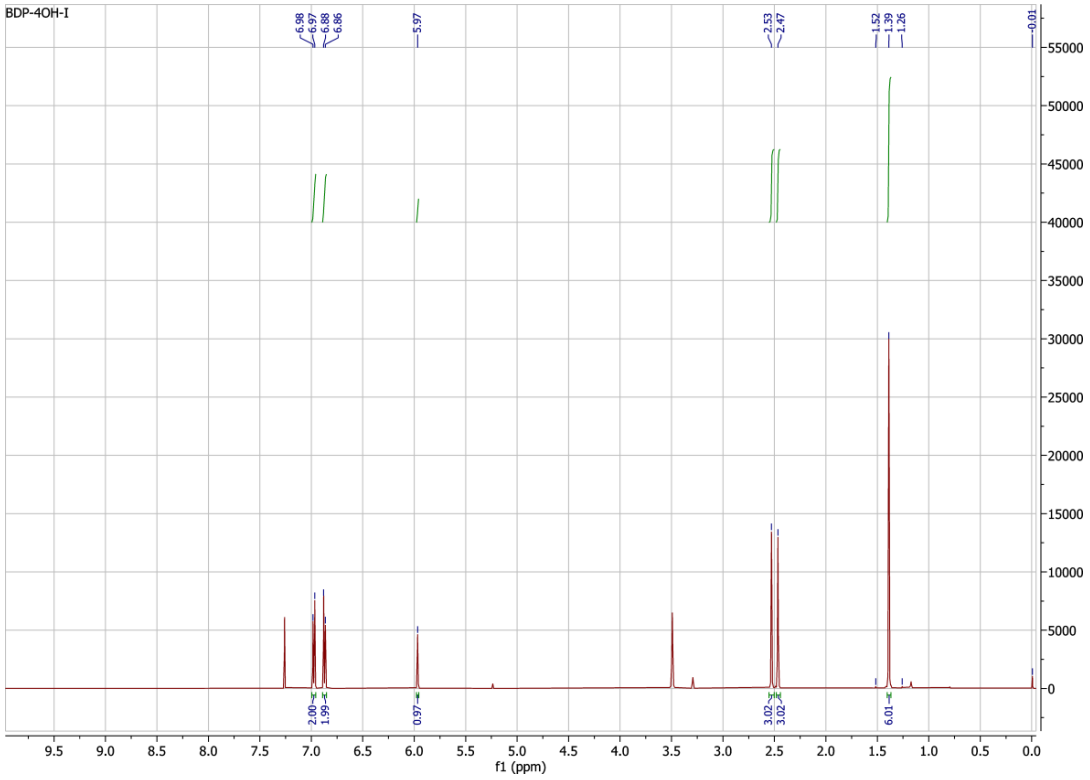

Figure S11. [1]H-NMR spectrum of compound **2a**.

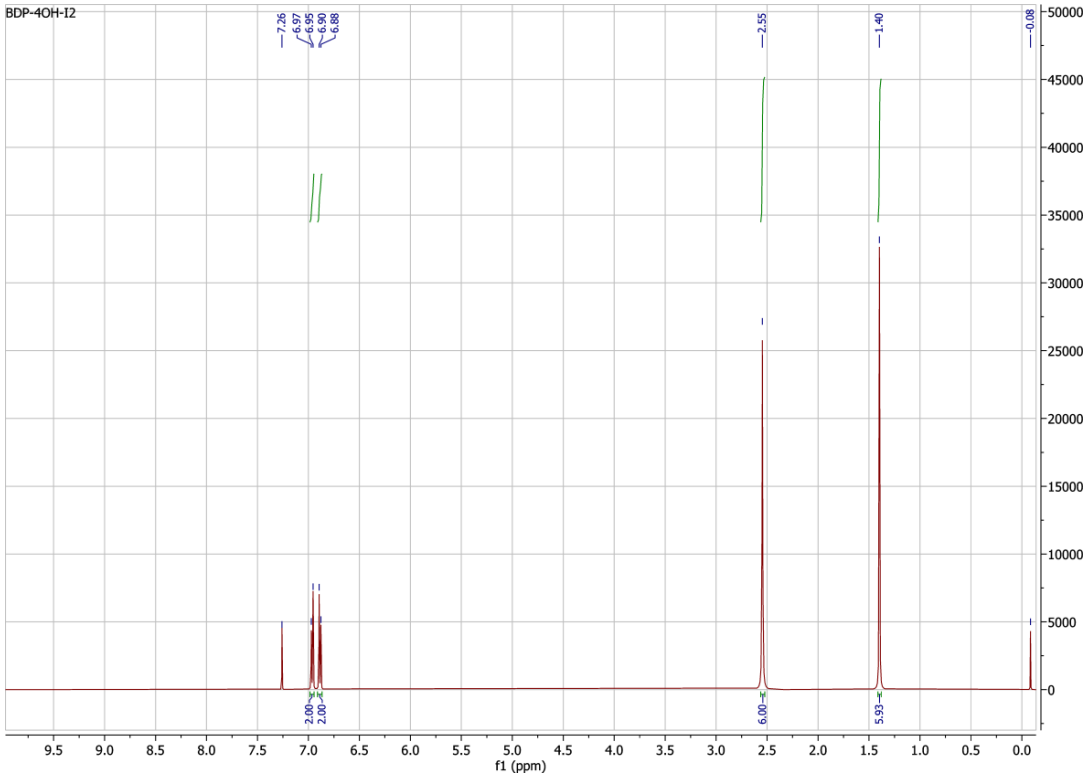

Figure S12. [1]H-NMR spectrum of compound **3a**.

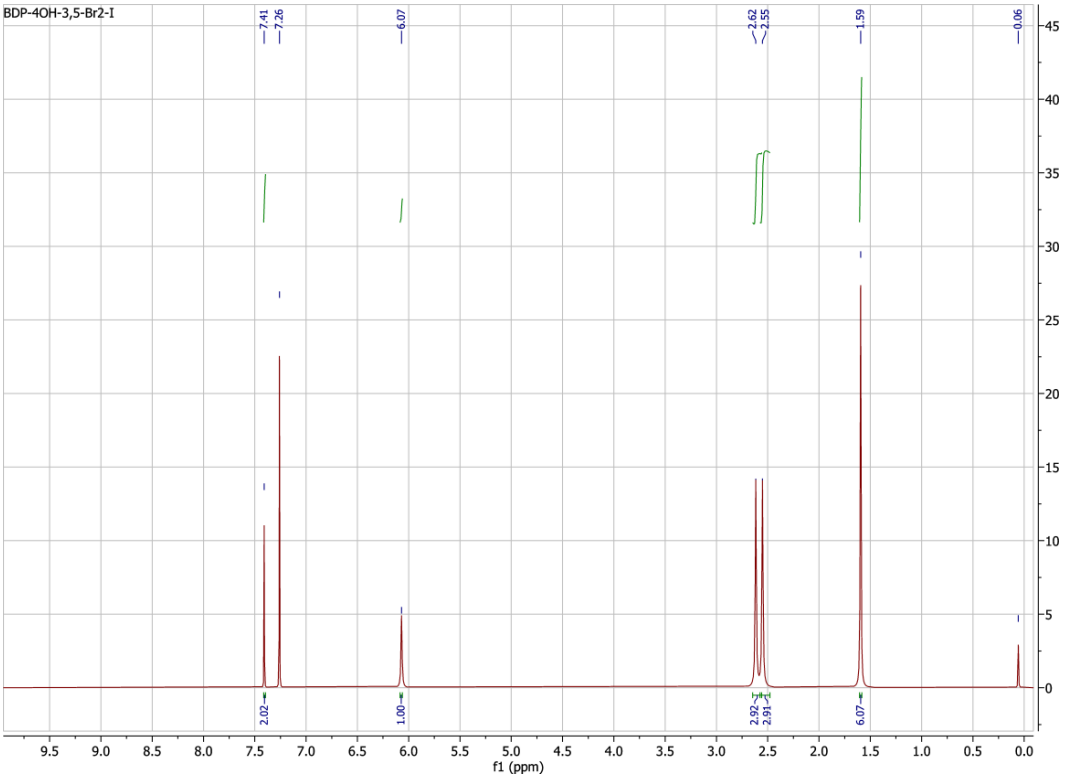

Figure S13. [1]H-NMR spectrum of compound **2b**.

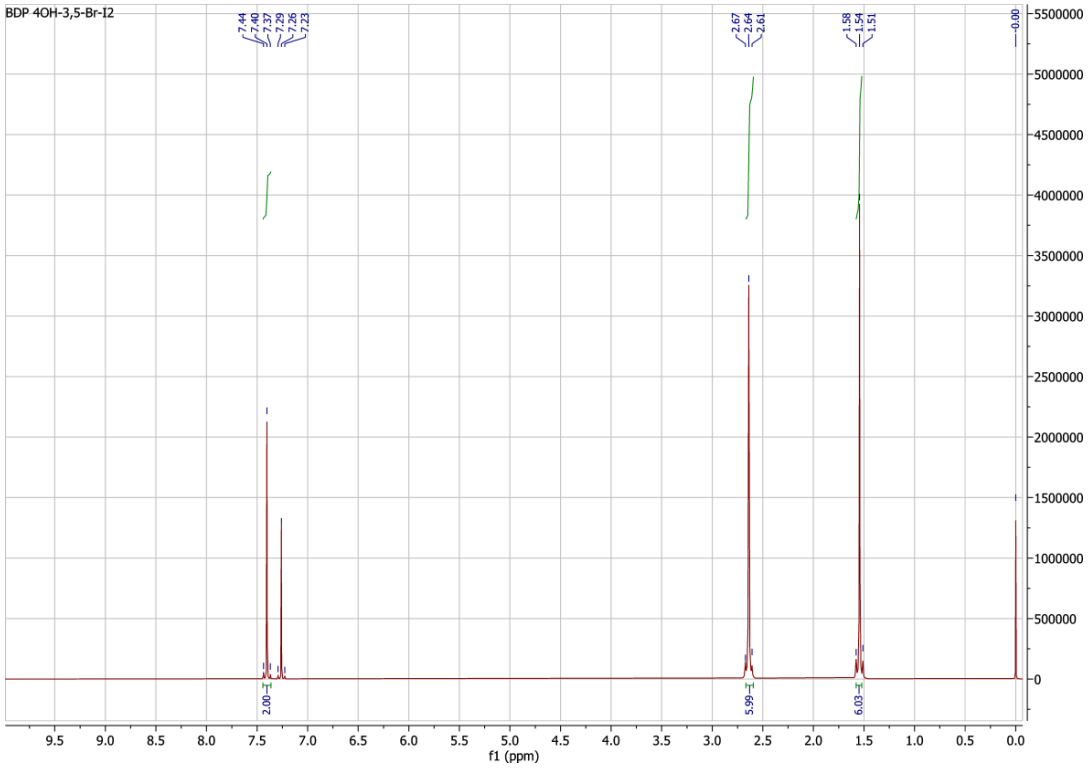

Figure S14. [1]H-NMR spectrum of compound **3b**.

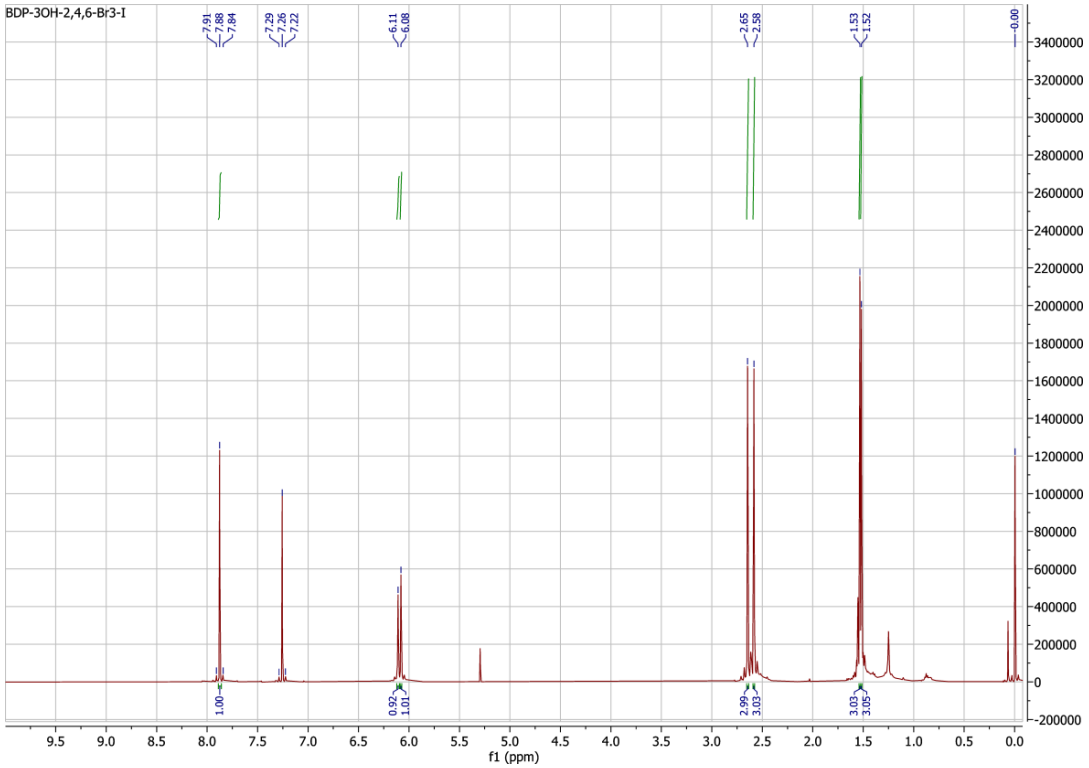

Figure S15. [1]H-NMR spectrum of compound **2c**.

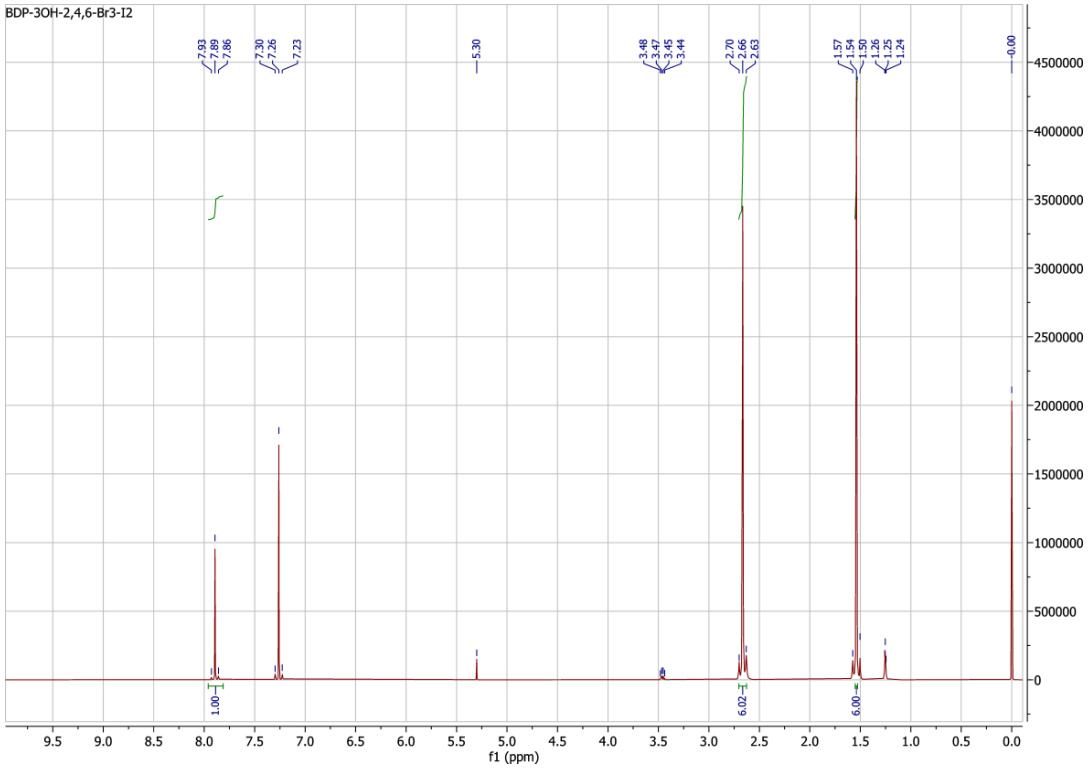

Figure S16. [1]H-NMR spectrum of compound **3c**.

Compound ID,SMILE CODES,HeLa ACC 57 IC50 (nM, illuminated, full medium) ,HeLa ACC 57 IC50 (nM, illuminated, pH 5.5) ,
HeLa ACC 57 IC50 (nM, illuminated, pH 7.5), HeLa ACC 57 IC50 (nM, not illuminated, full medium),
HeLa ACC 57 IC50 (nM, not illuminated, pH 5.5) ,HeLa ACC 57 IC50 (nM, not illuminated, pH 7.5)
1a,FB([N]1=C(C)C=C(C)C1=C2C3=CC=C(O)C=C3)(F)N4C2=C(C)C=C4C,n.d.,n.d.,n.d.,n.d.,n.d.
2a,FB([N]1=C(C)C=C(C)C1=C2C3=CC=C(O)C=C3)(F)N4C2=C(C)C(I)=C4C,n.d.,n.d.,n.d.,n.d.,n.d.
3a,FB([N]1=C(C)C(I)=C(C)C1=C2C3=CC=C(O)C=C3)(F)N4C2=C(C)C(I)=C4C,2 +- 10,20 +- 10,10 +- 10,> 10000,> 10000,> 10000
1b,FB([N]1=C(C)C=C(C)C1=C2C3=CC(Br)=C(O)C(Br)=C3)(F)N4C2=C(C)C=C4C,n.d.,> 10000,> 10000,n.d.,> 10000,> 10000
2b,FB([N]1=C(C)C=C(C)C1=C2C3=CC(Br)=C(O)C(Br)=C3)(F)N4C2=C(C)C(I)=C4C,n.d.,n.d.,n.d.,n.d.,n.d.
3b,FB([N]1=C(C)C(I)=C(C)C1=C2C3=CC(Br)=C(O)C(Br)=C3)(F)N4C2=C(C)C(I)=C4C,70 +- 40,30 +- 20,150 +- 60,8500 +- 1700,3600 +- 1500,7900 +- 2200
1c,FB([N]1=C(C)C=C(C)C1=C2C3=C(Br)C(O)=C(Br)C=C3Br)(F)N4C2=C(C)C=C4C,n.d.,n.d.,n.d.,n.d.,n.d.
2c,FB([N]1=C(C)C=C(C)C1=C2C3=C(Br)C(O)=C(Br)C=C3Br)(F)N4C2=C(C)C(I)=C4C,n.d.,n.d.,n.d.,n.d.,n.d.
3c,FB([N]1=C(C)C(I)=C(C)C1=C2C3=C(Br)C(O)=C(Br)C=C3Br)(F)N4C2=C(C)C(I)=C4C,n.d.,480 +- 230,1000 +- 200,n.d.,4400 +- 1700,9300 +- 5500

2.4 Evolution of Size and Optical Properties of Upconverting Nanoparticles during High-Temperature Synthesis

Sebastian Radunz, Alexander Schavkan, Sebastian Wahl, Christian Würth, Harald Rune Tschiche, Michael Krumrey, Ute Resch-Genger*

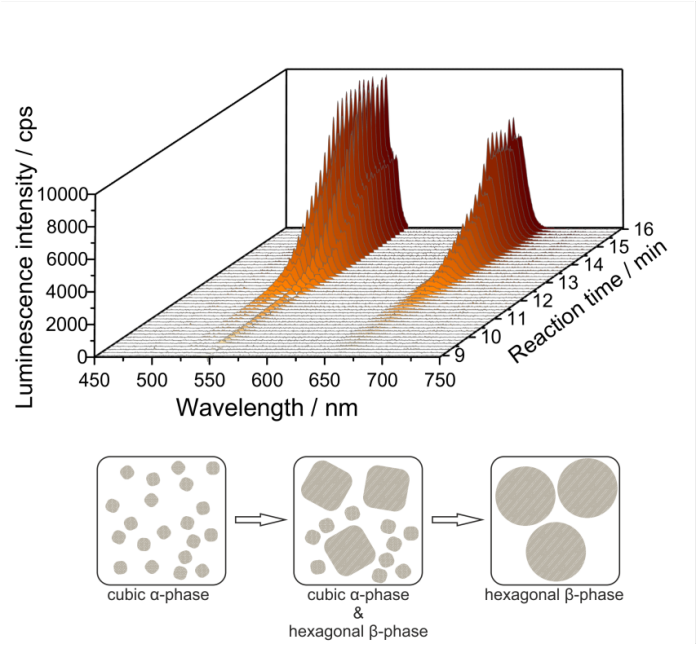

Figure 15: Reprinted with permission from S. Radunz *et al.*.[159] Copyright 2018 American Chemical Society.

In this publication S. Radunz contributed to the conceptual design of the study. He established the synthesis and parts of the analytical characterization. All spectroscopic characterization was established by him. He performed all synthesis and *in situ* related experiments while he contributed in parts to the *ex situ* related experiments. He performed most of the data evaluation and most of the scientific interpretation of the results. The publication was mainly conceived and written by him.

THE JOURNAL OF PHYSICAL CHEMISTRY C

Article

Cite This: J. Phys. Chem. C 2018, 122, 28958−28967

pubs.acs.org/JPCC

Evolution of Size and Optical Properties of Upconverting Nanoparticles during High-Temperature Synthesis

Sebastian Radunz,[†] Alexander Schavkan,[‡] Sebastian Wahl,[§] Christian Würth,[†] Harald R. Tschiche,[†,∥] Michael Krumrey,[‡] and Ute Resch-Genger*[,†]

[†]Division Biophotonics, BAM Federal Institute for Materials Research and Testing, Richard-Willstaetter-Strasse 11, 12489 Berlin, Germany

[‡]Physikalisch-Technische Bundesanstalt (PTB), Abbestrasse 2-12, 10587 Berlin, Germany

[§]Department of Chemistry, Humboldt-Universität zu Berlin, Brook-Taylor-Strasse 2, 12489 Berlin, Germany

[∥]Department 7, BfR German Federal Institute for Risk Assessment, Max-Dohrn-Strasse 8-10, 10589 Berlin, Germany

Supporting Information

ABSTRACT: We investigated the growth of β-phase $NaYF_4$:Yb^{3+},Er^{3+} upconversion nanoparticles synthesized by the thermal decomposition method using a combination of in situ and offline analytical methods for determining the application-relevant optical properties, size, crystal phase, and chemical composition. This included in situ steady state luminescence in combination with offline time-resolved luminescence spectroscopy as well as small-angle X-ray scattering (SAXS) transmission electron microscopy (TEM), X-ray diffraction analysis (XRD), and inductively coupled plasma optical emission spectrometry (ICP-OES). For assessing the suitability of our optical monitoring approach, the in situ-collected spectroscopic data, which reveal the luminescence evolution during nanocrystal synthesis, were compared to measurements done after cooling of the reaction mixture of the as-synthesized particles. The excellent correlation of the in situ and time-resolved upconversion luminescence with the nanoparticle sizes determined during the course of the reaction provides important insights into the various stages of nanoparticle growth. This study highlights the capability of in situ luminescence monitoring to control the efficiency of UCNP synthesis, particularly the reaction times at elevated temperatures and the particle quality in terms of size, shape, and crystal structure, as well as luminescence lifetime and upconversion quantum yield.

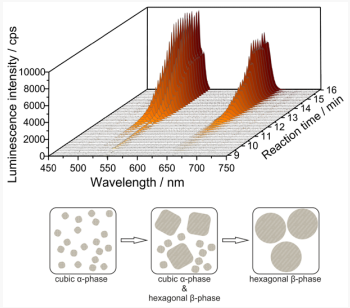

INTRODUCTION

Upconversion (UC) is a unique multiphotonic process for generating short-wavelength light from long-wavelength excitation. Aside from second-harmonic generation (SHG)[1] and two-photon absorption (TPA),[2] UC can be achieved by triplet−triplet annihilation (TTA-UC) utilizing molecular triplet sensitizers and singlet emitters[3] or by exploiting the manifold of energy levels and unique optical properties of lanthanide ions.[4] The latter UC mechanism involves multiple, sequential absorption and energy transfer events by nonvirtual, metastable electronic states.[4]

UC in lanthanide-based materials like crystals or micrometer-sized phosphors has been known for decades.[4] In recent years, the development of nanocrystalline (NC) materials doped with UC-active trivalent lanthanide ions has emerged as a very active research field and paved the road for new applications of these materials in the life and material sciences.[5−9] This is related to the long-lived multicolour emission of these materials and their high robustness in terms of their luminescence properties and resistance to photobleaching in comparison to, e.g., organic fluorophores and semiconductor quantum dots. Furthermore, UCNCs show no blinking and have a low cytotoxicity, which is advantageous for bioanalytical and biological applications.[10−13] While UC nanoparticles (UCNPs) have been already used for applications in sensing,[5,8,9,14−17] bioimaging,[8,18−20] photodynamic therapy,[8,21] spectral conversion in solar cells,[7] and security printing,[22−24] there are still some major challenges to overcome for a successful transfer of UC nanotechnology into real-world applications. Particularly relevant are the enhancement of the brightness and efficiency of small and ultrasmall UCNPs.[25,26]

The by far most-studied NIR-to-visible UCNPs are based on the lanthanide-doped β-$NaYF_4$ host lattice, doped with Yb^{3+} used as the sensitizer, absorbing 980 nm excitation light, and either Er^{3+}, Tm^{3+}, or Ho^{3+} as the activator emitting visible light.[27] These materials are among the most efficient upconverters known. A variety of synthetic methods have been meanwhile described for producing solvent-dispersible UCNPs with controlled size and size distribution, shape, crystal phase, morphology, and surface-capping ligands.[5,6,28−34]

Received: October 8, 2018
Revised: November 15, 2018
Published: November 19, 2018

DOI: 10.1021/acs.jpcc.8b09819
J. Phys. Chem. C 2018, 122, 28958−28967

High-quality UCNP can be synthesized by either thermal decomposition[29,34−36] or hydrothermal/solvothermal methods.[37,38] Thermal decomposition has become a common route for preparing highly uniform and colloidally stable nanoparticles, as required for fundamental photophysical studies, as well as sensing and therapeutic applications. Zhang et al. first reported the synthesis of novel single-crystalline and monodisperse LaF_3 nanoplates via thermal decomposition of the trifluoroacetate precursor $La(CF_3COO)_3$.[39] Subsequently, a general synthesis procedure for high-quality $NaREF_4$ (RE = Pr to Lu, Y) nanocrystals via thermal decomposition of trifluoroacetate precursors in the high-boiling solvents 1-octadecene (ODE) and oleic acid (OA)/oleylamine (OM) was published by Mai et al.[34] These authors were already able to distinguish between different reaction conditions to synthesize $NaYF_4$:Yb,Er/Tm UCNPs either in the cubic α-phase or in the hexagonal β-phase. Further investigations by Mai et al. revealed that the formation of β-phase $NaYF_4$:Yb,Er UCNPs occurred via a unique delayed nucleation pathway involving an α-phase intermediate.[40] While the thermal decomposition method usually provides UCNPs with nonpolar surface-capping ligands due to the use of organic high-boiling solvents, the solvothermal method can be performed in water-based systems yielding UCNPs with polar surface-capping ligands as well as controllable size, size distribution, structure, and morphology.[28]

For both thermal decomposition and hydrothermal/solvothermal methods, a reaction mechanism has been proposed that involves the initial formation of small α-phase UCNPs, which are then converted by a dissolution/recrystallization step to larger β-phase UCNPs.[37,40−44] In previous studies, the course of the reactions has been mostly studied either by collecting samples during the synthesis or by prematurely terminating the reactions, thereby varying the reaction time. Both approaches require, however, multiple syntheses and a high reproducibility of the particles formed. In 2014, Suter et al. published a study in which they followed the synthesis of UCNPs via real-time monitoring using NIR-to-visible UC luminescence.[43] This approach allows a constant noninvasive sampling of the reaction mixtures and thus continuous quality control during synthesis. These authors proposed a four-stage particle formation process by combining results from in situ luminescence measurements with offline transmission electron microscopy (TEM) data. In their study they also found a large batch-to-batch variation of the reaction time associated with the onset of the actual $\alpha \rightarrow \beta$ phase transition. The origin of these variations as well as the origin of the first β-phase seeds could not be determined. Further studies by May et al. provided more insights in the dynamics of nanoparticle growth by applying a theoretical model using data obtained by real-time luminescence monitoring of the synthesis and offline TEM measurements to simulate the actual nanoparticle growth.[45] This supported a thermodynamically driven dissolution/recrystallization process for the growth of β-phase UCNPs. Stage I was defined as α-particle formation phase during heat-up to the eventual reaction temperature and stage II as relative stasis phase with highly variable duration and only minor changes in α-particle distribution, attributed to Ostwald ripening processes. Stage III was characterized by an exponential increase of the luminescence intensity originating from newly formed and grown β-particles during the rapid $\alpha \rightarrow \beta$ phase transition and stage IV (completed reaction) by an eventually reached constant luminescence intensity.

In the past we described a first less refined attempt to control UCNP synthesis via in situ luminescence measurements. Here, solely monitoring of the formation of β-phase particles was done, exploiting the concomitant increase in fluorescence intensity.[29] Aiming at developing tools for the simple control and optimization of the synthesis, codoped UCNPs were synthesized using the thermal decomposition method.[31,34] For optimizing the reaction conditions, particularly the reduction of energy consuming heating steps, and particle quality, we systematically studied the potential of in situ spectrally resolved fluorescence spectroscopy. The optical measurements were completed with offline steady state, time-resolved fluorometry, small-angle X-ray scattering (SAXS), and transmission electron microscopy (TEM) measurements to gain mechanistic insights into particle formation. The overall goal is to provide the basis for an eventual standardization and automation of UCNP synthesis.

EXPERIMENTAL SECTION

Materials. For the synthesis of UCNPs, $YCl_3{\cdot}6H_2O$ (99.99%), $YbCl_3{\cdot}6H_2O$ (99.99%), $ErCl_3{\cdot}6H_2O$ (99.99%), oleic acid (90% technical grade), and NaOH (99.99%) were purchased from Sigma-Aldrich. 1-octadecene (ODE, 90% technical grade) and NH_4F (99.99%) were obtained from Alfa Aesar. Chloroform, cyclohexane, acetone, and ethanol were purchased from Carl Roth GmbH. All chemicals were used without further purification.

Preparation of $NaYF_4$:Yb^{3+},Er^{3+} Upconversion Nanoparticles. The codoped UCNPs were synthesized using the thermal decomposition method.[31,34] Following the procedure for the large-scale synthesis of hexagonal-phase UCNPs reported by Wilhelm et al.,[29] the synthesis was carried out in a mixture of oleic acid and 1-octadecene. $YCl_3{\cdot}6H_2O$ (1183.10 mg, 3.80 mmol), $YbCl_3{\cdot}6H_2O$ (387.50 mg, 1 mmol), and $ErCl_3{\cdot}6H_2O$ (38.17 mg, 0.20 mmol) were dissolved in 15 mL of methanol by sonication and subsequently added to a mixture of OA (40 mL) and ODE (75 mL) in a 250 mL three-necked flask. The stirred reaction mixture was then heated to 150 °C under argon flow. After 30 min, vacuum was applied for further 45 min at 150 °C to remove remaining low-boiling impurities. The lanthanide precursor-containing reaction mixture was then cooled down to room temperature under a constant argon flow. Subsequently, a methanolic solution (30 mL) containing NaOH (500 mg, 12.5 mmol) and NH_4F (741 mg, 20 mmol) was added, and the resulting suspension was heated to 120 °C for 30 min to remove excess methanol. The reaction mixture was then heated to 300, 315, or 325 °C under reflux while applying a gentle flow of argon. When the temperature reached 300 °C, the reaction timer was set to t = 0 s, and subsequently, roughly 0.3 mL samples were taken in periodical time intervals of 90 s using a syringe with a long steel cannula. The formation of the nanoparticles was allowed to proceed while the upconversion luminescence (UCL) was monitored in situ with a CCD spectrometer. As previously reported, an increase in UCL is characteristic for the transformation of less emissive α-phase UCNPs into more strongly luminescent β-phase UCNPs.[29] When the reaction was completed, as indicated by a constant UCL, the reaction mixture was cooled down to room temperature and the UCL was monitored until no further changes could be observed. The resulting UCNPs were purified following the procedure given in the Supporting Information (SI).

DOI: 10.1021/acs.jpcc.8b09819
J. Phys. Chem. C 2018, 122, 28958−28967

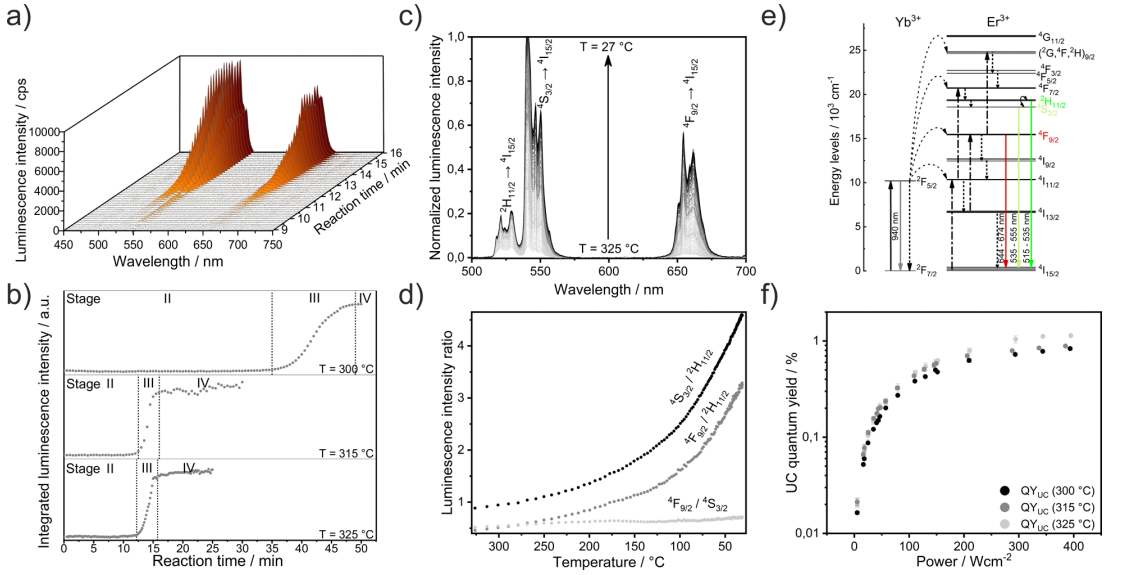

Figure 1. (a) Measured luminescence spectra showing the evolution of green and red upconversion emissions during the course of reaction at 325 °C. (b) Integrated luminescence intensity of the overall UCL versus reactions time for syntheses performed at 300, 315, and 325 °C (from top to bottom, respectively). (c) Temperature-dependent luminescence intensity (normalized) recorded during the cooling process after finished UCNP synthesis. Spectra were collected every 30 s with an integration time of 1 s until the reaction temperature reached room temperature (65 min). (d) Evolution of the intensity ratios of the integrated green emission bands $^2H_{11/2} \rightarrow {}^4I_{15/2}$ (515−535 nm) and $^4S_{3/2} \rightarrow {}^4I_{15/2}$ (535−555 nm) as well as the red emission $^4F_{9/2} \rightarrow {}^4I_{15/2}$ (644−674 nm). (e) Energy scheme of Yb^{3+} and Er^{3+} in $NaYF_4$ showing possible energy transfer upconversion (ETU) pathways. (f) Power density dependence of the upconversion quantum yield of the purified UCNPs in cyclohexane.

Characterization of $NaYF_4$:Yb^{3+},Er^{3+} Upconversion Nanoparticles. For determination of the size, crystal phase, as well as UCL decay kinetics of the UCNPs formed at different stages of the reactions, samples were taken from the reaction mixture in regular intervals and subsequently analyzed using TEM, SAXS, and luminescence spectroscopy. The batches of the eventually resulting nanoparticles synthesized at different temperatures were further characterized by X-ray diffraction analysis (XRD) and inductively coupled plasma optical emission spectrometry (ICP-OES) for comparison of their chemical composition and crystal phase. In addition, the quantum yield of their UCL was measured absolutely to provide a comparable measure for their luminescence efficiency. The crystal phase was determined by XRD (Seifert XRD 3003 TT with a rotating sample holder using Cu radiation, Cu $K_{\alpha 1,2}$; λ = 1.54 Å; U = 40 kV; I = 40 mA; Ni filter; all samples measured in Bragg−Brentano geometry). The dopant ratio was verified by ICP-OES (Spectro Arcos, Spectro Analytical Instruments GmbH, Kleve, Germany). Time-resolved measurements of the UCL were done with an Edinburgh Instruments spectrofluorometer FLS-980 (Edinburgh Instruments Ltd., Livingston, United Kingdom) equipped with an electrically pulsable 8 W 978 nm laser diode (Roithner Lasertechnik GmbH, Vienna, Austria). These luminescence lifetimes subsequently given represent amplitude-weighted averages of decay components obtained by exponential tail fitting. Power-dependent upconverting quantum yields were determined absolutely with a custom-made integrating sphere setup equipped with a high power stability 8 W 976 nm laser diode (Roithner Lasertechnik GmbH, Vienna, Austria) using spectrally corrected integral emission intensities of the UC emission bands.[46−48] All spectroscopic measurements were performed in 10 mm quartz cuvettes (Hellma, QS cell).

In Situ Real-Time Spectroscopy. The UCL of the reaction mixture was monitored continuously using a custom-designed experimental setup which closely matched the setup employed by Suter et al. in a previous study.[43] However, our setup contained a 2 W 980 nm laser diode (Roithner Lasertechnik GmbH, Vienna, Austria) and an Ocean Optics CCD spectrometer QE65000 (Ocean Optics, Inc., Largo, USA) coupled to a bifurcated fiber to simultaneously excite the reaction mixture and measure its UCL at the same spot. Further optical components like collimating and focusing lens as well as an 800 nm cutoff filter were used for setup optimization. Luminescence spectra were collected during the synthesis and during cooling after the reaction was finished every 30 s with an integration time of 1 s, respectively.

Transmission Electron Microscopy (TEM) Measurements. Size determinations of the nanoparticles by TEM were done with a Philips CM200 LaB6 microscope, operated at 200 kV, equipped with an EDAX energy-dispersive X-ray spectroscopy (EDX) detector. Carbon film coated copper TEM grids (300 mesh, Science Services, Munich, Germany) were used as specimen. Each grid was drop coated with nanoparticles dispersed in cyclohexane (<3 mg/mL) prior to measurement. The size distribution of each sample was derived from TEM data measuring the diameters of roughly 150 single nanoparticles in multiple images using the open source software ImageJ.

Small-Angle X-ray Scattering (SAXS) Measurements. SAXS measurements were performed at the four-crystal monochromator (FCM) beamline in the synchrotron radiation laboratory of PTB at the electron storage ring BESSY II (see SI, Figure S1). The samples were filled in thin-walled glass

DOI: 10.1021/acs.jpcc.8b09819
J. Phys. Chem. C 2018, 122, 28958−28967

capillaries and exposed to monochromatic radiation. The photon energy was set to 8 keV and is known with a relative uncertainty of 10^{-4}.[49] The scattering pattern was recorded with a large area in-vacuum hybrid pixel PILATUS detector.[50] The direct beam was blocked by a beamstop with an integrated photodiode. The scattering angle can be calculated using the distance between the sample and the detector, which could be varied between about 2.4 and 4.5 m, as well as the detector pixel size. The incident photon flux was measured with calibrated photodiodes. The scattered intensity was calculated from the previously determined quantum efficiency (QE) of the area detector. From a circular integration of the scattering pattern, the scattered intensity was obtained as a function of the momentum transfer q which is related to θ, one-half of the scattering angle between the direction of the incident beam and the scattered light, according to $q = 4\pi E/(hc)\ \sin(\theta)$. Here, h is Planck's constant and c is the speed of light in vacuum. The scattering curves were interpreted in terms of least-squares fitting of a model function describing spherical particles with a Gaussian size distribution.

RESULTS AND DISCUSSION

In our study, in situ spectroscopy and final TEM measurements were performed for reaction temperatures of 300, 315, and 325 °C as stated in the Experimental Section. The SAXS, TEM, and time-resolved luminescence measurements shown here were exemplarily performed for samples collected from the reaction mixture at 325 °C if not otherwise stated. The UCNP synthesis conditions given in the Experimental Section were chosen to obtain spherical particles to apply a corresponding model function for the evaluation of the SAXS measurements (see eq S4, SI). Therefore, respective amounts of OA and ODE were used in a ratio known to provide this particle shape.[30]

The UCNP syntheses performed at reaction temperatures of 300, 315, and 325 °C yielded spherical UCNPs with very narrow size distributions of around 25 ± 1, 28 ± 1, and 27 ± 1 nm, respectively (see Figure 4a and SI, Figures S2 and S3). The diffraction patterns determined by XRD for each particle batch could be assigned to the pure hexagonal phase of the host material $NaYF_4$ (see XRD pattern in Figure 4d and SI, Figures S2 and S3). Elemental analysis by ICP-OES gave Y^{3+}, Yb^{3+}, and Er^{3+} contents (provided in percentage of the total amount of lanthanides) of (79 ± 1)%, (19 ± 1)%, and (2 ± 1)% for all three batches, respectively (see SI, Table S1). This corresponds well with the precursor amounts used.

In Situ Optical Spectroscopy. As exemplarily shown in the three-dimensional plot in Figure 1a, the UCL of the reaction mixture excited at 980 nm light noticeably increases during the course of the reaction. A strong and rapid increase of the green ($^2H_{11/2}/^4S_{3/2} \rightarrow {}^4I_{15/2}$ transition) and red ($^4F_{9/2} \rightarrow {}^4I_{15/2}$ transition) Er^{3+} UCL started around t = 12 min after the reaction mixture reached 300 °C (denoted as t = 0 min throughout the manuscript). The final reaction temperature of 325 °C was already reached after t = 5 min as shown in the temperature ramp (SI, Figure S4). However, the formation of the α-phase particles (stage I) was not explicitly monitored by in situ spectroscopy. The initial intensity increase occurred exponentially within approximately 5 min. This corresponds to the actual growth of the luminescent hexagonal β-phase particles (stage III) as proposed by several research groups.[34,37,40,41] The luminescence reached a plateau after t = 15−16 min without significant changes until the reaction was stopped after 25 min (stage IV, see Figure 1b, lower panel). As shown in Figure 1b a similar luminescence behavior of the reaction mixture was observed for the reaction at 315 °C showing only a small shift of the starting time of stage III, followed by a very similar rise time of the luminescence intensity of approximately 5 min. However, major differences are noticed for the reaction carried out at 300 °C. As previously reported by Suter et al. and May et al., the reproducibility of the synthesis at 300 °C is good regarding the heat-up time (the authors used a different description of t = 0 min, stage I), the duration of the main increase of the luminescence intensity of about 15 min (stage III), and the final size distribution.[43,45] However, these authors observed considerable differences with regard to the onset of the main luminescence intensity increase, signaling the start of the actual growth of β-phase particles (duration of stage II). For our experiment at 300 °C, stage III started at around t = 36 min and ended after further 12 min. This observation is at least in good agreement with the experiments of Suter et al. and May et al. However, the duration of the relative stasis phase (stage II) and the final particle size differ drastically, showing a shorter duration of stage II and yielding significantly smaller nanoparticles.[43,45] It is noteworthy to mention that our reaction temperature usually slightly exceeds the set temperature within the first few minutes (<5 min) until it equilibrates as can be seen in the recorded temperature ramps (see SI, Figure S4). One of the processes during stage II affected by temperature, which leads to an earlier start of the β-phase particle growth, seems to be the ripening process of the α-particles (stage II). As already shown by Mai and co-workers, the duration of the relative stasis phase (stage II) is shortened with increasing reaction temperature.[40] Higher temperatures lead to a faster growth of the α-particles until a radius thermodynamically favoring the $\alpha \rightarrow \beta$ transition is reached and individual α-particles are transformed into β-particles.[45] Subsequently, a shortening of the duration of stage II should be observed in our case, which is in good agreement with our data considering a short overextension of the reaction temperature. An influence from the molar Na/RE/F ratio ($NaOH:RECl_3{\cdot}6H_2O:NH_4F$) known to strongly affect the starting time of the $\alpha \rightarrow \beta$ transition can be neglected here because similar conditions have been used throughout this study, which match those previously employed by other groups.[44]

After the reaction was finished, the reaction mixture was allowed to cool down to room temperature (here 27 °C). During this cooling process, the luminescence spectra were collected every 30 s with an integration time of 1 s. As the energy transfer upconversion (ETU) processes in lanthanide-doped systems involve multiphotonic excitation and a multitude of long-lived excited states, this introduces also a considerable temperature sensitivity of UCL. Higher temperatures result in UCL quenching by thermally induced nonradiative relaxation processes of the excited states of the lanthanides, e.g., by enhanced vibrational interaction with the host lattice or the solvents.[51] Thus, cooling the reaction mixture is expected to increase UCL. This can be clearly seen in Figure 1c. While the intensity of the green emission originating from the upper $^2H_{11/2}$ state ($^2H_{11/2} \rightarrow {}^4I_{15/2}$, 515−535 nm, see energy scheme in Figure 1e) shows only a minor increase by approximately a factor of 5 after cooling of the reaction mixture, the green $^4S_{3/2} \rightarrow {}^4I_{15/2}$ emission (535−555 nm) and the red $^4F_{9/2} \rightarrow {}^4I_{15/2}$ emission (644−

DOI: 10.1021/acs.jpcc.8b09819
J. Phys. Chem. C 2018, 122, 28958−28967

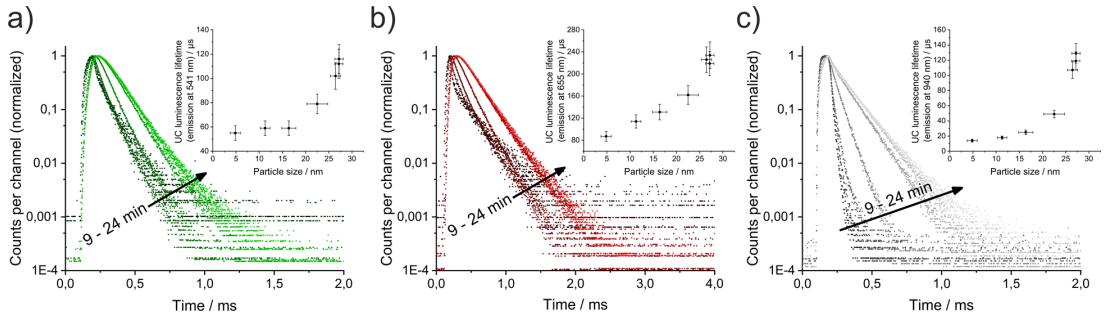

Figure 2. Decay curves of upconversion emissions (541, 655, and 940 nm, from left to right, respectively) of samples collected at different times during synthesis. Insets show the fitted and amplitude-weighted luminescence lifetimes in dependence of the size determined by TEM and SAXS.

674 nm, Figure 1e) show enhancement factors of about 20 and 30, respectively. The thermal coupling of the $^2H_{11/2}$ and $^4S_{3/2}$ energy levels can be visualized by calculating the luminescence intensity ratios of the UC emission bands (Figure 1d). Luminescence intensity ratios of UCNPs systems with thermally coupled states, e.g., Yb^{3+}/Er^{3+} or Yb^{3+}/Tm^{3+}, are a useful tool to understand fundamental characteristics (excitation pathways, nonradiative relaxations) as well as for broad-range temperature sensing.[14−17,52] The green Er^{3+} emission bands originate from a two-photonic excitation involving the excited states $^4I_{11/2}$ and $^4F_{7/2}$. Subsequently, the lower lying green energy levels $^2H_{11/2}$ and $^4S_{3/2}$ are fed by relaxation from the $^4F_{7/2}$ state. The population equilibrium of these thermally coupled states highly depends on the energy difference of these energy levels and can be mathematically described by a Boltzmann distribution. This allows a quantitative comparison of the temperature sensitivity of different systems as shown previously in several publications.[53−56] At lower temperatures the main emission in our systems occurs from the lower lying $^4S_{3/2}$ state as can be seen in Figure 1d with a luminescence intensity ratio of 4.6 of the $^4S_{3/2}$ and $^2H_{11/2}$ emission bands. However, at higher temperatures the equilibrium is shifted and the population of the $^2H_{11/2}$ and $^4S_{3/2}$ energy levels is drastically changed. Subsequently, the upper $^2H_{11/2}$ state is fed by the lower $^4S_{3/2}$ state, resulting in a luminescence intensity ratio below 1 (0.9 at 326 °C; see Figure 1d) as now the main luminescence occurs from the upper $^2H_{11/2}$ state (see Figure 1e). This is reflected also by the luminescence intensity ratio of the red-emitting $^4F_{9/2}$ state and the green-emitting $^2H_{11/2}$ state that decreases from 3.2 at 27 °C to 0.5 at 326 °C.

These results underline the potential of in situ luminescence spectroscopy for real-time quality control of UCNP synthesis, enabling the optimization of the reaction time required for completion of the formation of ß-phase UCNPs, using changes of the luminescence intensity as a parameter. This can be exploited for reducing energy consumption in potential mass production by minimizing heating steps and heating duration and hence costs.

Offline Fluorescence Measurements. Subsequently, we characterized the obtained UCNPs with regard to their optical properties in more detail. As can be seen in Figure 1f, the differences of the excitation power-dependent luminescence quantum yields (QY) of the core-only UCNPs in cyclohexane, which show the typical saturation behavior,[48,57−59] are small, ranging from 0.016% to 0.02% at a low excitation power density of roughly 5.3 W cm^{-2} to from 0.85% to 1.1% at a high excitation power density of 390 W cm^{-2}. Here, also small differences can originate from slightly different nanocrystal sizes, and size distributions as the QY of UCL are known to be size dependent. Furthermore, power-dependent green-to-red intensity ratios of the UCNPs as well as relative photon fluxes and slope factors *n* for the different emissions differ only slightly (see SI, Figure S5). The green-to-red intensity ratios of the three UCNP batches show a similar behavior, i.e., a decrease from roughly 2 to 0.5 for excitation power densities changing from 5.3 to 390 W cm^{-2}, respectively. Furthermore, the power density-dependent spectral contributions of the green and red emission to overall UCL in dependency of the reaction temperature is negligible. While the percent contributions of the red $^4F_{9/2} \rightarrow {}^4I_{15/2}$ emission to the overall UCL increase drastically from 25% to 55% for all batches in dependence of the excitation power density, the percent contributions of the green $^4S_{3/2} \rightarrow {}^4I_{15/2}$ and $^2H_{11/2} \rightarrow {}^4I_{15/2}$ emissions decrease from 40% to 25% and 10% to 5%, respectively. This indicates a similar particle performance with respect to the optical properties such as UCL efficiency, which is additionally supported as the percent contributions of the green $^4S_{3/2} \rightarrow {}^4I_{15/2}$ and red $^4F_{9/2} \rightarrow {}^4I_{15/2}$ emissions for all three batches have a cross-section at around 35 W cm^{-2}. The slope factors *n* of the different UCL bands, calculated from the change of the emission intensity of each band in dependence of the excitation power density, provides the number of low-energy photons contributing to each UCL emission. As can be seen in Figure 1e, the green and red emission bands originate mainly from a two-photonic excitation (at least for lower excitation powers[58]), while the blue emission at 410 nm ($(^2G,^4F,^2H)_{9/2} \rightarrow {}^4I_{15/2}$) originates from three photonic processes.[60,61]

The fact that the UCNPs synthesized at different temperatures show relatively similar optical properties, although the time scales during syntheses differ, suggests that the reaction temperature affects only the speed of nanoparticle growth but not the mechanism of the growth process itself, which mainly takes place during the rapid luminescence intensity increase (stage III). Therefore, further investigations of the growth process were carried out only for the particles synthesized at 325 °C.

Time-Resolved Luminescence Measurements. As can be seen in Figure 2, the UCL decay curves of the green and red Er^{3+} emission at 541 and 655 nm as well as the Yb^{3+} emission at 940 nm show longer decay kinetics with increasing reaction time. Each luminescence decay curve represents a sample collected during the reaction. The corresponding luminescence

DOI: 10.1021/acs.jpcc.8b09819
J. Phys. Chem. C 2018, 122, 28958−28967

Table 1. Diameter of α- and β-Phase Nanocrystals (NC) Derived from SAXS and TEM Measurements and Luminescence Lifetimes[a] for Emissions at 541, 655, and 940 nm[b] in Dependence of the Reaction Time

reaction time (min)	diameter α-phase NCs (TEM) (nm)	diameter β-phase NCs (TEM) (nm)	diameter α-phase NCs (SAXS) (nm)	diameter β-phase NCs (SAXS) (nm)	τ_{Lum} (541 nm) (μs)	τ_{Lum} (655 nm) (μs)	τ_{Lum} (940 nm) (μs)
6.0	3.5 ± 0.3		4.2 ± 1.0		[c]	[c]	[c]
9.0	4.8 ± 1.1		4.2 ± 1.8		55 ± 6	87 ± 9	14 ± 2
10.5	5.3 ± 1.0	11.3 ± 1.1	4.9 ± 1.5	10.5 ± 2.4	59 ± 6	114 ± 12	18 ± 2
12.0	5.0 ± 1.3	16.4 ± 1.5	4.3 ± 2.2	16.9 ± 0.9	59 ± 6	131 ± 14	25 ± 3
13.5	6.1 ± 1.2	22.5 ± 2.2	6.4 ± 1.4	22.4 ± 1.0	79 ± 8	162 ± 17	48 ± 5
15.0		26.5 ± 1.1		26.8 ± 0.5	102 ± 11	226 ± 23	107 ± 11
19.5		27.2 ± 0.9		27.0 ± 1.1	112 ± 12	219 ± 22	119 ± 12
24.0		27.2 ± 0.9		26.5 ± 1.2	116 ± 12	234 ± 24	129 ± 13

[a]Amplitude-weighted average; obtained by tail fitting of the luminescence decay curves. [b]Excitation of the nanocrystals at 978 nm with 8 W electrically pulsable laser diode; measurements at room temperature. [c]Luminescence signal too weak.

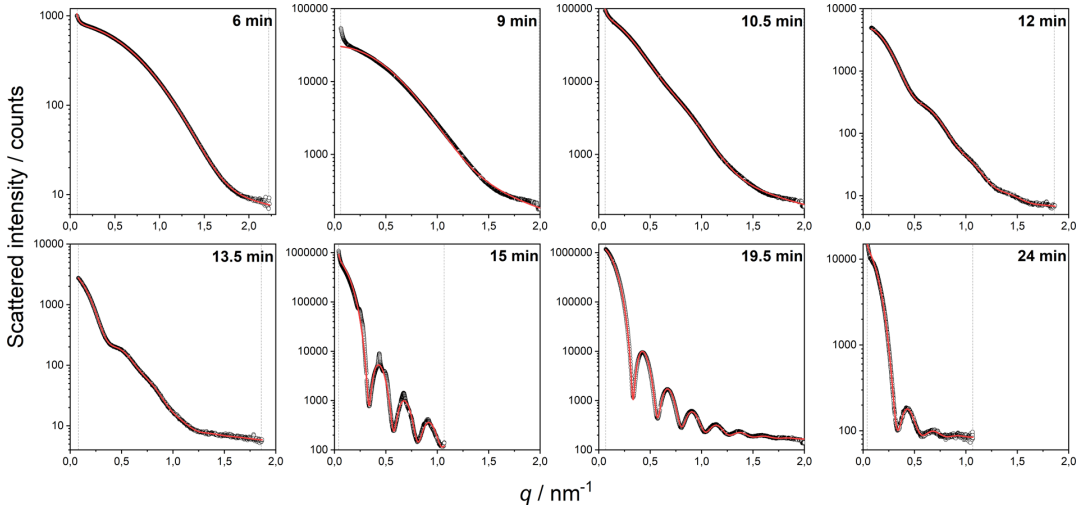

Figure 3. SAXS measurements and corresponding fits for samples collected from the reaction at 325 °C at t = 6.0, 9.0, 10.5, 12.0, 13.5, 15.0, 19.5, and 24.0 min (from top left to right and bottom left to right, respectively).

lifetimes of the UC emissions are summarized in Table 1. Apparently, the most pronounced changes are found for the decay of the Yb^{3+} emission (Figure 2c), showing a roughly 10-fold increase of the luminescence lifetime from 14 to 129 μs with increasing reaction time (see Table 1). As Yb^{3+} acts as sensitizer in this UC system, transferring its energy to Er^{3+} upon excitation at 980 nm, the decay kinetics of the green and red Er^{3+} emissions (Figure 2a and 2b, respectively) are closely correlated with the Yb^{3+} emission. While the amplitude-weighted luminescence lifetime of the green emission increases by roughly a factor of 2 from 55 to 116 μs during the course of the reaction, the luminescence lifetime of the red emission rose approximately by a factor of 2.5 from 87 to 237 μs. For samples collected at t = 9−13.5 min, the luminescence decay of the 940 nm emission could be best described by a triexponential fit, whereas biexponential fits gave the best results for the samples collected at t = 15−24 min. This indicates differences in the contributions of the different decay components to the overall UCL decay kinetics. We explain this by slight differences in the size and size distribution and/or chemical composition of the UCNP samples as shown later. We are aware that amplitude-weighted averaging of the luminescence lifetime components obtained by fitting is critical because of the presence of differently contributing particle populations. However, with respect to the significant differences of the upconverting efficiency of the two possible crystal phases, the UCL contribution of the weakly emissive cubic α-phase particles is assumed to become negligible as soon as an increasing fraction of hexagonal β-phase particles is present. This can be derived from the evolution of UCL during synthesis (see Figure 2a and 2b).

Small-Angle X-ray Scattering (SAXS) Measurements. SAXS is an increasingly used technique for particle characterization that provides the size, size distribution, and shape of dispersed and dried nanoparticles based on measurements of the scattered intensity. The most important material parameter that affects the signal intensity is the scattering cross-section which depends on the contrast between solvent and nanoparticles.[32] The SAXS curves obtained for the samples taken from the reaction at 325 °C are shown in Figure 3 including the respective fits. Fitting of the scattering curves for t = 0 min was not possible as the setup-specific q range was too small to access the size of the particles. Nevertheless, based on the intensity and shape of the curve the assumption can be made that the initially formed particles collected at t = 0 min are significantly smaller than 1 nm (probably <0.5 nm). For the

DOI: 10.1021/acs.jpcc.8b09819
J. Phys. Chem. C 2018, 122, 28958−28967

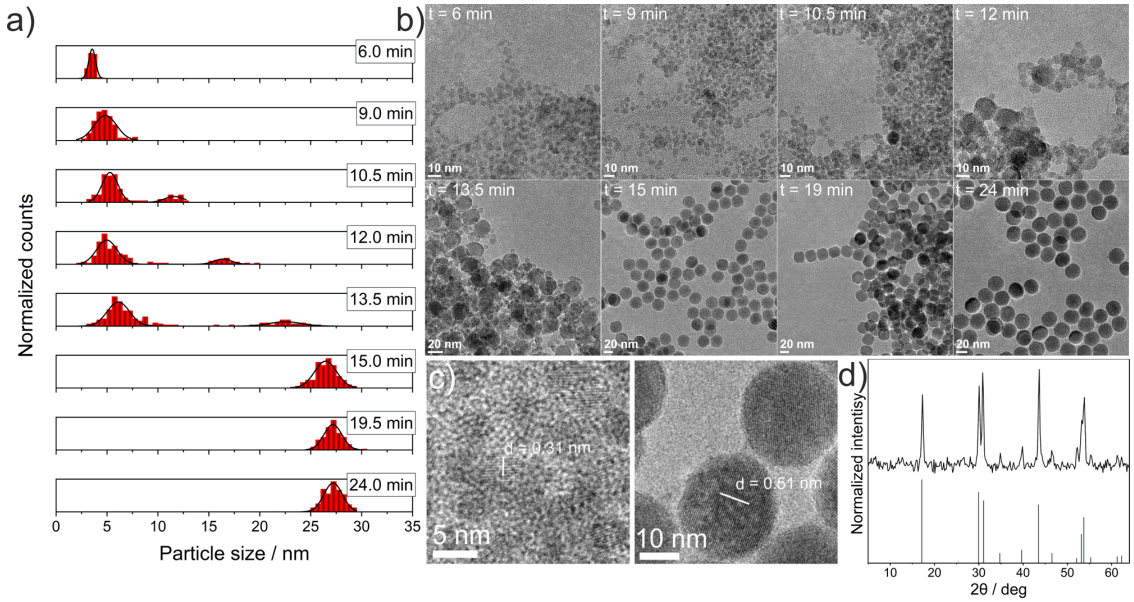

Figure 4. (a) Size histograms derived from TEM data. Size distribution was fitted applying a Gaussian normal distribution. (b) TEM images from aliquots of the reaction mixture collected at different reaction times t = 6, 9, 10.5, 12, 13.5, 15, 19.5, and 24 min, from upper left to bottom right, respectively. All samples were purified prior to measurement following the procedure given in the SI. (c) TEM image of purified UCNPs collected at t = 6 and 24 min showing the crystal lattice spacing for α-phase particles (left) and β-phase particles (right), respectively. (d) XRD pattern of the synthesized and purified β-phase UCNPs in comparison to standard data of hexagonal $NaYF_4$ (JCPDS No. 28-1192).

samples collected at t = 6.0 and 9.0 min one particle population with a particle diameter of around 4 nm can be derived (see Table 1). We assume that the UCNP population in this early stage of the synthesis consists of pure α-phase particles. However, statements about the crystallinity of the particle population cannot be made by SAXS in this q range. The approximated sizes of the UCNPs formed in the first minutes of the reaction suggest a rapid early-stage formation of the α-particles. After t = 10.5 min, α-particles with a particle diameter of about 5 nm are present. The scattering curves change drastically for the samples collected at t = 10.5, 12.0, and 13.5 min, respectively. Applying a model of two particle populations of different sizes following eq S5 (see SI) yielded best fits for particle diameters from 5 to 6.4 nm for the smaller, α-particle population and for diameters from 9 to 22 nm for the rapidly growing, most likely β-particle population. For the sample collected at t = 15.0 min the main UCNP population has a diameter of 27 nm. Nevertheless, the shape of the scattering curve of the sample obtained for t = 15.0 min (Figure 3) still indicates the presence of a very small fraction of α-phase particles that disappeared only at longer reaction times. The particle diameter remained constant until the reaction was finished, as can be seen for the samples collected at t = 19.5 and 24.0 min. Table 1 summarizes the size data of the particles and particle populations.

Transmission Electron Microscopy (TEM) Measurements. For the comparison of the UCNP sizes obtained by SAXS and to verify the assumed crystal phases, TEM measurements of the same samples were performed. The obtained TEM images and derived size distributions are shown in Figure 4a and 4b, respectively, and are summarized in Table 1. After t = 6 min, particles with a diameter of about 3.5 nm and a very narrow size distribution are present. A small increase of the particle diameter to roughly 5 nm can be observed after further 3 min (t = 9 min). The lattice spacing of about 0.31 nm derived from the TEM data of the crystalline UCNPs indicates pure cubic α-phase $NaYF_4$ ({111} plane, JCPDS No. 6-342, see Figure 4 c). After t = 10.5 min, a second population of crystalline particles with a size of roughly 11 nm occurred showing a lattice spacing of about 0.51 nm. This is assigned to hexagonal β-phase $NaYF_4$ ({100} plane, JCPDS No. 16-334). As shown in Figure 4a, the size of the second particle population grows drastically until it remains constant at t = 15.0 min. During the strong growth of the β-particles, also a slight increase of the size of the α-particles is noticeable. On one hand, there might be still some Ostwald ripening leading to a small increase in size during the reaction. On the other hand, following the theory of particle growth by supersaturation,[62] smaller α-particles are expected to dissolve faster, leading to a shift in size until even the larger α-particles are dissolved. The thereby released particles constituents grow onto the thermodynamically more stable β-phase UCNPs. A complete depletion of the reaction mixture of α-phase particles in the reaction mixture is observed after t = 15 min (Figure 4b). The final size of the β-phase particles, obtained after t = 24 min, is about 27 nm, and the size distribution is very narrow. The XRD pattern of these particles indicates the presence of only hexagonal β-phase nanocrystals (see Figure 4d).

Correlation of in Situ and Time-Resolved Optical Spectroscopy, SAXS, and TEM Measurements. In Figure 5 the correlation of the independently online and offline determined parameters characterizing the UCNPs synthesized at 325 °C, namely, luminescence intensity of the green and red emission, luminescence lifetime (exemplarily 940 nm Yb^{3+} emission), and the sizes determined by TEM and SAXS are

DOI: 10.1021/acs.jpcc.8b09819
J. Phys. Chem. C 2018, 122, 28958−28967

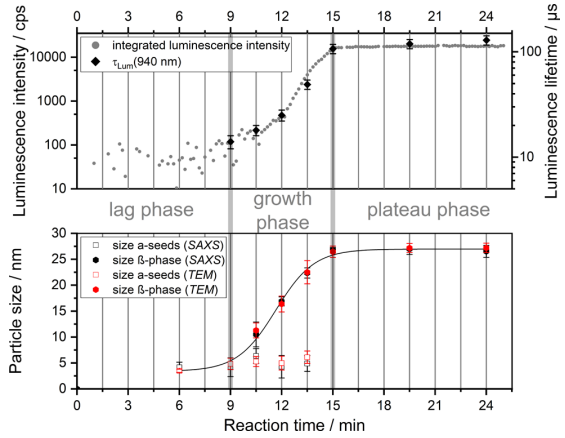

Figure 5. (Top) Evolution of the integral UCL (green and red bands considered) and the luminescence lifetime (Yb^{3+}) during the UCNP synthesis. Each vertical line represents the time of a sample collection from the reaction mixture (every 1.5 min) after reaching 300 °C (t = 0 min). (Bottom) Evolution of UCNP diameter during the synthesis derived from SAXS (black) and TEM (red) measurements. Open cubic and full hexagonal symbols represent the α-phase and β-phase, respectively. Sigmoidal fit (black line) represents the particle growth over time.

plotted against the reaction time. As can be seen in the lower panel of Figure 5, the size distributions obtained by TEM and SAXS show a very good agreement not only for the actual particle diameter but also with respect to the presence of two different nanoparticle populations identified by TEM as crystalline α- and β-phase UCNPs (Figure 4c). The particle sizes can be simulated by applying a sigmoidal fit (eq S6) showing a typical course for nanoparticle growth including a lag, growth, and plateau phase.[62] Fitting parameters can be found in the SI (Table S2). During the lag phase (t < 9 min), which correlates with the relative stasis phase (stage II) mentioned above, only minimal changes in the particle size distribution as well as the luminescence intensity are observed (see Figure 5). The main growth mechanism during this phase is probably Ostwald ripening of the α-phase seeds. At some point of the synthesis, defining the end of the lag phase and the beginning of the growth phase (corresponding to stage III), a critical point is reached and a new particle population with a β-phase crystal lattice of $NaYF_4$ appears, which grows exponentially as can be seen by SAXS and TEM, as well as the strong increase of UCL. Furthermore, an increase of the luminescence lifetimes of the 541 and 655 nm Er^{3+} emissions as well as the 940 nm Yb^{3+} emission is observed, which shows a typical nonlinear correlation with the determined nanoparticle size (see insets of Figure 2).[63]

It is still not completely clear where the β-phase seeds originate from. Plausible explanations are a rearrangement of the ions in the crystal lattice of some single α-phase particles by overcoming a phase transition activation barrier after reaching a critical size and thus a real $\alpha \rightarrow \beta$ phase transition[33] or the random recrystallization of thermodynamically more stable β-phase seeds from the precursor solution, which is supersaturated due to dissolution of the α-phase seeds.[41] In both cases, the onset of the growth phase (stage III) is expected to be highly dependent on the reaction temperature as shown here (Figure 1a–c). In any case, the overall growth of the β-phase particles takes place by Ostwald ripening by dissolution of α-phase particles, which was confirmed in this study.[42,64] While in the beginning a continuous supply of dissolved Na^+, Re^{3+}, and F^- precursors enables an exponential growth of the β-particles as revealed also by the increase of the UCL as well as the luminescence lifetime of Yb^{3+} which both correlate with particle size (Figure 5),[33,63] the amount of α-phase particles probably drastically decreases. Smaller α-particles probably dissolve faster, as follows from the small trend of increasing α-particles size during the growth phase. Subsequently, the growth rapidly slows down and finally stops after complete consumption of the α-particles (t > 15 min). Accordingly, significant changes neither in the size distribution nor in luminescence intensity and lifetimes can be observed in the plateau phase (stage IV), indicating the end of the actual nanoparticle growth period.

CONCLUSION

In summary, the in situ and time-resolved luminescence measurements as well as offline SAXS and TEM measurements used for monitoring the formation and growth of $NaYF_4$:Yb,Er nanoparticles showed good agreement with the proposed nanoparticle growth mechanism for β-phase $NaYF_4$ UCNPs involving α-phase particles as intermediate species. We could show that temperature is a critical parameter for the UCNPs synthesis that largely controls the onset of the actual β-phase particle. However, this parameter does not seem to influence the growth mechanism as suggested by the very similar optical and structural properties of the β-phase $NaYF_4$ UCNPs obtained at three different temperatures. Moreover, with the demonstrated good correlation of optical and sizing techniques we could underline the potential of in situ measurements of the upconversion luminescence (UCL) of reaction mixtures for the online control of UCNP synthesis and the reaction progress as well as UCNP quality. This can be eventually extended to the continuous monitoring of UCPN synthesis to further improve the particle batch-to-batch reproducibility, e.g., in a flow reactor as done for high-quality semiconductor quantum dots. It could be also used to increase the efficiency of the synthesis of core–shell particles with regard to optimal shell thickness for successive ionic layer adsorption and reaction (SILAR) approaches.

ASSOCIATED CONTENT

Supporting Information

The Supporting Information is available free of charge on the ACS Publications website at DOI: 10.1021/acs.jpcc.8b09819.

Purification of UCNPs; evaluation of SAXS data, analytical characterization of UCNP; temperature ramp for the synthesis performed at 300, 315, and 325 °C; power-dependent measurements of the UCNP batches; ICP-OES data (PDF)

AUTHOR INFORMATION

Corresponding Author

*E-mail: Ute.Resch@bam.de.

ORCID

Christian Würth: 0000-0002-0204-9727

Ute Resch-Genger: 0000-0002-0944-1115

Notes

The authors declare no competing financial interest.

DOI: 10.1021/acs.jpcc.8b09819
J. Phys. Chem. C 2018, 122, 28958–28967

■ ACKNOWLEDGMENTS

We gratefully acknowledge financial support from the EU-financed EMPIR initiative within the project 14IND12 "INNANOPART", from the M-ERA.NET network within the project 2179 "NANOHYPE" (German Research Council (DFG)), and from the Ph.D. program of BAM.

■ REFERENCES

(1) Scheps, R. Upconversion Laser Processes. *Prog. Quantum Electron.* **1996**, *20* (4), 271−358.
(2) Dong, Y.; Xu, J.; Zhou, G.; Zhao, G.; Jie, M.; Yang, L. Y.; Su, L.; Qiu, J.; Feng, W.; lin, L. Blue Upconversion Luminescence Generation in Ce^{3+}:Gd_2SiO_5 Crystals by Infrared Femtosecond Laser Irradiation. *Opt. Express* **2006**, *14* (5), 1899−1904.
(3) Singh-Rachford, T. N.; Castellano, F. N. Photon Upconversion Based on Sensitized Triplet−Triplet Annihilation. *Coord. Chem. Rev.* **2010**, *254* (21), 2560−2573.
(4) Auzel, F. Upconversion and Anti-Stokes Processes with f and d Ions in Solids. *Chem. Rev.* **2004**, *104* (1), 139−174.
(5) Chen, G.; Qiu, H.; Prasad, P. N.; Chen, X. Upconversion Nanoparticles: Design, Nanochemistry, and Applications in Theranostics. *Chem. Rev.* **2014**, *114* (10), 5161−5214.
(6) Haase, M.; Schäfer, H. Upconverting Nanoparticles. *Angew. Chem., Int. Ed.* **2011**, *50* (26), 5808−5829.
(7) van der Ende, B. M.; Aarts, L.; Meijerink, A. Lanthanide Ions as Spectral Converters for Solar Cells. *Phys. Chem. Chem. Phys.* **2009**, *11* (47), 11081−11095.
(8) Wang, F.; Banerjee, D.; Liu, Y.; Chen, X.; Liu, X. Upconversion Nanoparticles in Biological Labeling, Imaging, and Therapy. *Analyst* **2010**, *135* (8), 1839−1854.
(9) Wang, F.; Liu, X. Recent Advances in the Chemistry of Lanthanide-doped Upconversion Nanocrystals. *Chem. Soc. Rev.* **2009**, *38* (4), 976−989.
(10) Wu, S.; Han, G.; Milliron, D. J.; Aloni, S.; Altoe, V.; Talapin, D. V.; Cohen, B. E.; Schuck, P. J. Non-blinking and Photostable Upconverted Luminescence from Single Lanthanide-doped Nanocrystals. *Proc. Natl. Acad. Sci. U. S. A.* **2009**, *106* (27), 10917−10921.
(11) Xie, L.; Qin, Y.; Chen, H.-Y. Direct Fluorescent Measurement of Blood Potassium with Polymeric Optical Sensors Based on Upconverting Nanomaterials. *Anal. Chem.* **2013**, *85* (5), 2617−2622.
(12) Wang, C.; Cheng, L.; Xu, H.; Liu, Z. Towards Whole-body Imaging at the Single Cell Level Using Ultra-sensitive Stem Cell Labeling with Oligo-arginine Modified Upconversion Nanoparticles. *Biomaterials* **2012**, *33* (19), 4872−4881.
(13) Nadort, A.; Sreenivasan, V. K. A.; Song, Z.; Grebenik, E. A.; Nechaev, A. V.; Semchishen, V. A.; Panchenko, V. Y.; Zvyagin, A. V. Quantitative Imaging of Single Upconversion Nanoparticles in Biological Tissue. *PLoS One* **2013**, *8* (5), e63292.
(14) Fischer, L. H.; Harms, G. S.; Wolfbeis, O. S. Upconverting Nanoparticles for Nanoscale Thermometry. *Angew. Chem., Int. Ed.* **2011**, *50* (20), 4546−4551.
(15) Hyppänen, I.; Perälä, N.; Arppe, R.; Schäferling, M.; Soukka, T. Environmental and Excitation Power Effects on the Ratiometric Upconversion Luminescence Based Temperature Sensing Using Nanocrystalline NaYF4:Yb3+,Er3. *ChemPhysChem* **2017**, *18* (6), 692−701.
(16) Li, D. D.; Shao, Q. Y.; Dong, Y.; Jiang, J. Q. Multifunctional NaYF4:Yb3+, Er3+@Au Nanocomposites: Upconversion Luminescence, Temperature Sensing and Photothermal Therapy. *Adv. Mater. Res.* **2015**, *1088*, 23−27.
(17) Vetrone, F.; Naccache, R.; Zamarrón, A.; Juarranz de la Fuente, A.; Sanz-Rodríguez, F.; Martinez Maestro, L.; Martín Rodriguez, E.; Jaque, D.; García Solé, J.; Capobianco, J. A. Temperature Sensing Using Fluorescent Nanothermometers. *ACS Nano* **2010**, *4* (6), 3254−3258.
(18) Lim, S. F.; Riehn, R.; Ryu, W. S.; Khanarian, N.; Tung, C.-k.; Tank, D.; Austin, R. H. In Vivo and Scanning Electron Microscopy Imaging of Upconverting Nanophosphors in Caenorhabditis elegans. *Nano Lett.* **2006**, *6* (2), 169−174.
(19) Chatterjee, D. K.; Rufaihah, A. J.; Zhang, Y. Upconversion Fluorescence Imaging of Cells and Small Animals Using Lanthanide-doped Nanocrystals. *Biomaterials* **2008**, *29* (7), 937−943.
(20) Zhou, J.; Sun, Y.; Du, X.; Xiong, L.; Hu, H.; Li, F. Dual-modality in vivo Imaging Using Rare-earth Nanocrystals with Near-infrared to Near-infrared (NIR-to-NIR) Upconversion Luminescence and Magnetic Resonance Properties. *Biomaterials* **2010**, *31* (12), 3287−3295.
(21) Wang, C.; Cheng, L.; Liu, Z. Upconversion Nanoparticles for Photodynamic Therapy and Other Cancer Therapeutics. *Theranostics* **2013**, *3* (5), 317−330.
(22) Kim, W. J.; Nyk, M.; Prasad, P. N. Color-coded Multilayer Photopatterned Microstructures Using Lanthanide (III) Ion co-doped $NaYF_4$ Nanoparticles with Upconversion Luminescence for Possible Applications in Security. *Nanotechnology* **2009**, *20* (18), 185301.
(23) Blumenthal, T.; Meruga, J.; May, P. S.; Kellar, J.; Cross, W.; Ankireddy, K.; Vunnam, S.; Luu, Q. N. Patterned Direct-write and Screen-printing of NIR-to-visible Upconverting Inks for Security Applications. *Nanotechnology* **2012**, *23* (18), 185305.
(24) Meruga, J. M.; Baride, A.; Cross, W.; Kellar, J. J.; May, P. S. Red-green-blue Printing Using Luminescence-upconversion Inks. *J. Mater. Chem. C* **2014**, *2* (12), 2221−2227.
(25) Wilhelm, S. Perspectives for Upconverting Nanoparticles. *ACS Nano* **2017**, *11* (11), 10644−10653.
(26) Resch-Genger, U.; Gorris, H. H. Perspectives and Challenges of Photon-upconversion Nanoparticles - Part I: Routes to Brighter Particles and Quantitative Spectroscopic Studies. *Anal. Bioanal. Chem.* **2017**, *409* (25), 5855−5874.
(27) Ehlert, O.; Thomann, R.; Darbandi, M.; Nann, T. A Four-Color Colloidal Multiplexing Nanoparticle System. *ACS Nano* **2008**, *2* (1), 120−124.
(28) Wang, M.; Abbineni, G.; Clevenger, A.; Mao, C.; Xu, S. Upconversion Nanoparticles: Synthesis, Surface Modification, and Biological Applications. *Nanomedicine* **2011**, *7* (6), 710−729.
(29) Wilhelm, S.; Kaiser, M.; Wurth, C.; Heiland, J.; Carrillo-Carrion, C.; Muhr, V.; Wolfbeis, O. S.; Parak, W. J.; Resch-Genger, U.; Hirsch, T. Water Dispersible Upconverting Nanoparticles: Effects of Surface Modification on their Luminescence and Colloidal Stability. *Nanoscale* **2015**, *7* (4), 1403−1410.
(30) Na, H.; Woo, K.; Lim, K.; Jang, H. S. Rational Morphology Control of β-$NaYF_4$:Yb,Er/Tm Upconversion Nanophosphors Using a Ligand, an Additive, and Lanthanide Doping. *Nanoscale* **2013**, *5* (10), 4242−4251.
(31) Heer, S.; Kömpe, K.; Güdel, H. U.; Haase, M. Highly Efficient Multicolour Upconversion Emission in Transparent Colloids of Lanthanide-Doped $NaYF_4$ Nanocrystals. *Adv. Mater.* **2004**, *16* (23−24), 2102−2105.
(32) Hesse, J.; Klier, D. T.; Sgarzi, M.; Nsubuga, A.; Bauer, C.; Grenzer, J.; Hübner, R.; Wislicenus, M.; Joshi, T.; Kumke, M. U.; Stephan, H. Rapid Synthesis of Sub-10 nm Hexagonal $NaYF_4$-Based Upconverting Nanoparticles using Therminol® 66. *ChemistryOpen* **2018**, *7* (2), 159−168.
(33) Shan, J.; Ju, Y. A Single-step Synthesis and the Kinetic Mechanism for Monodisperse and Hexagonal-phase $NaYF_4$:Yb, Er Upconversion Nanophosphors. *Nanotechnology* **2009**, *20* (27), 275603.
(34) Mai, H.-X.; Zhang, Y.-W.; Si, R.; Yan, Z.-G.; Sun, L.-d.; You, L.-P.; Yan, C.-H. High-Quality Sodium Rare-Earth Fluoride Nanocrystals: Controlled Synthesis and Optical Properties. *J. Am. Chem. Soc.* **2006**, *128* (19), 6426−6436.
(35) Boyer, J.-C.; Vetrone, F.; Cuccia, L. A.; Capobianco, J. A. Synthesis of Colloidal Upconverting NaYF4 Nanocrystals Doped with Er^{3+}, Yb^{3+} and Tm^{3+}, Yb^{3+} via Thermal Decomposition of Lanthanide Trifluoroacetate Precursors. *J. Am. Chem. Soc.* **2006**, *128* (23), 7444−7445.
(36) Mai, H.-X.; Zhang, Y.-W.; Sun, L.-D.; Yan, C.-H. Highly Efficient Multicolor Up-Conversion Emissions and Their Mechanisms

DOI: 10.1021/acs.jpcc.8b09819
J. Phys. Chem. C 2018, 122, 28958−28967

of Monodisperse $NaYF_4$:Yb,Er Core and Core/Shell-Structured Nanocrystals. *J. Phys. Chem. C* **2007**, *111* (37), 13721−13729.
(37) Liang, X.; Wang, X.; Zhuang, J.; Peng, Q.; Li, Y. Synthesis of $NaYF_4$ Nanocrystals with Predictable Phase and Shape. *Adv. Funct. Mater.* **2007**, *17* (15), 2757−2765.
(38) Li, C.; Quan, Z.; Yang, J.; Yang, P.; Lin, J. Highly Uniform and Monodisperse β-$NaYF_4$:Ln^{3+} (Ln = Eu, Tb, Yb/Er, and Yb/Tm) Hexagonal Microprism Crystals: Hydrothermal Synthesis and Luminescent Properties. *Inorg. Chem.* **2007**, *46* (16), 6329−6337.
(39) Zhang, Y.-W.; Sun, X.; Si, R.; You, L.-P.; Yan, C.-H. Single-Crystalline and Monodisperse LaF_3 Triangular Nanoplates from a Single-Source Precursor. *J. Am. Chem. Soc.* **2005**, *127* (10), 3260−3261.
(40) Mai, H.-X.; Zhang, Y.-W.; Sun, L.-D.; Yan, C.-H. Size- and Phase-Controlled Synthesis of Monodisperse $NaYF_4$:Yb,Er Nanocrystals from a Unique Delayed Nucleation Pathway Monitored with Upconversion Spectroscopy. *J. Phys. Chem. C* **2007**, *111* (37), 13730−13739.
(41) Komban, R.; Klare, J. P.; Voss, B.; Nordmann, J.; Steinhoff, H.-J.; Haase, M. An Electron Paramagnetic Resonance Spectroscopic Investigation on the Growth Mechanism of $NaYF_4$:Gd Nanocrystals. *Angew. Chem., Int. Ed.* **2012**, *51* (26), 6506−6510.
(42) Voß, B.; Nordmann, J.; Uhl, A.; Komban, R.; Haase, M. Effect of the Crystal Structure of Small Precursor Particles on the Growth of β-$NaREF_4$ (RE = Sm, Eu, Gd, Tb) Nanocrystals. *Nanoscale* **2013**, *5* (2), 806−812.
(43) Suter, J. D.; Pekas, N. J.; Berry, M. T.; May, P. S. Real-Time-Monitoring of the Synthesis of β-$NaYF_4$:17% Yb,3% Er Nanocrystals Using NIR-to-Visible Upconversion Luminescence. *J. Phys. Chem. C* **2014**, *118* (24), 13238−13247.
(44) Rinkel, T.; Nordmann, J.; Raj, A. N.; Haase, M. Ostwald-ripening and Particle Size Focussing of sub-10 nm $NaYF_4$ Upconversion Nanocrystals. *Nanoscale* **2014**, *6* (23), 14523−14530.
(45) May, P. B.; Suter, J. D.; May, P. S.; Berry, M. T. The Dynamics of Nanoparticle Growth and Phase Change During Synthesis of β-$NaYF_4$. *J. Phys. Chem. C* **2016**, *120* (17), 9482−9489.
(46) Würth, C.; Grabolle, M.; Pauli, J.; Spieles, M.; Resch-Genger, U. Comparison of Methods and Achievable Uncertainties for the Relative and Absolute Measurement of Photoluminescence Quantum Yields. *Anal. Chem.* **2011**, *83* (9), 3431−3439.
(47) Resch-Genger, U.; DeRose, P. C. Characterization of Photoluminescence Measuring Systems (IUPAC Technical Report). *Pure Appl. Chem.* **2012**, *84*, 1815.
(48) Würth, C.; Kaiser, M.; Wilhelm, S.; Grauel, B.; Hirsch, T.; Resch-Genger, U. Excitation Power Dependent Population Pathways and Absolute Quantum Yields of Upconversion Nanoparticles in Different Solvents. *Nanoscale* **2017**, *9* (12), 4283−4294.
(49) Krumrey, M.; Ulm, G. High-accuracy Detector Calibration at the PTB Four-crystal Monochromator Beamline. *Nucl. Instrum. Methods Phys. Res., Sect. A* **2001**, *467*−*468*, 1175−1178.
(50) Wernecke, J.; Gollwitzer, C.; Muller, P.; Krumrey, M. Characterization of an In-vacuum PILATUS 1M detector. *J. Synchrotron Radiat.* **2014**, *21* (3), 529−536.
(51) Wang, X.; Liu, Q.; Cai, P.; Wang, J.; Qin, L.; Vu, T.; Seo, H. J. Excitation Powder Dependent Optical Temperature Behavior of Er^{3+} Doped Transparent $Sr_{0.69}La_{0.31}F_{2.31}$ Glass Ceramics. *Opt. Express* **2016**, *24* (16), 17792−17804.
(52) Xu, X.; Wang, Z.; Lei, P.; Yu, Y.; Yao, S.; Song, S.; Liu, X.; Su, Y.; Dong, L.; Feng, J.; Zhang, H. α-NaYb(Mn)F_4:Er^{3+}/Tm^{3+}@$NaYF_4$ UCNPs as "Band-Shape" Luminescent Nanothermometers over a Wide Temperature Range. *ACS Appl. Mater. Interfaces* **2015**, *7* (37), 20813−20819.
(53) Singh, S. K.; Kumar, K.; Rai, S. B. Er^{3+}/Yb^{3+} Codoped Gd_2O_3 Nano-phosphor for Optical Thermometry. *Sens. Actuators, A* **2009**, *149* (1), 16−20.
(54) Dong, B.; Cao, B.; He, Y.; Liu, Z.; Li, Z.; Feng, Z. Temperature Sensing and In Vivo Imaging by Molybdenum Sensitized Visible Upconversion Luminescence of Rare-Earth Oxides. *Adv. Mater.* **2012**, *24* (15), 1987−1993.
(55) Chen, D.; Wan, Z.; Zhou, Y.; Zhou, X.; Yu, Y.; Zhong, J.; Ding, M.; Ji, Z. Dual-Phase Glass Ceramic: Structure, Dual-Modal Luminescence, and Temperature Sensing Behaviors. *ACS Appl. Mater. Interfaces* **2015**, *7* (34), 19484−19493.
(56) Suo, H.; Guo, C.; Li, T. Broad-Scope Thermometry Based on Dual-Color Modulation up-Conversion Phosphor $Ba_5Gd_8Zn_4O_{21}$:Er^{3+}/Yb^{3+}. *J. Phys. Chem. C* **2016**, *120* (5), 2914−2924.
(57) Liu, H.; Xu, C. T.; Lindgren, D.; Xie, H.; Thomas, D.; Gundlach, C.; Andersson-Engels, S. Balancing Power Density Based Quantum Yield Characterization of Upconverting Nanoparticles for Arbitrary Excitation Intensities. *Nanoscale* **2013**, *5* (11), 4770−4775.
(58) Qu, Y.; Kong, X.; Sun, Y.; Zeng, Q.; Zhang, H. Effect of Excitation Power Density on the Upconversion Luminescence of LaF_3:Yb^{3+}, Er^{3+} Nanocrystals. *J. Alloys Compd.* **2009**, *485* (1), 493−496.
(59) Suyver, J. F.; Grimm, J.; van Veen, M. K.; Biner, D.; Krämer, K. W.; Güdel, H. U. Upconversion Spectroscopy and Properties of $NaYF_4$ Doped with Er^{3+}, Tm^{3+} and/or Yb^{3+}. *J. Lumin.* **2006**, *117* (1), 1−12.
(60) Yan, R. X.; Li, Y. D. Down/Up Conversion in Ln^{3+}-Doped YF_3 Nanocrystals. *Adv. Funct. Mater.* **2005**, *15* (5), 763−770.
(61) Lihui, H.; Xingren, L.; Wu, X.; Baojiu, C.; Jiuling, L. Infrared and Visible Luminescence Properties of Er^{3+} and Yb^{3+} Ions Codoped $Ca_3Al_2Ge_3O_{12}$ Glass Under 978 nm Diode Laser Excitation. *J. Appl. Phys.* **2001**, *90* (11), 5550−5553.
(62) Thanh, N. T. K.; Maclean, N.; Mahiddine, S. Mechanisms of Nucleation and Growth of Nanoparticles in Solution. *Chem. Rev.* **2014**, *114* (15), 7610−7630.
(63) Zhao, J.; Lu, Z.; Yin, Y.; McRae, C.; Piper, J. A.; Dawes, J. M.; Jin, D.; Goldys, E. M. Upconversion Luminescence with Tunable Lifetime in $NaYF_4$:Yb,Er Nanocrystals: Role of Nanocrystal Size. *Nanoscale* **2013**, *5* (3), 944−952.
(64) Voss, B.; Haase, M. Intrinsic Focusing of the Particle Size Distribution in Colloids Containing Nanocrystals of Two Different Crystal Phases. *ACS Nano* **2013**, *7* (12), 11242−11254.

DOI: 10.1021/acs.jpcc.8b09819
J. Phys. Chem. C 2018, 122, 28958−28967

Evolution of Size and Optical Properties of Upconverting Nanoparticles during High Temperature Synthesis

Sebastian Radunz,[a] Alexander Schavkan,[b] Sebastian Wahl,[c] Christian Würth,[a] Harald R. Tschiche,[a,d] Michael Krumrey[b] and Ute Resch-Genger*[a]

[a] BAM Federal Institute for Materials Research and Testing, Division Biophotonics, Richard-Willstaetter-Str. 11, 12489 Berlin, Germany. E-mail: ute.resch@bam.de.

[b] Physikalisch-Technische Bundesanstalt (PTB), Berlin, Germany.

[c] Department of Chemistry, Humboldt-Universität zu Berlin, Brook-Taylor-Straße 2, 12489 Berlin, Germany.

[d] BfR German Federal Institute for Risk Assessment, Department 7, Max-Dohrn-Str. 8-10, 10589 Berlin, Germany.

Supplementary Information (SI)

Experimental Section

Purification of UCNPs:
For the purification of the nanoparticles, small volumes (5 mL) of the reaction mixture were transferred into centrifuge tubes after cooled down to room temperature and were treated with ethanol (45 mL) leading to precipitation of the oleate-capped nanoparticles. Each centrifugation step was carried out for 10 minutes at 1000 g, yielding particle pellets which were further purified by washing – two times using chloroform for dispersing and ethanol for precipitation, followed by three times using cyclohexane for dispersing and acetone for precipitation. The purified upconversion nanoparticles were dispersed in cyclohexane (20 mL) and a final centrifugation step for 3 minutes at 1000 g was carried out to get rid of larger agglomerates. The clear particle dispersion was then transferred to a glass vial for storage. Furthermore, the mass concentration of the nanoparticle supsension was determined, giving values between 45 – 50 mg/mL.

Evaluation of SAXS data:
The obtained SAXS curves were fitted with the following equations (eq.):

$$\boldsymbol{I(q) = N \cdot \int_0^\infty g(R)|f(q,R)|^2 dR + BG}\,, \qquad \text{eq. S1}$$

In eq. 1, *I(q)* is the scattering intensity depending on momentum transfer vector *q*, *N* is proportionality factor and *BG* is background. BG was fitted using eq. 2.

$$\boldsymbol{BG = c_0 + c_1 \cdot q^{-\alpha}}. \qquad \text{eq. S2}$$

Here c_0 and c_1 are constants and α is a fitting parameter varying from $1 \leq \alpha \leq 5$. g(R) is a Gaussian distribution of the particle sizes expressed as by eq. 3.

$$\mathbf{g(R)} = \frac{1}{\sigma_R\sqrt{2\pi}} \cdot \exp\left(-\frac{(R-\bar{R})^2}{2\sigma_R^2}\right). \qquad \text{eq. S3}$$

Here *R* is the radius of the particles, $\bar{R}$ is the mean radius of the particles and σ_R is the standard deviation of the size distribution. The sphere form factor is defined as:

$$f_{sph}(q,R) = \frac{4\pi}{3}R^3\left(3\frac{\sin(qR)-qR\cdot\cos(qR)}{(qR)^3}\right). \qquad \text{eq. S4}$$

In case of two populations, eq. **1** has to be extended to:

$$I(q) = N_1 \cdot \int_0^\infty g_1(R_1)|f_1(q,R_1)|^2 dR_1 + N_2 \cdot \int_0^\infty g_2(R_2)|f_2(q,R_2)|^2 dR_2 + BG. \qquad \text{eq. S5}$$

Sigmoidal fit for particle size evolution following eq:

$$d(t) = \frac{A_1 - A_2}{1 + e^{(t - t_0)/dt}} + A_2 \qquad \text{eq. S6}$$

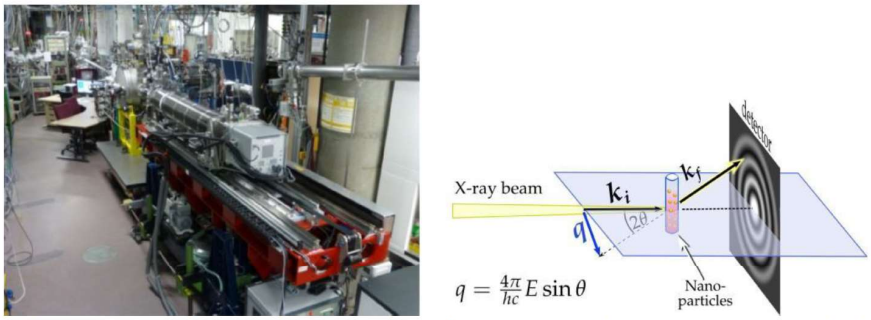

Figure S1. Left: Four-crystal monochromator beamline (FCM) of PTB with the standard SAXS setup at the BESSY II synchrotron radiation facility (Helmholtz-Zentrum Berlin). Right: Schematic representation of an SAXS experiment.

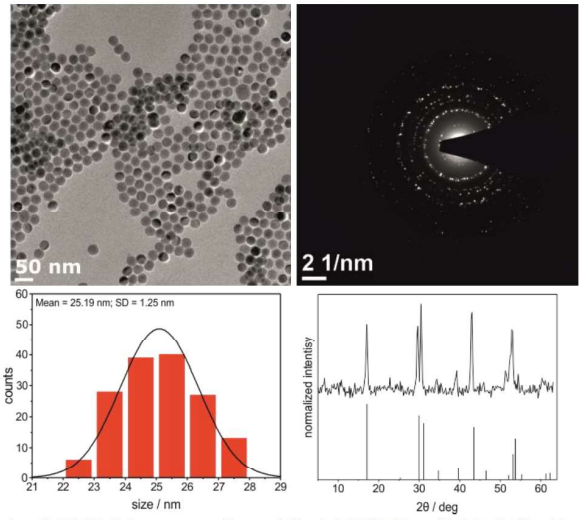

Figure S2. Top left) Typical TEM image of purified UCNPs (300 °C). Bottom left) Corresponding histogram of the size distribution showing the size and a small polydispersity of the synthesized UCNPs. Top right) Corresponding selected area electron diffraction (SAED) of the UCNP sample showing a high crystallinity and typical β-phase reflexes. Bottom right) XRD-pattern of the synthesized and purified β-phase UCNP in comparison to JCPDS 28-1192.

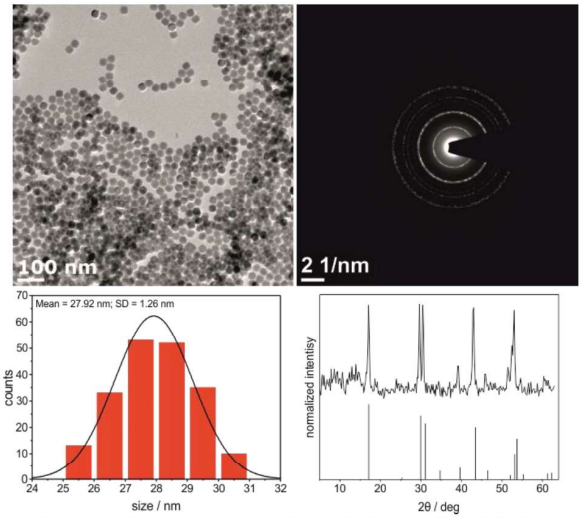

Figure S3. Top left) Typical TEM image of purified UCNPs (315 °C). Bottom left) Corresponding histogram of the size distribution showing the size and a small polydispersity of the synthesized UCNPs. Top right) Corresponding selected area electron diffraction (SAED) of the UCNP sample showing a high crystallinity and typical β-phase reflexes. Bottom right) XRD-pattern of the synthesized and purified β-phase UCNP in comparison to JCPDS 28-1192.

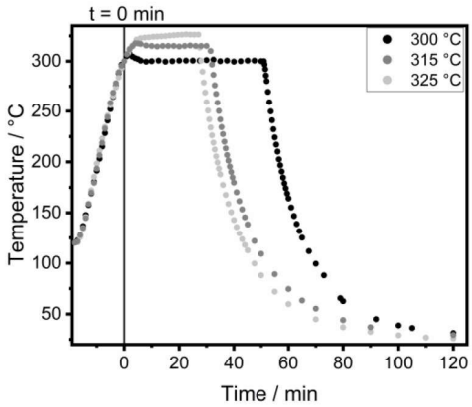

Figure S4. Temperature ramp for the synthesis performed at 300, 315 and 325 °C showing a rapid temperature increase of roughly 10 K/min until the reaction temperature is reached, a temperature plateau at the target temperature until the reaction is terminated and subsequently, the cooling phase to room temperature. t = 0 min is defined as starting time, triggered as soon as the reaction mixture reaches 300 °C.

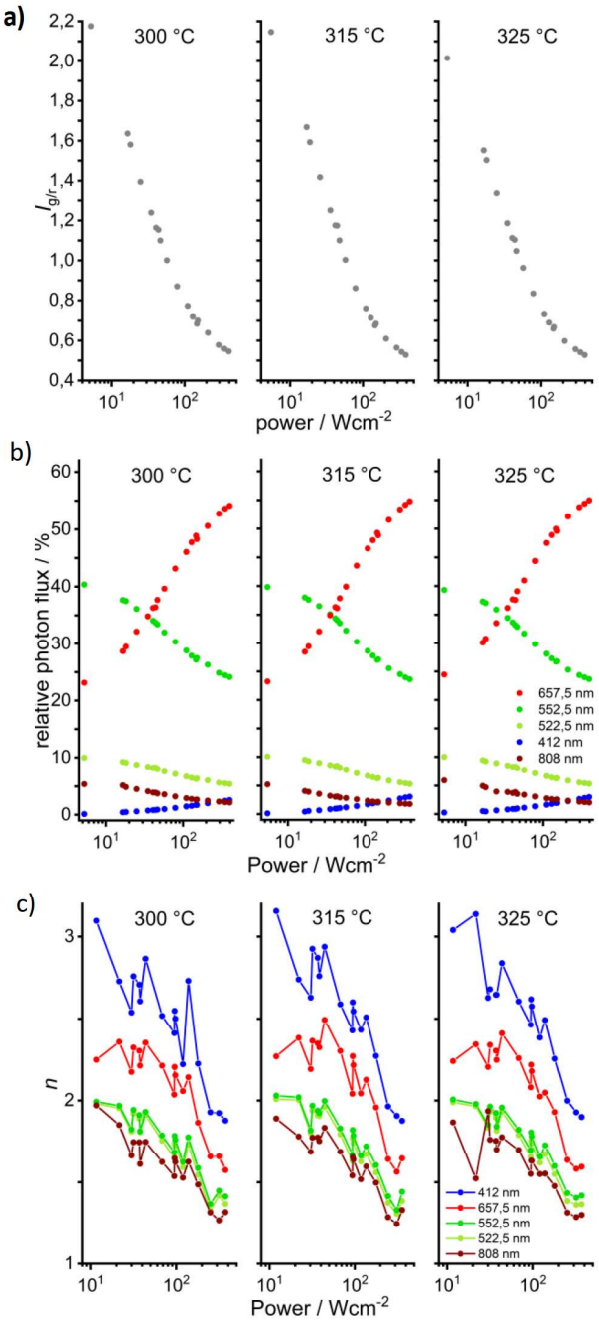

Figure S5. a) Power-dependent green-to-red ratio in cyclohexane varied between 5 and 390 Wcm^{-2}. b) Contributions (%) of the intensities of the different upconversion emissions to the overall luminescence intensity. c) Power-dependence of the slope factors *n* of the different upconversion emissions.

Table S1. Molar ratios of the lanthanide ions of the particles determined by *ICP-OES*.

T / °C	Y/(Y+Yb+Er) / %	Yb/(Y+Yb+Er) / %	Er/(Y+Yb+Er) / %
300	79.03 ± 1.25	18.77 ± 1.02	2.19 ± 1.01
315	79.09 ± 1.21	18.87 ± 0.85	2.04 ± 0.85
325	79.35 ± 1.18	18.60 ± 0.72	2.05 ± 0.71

Table S2. Fitting parameters for evolution of nanoparticle sizes following eq. S6.

A_1	A_2	t_0	dt	R^2
3.27 ± 0.27	27.29 ± 0.42	11.63 ± 0.16	1.18 ± 0.14	0.998

2.5 Simple Self-Referenced Luminescent pH Sensors Based on Upconversion Nanocrystals and pH-Sensitive Fluorescent BODIPY Dyes

Sebastian Radunz, Elina Andresen, Christian Würth, Andrea Koerdt, Harald Rune Tschiche, Ute Resch-Genger*

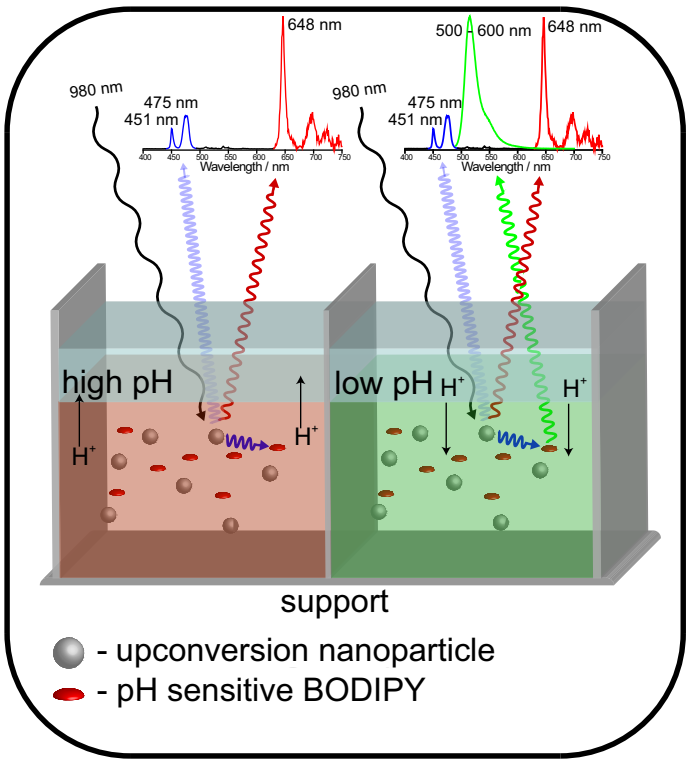

Figure 16: Reprinted with permission from S. Radunz *et al.*.[21] Copyright 2019 American Chemical Society.

In this publication S. Radunz established the concept, the synthesis and the analytical and spectroscopic characterization of all components reported. He performed all experiments and data evaluations as well as he performed the scientific interpretation of the results. The publication was mainly conceived and written by him.

analytical chemistry

Article

Cite This: *Anal. Chem.* 2019, 91, 7756−7764

pubs.acs.org/ac

Simple Self-Referenced Luminescent pH Sensors Based on Upconversion Nanocrystals and pH-Sensitive Fluorescent BODIPY Dyes

Sebastian Radunz,[†] Elina Andresen,[†] Christian Würth,[†] Andrea Koerdt,[†] Harald Rune Tschiche,[†,‡] and Ute Resch-Genger*[,†]

[†]Division Biophotonics, BAM Federal Institute for Materials Research and Testing, Richard-Willstaetter-Str. 11, 12489 Berlin, Germany

[‡]Department 7, BfR German Federal Institute for Risk Assessment, Max-Dohrn-Str. 8-10, 10589 Berlin, Germany

Supporting Information

ABSTRACT: We present the design and fabrication of pH responsive ratiometric dual component sensor systems based on multicolor emissive upconversion nanoparticles (UCNP) and pH sensitive BODIPY dyes with tunable pK_a values embedded into a polymeric hydrogel matrix. The use of NIR excitable $NaYF_4$:Yb^{3+},Tm^{3+} UCNPs enables background free read-out. Furthermore, the spectrally matching optical properties of the UCNPs and the dyes allow the UCNPs to serve as excitation light source for the analyte-responsive BODIPY as well as intrinsic reference. The blue upconversion luminescence (UCL) of $NaYF_4$:Yb^{3+},Tm^{3+} UCNPs excited at 980 nm, that overlaps with the absorption of the pH-sensitive fluorophore, provides reabsorption based excitation of the dye, the spectrally distinguishable green fluorescence of which is switched ON upon protonation, preventing photoinduced electron transfer (PET) within the dye moiety, and the pH-inert red UCL act as reference. The intensities ratios of the dye's fluorescence and the analyte-inert red Tm^{3+} UCL correlate directly with pH, which was successfully utilized for monitoring time-dependent pH changes of a suspension of quiescent *E. coli* metabolizing D-glucose.

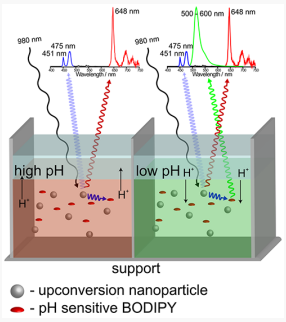

In the past decade, optical probes for imaging and sensing have found widespread applications in the life and materials sciences. A prominent example is the determination of pH, a crucial marker for many processes in biotechnology, biology, medical diagnostics, biomedical research, and material corrosion.[1−4] Especially fluorescent pH sensors have attracted considerable interest due to their high sensitivity and versatility of formats ranging from molecular and nanosensors for, e.g., cell studies, to planar optodes and fiber-optic sensors. As the fluorescence intensity is affected by fluctuations of the excitation light intensity and changes in probe concentration, many fluorescence sensors are utilized in referenced systems enabling two-wavelength ratiometric measurements of fluorescence intensity; alternatively, lifetime measurements or dual-lifetime referencing is done.[5,6] Ratiometric sensing in the intensity domain is based on the read out of two simultaneously excited, spectrally distinguishable fluorescence emission bands, one being commonly analyte-inert and the other one analyte-responsive. The measurement of this quotient minimizes the dependence of the sensor's signal on its environment (except for the target concentration).[7] As most dyes do not show dual emission,[8] single fluorescence band-emissive pH-sensitive dyes are usually combined with target-inert reference dyes, that can be excited at the same wavelength, often utilizing nanoparticles as carriers for a multitude of dye molecules. Such systems can be realized with organic polymer particles like latex polymer dots, silica nanoparticles, quantum dots (e.g., CdSe/ZnSe/ZnS), etc.[9−11] A disadvantage of these systems is the excitation with ultraviolet (UV) or visible light, leading to autofluorescence particularly in biological environments. This can result in a poor signal-to-noise ratio and can even damage biological samples, thereby limiting the versatility of such sensor systems. This and other limitations, like the poor photostability of many organic dyes upon illumination with UV light, can be overcome with the aid of photon upconversion (UC) materials that are excited with near-infrared (NIR) light. Particularly for life sciences applications, the NIR excitability presents a huge advantage in terms of very low autofluorescence, deep tissue penetration, as well as strongly reduced scattering and light damage of cells, microorganism, and tissue.

The by far most-studied NIR-to-visible light converting upconverting nanoparticles (UCNPs) consist of a β-$NaYF_4$ host lattice, doped with the optically active rare earth (RE) ions Yb^{3+} as sensitizer, absorbing 980 nm light, and either Er^{3+}, Tm^{3+} or Ho^{3+} as activator, emitting several narrow and well-defined emission bands in the UV, visible, and NIR region.[12] These properties as well as their high chemical inertness and a

Received: March 6, 2019
Accepted: May 16, 2019
Published: May 16, 2019

DOI: 10.1021/acs.analchem.9b01174
Anal. Chem. 2019, 91, 7756−7764

very high photostability make UCNPs promising reporters for biosensing, bioimaging, and theranostics.[13−18] This has meanwhile led to many applications in sensing[13,14,19−23] and bioimaging,[13,24−26] photodynamic therapy,[13,27] spectral conversion in solar cells[28] and security printing.[29−31] Nevertheless, there are still some major challenges to be overcome for the broad use of UC nanotechnology, particularly the enhancement of the brightness and luminescence efficiency of very small and ultrasmall UCNPs.[32]

For sensing applications, the upconversion luminescence (UCL) of UCNPs must be rendered analyte-responsive. Due to their multicolor emission, UCNPs are principally ideal energy donors in two component sensing systems. The combination of UCNPs and pH-sensitive dyes as energy acceptors, for instance, can yield ratiometric pH-sensors utilizing either resonance energy transfer (RET) processes[33−35] or reabsorption-related inner filter effects.[36−40] As energy acceptor, typically an analyte-responsive organic dye is used. For both sensor principles, the absorption of the indicator dye must overlap with one of the UCL bands, typically the green and blue emission for Er^{3+}- and Tm^{3+}-based UCNPs, and referencing to an analyte-inert UCL band is essential. The latter provides the basis for the sensor's ratiometric response to the presence of the target, namely the read out of the quotient of the fluorescence intensities of an analyte-responsive and a target-inert emission band, that are spectrally distinguishable. RET-based systems rely on a radiationless process with a highly distance-dependent efficiency. In addition to the challenging multistep synthesis of RET sensor systems, requiring dye conjugation to the UCNP surface, the fact that in the case of the UCNP, the donor quantum yield (here the UC quantum yield ϕ_{UC}) is affected by surface quenching and every emissive RE ion acts as individual RET donor leads to size restrictions.[41] Hence, for larger and thus brighter UCNP, the UCL originating from RE ions in the inner core, that do not contribute to RET, can lead to a large background. In contrast, inner filter-based UCNP sensors, that use the UCNPs as intrinsic nanolamp, are readily accessible and do not require dye conjugation and thus, no dyes with reactive groups. Hence, additional synthetic efforts can be avoided. Such systems generally provide a greater versatility regarding usable dyes and UCNP size restrictions can be circumvented.

Here, we use the elegant concept of a reabsorption-operated sensor to realize a pH sensor by combining Yb^{3+},Tm^{3+}-codoped $NaYF_4$ UCNPs and fluorescent 4-bora-3a,4a-diaza-s-indacenes (BODIPYs) as pH-sensitive components. These fluorophores were chosen since this dye class shows an easily controllable chemical and photophysical diversity, provided by versatile synthetic pathways, which allow an optimal adjustment of the spectral properties with regard to the emission of the UCNPs. Furthermore, BODIPYs have relatively high molar absorption coefficients and high fluorescence quantum yields and an outstanding thermal and photochemical stability. This makes them ideal candidates not only for pH-sensing as demonstrated here but also for the sensing of metal ions.[42−44] The pH-responsivity and pK_a-tunability of our BODIPYs is achieved by introducing substituted phenolic subunits into the chromophore system, which provide a reversible pH-dependent control of the fluorescence intensity by highly efficient photoinduced electron transfer (PET).[45−48]

A defined spatial distribution of the dyes and UCNPs in the sensor system is achieved by incorporating both sensor components into a hydrogel which swells upon treatment with water. This is advantageous in multiple ways. The hydrogel is permeable for protons, which is essential for pH sensing. Additionally, particle related colloidal stability issues due to changes of the zeta potential accompanying the adjustment of different pH values are prevented as the particles are immobilized. This can, e.g., affect the colloidal stability of RET-based UCNP-dye conjugates in aqueous dispersion by pH-induced changes in surface charge. The hydrophobic nature of our BODIPY dyes prevents leaking from the hydrogel upon treatment with buffered solutions shown by many other indicator dyes being more hydrophilic. This is an essential prerequisite for reliable and multiple pH measurements.

In the following, the fabrication of 2D two-component sensor systems utilizing $NaYF_4$:Yb^{3+},Tm^{3+} UCNPs and spectrally matching BODIPY dyes with different pK_a values and their spectroscopic as well as performance characterization are presented including the preparation of the individual components. As representative bioapplication, subsequently, pH-changes initiated by the metabolism of *Escherichia coli* (*E. coli*) are optically monitored with our sensor system.

EXPERIMENTAL SECTION

Materials. For the synthesis of UCNPs, $YCl_3·6H_2O$ (99.99%), $YbCl_3·6H_2O$ (99.99%), $TmCl_3·6H_2O$ (99.99%), oleic acid (OA, 90% technical grade), NaOH (99.99%), nitrosyl tetrafluoroborate ($NOBF_4$, 95%), and trisodium citrate dihydrate (99%) were purchased from Sigma-Aldrich. 1-Octadecene (ODE, 90% technical grade) and NH_4F (99.99%) were obtained from Alfa Aesar. For the synthesis of the BODIPY dyes, 2,4-dimethylpyrrole (98%) and trifluoroacetic acid (99%) were purchased from ABCR. *N*,*N*-Diisopropylethylamine (99% purity), boron trifluoride diethyl etherate, and silica gel (40−63 μm, 230−400 mesh) were purchased from Sigma-Aldrich. Deuterated dimethyl sulfoxide (DMSO-d6) was obtained from Deutero GmbH. Chloroform, dichloromethane, *n*-hexane, cyclohexane, acetone, and ethanol were purchased from Carl Roth GmbH. All chemicals were used without further purification.

Synthesis of $NaYF_4$:Yb^{3+},Tm^{3+} UCNPs. The synthesis of the Yb^{3+},Tm^{3+}-codoped $NaYF_4$ nanocrystals was performed analogously to our recently reported procedure for the synthesis of $NaYF_4$:Yb^{3+},Er^{3+} UCNPs[49] following the procedure for large-scale synthesis of hexagonal-phase UCNPs by Wilhelm et al.[50] The reaction was carried out in a mixture of the high-boiling solvents oleic acid and 1-octadecene, using the thermal decomposition method.[51,52] $YCl_3·6H_2O$ (1205.85 mg, 3.975 mmol), $YbCl_3·6H_2O$ (387.50 mg, 1 mmol), and $TmCl_3·6H_2O$ (9.59 mg, 0.025 mmol) were dissolved in 15 mL of methanol and subsequently added to a mixture of OA (40 mL) and ODE (75 mL) in a 250 mL three-necked flask. The solution was then heated to 150 °C under argon flow, and the temperature was held constant for 30 min. Eventually, vacuum was applied for further 45 min at 150 °C to remove remaining low boiling impurities. The reaction mixture was then cooled to room temperature under a constant argon flow. Subsequently, a methanolic solution (30 mL) containing NaOH (500 mg, 12.5 mmol) and NH_4F (741 mg, 20 mmol) was added in one portion. To remove excess methanol the reaction mixture was heated to 120 °C under constant argon flow. After 30 min, the reaction mixture was refluxed at 325 °C. The argon flow was reduced to a gentle flow. After reaching the reaction

DOI: 10.1021/acs.analchem.9b01174
Anal. Chem. 2019, 91, 7756−7764

temperature, the UC luminescence of the particles was monitored periodically by using a small 980 nm hand laser. The formation of the nanoparticles was allowed to proceed for approximately 30 min while the visible blue emission of the $NaYF_4$:Yb^{3+},Tm^{3+} UCNPs increased drastically during the course of the reaction. Subsequently, the reaction mixture was cooled to room temperature, and the nanoparticles were purified. Successively, small volumes (5 mL) of the reaction mixture were treated with ethanol (45 mL) in centrifuge tubes leading to the precipitation of the oleate-capped nanoparticles after centrifugation. Centrifugation was always done for 10 min at 1000*g*, yielding particle pellets which were further purified by washing, two times using chloroform for dispersing and ethanol for precipitation followed by three times using cyclohexane for dispersing and acetone for precipitation. The purified UCNPs were finally dispersed in cyclohexane (40 mL) and a final centrifugation step for 3 min at 1000*g* was applied to remove larger agglomerates. The mass concentration was determined to approximately 25 mg/mL. Surface modifications with BF_4^- or citrate as capping ligands were done as reported in the literature.[50,53]

BF_4^- Surface Modification of the UCNPs. A total of 10 mL of the OA-capped UCNPs in cyclohexane was added to 10 mL of DMF. Under vigorous stirring, nitrosyl tetrafluoroborate ($NOBF_4$, 250 mg) was added in one portion. After 30 min, stirring was stopped, and after phase separation, the particle free cyclohexane phase was decanted. Subsequently, the remaining UCNP containing DMF phase was treated with chloroform. The precipitated particles were collected as pellet by centrifugation (10 min at 1000*g*). Washing of the particles by redispersing them in DMF followed by precipitation with chloroform was repeated twice, yielding a transparent pellet which was finally redispersed in 5 mL of DMF. To remove larger agglomerates the final dispersion was again centrifuged (3 min at 1000*g*), and eventually the supernatant was transferred to a glass vial for storage. The mass concentration was determined to approximately 51 mg/mL.

Citrate Surface Modification of the UCNPs. A total of 5 mL of the BF_4^--capped UCNPs in DMF was added to a solution of trisodium citrate dihydrate (2 g, 7 mmol) in water. After 30 min of vigorous stirring, the dispersion was centrifuged for 10 min at 1000*g*, yielding a transparent particle pellet. The purification of the citrate-capped particles was carried out twice by redispersing in 5 mL of H_2O followed by centrifugation for 30 min at 15000*g*. The purified pellet was finally redispersed in 5 mL of H_2O and again centrifuged (3 min at 1000*g*) to remove larger agglomerates. The resulting dispersion was transferred to a glass vial for storage and the mass concentration was determined to approximately 50 mg/mL.

Synthesis of the Fluorescent pH Sensitive BODIPYs. The synthesis, and the analytical and optical characterization of the pH sensitive BODIPY dyes and their precursor hydroxybenzaldehyde derivatives have been reported previously by our group.[47] For this publication, the synthesis of the dyes was slightly optimized using ethanol as cosolvent which drastically increased the reaction yields up to yields of 60% (see the Supporting Information, Scheme S1).[54,55]

Preparation of the Sensing Materials. For the preparation of the sensor systems, each consisting of one pH-sensitive BODIPY dye and citrate-capped UCNPs, 5 mg of the respective dye (0.25%, w/w with respect to the polymer) and 1 mL of a UCNP suspension (50 mg/mL in THF, 2.5%, w/w with respect to the polymer) were added to a viscous solution of 2 g of D4 hydrogel in 19 mL of THF. Subsequently, 300 μL of the sensor system was filled into the wells of a 8-well ibidi slide with glass bottom. The solvent was left to evaporate at room temperature in a fume hood for at least 120 min to obtain smooth sensor layers with an area of roughly 100 mm^2/well.

Methods. The purified UCNPs were analytically characterized with respect to size, crystallinity, and RE doping ratio. The size of the nanoparticles were determined by TEM using a Philips CM200 LaB6 microscope. 300 mesh copper TEM grids (Carbon coated, Science Services, Munich, Germany) were used as specimen. The crystal phase was determined by X-ray diffraction analysis (XRD, Seifert XRD 3003 TT with rotating sample holder using Cu radiation, Cu $K_{\alpha 1,2}$; λ = 1.54 Å; U = 40 kV; I = 40 mA; Ni filter; all samples measured in Bragg–Brentano geometry) and the dopant ratio was verified by inductively coupled plasma optical emission spectrometry (ICP-OES, Spectro Arcos, Spectro Analytical Instruments GmbH, Kleve, Germany).

UCL and fluorescence measurements were performed with an Edinburgh Instruments spectrofluorometer FLS-980 (Edinburgh Instruments Ltd., Livingston, United Kingdom) equipped with an 8 W 978 nm laser diode (Roithner Lasertechnik GmbH, Vienna, Austria). All spectroscopic measurements were done in 10 mm quartz cuvettes (Hellma, QS cell).

The ratiometric pK_a determination in solution was carried out by mixing citrate-capped $NaYF_4$:Yb^{3+},Tm^{3+} UCNP (3 mg/mL) with the respective BODIPY dye (5×10^{-6} mol/L) to be examined in 2 mL of methanol and 1 mL of aqueous citrate/borate buffered solution ($MeOH/H_2O$ 2/1 vol. %, 25 mM). Successively, defined amounts of concentrated HCl were added and the respective emission spectra obtained by excitation with 8 W 978 nm laser diode were collected at the respective pH. pK_a values were determined ratiometrically from at least three independent samples and measurements by fitting of the sigmoidal curve of the calculated ratio of the integrated BODIPY emission (500–600 nm) and the analyte-inert integrated red Tm^{3+} emission ($^1G_4 \rightarrow {}^3F_4$, 630–675 nm).

Ratiometric pH sensing studies with the sensor films were performed with a custom-made automated mapping setup consisting of a 980 nm 2W laser diode (Roithner Lasertechnik GmbH, Vienna, Austria) and an Ocean Optics CCD spectrometer QE65000 (Ocean Optics, Inc., Largo, U.S.A.) coupled to a bifurcated fiber to simultaneously excite the sensor layer and measure its emission spectrum at the same spot. Further optical components like collimating and focusing lenses as well as an 800 nm cutoff filter were used for setup optimization.

Prior to the pH measurements using the prepared sensor layers, every well was treated with 500 μL buffer (Britton-Robinson, pH 7, 50 mM) for at least 15 min for equilibrating the sensor layer. For pH calibration measurements, the initial buffer solution was replaced by buffer solutions of different pH (pH range depends on the pK_a value of the dye, each well was treated with a different pH). Each well of the 8-well ibidi slide was measured with a step width of 0.5 mm and background corrected yielding a resolution of roughly 400 spectra/cm^2, thus, 400 spectra/well. The integration time of the CCD spectrometer was set to 500 ms. The obtained data were evaluated using a self-written Fortran 95 code, calculating the integrated intensities for all emissions and their corresponding

DOI: 10.1021/acs.analchem.9b01174
Anal. Chem. 2019, 91, 7756–7764

ratios. Subsequently, the pK_a-values were calculated similarly as done for the measurements in solutions. Ratiometric pH sensing experiments of bacterial metabolism utilizing the sensor layer containing dye **2** were performed with quiescent *Escherichia coli* K12 (*E. coli*). Therefore, a single *E. coli* K12 colony was picked from a LB-plate and inoculated into 10 mL of LB-medium for several hours. Then, 5 mL of the culture was inoculated into 300 mL of LB-media and incubated for 12−14 h until the late exponential phase was reached. The bacterial culture was cooled on ice for 15 min. All following steps were performed at 4 °C. The cells were centrifuged at 6500 rpm for 8 min at 4 °C (Beckman Coulter, Avanti J-26 XP, Rotor JA-18). The cell pellet was washed with 50 mL of ice cold PBS-buffer (pH 8). The washing steps were performed three time in total. The final cell pellet was resuspended in 10 mL of PBS and stored on ice. For the pH studies, 500 μL of a *E. coli* suspension of about 1−2 × 10^9 cells in 2.5 mM buffered medium (Britton-Robinson buffer, starting pH 8.0) containing agar (2% w/w) and 40 mM D-glucose was added into at least 4 wells of a 8-well ibidi slide, while 2 wells were used as reference with *E. coli* without addition of D-glucose and 2 wells were used as blank (Britton-Robinson buffer, pH 8.0). The step width was adjusted to 1 mm, yielding a resolution of 100 spectra/well.

The pH values of the buffer solutions (citrate/borate, Britton-Robinson) were adjusted with a 780 pH-meter using a glass electrode from Deutsche METROHM GmbH & Co. KG and were verified with a pH 211 microprocessor pH meter from Hanna Instruments. The pH meters were calibrated at 25 °C with standard buffers of pH 10.01, pH 7.01, and pH 4.01 (Hanna Instruments) in a two-point and three-point calibration for pH 211 microprocessor pH meter and 780 pH-meter, respectively.

RESULTS AND DISCUSSION

Synthesis and Characterization of the Sensor Components. As our presented ratiometric sensor is based on the combination of UCNPs and pH-sensitive fluorescent BODIPY dyes, Yb^{3+},Tm^{3+}-codoped UCNPs as well as spectrally matching BODIPYs with different pK_a values were synthesized following our recently reported procedures.[47,49]

As can be seen in Figure 1, spherical particles with a size distribution of 26.9 ± 1 nm and a high crystallinity were obtained verified by selected area electron diffraction (SAED) as well as by the diffraction pattern determined by XRD. The diffraction pattern could be assigned to the pure hexagonal phase of the host material $NaYF_4$ (JCPDS No. 28-1192). Elemental analysis by ICP-OES gave Y^{3+}, Yb^{3+}, and Tm^{3+} contents of (81 ± 1) %, (19 ± 1) %, and (0.5 ± 1) % (provided in percentage of the total amount of RE ions, see Table S1), which corresponds well with the precursor amounts used. For the preparation of a sensor film the UCNPs had to be dispersible in THF. Therefore, the native oleic acid capping ligands were exchanged for citrate ligands. The ligand exchange was performed following a two-step ligand exchange procedure reported by Wilhelm et al.[50] At first BF_4^--capping using $NOBF_4$ was carried out to obtain UCNPs that were colloidally stable in DMF. Subsequently, BF_4^- was replaced by citrate yielding a stable aqueous suspension of citrate-capped UCNP.

In Figure 2 a), the structures of the synthesized pH-sensitive dyes used in this study are summarized. As previously demonstrated, these BODIPY dyes show a fast and highly efficient PET-based ON/OFF switching of their fluorescence

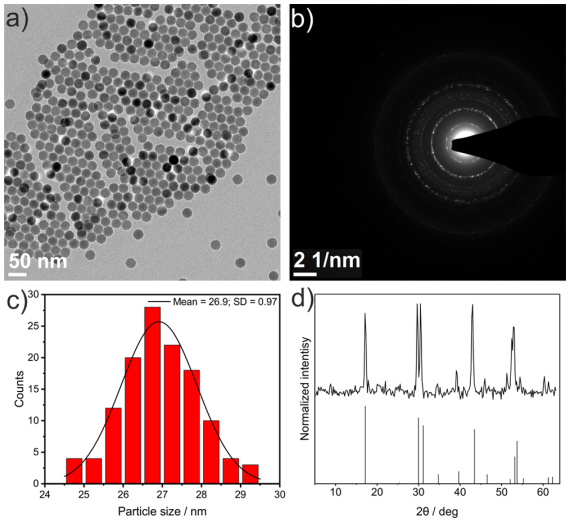

Figure 1. (a) TEM image of the OA-capped UCNPs after synthesis and purification. (b) Selected area electron diffraction (SAED) of the UCNPs recorded for the image shown in panel a. (c) Size histograms derived from TEM data. Size distribution was fitted applying a Gaussian normal distribution. (d) XRD pattern of the synthesized and purified OA-capped UCNPs in comparison to standard data of hexagonal β-phase $NaYF_4$ (JCPDS No. 28-1192).

in dependence of the pH/protonation of the phenolic group. Moreover, they have high molar absorption coefficients ε (>70 000 M^{-1} cm^{-1}) and high fluorescence quantum yields ϕ_{Fl} (>54%), which renders them optimal dyes for our purpose. Particularly relevant for the desired application are the closely matching absorption and fluorescence spectra of the different BODIPY dyes that all absorb strongly from 460 to 510 nm where the blue emission of Tm^{3+} appears (bands at 451 and 475 nm) and emit from about 500 to 600 nm, where the UCNPs do not show luminescence bands. Additionally, we were able to increase the yield for the synthesis of our BODIPY dyes by slightly modifying the reaction conditions using ethanol as cosolvent during the formation of the dipyrromethane-intermediate as well as the subsequent oxidation to the dipyrromethene prior final complexation.[54,55] This resulted in reaction yields of 52% to 60%. This is a huge step forward compared to standard reaction conditions rarely exceeding reaction yields of 20%.

Sensor Design and Principle of Referencing. Ratiometric sensors offer several unique advantages compared to purely intensity-based sensors as highlighted in the introduction. Once optimized and calibrated, these systems provide reproduceable results and prevent measurement uncertainties originating from an inhomogeneous distribution of the sensor components due to accumulation or aggregation and concentration changes of the sensor component/s, especially for multicomponent systems. Our ratiometric dual component sensor exploits the multicolor emission of UCNPs and an inner filter effect. Excitation of the Yb^{3+},Tm^{3+}-codoped UCNPs with 980 nm leads to UCL with emission bands located at 451, 475, 646, and 805 nm originating from the $^1D_2 \rightarrow {}^3F_4$, $^1G_4 \rightarrow {}^3H_6$, $^1G_4 \rightarrow {}^3F_4$, and $^3H_4 \rightarrow {}^3H_6$ transitions of Tm^{3+}, respectively (see Figure 2b). For the UC process itself the basic principle is retained, by means of Yb^{3+} acting as sensitizer and Tm^{3+} as

DOI: 10.1021/acs.analchem.9b01174
Anal. Chem. 2019, 91, 7756−7764

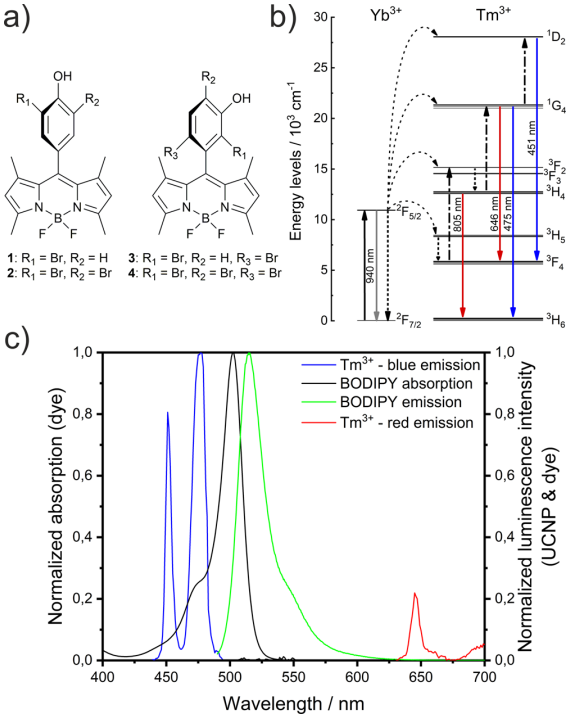

Figure 2. (a) Structures of the pH-sensitive BODIPY dyes used in combination with UCNPs. (b) Energy scheme of Yb^{3+} and Tm^{3+} in $NaYF_4$ host lattice showing possible energy transfer upconversion (ETU) pathways. (c) Referencing scheme showing the overlap of the characteristic blue upconverting luminescence emitted by OA-capped $NaYF_4$:Yb^{3+},Tm^{3+} UCNPs in cyclohexane upon excitation with 980 nm (blue line) with the absorption of the presented BODIPYs (black line, exemplarily shown for compound 1). The fluorescence of BODIPY **1** (green line) lies between the UCL of the nanoparticles, while the red Tm^{3+} UCL (red line) serves as reference.

activator. As shown in Figure 2c), the absorption bands of the pH-sensitive BODIPYs overlap with the blue UC emission bands of Tm^{3+}, thus enabling the reabsorption-based excitation of the dyes by these UC emissions. The major contribution of the dye excitation, however, results from the 475 nm Tm^{3+} emission. This is advantageous as both the blue UCL at 475 nm and the red UCL at 648 nm, which does not overlap with the dye's absorption and emission and thus is used as internal reference, originate from the same Tm^{3+} energy level $^1G_4$. Consequently, the pH-dependent intensity ratios of the dye fluorescence and the analyte-inert reference UCL band are expected to be (nearly) independent of the excitation power density. For nonlinear emitters like UCNPs with excitation power density-dependent photoluminescence quantum yields, this parameter controls the spectral distribution of the resulting UCL with higher excitation power densities favoring UC processes requiring a higher number of photons.[56,57]

Ratiometric Determination of pK_a Values in Solution. The optimization, i.e., the concentration fine-tuning of our sensor systems was first done in solution. Therefore, a set of self-referenced dual component sensor solutions, each consisting of citrate-capped UCNPs and a pH-sensitive BODIPY (**1**–**4**) in a buffered methanol/aqueous solution (2/1 vol %, 25 mM), were prepared. Subsequently, the pK_a values were determined by pH titrations where the pH value was change incrementally while measuring the luminescence resulting upon excitation of the UCNPs with 980 nm light. As shown exemplarily in Figure 3 for a sensor system containing

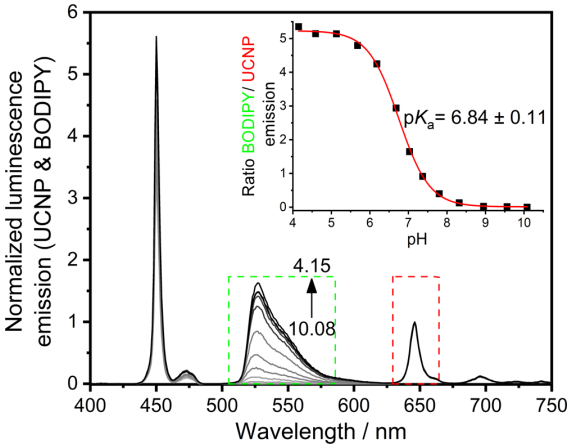

Figure 3. Normalized luminescence emission of a pH sensor systems consisting of 3 mg/mL citrate-capped Yb^{3+},Tm^{3+}-codoped UCNPs and BODIPY **2** (5×10^{-6} M) in buffered mixture of methanol and water (2/1 vol. %, 25 mM) in dependence of pH upon excitation at 980 nm. The inset shows the ratio of the integrated luminescence intensities of the green BODIPY fluorescence and the red UC emission of the UCNPs and the corresponding sigmoidal curve fit. The presented pK_a value is averaged from three independent measurements.

dye **2**, the blue UCL at 475 nm is strongly decreased by dye absorption, leading to the appearance of the highly pH-dependent BODIPY emission centered at 528 nm. A RET process is unlikely here due to the comparably large distance between the UCNPs and the dye molecules exceeding commonly observed Förster radii of <10 nm.[41] With decreasing pH, the dye fluorescence is switched ON and eventually reaches its maximum value determined by the dye's quantum yield ϕ_{Fl}. The maximum luminescence intensity of the single components and the intensity ratios depend on several factors. Instrument-specific contributions are the excitation power density and the spectral responsivity of the detection system. Contributions from the side of the sensor system are the concentrations of the dye and the UCNPs and the matrix-dependent spectroscopic properties of these components, namely the (integral) molar absorption coefficient of the dye (ε) within the wavelength region covered by the blue Tm^{3+} emission as well as the luminescence efficiencies of both components governed by ϕ_{UC} and ϕ_{Fl}. An increase in pH results in a decrease in the fluorescence intensity as the amount of the emissive protonated BODIPY dye molecules is reduced until the fluorescence is finally switched OFF completely. This underlines the high efficiency of the PET mechanism responsible for the quenching of the fluorescence of the unprotonated dye.

The small pH-dependent changes of the intensity of the two blue UC emission bands at 451 and 475 nm are attributed to small changes in the absorption of BODIPY **2**. Furthermore, a huge difference of the intensity ratios of these two blue emission bands can be observed when comparing the emission features of the single sensor components separately (see Figure

DOI: 10.1021/acs.analchem.9b01174
Anal. Chem. 2019, 91, 7756−7764

2c) and within the two-component sensor system (see Figure 3). While the 475 nm UCL is usually more intense than the 450 nm emission, it is barely noticeable in the sensor systems as it is mainly reabsorbed by the dye due to its much stronger overlap with the dye's absorption band.

Subsequently, the ratios of the integrated emission intensities of the pH-sensitive green BODIPY fluorescence (500−600 nm) and the red pH-inert UC emission (630−675 nm) were calculated for the different pH values. This yields a typical sigmoidal curve for the normalized fluorescence intensity of the dye (see insets of Figures 3 and S1−S3, Supporting Information). The corresponding pK_a values of the dyes were obtained by sigmoidal curve fitting using a dose response function (see Table S2 for the equation and fitting parameters used for the curves shown in the insets). They were determined to be 8.79 ± 0.17, 6.84 ± 0.11, 8.03 ± 0.11, and 6.21 ± 0.13 for dyes **1**−**4**, respectively, see Table 1. Although

Table 1. pK_a Values of the pH-Sensitive BODIPY Dyes Utilized in the Sensor Systems in Solution and Incorporated in Hydromed D4

pH sensor	pK_a (solution[a])[c]	pK_a (D4[b])[c]
UCNP+1	8.79 ± 0.17	8.31 ± 0.08
UCNP+2	6.84 ± 0.11	5.90 ± 0.14
UCNP+3	8.03 ± 0.11	7.69 ± 0.21
UCNP+4	6.21 ± 0.13	5.58 ± 0.21

[a](MeOH/H_2O 2/1 vol. %, 25 mM buffered solution), excitation at 980 nm. [b]Excitation at 980 nm. [c]Averaged values from three independent measurements.

these values were determined from an inner filter effect-based ratiometric system by secondary excitation of the dye via UCL, they are in good agreement with the pK_a values obtained by direct excitation of the dyes.[47] The strong variations in the pK_a values of the different BODIPYs and their remarkable shifts reflect the previously described substitution pattern controlled and halogenation-induced changes of the electron density at the pH-sensitive hydroxyl group.[47]

Ratiometric Determination of pK_a Values in D4 Hydrogel. To enable a widespread use of our sensor system, the sensor components were immobilized in a Hydromed D4 hydrogel. This hydrogel is an optically transparent polymer with an excellent capability of water uptake and proton diffusion, which are mandatory for pH sensing. Furthermore, this matrix allows partially hydrophobic compounds like our BODIPY dyes as wells as citrate-capped UCNPs to be embedded and completely retained. The colloidal stability and lack of leaking of the unprotonated and protonated dyes were addressed in separate stability tests prior to the pH studies. The latter is a huge advantage of our BODIPYs as for example the majority of pH indicators like neutral red and bromothymol blue change their polarity with changing pH and leak typically in the charged form from sensor matrices. This hampers the fabrication of a long-term stable sensor layer and requires a more sophisticated design of sensor systems.

The UCNP-to-dye concentration ratio was optimized with respect to UCL reabsorption and minimum self-absorption of the dye's fluorescence. The latter occurs with increasing dye concentration for dyes with a small Stokes shift like the BODIPYs (see Figure S4). A dye concentration of 0.25% (w/w) and a UCNP concentration of 2.5% (w/w) in 10% D4 (w/w) in THF were found to be best suited in terms of processing the sensor cocktail, dye concentration, UCNP/dye intensity ratio, and signal-to-noise ratio. The fabrication of the sensor material was performed by first dispersing the respective amount of dye, UCNP, and hydrogel as a mixture in a THF solution as described in the Experimental Section, followed by applying equivalent volumes into the wells of a 8-well ibidi slide to obtain a readily accessible one-layer sensor system. To verify the conceptual design of our ratiometric dual component pH sensor we performed pH titrations and determined the pK_a of the dyes in the hydrogel by treating each sensor layer with buffer of different pH and measuring the ratios of the integrated intensities of the green (G) BODIPY emission (500−600 nm) and the red (R) Tm^{3+} UCL (630−675 nm). The resulting G/R ratios are presented in Figure 4a). The wells

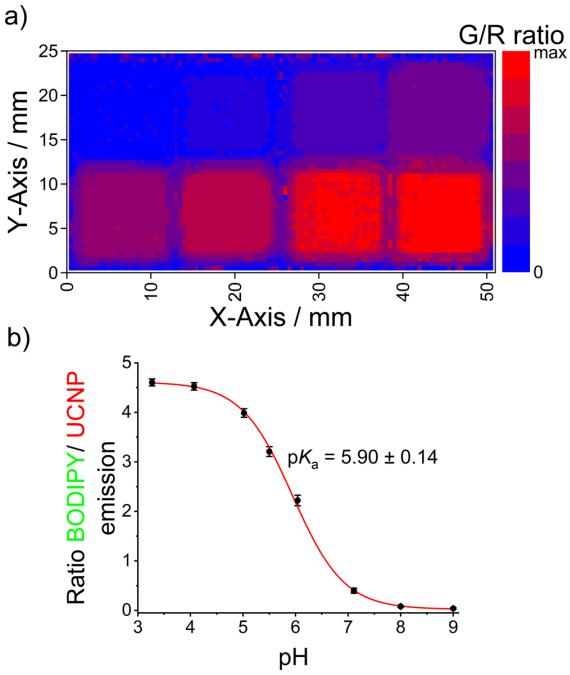

Figure 4. (a) Calculated luminescence intensity ratios of the green (G) fluorescence of BODIPY **2** and the red (R) UCL of the UCNPs. pH values from top left to bottom right: 9.01, 7.98, 7.11, 6.04, 5.50, 5.02, 4.07, and 3.27. Each pixel represents a separately measured spectrum. Color-coding is done in a nonequidistant scaling. (b) G/R-ratio in dependence of pH and the corresponding sigmoidal curve fit.

of the ibidi slide containing different proton concentrations can be clearly separated by their G/R ratios. While the G/R ratio is roughly zero at basic pH (>9, deep blue) as the BODIPY fluorescence is switched OFF, the ratio increases (see Figure 4a) following the switching ON of the dye upon acidification as can be seen in Figure 4b). The ON/OFF switching of the fluorescence of the dye is reversible as it is simply based on protonation/deprotonation (see Figure S5). For properly calibrated detection systems the maximal value of the G/R ratio depends only on the UCNP-to-dye concentration ratio. It is independent of the actual layer homogeneity as the UCNP-to-dye concentration ratio remains constant within the layers. Also, it is independent of excitation power density at least for the relatively moderate excitation power densities used for sensing. While the analysis of the raw luminescence intensities

DOI: 10.1021/acs.analchem.9b01174
Anal. Chem. 2019, 91, 7756−7764

for each of the separately measured spectra provided rather unsatisfactory results with strong intensity fluctuations and high standard deviations in the range of 30−80%, the advantage of the used ratiometric system is highlighted in Figure 4a) showing an excellent homogeneity of the calculated G/R values with small standard deviations within the wells of the ibidi slide. The relatively small standard deviations allow to distinguish between small changes of the G/R ratio, e.g., color coding of small changes of the G/R ratio from 0.04 ± 0.01 to 0.08 ± 0.02 for a pH change from 9 to 8 is possible (see Figure 4a). This underlines the high sensitivity of the sensor layers as it is even more beneficial for the linear region of the sigmoidal pH response at pH values around pK_a ± 1 allowing a more accurate determination of the pH from the measured G/R ratio. For instance, a change of the G/R ratio of roughly 0.04 as observed for a decrease in pH from pH 9 to 8 corresponds to a change of about 0.02 pH units in the linear range.

The pK_a values of the sensor systems using dyes **1**−**4** (see Figures 4 and S6−S8) were calculated to 8.31 ± 0.08, 5.90 ± 0.14, 7.69 ± 0.21, and 5.58 ± 0.12, respectively (see Table 1 and Figure 4b and for fitting parameters see Table S4), revealing a significant shift of the pK_a values in the polymer matrix to the more acid region due to the changed chemical environment. The obtained values as well as the shifts are in a good agreement with previously determined values by direct excitation of the dye.[47]

Monitoring Biologically Induced pH Changes. To assess the potential of our sensor layers for applications in the life sciences, we monitored exemplarily biologically induced changes in pH caused by the metabolism of *Enterobacteriaceae*. We chose here *E. coli* bacteria, which are known to acidify their surrounding medium by the mixed acid fermentation of D-glucose into lactate, acetate, succinate, formate, ethanol, and H_2. Subsequently, time-dependent pH changes induced by quiescent *E. coli*, upon addition of D-glucose (t = 0 min) were examined. In Figure 5a, the change of the color-encoded G/R ratios derived from our sensor layers upon excitation with 980 nm is shown as a function of time for a sensor system containing BODIPY **2**. As can be seen for the blank sample treated only with buffer (pH 8) and for the control sample containing *E. coli*, but no D-glucose, no significant changes of the G/R ratio occur. However, the G/R is not zero as the fluorescence of BODIPY **2** is not switched OFF completely at a pH value of 8 (see Figure 4). In contrast, strong changes of the dye's fluorescence upon excitation of the UCNPs can be observed for all samples containing *E. coli* and D-glucose, which lead to strong changes of the G/R ratio as exemplarily shown for one sample in Figure 5a. These changes are attributed to changes of the pH value of the suspensions on top of the sensor layer induced by the metabolic products of *E. coli*. We were able to derive the pH values of the system from the G/R values utilizing our previously determined calibration function. The resulting pH values in dependence of time are shown in Figure 5b. While the pH values remained more or less constant for the sample treated only with buffer (pH 8) as well for the *E. coli* samples lacking D-glucose, the pH value of the D-glucose fed *E. coli* samples showed strong time-dependent changes. Since the Britton-Robinson buffer used for this study is known to show a pH response approximately proportional to the amount of acid/base added and the pK_a value for BODIPY dye **2** is 5.90 ± 0.14, a linear pH decrease can be observed in the range from pH 7 to 5 (pK_a ± 1). Finally, the pH decay curve flattened because the pH of the systems falls below the

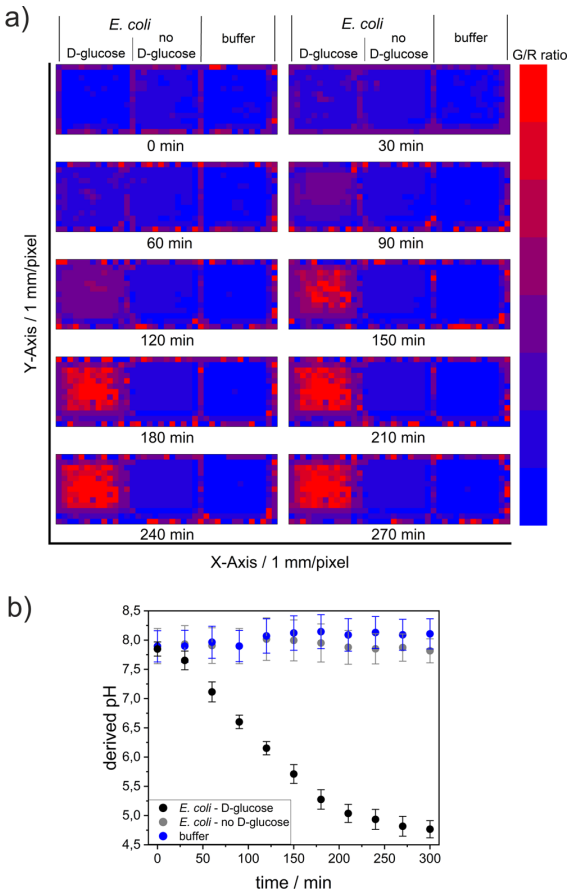

Figure 5. (a) Time-dependent changes of the G/R ratio of the pH sensor layers treated with a suspension of *E. coli* with D-glucose and a suspension of *E. coli* without D-glucose or pure buffer. (b) Calculated pH values in dependence of time averaged from quadruplicate measurements.

detection range of our sensor and/or the low pH due to the accumulated metabolites prevents further utilization of glucose by *E. coli*.

■ CONCLUSION AND OUTLOOK

In summary, the conceptual design and fabrication of a reversibly pH responsive ratiometric dual component sensor system was described that utilizes the intensity ratios of the multicolor luminescence of $NaYF_4$:Yb^{3+},Tm^{3+} upconversion nanoparticles (UCNPs) excited at 980 nm, and the green fluorescence of pH-responsive BODIPY dyes excited by the blue upconversion luminescence (UCL) of Tm^{3+}. As internal reference, the red analyte-inert UCL was used. This design concept allows a correlation of the calculated intensity ratios of the BODIPY fluorescence and the red UCL of the nanoparticles with pH. Incorporation of both sensor components into a hydrogel provided a sensor film well suited for measuring the time-dependent change of the pH of a suspension containing quiescent *E. coli* metabolizing D-glucose. This versatile sensor concept could be applied for the design of a reversible broad band pH sensor measuring pH from 5 to 9 by combining the UCNP with our spectrally matching

DOI: 10.1021/acs.analchem.9b01174
Anal. Chem. 2019, 91, 7756−7764

BODIPY dyes differing in pK_a. However, as signal generation is based on UCL reabsorption a careful optimization of the concentration ratios of the single components is mandatory.

In the future, our ratiometric pH sensor system will be used for studying microbially influenced corrosion on surfaces. Further improvement of the sensor system currently done includes the use of UCNPs with a higher ϕ_{UC} by applying a surface-passivating and protecting shell,[40,58,59] thereby reducing the amount of UC material needed for sensor fabrication. Furthermore, different layer fabrication methods like spray- or dip-coating are studied as well as other combinations of spectrally matching UCNPs and dyes. This includes, e.g., the use of Yb^{3+},Er^{3+}- or Yb^{3+},Ho^{3+}-codoped UCNPs.

■ ASSOCIATED CONTENT

Supporting Information

The Supporting Information is available free of charge on the ACS Publications website at DOI: 10.1021/acs.analchem.9b01174.

Synthesis and analytical characterization of the BODIPY dyes; ICP-OES data of UCNPs; Figures of pH titration experiments for sensor systems in solution as well as for the sensor system in D4 and corresponding fitting parameters (PDF)

■ AUTHOR INFORMATION

Corresponding Author

*E-mail: Ute.Resch@bam.de.

ORCID

Christian Würth: 0000-0002-0204-9727

Ute Resch-Genger: 0000-0002-0944-1115

Notes

The authors declare no competing financial interest.

■ ACKNOWLEDGMENTS

We gratefully acknowledge financial support from the internal BAM project MIC (microbiologically influenced corrosion) and from the Ph.D. program of BAM. Also, financial support from the German Research Council (DFG) is gratefully acknowledged by Elina Andresen and Ute Resch-Genger (Grant SCHA 1009/17-1).

■ REFERENCES

(1) Jeevarajan, A. S.; Vani, S.; Taylor, T. D.; Anderson, M. M. *Biotechnol. Bioeng.* **2002**, *78* (4), 467−472.

(2) John, G. T.; Goelling, D.; Klimant, I.; Schneider, H.; Heinzle, E. *J. Dairy Res.* **2003**, *70* (3), 327−333.

(3) Zhang, W.; Tang, B.; Liu, X.; Liu, Y.; Xu, K.; Ma, J.; Tong, L.; Yang, G. *Analyst* **2009**, *134* (2), 367−371.

(4) Hilderbrand, S. A.; Kelly, K. A.; Niedre, M.; Weissleder, R. *Bioconjugate Chem.* **2008**, *19* (8), 1635−1639.

(5) Liebsch, G.; Klimant, I.; Krause, C.; Wolfbeis, O. S. *Anal. Chem.* **2001**, *73* (17), 4354−4363.

(6) Klymchenko, A. S.; Duportail, G.; Ozturk, T.; Pivovarenko, V. G.; Mély, Y.; Demchenko, A. P. *Chem. Biol.* **2002**, *9* (11), 1199−1208.

(7) Lakowicz, J. R. *Principles of Fluorescence Spectroscopy*, 3rd ed.; Springer: New York, 2006; pp XXVI, 954.

(8) Otto, S.; Scholz, N.; Behnke, T.; Resch-Genger, U.; Heinze, K. *Chem. - Eur. J.* **2017**, *23* (50), 12131−12135.

(9) Hornig, S.; Biskup, C.; Gräfe, A.; Wotschadlo, J.; Liebert, T.; Mohr, G. J.; Heinze, T. *Soft Matter* **2008**, *4* (6), 1169−1172.

(10) Burns, A.; Sengupta, P.; Zedayko, T.; Baird, B.; Wiesner, U. *Small* **2006**, *2* (6), 723−726.

(11) Liu, Y.-S.; Sun, Y.; Vernier, P. T.; Liang, C.-H.; Chong, S. Y. C.; Gundersen, M. A. *J. Phys. Chem. C* **2007**, *111* (7), 2872−2878.

(12) Ehlert, O.; Thomann, R.; Darbandi, M.; Nann, T. *ACS Nano* **2008**, *2* (1), 120−124.

(13) Wang, F.; Banerjee, D.; Liu, Y.; Chen, X.; Liu, X. *Analyst* **2010**, *135* (8), 1839−1854.

(14) Chen, G.; Qiu, H.; Prasad, P. N.; Chen, X. *Chem. Rev.* **2014**, *114* (10), 5161−5214.

(15) Wang, M.; Abbineni, G.; Clevenger, A.; Mao, C.; Xu, S. *Nanomedicine* **2011**, *7* (6), 710−729.

(16) Schäferling, M.; Resch-Genger, U. Luminescent Nanoparticles for Chemical Sensing and Imaging. In *Reviews in Fluorescence 2016*; Geddes, C. D., Ed.; Springer International Publishing: Berlin, 2017; pp 71−109.

(17) Gorris, H. H.; Resch-Genger, U. *Anal. Bioanal. Chem.* **2017**, *409* (25), 5875−5890.

(18) Singh, R.; Dumlupinar, G.; Andersson-Engels, S.; Melgar, S. *Int. J. Nanomed.* **2019**, *14*, 1027−1038.

(19) Wang, F.; Liu, X. *Chem. Soc. Rev.* **2009**, *38* (4), 976−989.

(20) Fischer, L. H.; Harms, G. S.; Wolfbeis, O. S. *Angew. Chem., Int. Ed.* **2011**, *50* (20), 4546−4551.

(21) Hyppänen, I.; Perälä, N.; Arppe, R.; Schäferling, M.; Soukka, T. *ChemPhysChem* **2017**, *18* (6), 692−701.

(22) Li, D. D.; Shao, Q. Y.; Dong, Y.; Jiang, J. Q. *Adv. Mater. Res.* **2015**, *1088*, 23−27.

(23) Vetrone, F.; Naccache, R.; Zamarrón, A.; Juarranz de la Fuente, A.; Sanz-Rodríguez, F.; Martinez Maestro, L.; Martín Rodriguez, E.; Jaque, D.; García Solé, J.; Capobianco, J. A. *ACS Nano* **2010**, *4* (6), 3254−3258.

(24) Lim, S. F.; Riehn, R.; Ryu, W. S.; Khanarian, N.; Tung, C.-k.; Tank, D.; Austin, R. H. *Nano Lett.* **2006**, *6* (2), 169−174.

(25) Chatterjee, D. K.; Rufaihah, A. J.; Zhang, Y. *Biomaterials* **2008**, *29* (7), 937−943.

(26) Zhou, J.; Sun, Y.; Du, X.; Xiong, L.; Hu, H.; Li, F. *Biomaterials* **2010**, *31* (12), 3287−3295.

(27) Wang, C.; Cheng, L.; Liu, Z. *Theranostics* **2013**, *3* (5), 317−330.

(28) van der Ende, B. M.; Aarts, L.; Meijerink, A. *Phys. Chem. Chem. Phys.* **2009**, *11* (47), 11081−11095.

(29) Won Jin, K.; Marcin, N.; Paras, N. P. *Nanotechnology* **2009**, *20* (18), 185301.

(30) Tyler, B.; Jeevan, M.; May, P. S.; Jon, K.; William, C.; Krishnamraju, A.; Swathi, V.; QuocAnh, N. L. *Nanotechnology* **2012**, *23* (18), 185305.

(31) Meruga, J. M.; Baride, A.; Cross, W.; Kellar, J. J.; May, P. S. *J. Mater. Chem. C* **2014**, *2* (12), 2221−2227.

(32) Wilhelm, S. *ACS Nano* **2017**, *11* (11), 10644−10653.

(33) Arppe, R.; Näreoja, T.; Nylund, S.; Mattsson, L.; Koho, S.; Rosenholm, J. M.; Soukka, T.; Schäferling, M. *Nanoscale* **2014**, *6* (12), 6837−6843.

(34) Du, S.; Hernández-Gil, J.; Dong, H.; Zheng, X.; Lyu, G.; Bañobre-López, M.; Gallo, J.; Sun, L.-d.; Yan, C.-h.; Long, N. J. *Dalton Transactions* **2017**, *46* (40), 13957−13965.

(35) Li, C.; Zuo, J.; Zhang, L.; Chang, Y.; Zhang, Y.; Tu, L.; Liu, X.; Xue, B.; Li, Q.; Zhao, H.; Zhang, H.; Kong, X. *Sci. Rep.* **2016**, *6*, 38617.

(36) Mahata, M.; Bae, H.; Lee, K. *Molecules* **2017**, *22* (12), 2064.

(37) Strobl, M.; Mayr, T.; Klimant, I.; Borisov, S. M. *Sens. Actuators, B* **2017**, *245*, 972−979.

(38) Wang, F.; Raval, Y.; Chen, H.; Tzeng, T.-R. J.; DesJardins, J. D.; Anker, J. N. *Adv. Healthcare Mater.* **2014**, *3* (2), 197−204.

(39) Meier, R. J.; Simbürger, J. M. B.; Soukka, T.; Schäferling, M. *Anal. Chem.* **2014**, *86* (11), 5535−5540.

(40) Andresen, E.; Resch-Genger, U.; Schäferling, M. *Langmuir* **2019**, *35* (15), 5093−5113.

(41) Muhr, V.; Würth, C.; Kraft, M.; Buchner, M.; Baeumner, A. J.; Resch-Genger, U.; Hirsch, T. *Anal. Chem.* **2017**, *89* (9), 4868−4874.

(42) Loudet, A.; Burgess, K. *Chem. Rev.* **2007**, *107* (11), 4891−4932.

(43) Ulrich, G.; Ziessel, R.; Harriman, A. *Angew. Chem., Int. Ed.* **2008**, *47* (7), 1184−1201.
(44) Boens, N.; Leen, V.; Dehaen, W. *Chem. Soc. Rev.* **2012**, *41* (3), 1130−1172.
(45) Baruah, M.; Qin, W.; Basarić, N.; De Borggraeve, W. M.; Boens, N. *J. Org. Chem.* **2005**, *70* (10), 4152−4157.
(46) Hecht, M.; Kraus, W.; Rurack, K. *Analyst* **2013**, *138* (1), 325−332.
(47) Radunz, S.; Tschiche, H. R.; Moldenhauer, D.; Resch-Genger, U. *Sens. Actuators, B* **2017**, *251*, 490−494.
(48) Prasannan, D.; Arunkumar, C. *New J. Chem.* **2018**, *42* (5), 3473−3482.
(49) Radunz, S.; Schavkan, A.; Wahl, S.; Würth, C.; Tschiche, H. R.; Krumrey, M.; Resch-Genger, U. *J. Phys. Chem. C* **2018**, *122* (50), 28958−28967.
(50) Wilhelm, S.; Kaiser, M.; Wurth, C.; Heiland, J.; Carrillo-Carrion, C.; Muhr, V.; Wolfbeis, O. S.; Parak, W. J.; Resch-Genger, U.; Hirsch, T. *Nanoscale* **2015**, *7* (4), 1403−1410.
(51) Heer, S.; Kömpe, K.; Güdel, H. U.; Haase, M. *Adv. Mater.* **2004**, *16* (23−24), 2102−2105.
(52) Mai, H.-X.; Zhang, Y.-W.; Si, R.; Yan, Z.-G.; Sun, L.-d.; You, L.-P.; Yan, C.-H. *J. Am. Chem. Soc.* **2006**, *128* (19), 6426−6436.
(53) Dong, A.; Ye, X.; Chen, J.; Kang, Y.; Gordon, T.; Kikkawa, J. M.; Murray, C. B. *J. Am. Chem. Soc.* **2011**, *133* (4), 998−1006.
(54) Lindsey, J. S.; Wagner, R. W. *J. Org. Chem.* **1989**, *54* (4), 828−836.
(55) Bartelmess, J.; Weare, W. W.; Latortue, N.; Duong, C.; Jones, D. S. *New J. Chem.* **2013**, *37* (9), 2663−2668.
(56) Würth, C.; Kaiser, M.; Wilhelm, S.; Grauel, B.; Hirsch, T.; Resch-Genger, U. *Nanoscale* **2017**, *9* (12), 4283−4294.
(57) Resch-Genger, U.; Gorris, H. H. *Anal. Bioanal. Chem.* **2017**, *409* (25), 5855−5874.
(58) Würth, C.; Fischer, S.; Grauel, B.; Alivisatos, A. P.; Resch-Genger, U. *J. Am. Chem. Soc.* **2018**, *140* (14), 4922−4928.
(59) Homann, C.; Krukewitt, L.; Frenzel, F.; Grauel, B.; Würth, C.; Resch-Genger, U.; Haase, M. *Angew. Chem., Int. Ed.* **2018**, *57* (28), 8765−8769.

DOI: 10.1021/acs.analchem.9b01174
Anal. Chem. 2019, 91, 7756−7764

Simple Self-referenced Luminescent pH Sensors based on Upconversion Nanocrystals and pH-sensitive Fluorescent BODIPY Dyes

Sebastian Radunz,[a] Elina Andresen,[a] Christian Würth,[a] Andrea Koerdt,[a] Harald Rune Tschiche,[a,b] and Ute Resch-Genger*[a]

[a] BAM Federal Institute for Materials Research and Testing, Division Biophotonics, Berlin, Germany. E-mail: ute.resch@bam.de.

[b] BfR German Federal Institute for Risk Assessment, Department 7, Max-Dohrn-Str. 8-10, 10589 Berlin, Germany.

Supplementary Information (SI)

Experimental Section

Synthesis of fluorescent pH sensitive BODIPYs:

The corresponding aldehyde (2.5 mmol, 1.0 eq.) and 2,4-dimethylpyrrole (5.0 mmol, 2.0 eq.) were dissolved in 140 ml dry DCM and 10 ml dry EtOH. After degassing by rapid vacuum-argon cycles (5 times), a few drops of TFA (30 µl) were added and the reaction mixture was stirred at room temperature under argon atmosphere in the dark overnight. *p*-Chloranil (2.5 mmol, 1.0 eq.) was added and the mixture was stirred for additional 60 min. Prior addition of $BF_3 \cdot OEt_2$ (25.0 mmol, 10.0 eq.) and 4.3 ml diisopropylethylamine (DIPEA) (25.0 mmol, 10.0 eq.), the DCM/EtOH solvent mixture was removed under reduced pressure and replaced by 100 ml of dry DCM to avoid a reaction between $BF_3 \cdot OEt_2$ and EtOH. After portionwise addition, the reaction mixture was stirred for 60 minutes. Subsequently, the reaction mixture was prepurified by carrying out a short silica-gel flash column chromatography with DCM as eluent. The resulting crude mixture was concentrated under reduced pressure and further purified by silica-gel flash column chromatography using DCM/n-hexane (ratio in dependence of product polarity) as eluents. Pure dyes as required for the spectroscopic studies were obtained by recrystallization from chloroform/n-hexane.

4,4-difluoro-1,3,5,7-tetramethyl-8-(3-bromo-4-hydroxyphenyl)-bora-3a,4a-diaza-s-indacene **(1)**
Compound **1** was synthesized according to the procedure mentioned above using 3-bromo-4-hydroxybenzaldehyde as corresponding aldehyde. Purification by column chromatography on silica gel using DCM/*n*-hexane (9:1) as eluent followed by recrystallization gave compound **2** as reddish-orange crystals (581 mg, 55 %).
^{1}H NMR (500 MHz, DMSO-d_6) [ppm]: δ = 10.73 (s, OH), 7.51 (d, $1H_{aryl}$), 7.16 (dd, $1H_{aryl}$), 7.11 (d, $1H_{aryl}$), 6.18 (s, $2H_{pyrrole}$), 2.44 (s, $6H_{methyl}$), 1.45 (s, $6H_{methyl}$)
^{13}C NMR (125 MHz, DMSO-d_6) [ppm]: δ = 154.9, 154.9, 142.6, 140.6, 132.1, 131.0, 128.5, 125.8, 121.4, 117.0, 109.9, 14.4, 14.2
ESI-TOF (ESI-): m/z calculated for $C_{19}H_{19}BBrF_2N_2O$ $[M-H]^-$: 417.0586, found 417.0659.

4,4-difluoro-1,3,5,7-tetramethyl-8-(3,5-dibromo-4-hydroxyphenyl)-bora-3a,4a-diaza-s-indacene **(2)**
Compound **3** was synthesized according to the procedure mentioned above using 3,5-dibromo-4-hydroxybenzaldehyde as corresponding aldehyde. Purification by column chromatography on silica gel using DCM/*n*-hexane (8:2) as eluent followed by recrystallization gave compound **3** as reddish crystals (510 mg, 41 %).
^{1}H NMR (500 MHz, DMSO-d_6) [ppm]: δ = 10.42 (s, OH), 7.64 (s, $2H_{aryl}$), 6.21 (s, $2H_{pyrrole}$), 2.44 (s, $6H_{methyl}$), 1.48 (s, $6H_{methyl}$)
^{13}C NMR (125 MHz, DMSO-d_6) [ppm]: δ = 155.2, 151.6, 142.5, 138.6, 131.8, 130.9, 127.7, 121.6, 112.5, 14.5, 14.3
ESI-TOF (ESI-): m/z calculated for $C_{19}H_{16}BBr_2F_2N_2O$ $[M-H]^-$: 496.9670, found 496.9742.

4,4-difluoro-1,3,5,7-tetramethyl-8-(2,6-dibromo-3-hydroxyphenyl)-bora-3a,4a-diaza-s-indacene **(3)**
Compound **9** was synthesized according to the procedure mentioned above using 2,6-dibromo-3-hydroxybenzaldehyde hydroxybenzaldehyde as corresponding aldehyde. Purification by column chromatography on silica gel using DCM/*n*-hexane (8:2) as eluent followed by recrystallization gave compound **3** as reddish crystals (651 mg, 52 %).

^{1}H NMR (500 MHz, DMSO-d_6) [ppm]: δ = 10.97 (s, OH), 7.65 (d, $1H_{aryl}$), 7.06 (d, $1H_{aryl}$), 6.19 (s, $2H_{pyrrole}$), 2.46 (s, $6H_{methyl}$), 1.46 (s, $6H_{methyl}$)
^{13}C NMR (125 MHz, , DMSO-d_6) [ppm]: δ = 155.6, 155.0, 141.3, 139.0, 135.6, 132.9, 129.5, 121.3, 118.3, 110.9, 110.3, 14.4, 12.9
ESI-TOF (ESI+): m/z calculated for $C_{19}H_{17}BBr_2F_2N_2ONa$ $[M+Na]^+$: 520.9646, found 520.9654.

4,4-difluoro-1,3,5,7-tetramethyl-8-(2,4,6-tribromo-3-hydroxyphenyl)-bora-3a,4a-diaza-s-indacene **(4)**
Compound **10** was synthesized according to the procedure mentioned above using 2,4,6-tribromo-4-hydroxybenzaldehyde **20** as corresponding aldehyde. Purification by column chromatography on silica gel using DCM/*n*-hexane (3:1) as eluent followed by recrystallization gave compound **10** as deep reddish crystals (864 mg, 60 %).
^{1}H NMR (500 MHz, DMSO-d_6) [ppm]: δ = 10.67 (s, OH), 8.12 (s, $1H_{aryl}$), 6.21 (s, $2H_{pyrrole}$), 2.46 (s, $6H_{methyl}$), 1.48 (s, $6H_{methyl}$)
^{13}C NMR (125 MHz, DMSO-d_6) [ppm]: δ = 155.9, 141.2, 138.2, 135.5, 135.1, 129.3, 121.5, 113.8, 113.7, 14.4, 13.1
ESI-TOF (ESI+): m/z calculated for $C_{19}H_{16}BBr_3F_2N_2ONa$ $[M+Na]^+$: 598.8751, found 598.8747.

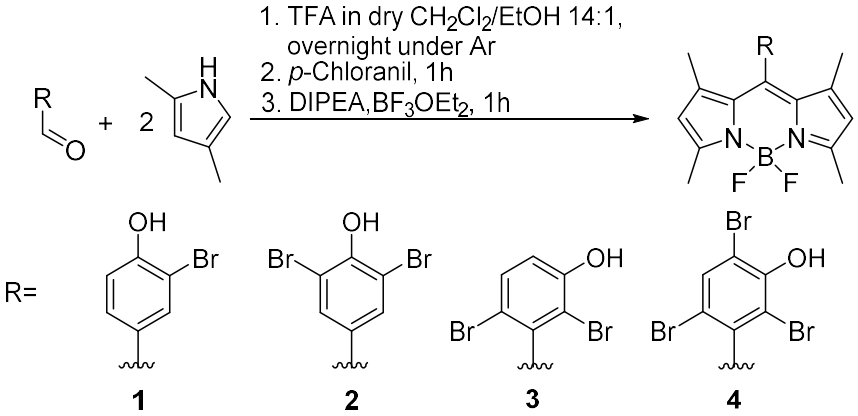

Scheme S1. Three-step reaction scheme of the synthesis of BODIPY dyes **1** – **3** using the corresponding benzaldehyde derivatives.

Table S1. Molar ratios of the lanthanide ions of the particles determined by *ICP-OES.*

Y/(Y+Yb+Tm) / %	Yb/(Y+Yb+Tm) / %	Tm/(Y+Yb+Tm) / %
80.79 ± 1.19	18.80 ± 0.92	0.49 ± 1.01

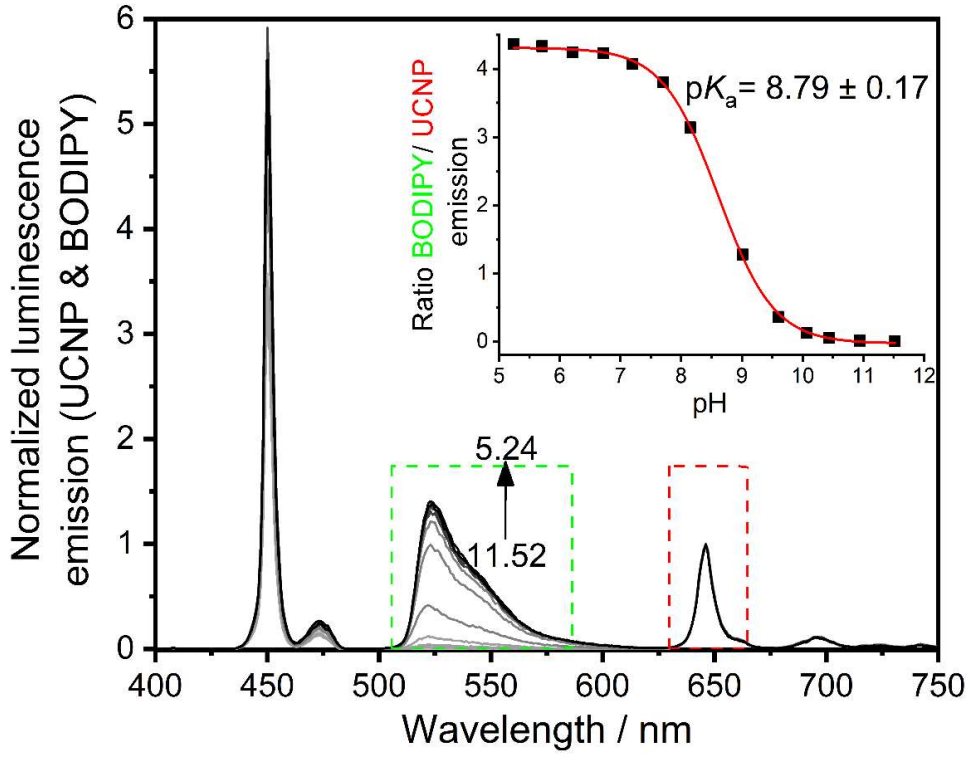

Figure S1. Normalized (red Tm^{3+} emission) luminescence emission of a pH sensor systems consisting of 3 mg/ml citrate-capped Yb^{3+},Er^{3+}-codoped UCNPs and BODIPY **1** ($5x10^{-6}$ M) in buffered mixture of methanol and water (2/1 vol%, 25 mM) in dependence of pH upon excitation with 980 nm. The inset shows the ratio of the integrated luminescence intensities of the green BODIPY fluorescence and the red UC emission of the UCNPs and the corresponding sigmoidal fit of the curve. The presented pK_a value presents an average value derived from three independent measurements.

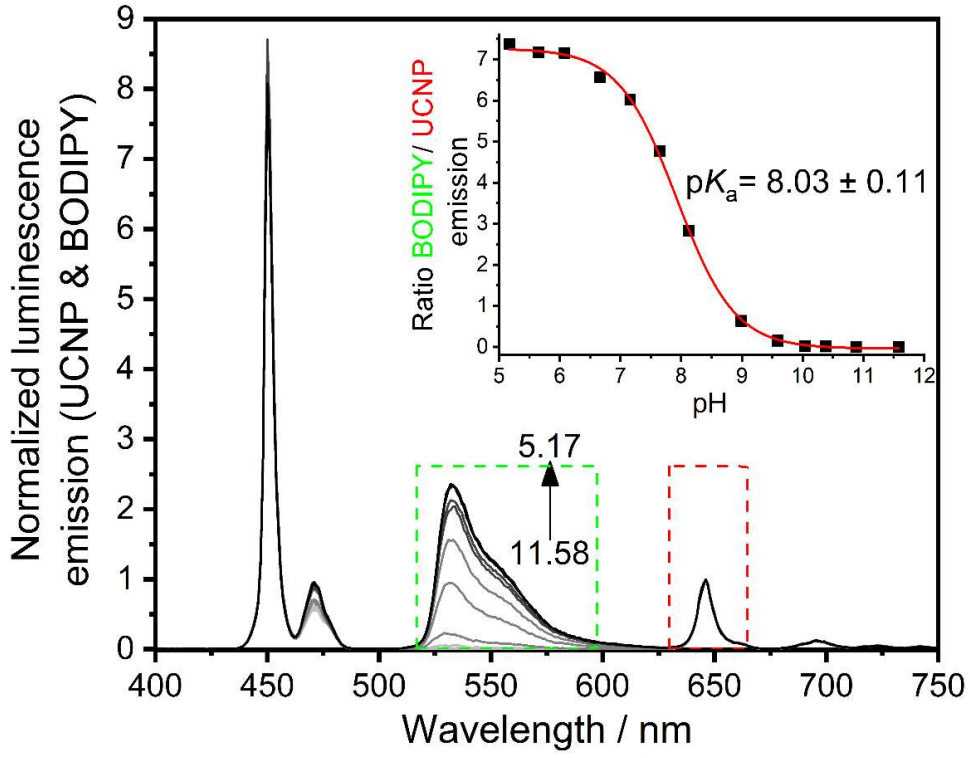

Figure S2. Normalized (red Tm^{3+} emission) luminescence emission of a pH sensor systems consisting of 3 mg/ml citrate-capped Yb^{3+},Er^{3+}-codoped UCNPs and BODIPY **3** ($5x10^{-6}$ M) in buffered mixture of methanol and water (2/1 vol%, 25 mM) in dependence of pH upon excitation with 980 nm. The inset shows the ratio of the integrated luminescence intensities of the green BODIPY fluorescence and the red UC emission of the UCNPs and the corresponding sigmoidal fit of the curve. The presented pK_a value presents an average value derived from three independent measurements.

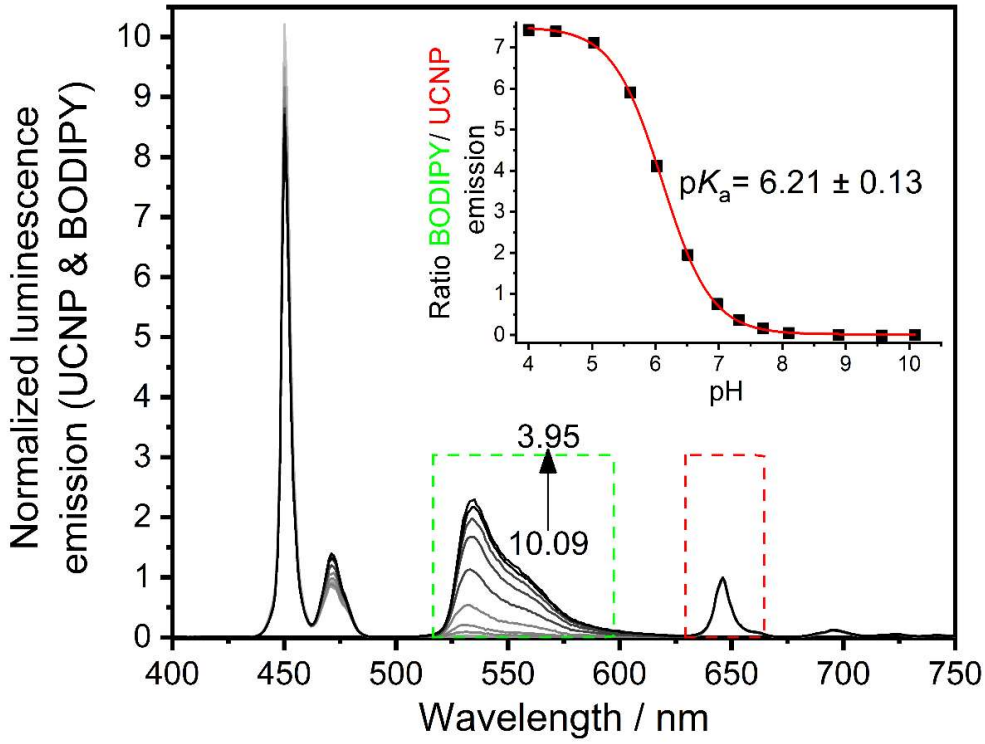

Figure S3. Normalized (red Tm^{3+} emission) luminescence emission of a pH sensor systems consisting of 3 mg/ml citrate-capped Yb^{3+},Er^{3+}-codoped UCNPs and BODIPY **4** ($5x10^{-6}$ M) in buffered mixture of methanol and water (2/1 vol%, 25 mM) in dependence of pH upon excitation with 980 nm. The inset shows the ratio of the integrated luminescence intensities of the green BODIPY fluorescence and the red UC emission of the UCNPs and the corresponding sigmoidal curve fit. The given pKa value is an averaged value derived from three independent measurements.

Table S2. Equation used for the sigmoidal curve fitting of pH titration experiments.

Model	Equation
Dose response	$y = A1 + \frac{A2 - A1}{1 + 10^{(LOGx_0 - x)p}}$

Table S3. Sigmoidal fitting parameters[a] of the ratios calculated from the integrated luminescence emissions of the BODIPYs and UCNPs (red emission) from pH titration in solution.

pH sensor	A1	A2	$LOGx_0$	P	R
UCNP+1	0.012 ± 0.054	4.102 ± 0.044	8.65 ± 0.04	-1.009 ± 0.076	0.9986
UCNP+2	0.011 ± 0.038	5.230 ± 0.045	6.75 ± 0.02	-1.092 ± 0.046	0.9989
UCNP+3	0.004 ± 0.051	7.265 ± 0.064	7.92 ± 0.02	-0.908 ± 0.043	0.9990
UCNP+4	0.013 ± 0.016	7.497 ± 0.025	6.10 ± 0.01	-1.118 ± 0.016	0.9998

[a] fitting parameters for fits shown in the insets of Fig. 3, S2, S3, and S4.

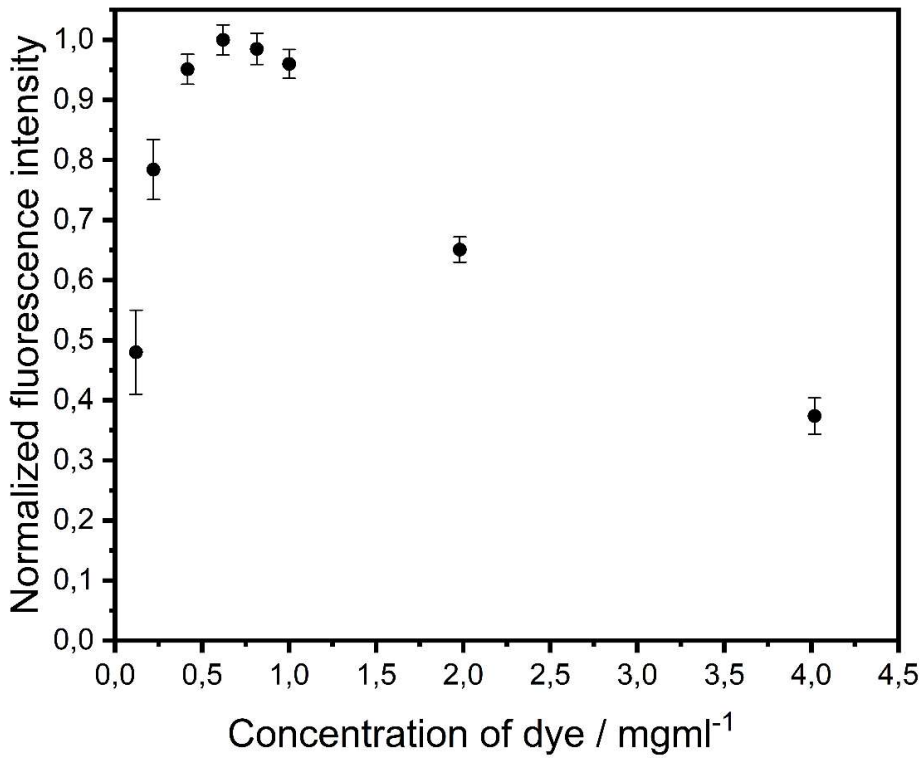

Figure S4. Normalized fluorescence signal of the BODIPY dye in dependence of the concentration of the dye embedded in the D4 polymere matrix.

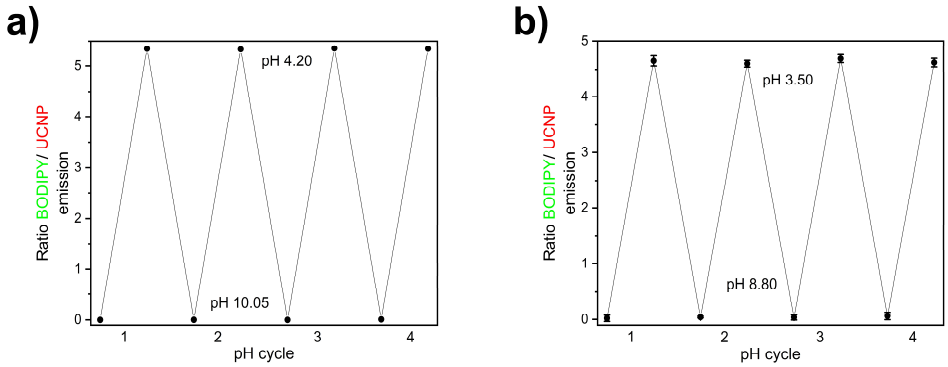

Figure S5. a) pH-dependent ratio of the integrated luminescence intensities of the green BODIPY **2** fluorescence and the red UC emission of the UCNPs in a buffered mixture of methanol and water (2/1 vol%, 25 mM) upon excitation at 980 nm showing a high reversibility of the pH-dependent ON/OFF-switching of the dyes fluorescence. b) pH-dependent ratio of the integrated luminescence intensities of the green BODIPY **2** fluorescence and the red UC emission of the UCNPs immobilized in D4 hydrogel upon excitation at 980 nm showing a high reversibility of the pH-dependent ON/OFF-switching of the dyes fluorescence.

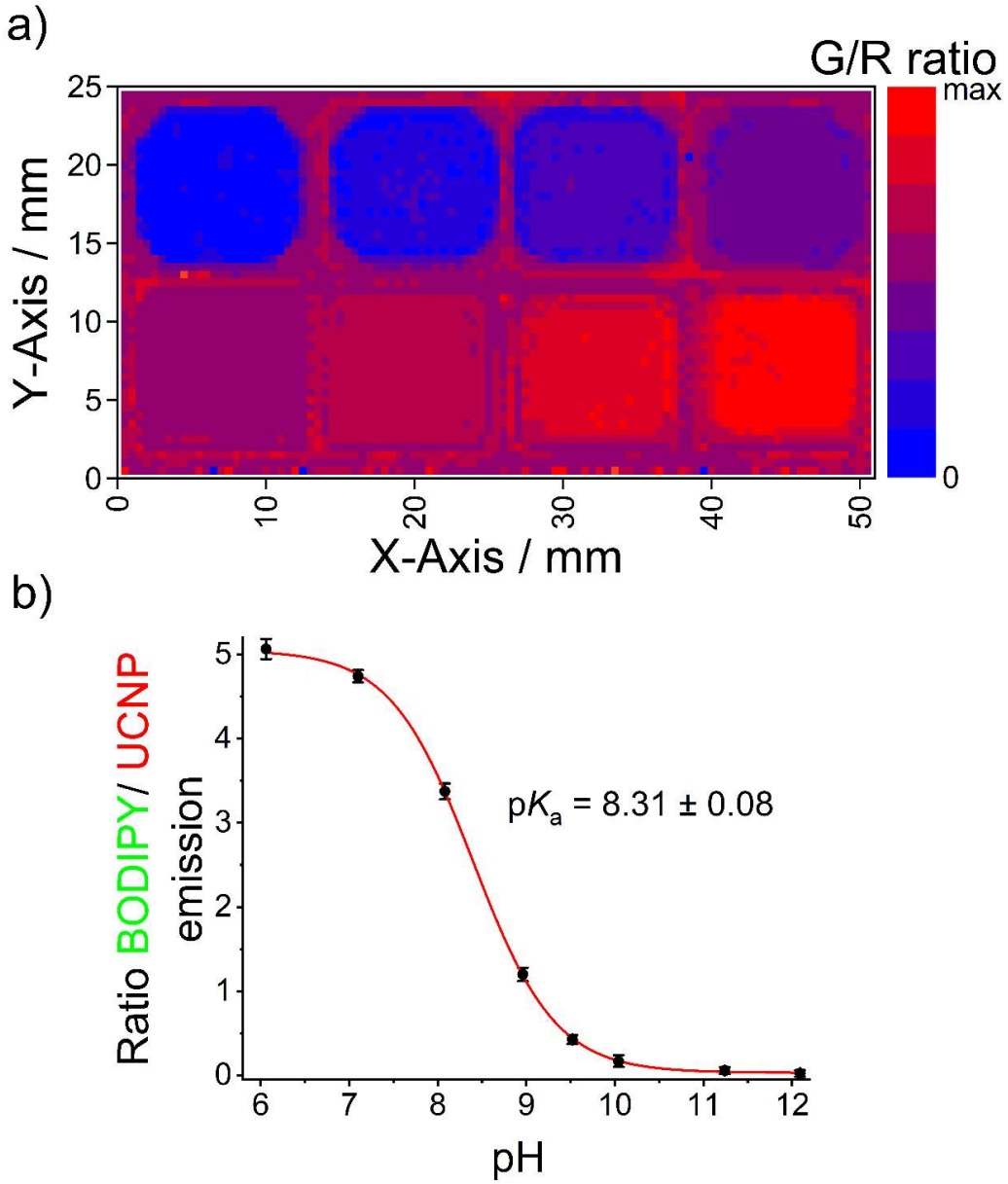

Figure S6. a) Calculated luminescence intensity ratios of BODIPY's **1** fluorescence and the red UCL of the UCNPs. Each pixel represents a separately measured spectrum. Color-coding is done in a non-equidistant scaling. b) G/R-ratio in dependence of pH and the corresponding sigmoidal fit of the curve.

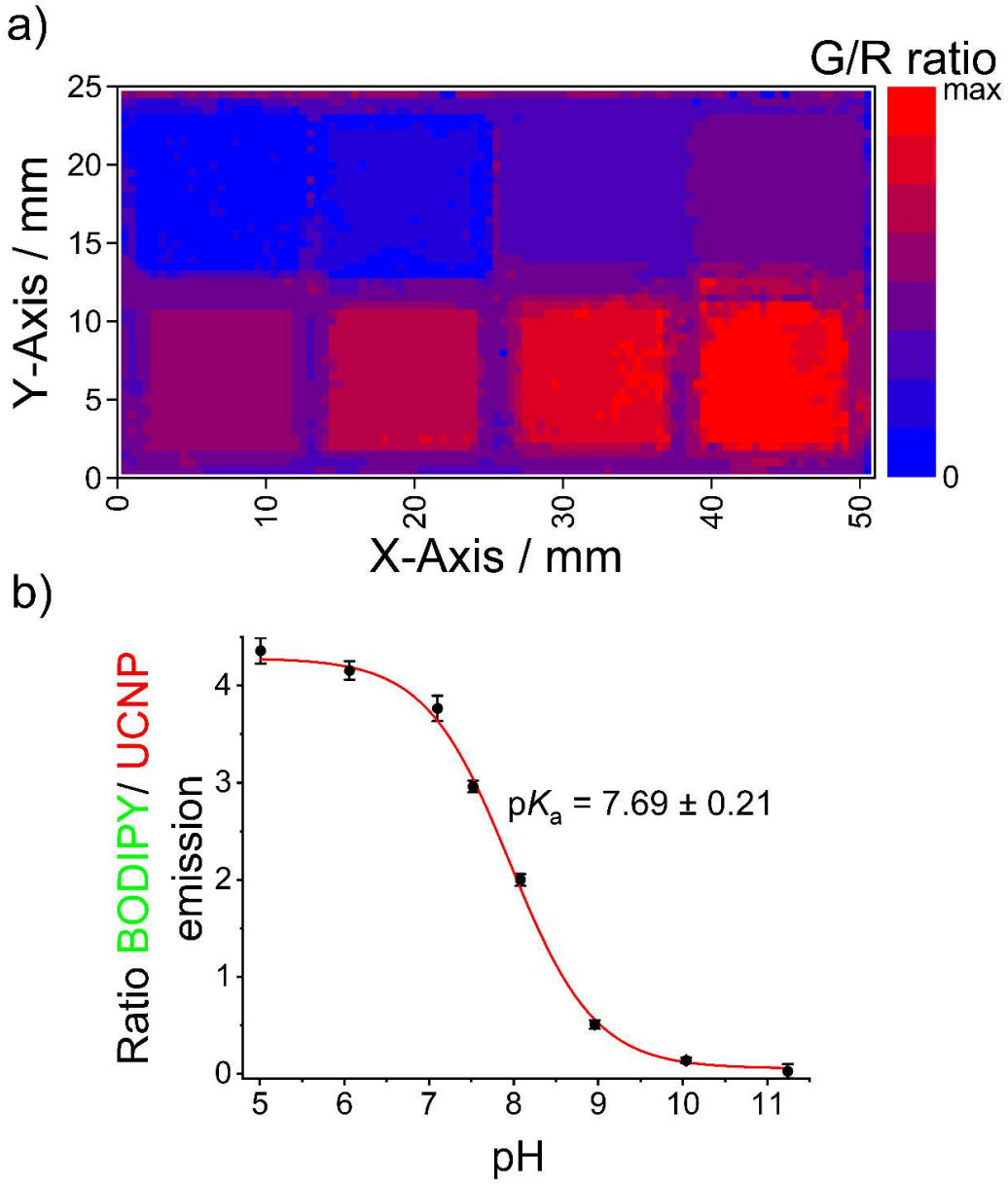

Figure S7. a) Calculated luminescence intensity ratios of BODIPY's **3** fluorescence and the red UCL of the UCNPs. Each pixel represents a separately measured spectrum. Color-coding is done in a non-equidistant scaling. b) G/R-ratio in dependence of pH and the corresponding sigmoidal fit of the curve.

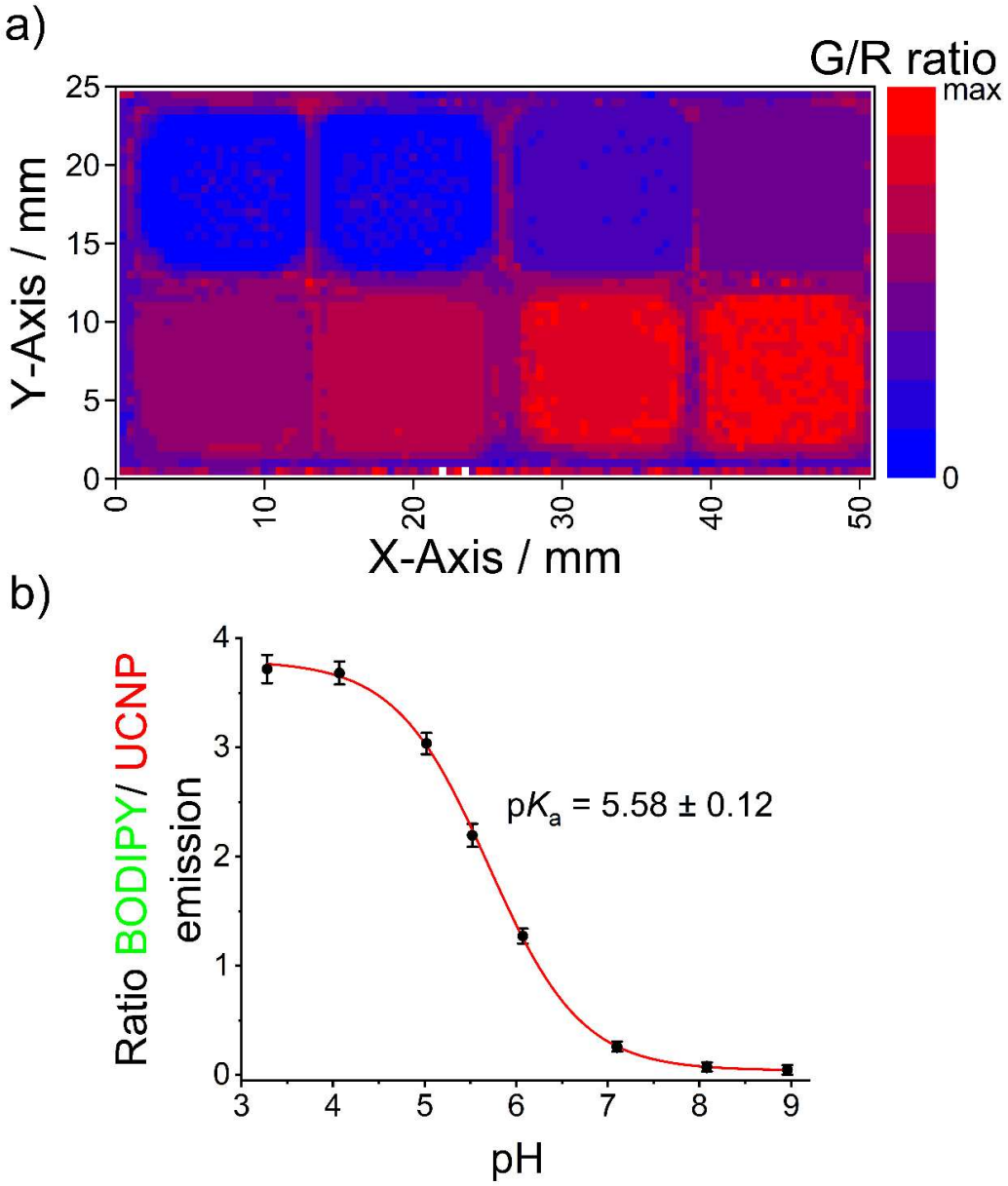

Figure S8. a) Calculated luminescence intensity ratios of BODIPY's **4** fluorescence and the red UCL of the UCNPs. Each pixel represents a separately measured spectrum. Color-coding is in a non-equidistant scaling. b) G/R-ratio in dependence of pH and the corresponding sigmoidal fit of the curve.

Table S4. Sigmoidal fitting parameters[a] of the ratios calculated from the integrated luminescence emissions of the BODIPYs and UCNPs (red emission) from pH titration in D4.

pH sensor	A1	A2	LOGx$_0$	P	R
UCNP+1	0.031 ± 0.010	5.054 ± 0.034	8.39 ± 0.01	-0.934 ± 0.076	0.9998
UCNP+2	0.023 ± 0.013	4.611 ± 0.050	5.94 ± 0.03	-0.889 ± 0.038	0.9995
UCNP+3	0.055 ± 0.045	4.285 ± 0.113	7.85 ± 0.04	-0.867 ± 0.063	0.9974
UCNP+4	0.041 ± 0.011	3.796 ± 0.036	5.68 ± 0.02	-0.858 ± 0.024	0.9997

[a] fitting parameters for fits shown in Fig. 4 b), S6 b), S7 b), and S8 b).

3 Conclusions and Outlook

The aim of the work is the design of a platform for optical sensing of biologically relevant analytes utilizing BODIPY dyes as versatile sensor molecules in combination with UCNPs acting as nanolamps and internal reference. This multi-component-based concept overcomes limitations of optical sensor systems such as intensity-based readouts and spectral limitations by the biological window as it combines NIR-excitable UCNP with analyte-responsive organic chromophores to establish a ratiometric system. The potential of this strategy was first demonstrated for pH, that presents a crucial parameter for material corrosion and is an important biomarker for medical diagnostics, molecular imaging, and cell biology. However, this can be easily expanded to other ionic or neutral analytes by using respective BODIPYs, thereby exploiting the unique versatility of this dye class. Basically, this dye class was not only chosen because of its versatility but also because of its spectral properties which match outstandingly well with $NaYF_4$:Yb^{3+}/Tm^{3+} UCNP. The findings presented in this work and the simple design of this reabsorption-based sensor platform are of considerable interest for the ever increasing number of researchers in the area of sensors for environmental parameters. In subsection 2.1 the facile synthesis and spectroscopic characterization of a set of pH responsive BODIPY-based optical pH sensors with tunable pK_a values is presented. In aqueous-organic mixed media and different sensor matrices, these dyes show an analyte-induced fluorescence enhancement which relies on analyte-mediated PET. By modifying the substitution pattern of the *meso*-aryl substituent of this BODIPY dyes, pK_a values from 6 to 11 were achieved, which enables broad band pH-sensing via fluorescence intensity and lifetime measurements in the pH range of about 5 to 12. The reported dyes are readily available in a two-step reaction in overall yields of up to 20% which was drastically improved to yields >50% in later studies..[12,13,21] As typical for BODIPY dyes, they reveal high ε and remarkable Φ_{Fl} of > 50% to up to 90% in methanol (MeOH). The obtained values for Φ_{Fl} already indicated a dependency of structural parameter with respect to their *meso*-aryl substitution pattern (see subsection 2.2). However, there are no significant shifts in absorption and emission as *meso*-subunit and chromophore core as electronically decoupled. This is advantageous and especially favorable for the desired application as a component of the optical sensing platform as it enables the access to multiple sensing systems, e.g., with different pK_a values, by simply replacing the dyes without affecting the functionality of the sensing platform as the spectral match of dye and used UCNP remain untouched. Although the hydrophobicity of these dyes is a disadvantage for sensing of pH in aqueous media, it is extremely beneficial for incorporation these dyes into polymeric hydrogel matrices as this prevents dye leakage,

which is observed for water soluble indicator dyes.[255] In addition to their general application potential as active components in pH sensors, with all sensor molecules providing a fast and fully reversible pH response strong enough for naked eye detection, several pH-sensitive BODIPYs can be combined yielding a broad range pH sensor with a single excitation wavelength. Furthermore, these dyes present interesting examples for BODIPYs with pK_a values in the neutral and near neutral range, which is particularly interesting for pH measurements in biological samples in the physiological range. As BODIPYs are highly versatile, these dyes can be easily post-functionalized, i.e., to introduce reactive groups for covalent coupling to biomolecules or hydrophilic substituents to render them more water soluble.

In subsection 2.2 the influence of different substitution patterns of the meso-aryl subunit at the BODIPY core on their optical properties and photophysics were studied in detail with respect to their temperature- and structural-dependency. Therefore, single-crystal X-ray diffraction analysis of the compounds were performed, which allowed a structural classification of the dyes into two groups, a sterically hindered and a non-hindered group. It was found, that the steric hindrance refers to a blocked rotational motion of the *meso*-aryl subunit around the bond connecting this moiety to the meso-position of the BODIPY core. These findings were supported by DFT calculations. As is evident from the relatively low calculated rotational barriers of around 17 kcal/mol, a free rotation in a defined motion is possible at room temperature for sterically non-hindered compounds. Rotational barriers of more than 40 kcal/mol determined for the sterically hindered compounds suggest an effective freezing of the rotational motion in these molecules. With the aid of temperature-dependent spectroscopic measurements it was shown, that the ability to rotate directly affects the optical properties of our set of BODIPY dyes. This accounts for the strong temperature dependence of the fluorescence of the sterically non-hindered compounds which shows a drastic decrease of Φ_{Fl} and a significant shortening of τ_{Fl} upon heating. The optical properties of the sterically hindered compounds, however, are barely affected by temperature. The rate constants for radiative and non-radiative deactivation of the S_1 state as well as activation energies for non-radiative decay of the S_1 state were derived from the obtained data. All findings suggest a non-radiative deactivation of the S_1 state of the sterically non-hindered compounds caused by a conical intersection (CI) of the potential energy surfaces (PESs) of the ground and S_1 state which is accessible by rotation of the *meso*-subunit. These findings are in good agreement with previously reported deactivation mechanisms.[66–68] In addition, these results suggest the presence of a second non-radiative depopulation pathway of the S_1 state which is particularly relevant for the sterically hindered compounds. Although, the results obtained in this study are already known from previous experimental studies, this work systematically covers the influence of temperature and *meso*-substitution patterns on optical properties of BODIPYs with the support of DFT calculations. Accordingly, it offers important hints for the rational design of BODIPYs for further applications, e.g., for the design of efficient BODIPY-based $^1O_2$ generators.

The capability of BODIPY dyes to act as $^1O_2$ generators after a slight modification at the chromophore core, namely the introduction of bromine or iodine, was exploited for the study presented in subsection 2.3. PDT has emerged as a promising therapeutic method for the treatment of a variety of cancers. For PDT, a PS is utilized to generate $^1O_2$ from ground state $^3O_2$ upon illumination with light. Due to the high reactivity of $^1O_2$ and additionally formed ROS massive cellular damage is observed that leads to cell death by apoptopic and/or necrotic processes. Although this damage occurs rather localized by illumination, a better local control of PDT is still desired to keep damage to healthy tissue as low as possible. Just recently, BODIPY dyes gained substantial attention as possible PS for PDT. For increasing the application potential of these dyes for PDT, heavy halogens such as bromine and iodine are often used as substituents as they increase the ISC rate from the S_1 state to the T_1 state of the dyes by enhanced spin-orbit coupling. This leads to a shift of the deactivation pathway from fluorescence to ISC, which is mandatory for $^1O_2$ generation. In the study presented in subsection 2.3 the design concepts of PET-based pH-sensitivity and heavy-atom effect induced ISC mediated $^1O_2$ generation were combined, yielding pH-activatable PSs. This work reports the synthesis and photophysical characterization of these BODIPY dyes with pH-controllable fluorescence and $^1O_2$ generation. Like their parent dyes, these dyes feature an on/off-switchable fluorescence due to a *meso*-substituted phenolic subunit that can efficiently deactivate the S_1 state via a PET in its deprotonated form and that also provides pK_a tunability. This was confirmed by spectroscopic studies of the fluorescence intensity as function of pH, which revealed, that iodination did not change the pH-sensitivity of the dyes as the *meso*-subunit is not affected by substitution at the chromophore core. Additionally, pH-controllable $^1O_2$ generation with remarkable values of the singlet oxygen quantum yield (Φ_Δ) of the dyes in their on-state upon protonation could be demonstrated. These findings support a highly efficient shift of the deactivation pathways of the S_1 state from fluorescence to ISC. The pH-activatable $^1O_2$ generation was exploited for *in vitro* studies using HeLa cell line. Thereby, markedly different cytotoxicities of the pH-activatable compounds upon illumination versus dark conditions were demonstrated, which underline their potential as potent PS. Furthermore, pH control of the optical features, and thereby also the $^1O_2$ production of these compounds, can provide the basis for a pH-dependent cytotoxicity. This was demonstrated *in vitro* for one dye with a pK_a of 6.4, that reveals a inceased ISC, hence on-switched $^1O_2$ formation at lower pH values.

These dyes could potentially be used as component in an optical platform. In this case, however, the analyte-responsivity is not suited for optical imaging but for triggering $^1O_2$ generation in a therapeutic manner. As the optical properties of these dyes are red-shifted compared to their parent dyes, they spectrally mismatch with Tm^{3+}-based UCNP. Alternatively, $NaYF_4$:Yb^{3+}/Er^{3+} UCNP could be used. Same as for their parent dyes, the presented BODIPY-based PS can be easily post-functionalized, i.e., to increase water solubility, to bathochromically shift spectral bands or to targeting ligands, which would be favourable

for their applicability in biological systems.
UCNPs utilize an unique multiphotonic UC process for generating short-wavelength light from long-wavelength excitation, which is already exploited in various applications, e.g. sensing, bioimaging, spectral conversion in solar cells and security printing. However, there are still some drawbacks with respect to particle quality like low upconversion luminescence quantum yield (Φ_{UC}) and reproducibility of the synthesis like different sizes and size distributions. In situ luminescence monitoring of the synthesis of UCNP could present a very useful tool for simple online quality control and minimization of energy consuming heating steps and periods. This could be developed into a routine method to improve the batch-to-batch reproducibility and it could also be used as parameter for the automation of the synthesis of UCNPs. Considering of the utilization of UCNPs as a component in a platform for optical sensing, a good synthetic reproducibility with respect to the size and quality of the particles is advantageous as size and optical properties are key parameters for UCNPs. Subsequently, the work presented in subsection 2.4 establishes a correlation between the easily online accessible optical properties and the structural properties of UCNP during their synthesis. The findings suggest a particle growth mechanism which is in good agreement with the previously proposed mechanism for the growth of β-phase $NaYF_4$:Yb^{3+}/Er^{3+} UCNPs. This mechanism includes the initial formation of very small α-phase $NaYF_4$:Yb^{3+}/Er^{3+} UCNPs, followed by the formation of β-phase particles by Ostwald ripening. The actual particle growth was monitored in detail by *in situ* UCL monitoring and *ex situ* time-resolved UCL measurements. Furthermore, offline SAXS and TEM measurements were carried out. The data obtained from SAXS and TEM for the particle sizes during the synthesis are in exceptionally good agreement with each other. Additionally, they confirm a good correlation with optical parameters such as the UC intensity and the UCL decay kinetics. By performing the UCNP syntheses at different temperatures, the importance of this parameter for the reaction kinetic was demonstrated. Although the reaction temperature controls the onset of the actual UCNP growth, the growth mechanism does not appear to be affected. These findings are of considerable significance for the ever increasing number of researchers in the area of UC nanotechnology. This could help to render UCNP synthesis less energy consuming, simplify reproducible UCNP production, and ease the automation of the UCNP synthesis.
In the study presented in subsection 2.5, the application potential of UCNPs in combination with pH-sensitive BODIPY dyes was evaluated by the rational design of a two-component sensing platform with a ratiometric optical output. Therefore, the advantage of UCNPs to generate background free, sharp and defined luminescence signals upon excitation with 980 nm light was fully exploited. The blue emission band of $NaYF_4$:Yb^{3+}/Tm^{3+} UCNPs was used for the excitation of a analyte-responsive BODIPY dye. While the dye's fluorescence intensity is dependent on the pH, the red UCL of the Tm^{3+}-based UCNPs was used as inert reference signal. By immobilizing both components in a hydrogel, pH-sensitve films were obtained, which were subsequently used to study the time-dependent changes of pH of

bacterial suspensions of *E. coli*. These monitored pH changes are caused by *E. coli* due to mixed acid fermentation of *D*-glucose into lactate, acetate, succinate, formate, ethanol, and hydrogen. In summary, the design of a new, simple, and modular platform for optical sensing was successfully established. The rational choice of the components used for the sensing platform, their syntheses and performance were studied in detail. The modular approach offers a huge potential as different designs are feasible, e.g., pH-sensors with different pK_a values in strip-format are readily accessible which in combination with handheld fluorometers and optical fibers are ideal for field use determination of pH. This could be exploited, e.g., to study microbiologically influenced corrosion processes on inner surfaces of biofuel storage tanks or other biotechnologically processes accompanied by changes in pH.

4 Reference

(1) Johnson-McDaniel, D.; Barrett, C. A.; Sharafi, A.; Salguero, T. T. *Journal of the American Chemical Society* **2013**, *135*, 1677–1679 (cit. on p. 1).

(2) Splitstoser, J. C.; Dillehay, T. D.; Wouters, J.; Claro, A. *Science Advances* **2016**, *2*, e1501623 (cit. on p. 1).

(3) De Moliner, F.; Kielland, N.; Lavilla, R.; Vendrell, M. *Angewandte Chemie International Edition* **2017**, *56*, 3758–3769 (cit. on p. 2).

(4) Lovell, J. F.; Liu, T. W. B.; Chen, J.; Zheng, G. *Chemical Reviews* **2010**, *110*, 2839–2857 (cit. on p. 2).

(5) Tang, Q.; Xiao, W.; Huang, C.; Si, W.; Shao, J.; Huang, W.; Chen, P.; Zhang, Q.; Dong, X. *Chemistry of Materials* **2017**, *29*, 5216–5224 (cit. on p. 2).

(6) Kreuzer, A. T. F.-H. *Justus Liebigs Annalen der Chemie* **1968**, *718*, 208–223 (cit. on p. 2).

(7) Entwistle, A.; Noble, M. *Journal of Microscopy* **1992**, *168*, 219–238 (cit. on p. 2).

(8) Ziessel, R.; Ulrich, G.; Harriman, A. *New Journal of Chemistry* **2007**, *31*, 496–501 (cit. on pp. 2, 3, 5).

(9) Ulrich, G.; Ziessel, R.; Harriman, A. *Angew. Chem., Int. Ed.* **2008**, *47*, 1184–1201 (cit. on pp. 2, 3, 5).

(10) Loudet, A.; Burgess, K. *Chem. Rev.* **2007**, *107*, 4891–4932 (cit. on pp. 2, 3).

(11) Bañuelos, J. *The Chemical Record* **2016**, *16*, 335–348 (cit. on pp. 2, 5–7).

(12) Radunz, S.; Tschiche, H. R.; Moldenhauer, D.; Resch-Genger, U. *Sensors and Actuators B: Chemical* **2017**, *251*, 490 –494 (cit. on pp. 3, 4, 8, 23, 147).

(13) Radunz, S.; Wedepohl, S.; Röhr, M.; Calderón, M.; Tschiche, H. R.; Resch-Genger, U. *Journal of Medicinal Chemistry* **2020**, *63*, 1699–1708 (cit. on pp. 3, 10, 85, 147).

(14) Lee, C.-H.; S. Lindsey, J. *Tetrahedron* **1994**, *50*, 11427–11440 (cit. on p. 3).

(15) Littler, B. J.; Miller, M. A.; Hung, C.-H.; Wagner, R. W.; O'Shea, D. F.; Boyle, P. D.; Lindsey, J. S. *The Journal of Organic Chemistry* **1999**, *64*, 1391–1396 (cit. on p. 3).

(16) Clarke, R. G.; Hall, M. J. In *Advances in Heterocyclic Chemistry*, Scriven, E. F. V., Ramsden, C. A., Eds.; Academic Press: 2019, pp 181–261 (cit. on p. 3).

(17) Pereira, N. A. M.; Pinho e Melo, T. M. V. D. *Organic Preparations and Procedures International* **2014**, *46*, 183–213 (cit. on p. 3).

(18) Nascimento, B. F. O.; Lopes, S. M. M.; Pineiro, M.; Pinho e Melo, T. M. V. D. *Molecules* **2019**, *24*, 4348 (cit. on p. 3).

(19) Bartelmess, J.; Weare, W. W.; Latortue, N.; Duong, C.; Jones, D. S. *New Journal of Chemistry* **2013**, *37*, 2663–2668 (cit. on pp. 3, 4).

(20) Lindsey, J. S.; Wagner, R. W. *The Journal of Organic Chemistry* **1989**, *54*, 828–836 (cit. on p. 4).

(21) Radunz, S.; Andresen, E.; Würth, C.; Koerdt, A.; Tschiche, H. R.; Resch-Genger, U. *Analytical Chemistry* **2019**, *91*, 7756–7764 (cit. on pp. 4, 12, 20, 127, 147).

(22) Bessette, A.; Hanan, G. S. *Chemical Society Reviews* **2014**, *43*, 3342–3405 (cit. on pp. 4–6).

(23) Boens, N.; Verbelen, B.; Dehaen, W. *European Journal of Organic Chemistry* **2015**, *2015*, 6577–6595 (cit. on pp. 4, 5).

(24) Sola, R.; Bañuelos-Prieto, J. In, 2019 (cit. on pp. 4, 5).

(25) De Rezende, L. C. D.; da Silva Emery, F. *Orbital: Electron. J. Chem. 5*, 62–83 (cit. on p. 4).

(26) Boens, N.; Leen, V.; Dehaen, W. *Chem. Soc. Rev.* **2012**, *41*, 1130–1172 (cit. on pp. 4, 6, 8).

(27) Bertrand, B.; Passador, K.; Goze, C.; Denat, F.; Bodio, E.; Salmain, M. *Coordination Chemistry Reviews* **2018**, *358*, 108–124 (cit. on pp. 4–6, 8).

(28) Kamkaew, A.; Lim, S. H.; Lee, H. B.; Kiew, L. V.; Chung, L. Y.; Burgess, K. *Chemical Society Reviews* **2013**, *42*, 77–88 (cit. on pp. 4, 10).

(29) Banfi, S.; Nasini, G.; Zaza, S.; Caruso, E. *Tetrahedron* **2013**, *69*, 4845–4856 (cit. on p. 4).

(30) Burghart, A.; Kim, H.; Welch, M. B.; Thoresen, L. H.; Reibenspies, J.; Burgess, K.; Bergström, F.; Johansson, L. B. A. *The Journal of Organic Chemistry* **1999**, *64*, 7813–7819 (cit. on p. 4).

(31) Kim, H.; Burghart, A.; B. Welch, M.; Reibenspies, J.; Burgess, K. *Chemical Communications* **1999**, 1889–1890 (cit. on p. 4).

(32) Antina, E. V.; Bumagina, N. A. *Chemistry of Heterocyclic Compounds* **2017**, *53*, 39–41 (cit. on p. 4).

(33) Sirbu, D.; Karlsson, J. K. G.; Harriman, A. *The Journal of Physical Chemistry A* **2018**, *122*, 9160–9170 (cit. on p. 4).

(34) Zhu, S.; Zhang, J.; Vegesna, G.; Tiwari, A.; Luo, F.-T.; Zeller, M.; Luck, R.; Li, H.; Green, S.; Liu, H. *RSC Advances* **2012**, *2*, 404–407 (cit. on p. 4).

(35) Umezawa, K.; Matsui, A.; Nakamura, Y.; Citterio, D.; Suzuki, K. *Chemistry – A European Journal* **2009**, *15*, 1096–1106 (cit. on p. 4).

(36) Durán-Sampedro, G.; Agarrabeitia, A. R.; Cerdán, L.; Pérez-Ojeda, M. E.; Costela, A.; García-Moreno, I.; Esnal, I.; Bañuelos, J.; Arbeloa, I. L.; Ortiz, M. J. *Advanced Functional Materials* **2013**, *23*, 4195–4205 (cit. on p. 6).

(37) Duran-Sampedro, G.; Esnal, I.; Agarrabeitia, A. R.; Bañuelos-Prieto, J.; Cerdán, L.; García-Moreno, I.; Costela, A.; Lopez-Arbeloa, I.; Ortiz, M. J. *Chemistry – A European Journal* **2014**, *20*, 2646–2653 (cit. on p. 6).

(38) Esnal, I.; Valois-Escamilla, I.; Gomez-Duran, C. F. A.; Urias-Benavides, A.; Betancourt-Mendiola, M. L.; Lopez-Arbeloa, I.; Banuelos, J.; Garcia-Moreno, I.; Costela, A.; Pena-Cabrera, E. *ChemPhysChem* **2013**, *14*, 4134–4142 (cit. on p. 6).

(39) Ortiz, M. J.; Garcia-Moreno, I.; Agarrabeitia, A. R.; Duran-Sampedro, G.; Costela, A.; Sastre, R.; López Arbeloa, F.; Bañuelos Prieto, J.; López Arbeloa, I. *Physical Chemistry Chemical Physics* **2010**, *12*, 7804–7811 (cit. on p. 6).

(40) McDonagh, C.; Burke, C. S.; MacCraith, B. D. *Chem. Rev.* **2008**, *108*, 400–422 (cit. on pp. 6, 8).

(41) Kolemen, S.; Akkaya, E. U. *Coordination Chemistry Reviews* **2018**, *354*, 121–134 (cit. on pp. 6, 8).

(42) Hendricks, J. A.; Keliher, E. J.; Wan, D.; Hilderbrand, S. A.; Weissleder, R.; Mazitschek, R. *Angewandte Chemie International Edition* **2012**, *51*, 4603–4606 (cit. on p. 6).

(43) Ceulemans, M.; Nuyts, K.; De Borggraeve, W. M.; Parac-Vogt, T. N. *Inorganics* **2015**, *3*, 516–533 (cit. on p. 6).

(44) Huynh, A. M.; Müller, A.; Kessler, S. M.; Henrikus, S.; Hoffmann, C.; Kiemer, A. K.; Bücker, A.; Jung, G. *ChemMedChem* **2016**, *11*, 1568–1575 (cit. on p. 6).

(45) Yuriy, S. M.; Alexey, V. S.; Alexander, S. T.; Evgeniy, V. R. *Current Medicinal Chemistry* **2017**, *24*, 2745–2772 (cit. on p. 6).

(46) Liu, J.-Y.; Huang, Y.; Menting, R.; Röder, B.; Ermilov, E. A.; Ng, D. K. P. *Chemical Communications* **2013**, *49*, 2998–3000 (cit. on p. 7).

(47) Duran-Sampedro, G.; Agarrabeitia, A. R.; Garcia-Moreno, I.; Gartzia-Rivero, L.; de la Moya, S.; Bañuelos, J.; López-Arbeloa, I.; Ortiz, M. J. *Chemical Communications* **2015**, *51*, 11382–11385 (cit. on p. 7).

(48) Ziessel, R.; Harriman, A. *Chemical Communications* **2011**, *47*, 611–631 (cit. on p. 7).

(49) Cihaner, A.; Algı, F. *Reactive and Functional Polymers* **2009**, *69*, 62–67 (cit. on p. 7).

(50) Burghart, A.; Thoresen, L. H.; Chen, J.; Burgess, K.; Bergström, F.; Johansson, L. B. A. *Chemical Communications* **2000**, 2203–2204 (cit. on p. 7).

(51) Meng, L.-B.; Li, D.; Xiong, S.; Hu, X.-Y.; Wang, L.; Li, G. *Chemical Communications* **2015**, *51*, 4643–4646 (cit. on p. 7).

(52) Cammann, K; Guibault, E.; Hall, H; Kellner, R; Wolfbeis, O. *Proceedings of the Cambridge workshop on chemical sensors and biosensors. Cambridge University Press, New York* (cit. on p. 8).

(53) Zhang, X.; Chi, R.; Zou, J.; Zhang, H.-S. *Spectrochimica Acta Part A: Molecular and Biomolecular Spectroscopy* **2004**, *60*, 3129–3134 (cit. on pp. 8, 9).

(54) Peng, X.; Du, J.; Fan, J.; Wang, J.; Wu, Y.; Zhao, J.; Sun, S.; Xu, T. *Journal of the American Chemical Society* **2007**, *129*, 1500–1501 (cit. on pp. 8, 9).

(55) Blakemore, J. D.; Chitta, R.; D'Souza, F. *Tetrahedron Letters* **2007**, *48*, 1977–1982 (cit. on pp. 8, 9).

(56) Choi, S. H.; Pang, K.; Kim, K.; Churchill, D. G. *Inorganic Chemistry* **2007**, *46*, 10564–10577 (cit. on pp. 8, 9).

(57) Domaille, D. W.; Zeng, L.; Chang, C. J. *Journal of the American Chemical Society* **2010**, *132*, 1194–1195 (cit. on pp. 8, 9).

(58) Lu, H.; Xue, Z.; Mack, J.; Shen, Z.; You, X.; Kobayashi, N. *Chemical Communications* **2010**, *46*, 3565–3567 (cit. on pp. 8, 9).

(59) Wang, D.; Miyamoto, R.; Shiraishi, Y.; Hirai, T. *Langmuir* **2009**, *25*, 13176–13182 (cit. on p. 8).

(60) Ogle, M. M.; Smith McWilliams, A. D.; Ware, M. J.; Curley, S. A.; Corr, S. J.; Martí, A. A. *The Journal of Physical Chemistry B* **2019**, *123*, 7282–7289 (cit. on p. 8).

(61) Li, X.; Qian, S.; He, Q.; Yang, B.; Li, J.; Hu, Y. *Organic & Biomolecular Chemistry* **2010**, *8*, 3627–3630 (cit. on pp. 8, 9).

(62) Sutter, A.; Elhabiri, M.; Ulrich, G. *Chemistry – A European Journal* **2018**, *24*, 11119–11130 (cit. on pp. 8, 9).

(63) Levitt, J. A.; Kuimova, M. K.; Yahioglu, G.; Chung, P.-H.; Suhling, K.; Phillips, D. *The Journal of Physical Chemistry C* **2009**, *113*, 11634–11642 (cit. on p. 8).

(64) Kuimova, M. K.; Yahioglu, G.; Levitt, J. A.; Suhling, K. *Journal of the American Chemical Society* **2008**, *130*, 6672–6673 (cit. on p. 8).

(65) Alamiry, M. A. H.; Benniston, A. C.; Copley, G.; Elliott, K. J.; Harriman, A.; Stewart, B.; Zhi, Y.-G. *Chemistry of Materials* **2008**, *20*, 4024–4032 (cit. on p. 8).

(66) Kee, H. L. et al. *The Journal of Physical Chemistry B* **2005**, *109*, 20433–20443 (cit. on pp. 8, 148).

(67) Prlj, A.; Vannay, L.; Corminboeuf, C. *Helvetica Chimica Acta* **2017**, *100*, e1700093 (cit. on pp. 8, 148).

(68) Lou, Z.; Hou, Y.; Chen, K.; Zhao, J.; Ji, S.; Zhong, F.; Dede, Y.; Dick, B. *The Journal of Physical Chemistry C* **2018**, *122*, 185–193 (cit. on pp. 8, 148).

(69) Lee, J.-S.; Kang, N.-y.; Kim, Y. K.; Samanta, A.; Feng, S.; Kim, H. K.; Vendrell, M.; Park, J. H.; Chang, Y.-T. *Journal of the American Chemical Society* **2009**, *131*, 10077–10082 (cit. on p. 9).

(70) Ali, F.; Aute, S.; Sreedharan, S.; Anila, H. A.; Saeed, H. K.; Smythe, C. G.; Thomas, J. A.; Das, A. *Chemical Communications* **2018**, *54*, 1849–1852 (cit. on p. 9).

(71) Yuan, S. et al. *Analytical Chemistry* **2018**, *90*, 3914–3919 (cit. on p. 9).

(72) Wang, J.; Hou, Y.; Li, C.; Zhang, B.; Wang, X. *Sens. Actuators, B* **2011**, *157*, 586–593 (cit. on p. 9).

(73) Wencel, D.; Abel, T.; McDonagh, C. *Analytical Chemistry* **2014**, *86*, 15–29 (cit. on p. 9).

(74) Werner, T.; Huber, C.; Heinl, S.; Kollmannsberger, M.; Daub, J.; Wolfbeis, S. O. *Fresenius' J. Anal. Chem.* **1997**, *359*, 150–154 (cit. on p. 9).

(75) Aigner, D.; Freunberger, S. A.; Wilkening, M.; Saf, R.; Borisov, S. M.; Klimant, I. *Anal. Chem.* **2014**, *86*, 9293–9300 (cit. on p. 9).

(76) Maus, M.; Rurack, K. *New Journal of Chemistry* **2000**, *24*, 677–686 (cit. on p. 9).

(77) Qi, J.; Liu, D.; Liu, X.; Guan, S.; Shi, F.; Chang, H.; He, H.; Yang, G. *Anal. Chem.* **2015**, *87*, 5897–5904 (cit. on p. 9).

(78) Qin, W.; Baruah, M.; De Borggraeve, W. M.; Boens, N. *J. Photochem. Photobiol., A* **2006**, *183*, 190–197 (cit. on p. 9).

(79) Qin, W.; Baruah, M.; Stefan, A.; Van der Auweraer, M.; Boens, N. *ChemPhysChem* **2005**, *6*, 2343–2351 (cit. on p. 9).

(80) Zhang, J.; Yang, M.; Li, C.; Dorh, N.; Xie, F.; Luo, F.-T.; Tiwari, A.; Liu, H. *J. Mater. Chem. B* **2015**, *3*, 2173–2184 (cit. on p. 9).

(81) Zhang, Y.; Fang, H.; Zhang, X.; Wang, S.; Xing, G. *ChemistrySelect* **2016**, *1*, 1–6 (cit. on p. 9).

(82) Hecht, M.; Kraus, W.; Rurack, K. *Analyst* **2013**, *138*, 325–332 (cit. on p. 9).

(83) Strobl, M.; Rappitsch, T.; Borisov, S. M.; Mayr, T.; Klimant, I. *Analyst* **2015**, *140*, 7150–7153 (cit. on p. 9).

(84) Hoogendoorn, S.; Blom, A. E. M.; Willems, L. I.; van der Marel, G. A.; Overkleeft, H. S. *Org. Lett.* **2011**, *13*, 5656–5659 (cit. on p. 9).

(85) Madhu, S.; Rao, M. R.; Shaikh, M. S.; Ravikanth, M. *Inorganic Chemistry* **2011**, *50*, 4392–4400 (cit. on p. 9).

(86) Gotor, R.; Ashokkumar, P.; Hecht, M.; Keil, K.; Rurack, K. *Analytical Chemistry* **2017**, *89*, 8437–8444 (cit. on p. 9).

(87) Boens, N.; Qin, W.; Baruah, M.; De Borggraeve, W. M.; Filarowski, A.; Smisdom, N.; Ameloot, M.; Crovetto, L.; Talavera, E. M.; Alvarez-Pez, J. M. *Chem. - Eur. J.* **2011**, *17*, 10924–10934 (cit. on p. 9).

(88) Baki, C. N.; Akkaya, E. U. *J. Org. Chem.* **2001**, *66*, 1512–1513 (cit. on p. 9).

(89) Baruah, M.; Qin, W.; Basarić, N.; De Borggraeve, W. M.; Boens, N. *J. Org. Chem.* **2005**, *70*, 4152–4157 (cit. on p. 9).

(90) Wang, R.; Yu, C.; Yu, F.; Chen, L.; Yu, C. *Trends Anal. Chem.* **2010**, *29*, 1004–1013 (cit. on p. 9).

(91) Han, J.; Burgess, K. *Chem. Rev.* **2010**, *110*, 2709–2728 (cit. on p. 9).

(92) Chen, S.; Zhao, M.; Su, J.; Zhang, Q.; Tian, X.; Li, S.; Zhou, H.; Wu, J.; Tian, Y. *Dyes Pigm.* **2017**, *136*, 807–816 (cit. on p. 9).

(93) Cakmak, Y. et al. *Angewandte Chemie International Edition* **2011**, *50*, 11937–11941 (cit. on pp. 9, 10).

(94) Awuah, S. G.; Polreis, J.; Biradar, V.; You, Y. *Organic Letters* **2011**, *13*, 3884–3887 (cit. on pp. 9, 10).

(95) Zou, J.; Yin, Z.; Ding, K.; Tang, Q.; Li, J.; Si, W.; Shao, J.; Zhang, Q.; Huang, W.; Dong, X. *ACS Applied Materials & Interfaces* **2017**, *9*, 32475–32481 (cit. on pp. 9, 10).

(96) Lincoln, R.; Durantini, A. M.; Greene, L. E.; Martínez, S. R.; Knox, R.; Becerra, M. C.; Cosa, G. *Photochemical & Photobiological Sciences* **2017**, *16*, 178–184 (cit. on pp. 9, 10).

(97) Van Straten, D.; Mashayekhi, V.; De Bruijn, S. H.; Oliveira, S.; Robinson, J. D. *Cancers* **2017**, *9*, DOI: 10.3390/cancers9020019 (cit. on p. 9).

(98) You, Y. *Organic & Biomolecular Chemistry* **2018**, *16*, 4044–4060 (cit. on p. 9).

(99) Almeida-Marrero, V.; van de Winckel, E.; Anaya-Plaza, E.; Torres, T.; de la Escosura, A. *Chemical Society Reviews* **2018**, *47*, 7369–7400 (cit. on p. 9).

(100) DeRosa, M. C.; Crutchley, R. J. *Coordination Chemistry Reviews* **2002**, *233-234*, 351–371 (cit. on p. 9).

(101) Yogo, T.; Urano, Y.; Ishitsuka, Y.; Maniwa, F.; Nagano, T. *Journal of the American Chemical Society* **2005**, *127*, 12162–12163 (cit. on p. 10).

(102) Atilgan, S.; Ekmekci, Z.; Dogan, A. L.; Guc, D.; Akkaya, E. U. *Chemical Communications* **2006**, 4398–4400 (cit. on p. 10).

(103) Gorbe, M.; Costero, A. M.; Sancenón, F.; Martínez-Máñez, R.; Ballesteros-Cillero, R.; Ochando, L. E.; Chulvi, K.; Gotor, R.; Gil, S. *Dyes and Pigments* **2019**, *160*, 198–207 (cit. on p. 10).

(104) Rey, Y. P.; Abradelo, D. G.; Santschi, N.; Strassert, C. A.; Gilmour, R. *European Journal of Organic Chemistry* **2017**, *2017*, 2170–2178 (cit. on p. 10).

(105) Epelde-Elezcano, N.; Martínez, V.; Pena-Cabrera, E.; Gomez Duran, C.; Lopez Arbeloa, I.; Lacombe, S. *RSC Adv.* **2016**, *6*, DOI: 10.1039/C6RA05820E (cit. on p. 10).

(106) Hu, W.; Zhang, X.-F.; Lu, X.; Lan, S.; Tian, D.; Li, T.; Wang, L.; Zhao, S.; Feng, M.; Zhang, J. *Journal of Luminescence* **2017**, *194*, DOI: 10.1016/j.jlumin.2017.10.018 (cit. on p. 10).

(107) Lai, Y.-C.; Su, S.-Y.; Chang, C.-C. *ACS Applied Materials & Interfaces* **2013**, *5*, 12935–12943 (cit. on p. 10).

(108) Agazzi, M. L.; Durantini, J. E.; Gsponer, N. S.; Durantini, A. M.; Bertolotti, S. G.; Durantini, E. N. *ChemPhysChem* **2019**, *20*, 1110–1125 (cit. on p. 10).

(109) Kue, C. S.; Ng, S. Y.; Voon, S. H.; Kamkaew, A.; Chung, L. Y.; Kiew, L. V.; Lee, H. B. *Photochemical & Photobiological Sciences* **2018**, *17*, 1691–1708 (cit. on p. 10).

(110) Turksoy, A.; Yildiz, D.; Akkaya, E. U. *Coordination Chemistry Reviews* **2019**, *379*, 47–64 (cit. on p. 10).

(111) Agazzi, M. L.; Ballatore, M. B.; Durantini, A. M.; Durantini, E. N.; Tomé, A. C. *Journal of Photochemistry and Photobiology C: Photochemistry Reviews* **2019**, *40*, 21–48 (cit. on p. 10).

(112) Durantini, A. M.; Heredia, D. A.; Durantini, J. E.; Durantini, E. N. *European Journal of Medicinal Chemistry* **2018**, *144*, 651–661 (cit. on p. 10).

(113) Ozlem, S.; Akkaya, E. U. *Journal of the American Chemical Society* **2009**, *131*, 48–49 (cit. on p. 10).

(114) Yogo, T.; Urano, Y.; Mizushima, A.; Sunahara, H.; Inoue, T.; Hirose, K.; Iino, M.; Kikuchi, K.; Nagano, T. *Proceedings of the National Academy of Sciences* **2008**, *105*, 28–32 (cit. on p. 10).

(115) Caltagirone, C. et al. *RSC Advances* **2015**, *5*, 23443–23449 (cit. on p. 10).

(116) Luby, B. M.; Walsh, C. D.; Zheng, G. *Angewandte Chemie International Edition* **2019**, *58*, 2558–2569 (cit. on p. 10).

(117) Wong, R. C. H.; Lo, P.-C.; Ng, D. K. P. *Coordination Chemistry Reviews* **2019**, *379*, 30–46 (cit. on p. 10).

(118) Urano, Y. et al. *Nat. Med.* **2009**, *15*, 104–109 (cit. on p. 10).

(119) Zhou, Y.; Wong, R. C. H.; Dai, G.; Ng, D. K. P. *Chemical Communications* **2020**, DOI: 10.1039/C9CC07938F (cit. on p. 10).

(120) Xiong, H.; Zhou, K.; Yan, Y.; Miller, J. B.; Siegwart, D. J. *ACS Applied Materials & Interfaces* **2018**, *10*, 16335–16343 (cit. on p. 10).

(121) Xue, F.; Wei, P.; Ge, X.; Zhong, Y.; Cao, C.; Yu, D.; Yi, T. *Dyes and Pigments* **2018**, *156*, 285–290 (cit. on p. 10).

(122) Topel, S. D.; Cin, G. T.; Akkaya, E. U. *Chemical Communications* **2014**, *50*, 8896–8899 (cit. on p. 10).

(123) Bloembergen, N. *Physical Review Letters* **1959**, *2*, 84–85 (cit. on pp. 10, 11).

(124) Auzel, F. *C. R. Acad. Sci* **1966**, *262*, 1016 (cit. on pp. 10, 11).

(125) Auzel, F. *C. R. Acad. Sci* **1966**, *263*, 819 (cit. on pp. 10, 11).

(126) Wang, F.; Liu, X. *Chemical Society Reviews* **2009**, *38*, 976–989 (cit. on pp. 11–13).

(127) Haase, M.; Schäfer, H. *Angewandte Chemie International Edition* **2011**, *50*, 5808–5829 (cit. on pp. 11, 12).

(128) Wang, M.; Abbineni, G.; Clevenger, A.; Mao, C.; Xu, S. *Nanomedicine* **2011**, *7*, 710–729 (cit. on pp. 11, 12, 14).

(129) Chen, J.; Zhao, J. X. *Sensors* **2012**, *12*, 2414 (cit. on pp. 11, 12, 14).

(130) Gorris, H. H.; Wolfbeis, O. S. *Angewandte Chemie International Edition* **2013**, *52*, 3584–3600 (cit. on pp. 11, 12).

(131) Hao, S.; Chen, G.; Yang, C. *Theranostics* **2013**, *3*, 331–345 (cit. on pp. 11, 12, 19).

(132) Gainer, C. F.; Romanowski, M. *Journal of Innovative Optical Health Sciences* **2013**, *07*, 1330007 (cit. on pp. 11, 12, 14).

(133) Gai, S.; Li, C.; Yang, P.; Lin, J. *Chemical Reviews* **2014**, *114*, 2343–2389 (cit. on pp. 11, 12, 14–17).

(134) Min, Y.; Li, J.; Liu, F.; Padmanabhan, P.; Yeow, E. K. L.; Xing, B. *Nanomaterials* **2014**, *4*, 129–154 (cit. on pp. 11, 12, 18).

(135) Dong, H.; Sun, L.-D.; Yan, C.-H. *Chemical Society Reviews* **2015**, *44*, 1608–1634 (cit. on pp. 11–13).

(136) Liu, X.; Deng, R.; Zhang, Y.; Wang, Y.; Chang, H.; Huang, L.; Liu, X. *Chemical Society Reviews* **2015**, *44*, 1479–1508 (cit. on pp. 11, 12).

(137) Yang, D.; Ma, P.; Hou, Z.; Cheng, Z.; Li, C.; Lin, J. *Chemical Society Reviews* **2015**, *44*, 1416–1448 (cit. on pp. 11, 12).

(138) Zheng, W.; Huang, P.; Tu, D.; Ma, E.; Zhu, H.; Chen, X. *Chemical Society Reviews* **2015**, *44*, 1379–1415 (cit. on pp. 11, 12).

(139) Zhu, X.; Zhang, J.; Liu, J.; Zhang, Y. *Advanced science (Weinheim, Baden-Wurttemberg, Germany)* **2019**, *6*, 1901358–1901358 (cit. on pp. 11, 12, 14).

(140) Andresen, E.; Resch-Genger, U.; Schäferling, M. *Langmuir* **2019**, *35*, 5093–5113 (cit. on pp. 11, 12, 18, 19).

(141) Tessitore, G.; Mandl, G. A.; Brik, M. G.; Park, W.; Capobianco, J. A. *Nanoscale* **2019**, *11*, 12015–12029 (cit. on pp. 11, 12, 14).

(142) Lakowicz, J. R., *Principles of Fluorescence Spectroscopy*, 3rd ed.; Springer US: **2006**, XXVI, 954 (cit. on p. 11).

(143) Valeur, B. In *digital Encyclopedia of Applied Physics*; Wiley-VCH Verlag GmbH & Co. KGaA: 2009, pp 477–531 (cit. on p. 11).

(144) Jacobsen, S. M.; Güdel, H. U. *Journal of Luminescence* **1989**, *43*, 125–137 (cit. on p. 11).

(145) Wenger, O. S.; Güdel, H. U. *Inorganic Chemistry* **2001**, *40*, 5747–5753 (cit. on p. 11).

(146) Wenger, O. S.; Güdel, H. U. *Inorganic Chemistry* **2001**, *40*, 157–164 (cit. on p. 11).

(147) Wenger, O. S.; Valiente, R.; Güdel, H. U. *Physical Review B* **2001**, *64*, 235116 (cit. on p. 11).

(148) Wenger, O. S.; Valiente, R.; Güdel, H. U. *High Pressure Research* **2002**, *22*, 57–62 (cit. on p. 11).

(149) Gamelin, D. R.; Güdel, H. U. *Journal of the American Chemical Society* **1998**, *120*, 12143–12144 (cit. on p. 11).

(150) Gamelin, D. R.; Güdel, H. U. *The Journal of Physical Chemistry B* **2000**, *104*, 10222–10234 (cit. on p. 11).

(151) Gamelin, D. R.; Güdel, H. U. *Inorganic Chemistry* **1999**, *38*, 5154–5164 (cit. on p. 11).

(152) Wermuth, M.; Güdel, H. U. *Chemical Physics Letters* **1997**, *281*, 81–85 (cit. on p. 11).

(153) Wermuth, M.; Güdel, H. U. *Journal of the American Chemical Society* **1999**, *121*, 10102–10111 (cit. on p. 11).

(154) Dereń, P. J.; Stręk, W.; Zych, E.; Drożdżyński, J. *Chemical Physics Letters* **2000**, *332*, 308–312 (cit. on p. 11).

(155) Generic, 1993 (cit. on p. 11).

(156) Menyuk, N.; Dwight, K.; Pierce, J. W. *Applied Physics Letters* **1972**, *21*, 159–161 (cit. on pp. 11, 13).

(157) Gamelin, D. R.; Güdel, H. U. *Accounts of Chemical Research* **2000**, *33*, 235–242 (cit. on p. 11).

(158) Auzel, F. *Chemical Reviews* **2004**, *104*, 139–174 (cit. on p. 11).

(159) Radunz, S.; Schavkan, A.; Wahl, S.; Würth, C.; Tschiche, H. R.; Krumrey, M.; Resch-Genger, U. *The Journal of Physical Chemistry C* **2018**, *122*, 28958–28967 (cit. on pp. 12, 18, 109).

(160) Capobianco, J. A.; Vetrone, F.; Boyer, J. C.; Speghini, A.; Bettinelli, M. *The Journal of Physical Chemistry B* **2002**, *106*, 1181–1187 (cit. on p. 13).

(161) Chen, X.; Ma, E.; Liu, G. *The Journal of Physical Chemistry C* **2007**, *111*, 10404–10411 (cit. on p. 13).

(162) Van de Rijke, F.; Zijlmans, H.; Li, S.; Vail, T.; Raap, A. K.; Niedbala, R. S.; Tanke, H. J. *Nature Biotechnology* **2001**, *19*, 273–276 (cit. on pp. 13, 17).

(163) Heer, S.; Lehmann, O.; Haase, M.; Güdel, H.-U. *Angewandte Chemie International Edition* **2003**, *42*, 3179–3182 (cit. on p. 13).

(164) Heer, S.; Kömpe, K.; Güdel, H. U.; Haase, M. *Advanced Materials* **2004**, *16*, 2102–2105 (cit. on p. 13).

(165) Soukka, T.; Kuningas, K.; Rantanen, T.; Haaslahti, V.; Lövgren, T. *Journal of Fluorescence* **2005**, *15*, 513–528 (cit. on p. 13).

(166) Ritter, B.; Haida, P.; Krahl, T.; Scholz, G.; Kemnitz, E. *Journal of Materials Chemistry C* **2017**, *5*, 5444–5450 (cit. on p. 13).

(167) Krämer, K. W.; Biner, D.; Frei, G.; Güdel, H. U.; Hehlen, M. P.; Lüthi, S. R. *Chemistry of Materials* **2004**, *16*, 1244–1251 (cit. on p. 13).

(168) Mai, H.-X.; Zhang, Y.-W.; Sun, L.-D.; Yan, C.-H. *The Journal of Physical Chemistry C* **2007**, *111*, 13721–13729 (cit. on p. 13).

(169) Zhao, J.; Sun, Y.; Kong, X.; Tian, L.; Wang, Y.; Tu, L.; Zhao, J.; Zhang, H. *The Journal of Physical Chemistry B* **2008**, *112*, 15666–15672 (cit. on p. 13).

(170) Yin, A.; Zhang, Y.; Sun, L.; Yan, C. *Nanoscale* **2010**, *2*, 953–959 (cit. on p. 13).

(171) Wisser, M. D.; Fischer, S.; Maurer, P. C.; Bronstein, N. D.; Chu, S.; Alivisatos, A. P.; Salleo, A.; Dionne, J. A. *ACS Photonics* **2016**, *3*, 1523–1530 (cit. on pp. 13, 14).

(172) Wang, F.; Han, Y.; Lim, C. S.; Lu, Y.; Wang, J.; Xu, J.; Chen, H.; Zhang, C.; Hong, M.; Liu, X. *Nature* **2010**, *463*, 1061–1065 (cit. on pp. 13, 18).

(173) Zou, W.; Visser, C.; Maduro, J. A.; Pshenichnikov, M. S.; Hummelen, J. C. *Nature Photonics* **2012**, *6*, 560–564 (cit. on p. 14).

(174) Chen, G. et al. *Nano Letters* **2015**, *15*, 7400–7407 (cit. on p. 14).

(175) Shao, W.; Chen, G.; Kuzmin, A.; Kutscher, H. L.; Pliss, A.; Ohulchanskyy, T. Y.; Prasad, P. N. *Journal of the American Chemical Society* **2016**, *138*, 16192–16195 (cit. on pp. 14, 16).

(176) Wisser, M. D.; Fischer, S.; Siefe, C.; Alivisatos, A. P.; Salleo, A.; Dionne, J. A. *Nano Letters* **2018**, *18*, 2689–2695 (cit. on p. 14).

(177) Wang, F.; Wang, J.; Liu, X. *Angewandte Chemie International Edition* **2010**, *49*, 7456–7460 (cit. on p. 14).

(178) Johnson, N. J. J.; He, S.; Diao, S.; Chan, E. M.; Dai, H.; Almutairi, A. *Journal of the American Chemical Society* **2017**, *139*, 3275–3282 (cit. on p. 14).

(179) Ma, C.; Xu, X.; Wang, F.; Zhou, Z.; Liu, D.; Zhao, J.; Guan, M.; Lang, C. I.; Jin, D. *Nano Letters* **2017**, *17*, 2858–2864 (cit. on p. 14).

(180) Liu, X.; Kong, X.; Zhang, Y.; Tu, L.; Wang, Y.; Zeng, Q.; Li, C.; Shi, Z.; Zhang, H. *Chemical Communications* **2011**, *47*, 11957–11959 (cit. on pp. 14, 16, 18).

(181) Huang, K.; Liu, H.; Kraft, M.; Shikha, S.; Zheng, X.; Ågren, H.; Würth, C.; Resch-Genger, U.; Zhang, Y. *Nanoscale* **2018**, *10*, 250–259 (cit. on p. 14).

(182) Chen, X.; Jin, L.; Kong, W.; Sun, T.; Zhang, W.; Liu, X.; Fan, J.; Yu, S. F.; Wang, F. *Nature Communications* **2016**, *7*, 10304 (cit. on p. 14).

(183) Vetrone, F.; Naccache, R.; Mahalingam, V.; Morgan, C. G.; Capobianco, J. A. *Advanced Functional Materials* **2009**, *19*, 2924–2929 (cit. on pp. 14, 16).

(184) Ding, M.; Chen, D.; Ma, D.; Dai, J.; Li, Y.; Ji, Z. *Journal of Materials Chemistry C* **2016**, *4*, 2432–2437 (cit. on p. 14).

(185) Wilhelm, S. *ACS Nano* **2017**, *11*, 10644–10653 (cit. on pp. 14, 18).

(186) Na, H.; Woo, K.; Lim, K.; Jang, H. S. *Nanoscale* **2013**, *5*, 4242–4251 (cit. on p. 15).

(187) Zhang, Y.-W.; Sun, X.; Si, R.; You, L.-P.; Yan, C.-H. *Journal of the American Chemical Society* **2005**, *127*, 3260–3261 (cit. on p. 15).

(188) Mai, H.-X.; Zhang, Y.-W.; Sun, L.-D.; Yan, C.-H. *The Journal of Physical Chemistry C* **2007**, *111*, 13730–13739 (cit. on pp. 15, 18).

(189) Mai, H.-X.; Zhang, Y.-W.; Si, R.; Yan, Z.-G.; Sun, L.-d.; You, L.-P.; Yan, C.-H. *Journal of the American Chemical Society* **2006**, *128*, 6426–6436 (cit. on p. 15).

(190) Du, Y.-P.; Zhang, Y.-W.; Sun, L.-D.; Yan, C.-H. *Dalton Transactions* **2009**, 8574–8581 (cit. on p. 15).

(191) Naccache, R.; Vetrone, F.; Mahalingam, V.; Cuccia, L. A.; Capobianco, J. A. *Chemistry of Materials* **2009**, *21*, 717–723 (cit. on p. 15).

(192) Park, Y. I. et al. *Advanced Materials* **2009**, *21*, 4467–4471 (cit. on pp. 15, 18).

(193) Chen, G. et al. *ACS Nano* **2012**, *6*, 8280–8287 (cit. on pp. 15, 18).

(194) Boyer, J.-C.; Gagnon, J.; Cuccia, L. A.; Capobianco, J. A. *Chemistry of Materials* **2007**, *19*, 3358–3360 (cit. on p. 16).

(195) Zhang, F.; Shi, Q.; Zhang, Y.; Shi, Y.; Ding, K.; Zhao, D.; Stucky, G. D. *Advanced Materials* **2011**, *23*, 3775–3779 (cit. on p. 16).

(196) Dong, H.; Sun, L.-D.; Feng, W.; Gu, Y.; Li, F.; Yan, C.-H. *ACS Nano* **2017**, *11*, 3289–3297 (cit. on pp. 16, 18).

(197) Zhuang, Z.; Peng, Q.; Li, Y. *Chemical Society Reviews* **2011**, *40*, 5492–5513 (cit. on pp. 16, 17).

(198) Johnson, N. J. J.; Korinek, A.; Dong, C.; van Veggel, F. C. J. M. *Journal of the American Chemical Society* **2012**, *134*, 11068–11071 (cit. on p. 17).

(199) Liu, C.; Wang, H.; Zhang, X.; Chen, D. *Journal of Materials Chemistry* **2009**, *19*, 489–496 (cit. on p. 17).

(200) Liu, C.; Wang, H.; Li, X.; Chen, D. *Journal of Materials Chemistry* **2009**, *19*, 3546–3553 (cit. on p. 17).

(201) Wei, Y.; Lu, F.; Zhang, X.; Chen, D. *Chemistry of Materials* **2006**, *18*, 5733–5737 (cit. on p. 17).

(202) Li, Z.; Zhang, Y. *Nanotechnology* **2008**, *19*, 345606 (cit. on p. 17).

(203) Park, J.; Joo, J.; Kwon, S. G.; Jang, Y.; Hyeon, T. *Angewandte Chemie International Edition* **2007**, *46*, 4630–4660 (cit. on p. 17).

(204) Shi, F.; Wang, J.; Zhang, D.; Qin, G.; Qin, W. *Journal of Materials Chemistry* **2011**, *21*, 13413–13421 (cit. on p. 17).

(205) Liu, D. et al. *Nature Communications* **2016**, *7*, 10254 (cit. on p. 17).

(206) Chen, D.; Lei, L.; Yang, A.; Wang, Z.; Wang, Y. *Chemical Communications* **2012**, *48*, 5898–5900 (cit. on p. 17).

(207) Qian, H.-S.; Zhang, Y. *Langmuir* **2008**, *24*, 12123–12125 (cit. on p. 17).

(208) Chen, F. et al. *Advanced Functional Materials* **2011**, *21*, 4285–4294 (cit. on pp. 17, 18).

(209) Pichaandi, J.; Boyer, J.-C.; Delaney, K. R.; van Veggel, F. C. J. M. *The Journal of Physical Chemistry C* **2011**, *115*, 19054–19064 (cit. on pp. 17, 18).

(210) Jiang, G.; Pichaandi, J.; Johnson, N. J. J.; Burke, R. D.; van Veggel, F. C. J. M. *Langmuir* **2012**, *28*, 3239–3247 (cit. on p. 17).

(211) Xu, C. T.; Svenmarker, P.; Liu, H.; Wu, X.; Messing, M. E.; Wallenberg, L. R.; Andersson-Engels, S. *ACS Nano* **2012**, *6*, 4788–4795 (cit. on p. 17).

(212) Rinkel, T.; Nordmann, J.; Raj, A. N.; Haase, M. *Nanoscale* **2014**, *6*, 14523–14530 (cit. on p. 18).

(213) Voß, B.; Nordmann, J.; Uhl, A.; Komban, R.; Haase, M. *Nanoscale* **2013**, *5*, 806–812 (cit. on p. 18).

(214) Komban, R.; Klare, J. P.; Voss, B.; Nordmann, J.; Steinhoff, H.-J.; Haase, M. *Angewandte Chemie International Edition* **2012**, *51*, 6506–6510 (cit. on p. 18).

(215) Liang, X.; Wang, X.; Zhuang, J.; Peng, Q.; Li, Y. *Advanced Functional Materials* **2007**, *17*, 2757–2765 (cit. on p. 18).

(216) Suter, J. D.; Pekas, N. J.; Berry, M. T.; May, P. S. *The Journal of Physical Chemistry C* **2014**, *118*, 13238–13247 (cit. on p. 18).

(217) May, P. B.; Suter, J. D.; May, P. S.; Berry, M. T. *The Journal of Physical Chemistry C* **2016**, *120*, 9482–9489 (cit. on p. 18).

(218) Wilhelm, S.; Kaiser, M.; Wurth, C.; Heiland, J.; Carrillo-Carrion, C.; Muhr, V.; Wolfbeis, O. S.; Parak, W. J.; Resch-Genger, U.; Hirsch, T. *Nanoscale* **2015**, *7*, 1403–1410 (cit. on p. 18).

(219) Liu, X. et al. *Nature Communications* **2017**, *8*, 899 (cit. on p. 18).

(220) Downing, E.; Hesselink, L.; Ralston, J.; Macfarlane, R. *Science* **1996**, *273*, 1185–1189 (cit. on p. 18).

(221) Deng, R.; Qin, F.; Chen, R.; Huang, W.; Hong, M.; Liu, X. *Nature Nanotechnology* **2015**, *10*, 237–242 (cit. on p. 18).

(222) Park, B. J.; Hong, A. R.; Park, S.; Kyung, K.-U.; Lee, K.; Seong Jang, H. *Scientific Reports* **2017**, *7*, 45659 (cit. on p. 18).

(223) Van Sark, W. G.; de Wild, J.; Rath, J. K.; Meijerink, A.; Schropp, R. E. *Nanoscale research letters* **2013**, *8*, 81–81 (cit. on p. 18).

(224) Shang, Y.; Hao, S.; Yang, C.; Chen, G. *Nanomaterials* **2015**, *5*, 1782–1809 (cit. on p. 18).

(225) Hao, S.; Shang, Y.; Li, D.; Ågren, H.; Yang, C.; Chen, G. *Nanoscale* **2017**, *9*, 6711–6715 (cit. on p. 18).

(226) Wei, R.; Wei, Z.; Sun, L.; Zhang, J. Z.; Liu, J.; Ge, X.; Shi, L. *ACS Applied Materials & Interfaces* **2016**, *8*, 400–410 (cit. on pp. 18, 19).

(227) Xu, Y.; Li, H.; Meng, X.; Liu, J.; Sun, L.; Fan, X.; Shi, L. *New Journal of Chemistry* **2016**, *40*, 3543–3551 (cit. on pp. 18, 19).

(228) Näreoja, T. et al. *Analytical Chemistry* **2017**, *89*, 1501–1508 (cit. on pp. 18–20).

(229) Cui, Z.; Bu, W.; Fan, W.; Zhang, J.; Ni, D.; Liu, Y.; Wang, J.; Liu, J.; Yao, Z.; Shi, J. *Biomaterials* **2016**, *104*, 158–167 (cit. on pp. 18, 19).

(230) Qian, H. S.; Guo, H. C.; Ho, P. C.-L.; Mahendran, R.; Zhang, Y. *Small* **2009**, *5*, 2285–2290 (cit. on p. 18).

(231) Wang, C.; Cheng, L.; Liu, Z. *Theranostics* **2013**, *3*, 317–330 (cit. on p. 18).

(232) Guan, M.; Dong, H.; Ge, J.; Chen, D.; Sun, L.; Li, S.; Wang, C.; Yan, C.; Wang, P.; Shu, C. *NPG Asia Materials* **2015**, *7*, e205–e205 (cit. on p. 18).

(233) Han, Y.; An, Y.; Jia, G.; Wang, X.; He, C.; Ding, Y.; Tang, Q. *Nanoscale* **2018**, *10*, 6511–6523 (cit. on p. 18).

(234) Jin, G.; He, R.; Liu, Q.; Lin, M.; Dong, Y.; Li, K.; Tang, B. Z.; Liu, B.; Xu, F. *Theranostics* **2019**, *9*, 246–264 (cit. on p. 18).

(235) Zhu, X.; Li, J.; Qiu, X.; Liu, Y.; Feng, W.; Li, F. *Nature communications* **2018**, *9*, 2176–2176 (cit. on p. 18).

(236) Singh, R.; Dumlupinar, G.; Andersson-Engels, S.; Melgar, S. *International journal of nanomedicine* **2019**, *14*, 1027–1038 (cit. on p. 18).

(237) Su, Q.; Feng, W.; Yang, D.; Li, F. *Accounts of Chemical Research* **2017**, *50*, 32–40 (cit. on p. 19).

(238) Tan, G.-R.; Wang, M.; Hsu, C.-Y.; Chen, N.; Zhang, Y. *Advanced Optical Materials* **2016**, *4*, 984–997 (cit. on p. 19).

(239) Tsang, M.-K.; Bai, G.; Hao, J. *Chemical Society Reviews* **2015**, *44*, 1585–1607 (cit. on p. 19).

(240) Vetrone, F.; Naccache, R.; Zamarrón, A.; Juarranz de la Fuente, A.; Sanz-Rodríguez, F.; Martinez Maestro, L.; Martín Rodriguez, E.; Jaque, D.; García Solé, J.; Capobianco, J. A. *ACS Nano* **2010**, *4*, 3254–3258 (cit. on p. 19).

(241) Xu, M.; Zou, X.; Su, Q.; Yuan, W.; Cao, C.; Wang, Q.; Zhu, X.; Feng, W.; Li, F. *Nature communications* **2018**, *9*, 2698–2698 (cit. on p. 19).

(242) Achatz, D. E.; Meier, R. J.; Fischer, L. H.; Wolfbeis, O. S. *Angewandte Chemie International Edition* **2011**, *50*, 260–263 (cit. on p. 19).

(243) Presley, K.; Hwang, J.; Cheong, S.; Tilley, R.; Collins, J.; Viapiano, M.; Lannutti, J. *Materials Science and Engineering: C* **2017**, *70*, 76–84 (cit. on p. 19).

(244) Wang, N.; Yu, X.; Zhang, K.; Mirkin, C. A.; Li, J. *Journal of the American Chemical Society* **2017**, *139*, 12354–12357 (cit. on p. 19).

(245) Ali, R.; Saleh, S. M.; Meier, R. J.; Azab, H. A.; Abdelgawad, I. I.; Wolfbeis, O. S. *Sensors and Actuators B: Chemical* **2010**, *150*, 126–131 (cit. on p. 19).

(246) Alonso-Cristobal, P.; Vilela, P.; El-Sagheer, A.; Lopez-Cabarcos, E.; Brown, T.; Muskens, O. L.; Rubio-Retama, J.; Kanaras, A. G. *ACS Applied Materials & Interfaces* **2015**, *7*, 12422–12429 (cit. on p. 19).

(247) Mader, H. S.; Wolfbeis, O. S. *Analytical Chemistry* **2010**, *82*, 5002–5004 (cit. on p. 19).

(248) Peng, J. et al. *Journal of the American Chemical Society* **2015**, *137*, 2336–2342 (cit. on p. 19).

(249) Li, Z.; Lv, S.; Wang, Y.; Chen, S.; Liu, Z. *Journal of the American Chemical Society* **2015**, *137*, 3421–3427 (cit. on p. 19).

(250) Zhao, L.; Peng, J.; Chen, M.; Liu, Y.; Yao, L.; Feng, W.; Li, F. *ACS Applied Materials & Interfaces* **2014**, *6*, 11190–11197 (cit. on p. 19).

(251) Liu, J.; Liu, Y.; Liu, Q.; Li, C.; Sun, L.; Li, F. *Journal of the American Chemical Society* **2011**, *133*, 15276–15279 (cit. on p. 19).

(252) Liu, Q.; Peng, J.; Sun, L.; Li, F. *ACS Nano* **2011**, *5*, 8040–8048 (cit. on p. 19).

(253) Liu, Y.; Chen, M.; Cao, T.; Sun, Y.; Li, C.; Liu, Q.; Yang, T.; Yao, L.; Feng, W.; Li, F. *Journal of the American Chemical Society* **2013**, *135*, 9869–9876 (cit. on p. 19).

(254) Sun, L.-N.; Peng, H.; Stich, M. I. J.; Achatz, D.; Wolfbeis, O. S. *Chemical Communications* **2009**, 5000–5002 (cit. on pp. 19, 20).

(255) Meier, R. J.; Simbürger, J. M. B.; Soukka, T.; Schäferling, M. *Analytical Chemistry* **2014**, *86*, 5535–5540 (cit. on pp. 19, 20, 148).

(256) Ni, Y.; Wu, J. *Org. Biomol. Chem.* **2014**, *12*, 3774–3791 (cit. on p. 20).

(257) Radunz, S.; Kraus, W.; Bischoff, F. A.; Emmerling, F.; Tschiche, H. R.; Resch-Genger, U. *The Journal of Physical Chemistry A* **2020**, *124*, 1789–1797 (cit. on p. 65).

Selbstständigkeitserklärung

Ich erkläre, dass ich die Dissertation selbständig und nur unter Verwendung der von mir gemäß § 7 Abs. 3 der Promotionsordnung der Mathematisch-Naturwissenschaftlichen Fakultät, veröffentlicht im Amtlichen Mitteilungsblatt der Humboldt-Universität zu Berlin Nr. 42/2018 am 11.07.2018, angegebenen Hilfsmittel angefertigt habe.

Berlin, Februar 2020 _____ (Sebastian Radunz)